



Uniwersytet
Wrocławski



UNIVERSITEIT
GENT

UNIVERSITY OF WROCLAW

Faculty of Physics and Astronomy

Institute of Theoretical Physics

PhD dissertation prepared as a conclusion of the joint PhD program conducted with

GHENT UNIVERSITY

DEPARTMENT OF PHYSICS AND ASTRONOMY

Multinucleon knock-out in neutrino-nucleus scattering: Merging theory and Monte Carlo simulations

Kajetan Niewczas

Supervisor (University of Wrocław)

prof. dr hab. Jan Sobczyk

Supervisor (Ghent University)

prof. dr. Natalie Jachowicz

Wrocław, May 11, 2023

Streszczenie

Precyzyjne pomiary własności neutrin są jednym z największych wyzwań fizyki cząstek elementarnych. Wiąże się to z przeprowadzaniem licznych i złożonych badań doświadczalnych na całym świecie. Eksperymenty, które wykorzystują akceleratory cząstek stanowią unikatowe środowisko do badań oscylacji neutrin i poszukiwania śladów łamania symetrii CP w sektorze leptonowym Modelu Standardowego. Jednakże, ponieważ eksperymenty te opierają się na detekcji oddziaływań neutrin na związanych nukleonach wewnątrz materii jądrowej, więc modelowanie takiego zjawiska stanowi znaczące źródło niepewności doświadczalnej. Tradycyjnie wykonujemy takie obliczenia traktując nukleony jako niezależne, skupiając się na kwazi-elastycznych oddziaływaniach neutrino-nukleon lub wzbudzeniu rezonansów. Rozszerzanie naszej wiedzy dotyczącej przekrojów czynnych na rozpraszanie neutrin jest niezbędne dla dalszego rozwoju badań eksperymentalnych. Aby temu sprostać, musimy przekroczyć próg pierwszego przybliżenia teoretycznego i korzystać z metodologii uwzględniającej efekty korelacji nukleonowych oraz procesów z wybiciem więcej niż jednego nukleonu.

W tej pracy prezentujemy nowatorskie badania będące efektem połączonych doświadczeń grupy teoretycznej z Gandawy oraz wrocławskiego generatora zdarzeń Monte Carlo—NuWro, który stanowi ważne ogniwo analiz eksperymentalnych. Gandawski model oddziaływań neutrin na jądrach atomowych traktuje zarówno początkowe jak i wybite nukleony w przybliżeniu średniopolowym, co prowadzi do spójnego opisu w ramach nierelatywistycznej mechaniki kwantowej. Do tej struktury dodajemy dynamicznie generowane korelacje par nukleonów oraz prądy dwuciałowe z wymianą pośredniczącego pionu, uwzględniając również wzbudzenia rezonansu Δ . Efekty te sumujemy koherentnie, co pozwala na działanie efektów interferencyjnych. Tak skonstruowany model, zweryfikowany poprzez porównania z danymi rozpraszania elektronów, dostarcza przewidywania inkluzywnych, półinkluzywnych i ekskluzywnych przekrojów czynnych w procesach z wybiciem jednego albo dwóch nukleonów.

NuWro to szeroko stosowany generator zdarzeń neutrinowych metodą Monte Carlo. Jest on rozwijany od 2005 przez wrocławską grupę teoretyczną i przez ten czas dostarczył wiele wiarygodnych przewidywań dla kanałów oddziaływań neutrino-jądro istotnych dla eksperymentów oscylacyjnych. Do symulacji hadronowych stanów końcowych, w NuWro, wykorzystujemy własny model kaskady wewnątrzjądrowej, która symuluje obserwowaną w eksperymentach krotkość cząstek wybijanych lub produkowanych w wyniku zdarzeń. Najważniejszym celem naszych badań był rozwój metodologii implementacji modeli teoretycznych w generatorach Monte Carlo tak, aby przewidywania modelu gandawskiego mogły być w przyszłości wykorzystywane w analizach eksperymentalnych. Dlatego skupiliśmy się na dwóch aspektach badań: nieelastycznych

oddziaływaniach stanów końcowych, których brakuje w kwantowomechanicznych modelach rozpraszania neutrin na jądrach atomowych oraz na metodologiach numerycznej optymalizacji implementacji. W pierwszym przypadku wprowadziliśmy efekty korelacji bliskiego zasięgu do modelu kaskady NuWro i zbadaliśmy zachowanie modelu z pomocą danych z ekskluzywnego rozpraszania elektronów. W drugim opracowaliśmy schemat, który umożliwia implementację wielowymiarowych przekrojów czynnych w ich pełnej złożoności ekskluzywnej. Uwzględniając te doświadczenia zaproponowaliśmy wstępną implementację modelu z Gandawy, która, razem z NuWro, tworzy pomost pomiędzy teorią, a eksperymentem.

Abstract

The precise measurement of neutrino properties is among the greatest challenges in fundamental particle physics. This involves conducting numerous and complex experimental studies around the world. Accelerator-based neutrino experiments provide a unique framework for such studies, providing oscillation measurements and hints of the CP violation in the leptonic sector. However, since these experiments rely on the interaction of neutrinos with bound nucleons inside atomic nuclei, understanding the hadronic and nuclear physics of these interactions constitutes a challenging source of uncertainty. Modeling neutrino-nucleus scattering processes is a complex many-body problem, traditionally performed in the independent-particle picture, focusing on the quasielastic neutrino-nucleon interactions or the excitation of nucleon resonances. Expanding our knowledge of cross sections for neutrino scattering is essential for further development of experimental research. To reach the required percent level precision, we need to conduct research beyond the first approximation, incorporating the effects of nucleon correlations and multinucleon knock-out processes.

The presented research involves a novel, multidirectional approach to tackling modern neutrino physics problems by combining the theoretical experiences of the Ghent group and the Monte Carlo neutrino event generator NuWro, explicitly used in experimental analyses. The nuclear physics of Ghent involves a non-relativistic, mean-field-based model for both the initial and final hadronic states. On top of that, we add dynamically generated short-range nucleon correlations and explicit two-body dynamics with meson-exchange currents involving isobar degrees of freedom. This framework, exhaustively compared against electron scattering, provides predictions of inclusive, semi-inclusive, and exclusive cross sections for neutrino-nucleus interactions leading to 1-particle-1-hole and 2-particle-2-hole final states.

NuWro is a Monte Carlo neutrino event generator widely used in the accelerator-based neutrino experiments community. This software, initiated in 2005 by the theoretical group from Wrocław, provides reliable predictions for the vital neutrino-nucleus scattering channels and involves a homegrown cascade model that simulates the final-state interactions of outgoing hadrons. Such a factorized approach allows for combining accurate inclusive cross section calculations while predicting the necessary multiplicity of particles, which we observe as experimental topologies in the detectors. Investigating the possibility of a consistent framework combining the interaction models of Ghent and NuWro is the ultimate goal of this research. Therefore, we focused on the following aspects of Monte Carlo simulations: the final-state interactions missing in quantum-mechanical lepton-nucleus scattering models and the methodology of optimizing generator implementations. In the former, we introduced the effects of short-range correlations into the cascade model of

NuWro and constrained its behavior with exclusive electron scattering data. In the latter, we developed a scheme that makes the implementation of multi-dimensional cross section models feasible in their full exclusive complexity. Facilitated by these advancements, we proposed a preliminary implementation of the Ghent model, which, together with NuWro, forms a bridge between theory and experiment.

Samenvatting

Het nauwkeurig meten van neutrino-eigenschappen is een van de grootste uitdagingen in de fundamentele deeltjesfysica vandaag. Hiervoor worden wereldwijd talrijke en complexe experimenten uitgevoerd. Op versnellers gebaseerde neutrino-experimenten bieden een uniek kader voor dergelijke studies, omdat ze oscillatiemetingen en aanwijzingen voor CP-schending in de leptonische sector leveren. Omdat deze experimenten echter afhankelijk zijn van de interactie van neutrino's met gebonden nucleonen in atoomkernen, vormt het begrijpen van de hadron- en kernfysica van deze interacties een uitdagende bron van onzekerheid. Het modelleren van neutrino-atoomkern verstrooiingsprocessen is een complex veeldeeltjesprobleem, dat traditioneel wordt uitgevoerd in een onafhankelijke-deeltjesbeeld, waarbij de nadruk ligt op de quasielastische neutrino-nucleoninteracties of de excitatie van nucleonresonanties. Het uitbreiden van onze kennis van werkzame doorsneden voor neutrino-verstrooiing is essentieel voor de verdere ontwikkeling van experimenteel onderzoek. Om de vereiste procentuele nauwkeurigheid te bereiken, moeten we onderzoek doen dat verder gaat dan de eerste benadering en waarin de effecten van nucleoncorrelaties en multinucleon-uitstotingsprocessen zijn opgenomen.

Het voorgestelde onderzoek behelst een nieuwe, multidirectionele aanpak van moderne neutrino-fysicaproblemen door de theoretische expertise van de Gentse groep te combineren met de Monte Carlo neutrino event-generator NuWro, die expliciet gebruikt wordt in experimentele analyses. Het Gentse model omvat een niet-relativistisch, gemiddeld-veld-gebaseerde beschrijving voor zowel de initiële als de finale hadron toestanden in de verstrooiingsreactie. Daarbovenop voegen we dynamisch gegenereerde nucleoncorrelaties op korte afstand en expliciete tweelichamendynamica met mesonuitwisselingsstromen waarbij isobarevrijheidsgraden betrokken zijn, toe. Dit raamwerk, uitvoerig vergeleken met elektronenverstrooiing, geeft voorspellingen van inclusieve, semi-inclusieve en exclusieve doorsneden voor neutrino-nucleusinteracties die leiden tot 1-deeltje-1-gat en 2-deeltje-2-gat eindtoestanden.

NuWro is een Monte Carlo neutrino event generator die veel gebruikt wordt in door laboraties de werken aan neutrino-experimenten met versnellers. Deze software, in 2005 ontwikkeld door de theoretische groep uit Wrocław, levert betrouwbare voorspellingen voor de essentiële neutrino-nucleus verstrooiingskanalen en omvat een zelfontwikkeld cascademodel dat de eindtoestand-interacties van uitgaande hadronen simuleert. Een dergelijke gefactoriseerde aanpak maakt het mogelijk om nauwkeurige inclusieve doorsnedenberekeningen te combineren met het voorspellen van de benodigde multipliciteit van deeltjes, die we waarnemen als experimentele topologieën in de detectoren. Het onderzoeken van de mogelijkheid van een consistent raamwerk dat de interactiemodellen van Gent en NuWro combineert, is het uiteindelijke doel

van dit onderzoek. Daarom hebben we ons gericht op de volgende aspecten van Monte Carlo simulaties: de eindtoestand interacties die ontbreken in kwantummechanische lepton-nucleus verstrooiingsmodellen en de methodologie voor het optimaliseren van generator implementaties. In het eerste geval introduceerden we de effecten van correlaties op korte afstand in het cascademodel van NuWro en beperkten we het gedrag ervan met exclusieve elektronenverstrooiingsgegevens. In het tweede hebben we een schema ontwikkeld dat de implementatie van multi-dimensionale doorsnedemodellen haalbaar maakt in hun volledige exclusieve complexiteit. Dankzij deze vooruitgang hebben we een voorlopige implementatie van het Gentse model voorgesteld, dat samen met NuWro een brug vormt tussen theorie en experiment.

List of publications

Theoretical papers

- 1. Study of final-state interactions of protons in neutrino-nucleus scattering with INCL and NuWro cascade models**
A. Ershova, S. Bolognesi, A. Letourneau, J.-C. David, S. Dolan, J. Hirtz, K. Niewczas, J.T. Sobczyk, A. Blanchet, M. Buizza Avanzini, J. Chakrani, J. Cugnon, C. Giganti, S. Hassani, C. Juszczak, L. Munteanu, V.Q. Nguyen, D. Sgalaberna, S. Suvorov
Physical Review D 106 (2022) 032009
- 2. Benchmarking intranuclear cascade models for neutrino scattering with relativistic optical potentials**
A. Nikolakopoulos, R. González-Jiménez, N. Jachowicz, K. Niewczas, F. Sánchez, J. M. Udías
Physical Review C 105 (2022) 054603
- 3. Neutrino energy reconstruction from semi-inclusive samples**
R. González-Jiménez, M. B. Barbaro, J. A. Caballero, T. W. Donnelly, N. Jachowicz, G. D. Megias, K. Niewczas, A. Nikolakopoulos, J. W. Van Orden, J. M. Udías
Physical Review C 105 (2022) 025502
- 4. Angular distributions in Monte Carlo event generation of weak single-pion production**
K. Niewczas, A. Nikolakopoulos, J. T. Sobczyk, N. Jachowicz, R. González-Jiménez
Physical Review D 103 (2021) 053003
- 5. Second class currents, axial mass, and nuclear effects in hyperon production**
C. Thorpe, J. Nowak, K. Niewczas, J. T. Sobczyk, C. Juszczak
Physical Review C 104 (2021) 035502
- 6. Monte Carlo event generation of neutrino-electron scattering**
D. Zhuridov, J. T. Sobczyk, C. Juszczak, K. Niewczas
Journal of Physics G 48 (2021) 055002
- 7. Constraints in modeling the quasielastic response in inclusive lepton-nucleus scattering**
R. González-Jiménez, M. B. Barbaro, J. A. Caballero, T. W. Donnelly, N. Jachowicz, G. D. Megias, K. Niewczas, A. Nikolakopoulos, J. M. Udías
Physical Review C 101 (2020) 015503

8. **Electron versus Muon Neutrino Induced Cross Sections in Charged Current Quasielastic Processes**
A. Nikolakopoulos, N. Jachowicz, N. Van Dessel, K. Niewczas, R. González-Jiménez, J. M. Udías, V. Pandey
Physical Review Letters 123 (2019) 052501
9. **Nuclear Transparency in Monte Carlo Neutrino Event Generators**
K. Niewczas, J. T. Sobczyk
Physical Review C 100 (2019) 015505
10. **Modeling neutrino-induced charged pion production on water at T2K kinematics**
A. Nikolakopoulos, R. González-Jiménez, K. Niewczas, J. Sobczyk, N. Jachowicz
Physical Review D 97 (2018) 093008
11. **Pion production within the hybrid relativistic plane wave impulse approximation model at MiniBooNE and MINERvA kinematics**
R. González-Jiménez, K. Niewczas, N. Jachowicz
Physical Review D 97 (2018) 013004
12. **Electroweak single-pion production off the nucleon: from threshold to high invariant masses**
R. González-Jiménez, N. Jachowicz, K. Niewczas, J. Nys, V. Pandey, T. Van Cuyck, N. Van Dessel
Physical Review D 95 (2017) 113007

Experimental papers

1. **Measurements of neutrino oscillation parameters from the T2K experiment using 3.6×10^{21} protons on target**
T2K Collaboration (K. Abe, ..., K. Niewczas, ... et al.)
arXiv:2303.03222 (submitted to European Physical Journal C)
2. **Scintillator ageing of the T2K near detectors from 2010 to 2021**
T2K Collaboration (K. Abe, ..., K. Niewczas, ... et al.)
JINST 17 (2022) 10, P10028
3. **Supernova Model Discrimination with Hyper-Kamiokande**
Hyper-Kamiokande Collaboration (K. Abe, ..., K. Niewczas, ... et al.)
The Astrophysical Journal 916 (2021) 15
4. **First T2K measurement of transverse kinematic imbalance in the muon-neutrino charged-current single- π^+ production channel containing at least one proton**
T2K Collaboration (K. Abe, ..., K. Niewczas, ... et al.)
Physical Review D 103 (2021) 112009

5. **Improved constraints on neutrino mixing from the T2K experiment with 3.13×10^{21} protons on target**
T2K Collaboration (K. Abe, ..., K. Niewczas, ... et al.)
Physical Review D 103 (2021) 112008
6. **Measurements of $\bar{\nu}_\mu$ and $\bar{\nu}_\mu + \nu_\mu$ charged-current cross-sections without detected pions nor protons on water and hydrocarbon at mean antineutrino energy of 0.86 GeV**
T2K Collaboration (K. Abe, ..., K. Niewczas, ... et al.)
Progress of Theoretical and Experimental Physics 2021 (2021) 043C01
7. **T2K measurements of muon neutrino and antineutrino disappearance using 3.13×10^{21} protons on target**
T2K Collaboration (K. Abe, ..., K. Niewczas, ... et al.)
Physical Review D 103 (2021) L011101
8. **Measurement of the charged-current electron (anti-)neutrino inclusive cross-sections at the T2K off-axis near detector ND280**
T2K Collaboration (K. Abe, ..., K. Niewczas, ... et al.)
Journal of High Energy Physics 10 (2020) 114
9. **The Hyper-Kamiokande Experiment**
Hyper-Kamiokande Collaboration (K. Abe, ..., K. Niewczas, ... et al.)
Snowmass LOI, 2021 Snowmass Summer Study
10. **First measurement of the charged current $\bar{\nu}_\mu$ double differential cross section on a water target without pions in the final state**
T2K Collaboration (K. Abe, ..., K. Niewczas, ... et al.)
Physical Review D 102 (2020) 012007
11. **Simultaneous measurement of the muon neutrino charged-current cross section on oxygen and carbon without pions in the final state at T2K**
T2K Collaboration (K. Abe, ..., K. Niewczas, ... et al.)
Physical Review D 101 (2020) 112004
12. **First combined measurement of the muon neutrino and antineutrino charged-current cross section without pions in the final state at T2K**
T2K Collaboration (K. Abe, ..., K. Niewczas, ... et al.)
Physical Review D 101 (2020) 112001
13. **Search for Electron Antineutrino Appearance in a Long-Baseline Muon Antineutrino Beam**
T2K Collaboration (K. Abe, ..., K. Niewczas, ... et al.)
Physical Review Letters 124 (2020) 161802
14. **Constraint on the matter–antimatter symmetry-violating phase in neutrino oscillations**
T2K Collaboration (K. Abe, ..., K. Niewczas, ... et al.)
Nature 580 (2020) 339–344

15. **Measurement of the muon neutrino charged-current single π^+ production on hydrocarbon using the T2K off-axis near detector ND280**
T2K Collaboration (K. Abe, ..., K. Niewczas, ... et al.)
Physical Review D 101 (2020) 012007
16. **Measurement of neutrino and antineutrino neutral-current quasielastic like interactions on oxygen by detecting nuclear deexcitation γ rays**
T2K Collaboration (K. Abe, ..., K. Niewczas, ... et al.)
Physical Review D 100 (2019) 112009
17. **Measurement of the muon neutrino charged-current cross sections on water, hydrocarbon and iron, and their ratios, with the T2K on-axis detectors**
T2K Collaboration (K. Abe, ..., K. Niewczas, ... et al.)
Progress of Theoretical and Experimental Physics 2019 093C02
18. **Search for heavy neutrinos with the T2K near detector ND280**
T2K Collaboration (K. Abe, ..., K. Niewczas, ... et al.)
Physical Review D 100 (2019) 052006
19. **Search for neutral-current induced single photon production at the ND280 near detector in T2K**
T2K Collaboration (K. Abe, ..., K. Niewczas, ... et al.)
Journal of Physics G 46 (2019) 08LT01
20. **Search for light sterile neutrinos with the T2K far detector Super-Kamiokande at a baseline of 295 km**
T2K Collaboration (K. Abe, ..., K. Niewczas, ... et al.)
Physical Review D 99 (2019) 071103
21. **Search for CP violation in Neutrino and Antineutrino Oscillations by the T2K experiment with 2.2×10^{21} protons on target**
T2K Collaboration (K. Abe, ..., K. Niewczas, ... et al.)
Physical Review Letters 121 (2018) 171802
22. **Characterization of nuclear effects in muon-neutrino scattering on hydrocarbon with a measurement of final-state kinematics and correlations in charged-current pionless interactions at T2K**
T2K Collaboration (K. Abe, ..., K. Niewczas, ... et al.)
Physical Review D 98 (2018) 032003
23. **Measurement of inclusive double-differential ν_μ charged-current cross section with improved acceptance in the T2K off-axis near detector**
T2K Collaboration (K. Abe, ... , K. Niewczas, ... et al.)
Physical Review D 98 (2018) 012004

Proceedings

1. **Electron-nucleus scattering in the NEUT event generator**
S. Dolan, J. McElwee, S. Bolognesi, Y. Hayato, K. McFarland, G. Megias, K. Niewczas, L. Pickering, J. Sobczyk, L. Thompson, C. Wret
arXiv:2301.09195
2. **Event Generators for High-Energy Physics Experiments**
Snowmass 2021 (J. M. Campbell, ..., K. Niewczas, ... et al.)
arXiv:2203.11110
3. **Summary of the NuSTEC Workshop on Neutrino-Nucleus Pion Production in the Resonance Region**
NuSTEC Collaboration (L. Aliaga, ..., K. Niewczas, ... et al.)
arXiv:2011.07166
4. **Non-trivial differences between charged current ν_e and ν_μ induced interactions with nuclei**
A. Nikolakopoulos, N. Jachowicz, R. González-Jiménez, J. M. Udías, K. Niewczas, V. Pandey
PoS NuFact2019 (2020) 048
5. **Modeling neutrino-nucleus interactions in the few-GeV region**
K. Niewczas, N. Jachowicz, A. Nikolakopoulos, J. Nys, N. Van Dessel, R. González-Jiménez, V. Pandey
PoS NuFACT2018 (2019) 031
6. **Modeling Nuclear Effects for Neutrino-Nucleus Scattering in the Few-GeV Region**
K. Niewczas, R. González-Jiménez, N. Jachowicz, A. Nikolakopoulos, J.T. Sobczyk
Springer Proc.Phys. 225 (2019) 155-156
7. **Effect of Outgoing Nucleon Wave Function on Reconstructed Neutrino Energy**
A. Nikolakopoulos, M. Martini, N. Dessel, K. Niewczas, R. González-Jiménez, N. Jachowicz
Springer Proc.Phys. 225 (2019) 157-158
8. **Modeling neutrino-nucleus interaction at intermediate energies**
R. González-Jiménez, N. Jachowicz, A. Nikolakopoulos, J. Nys, T. Van Cuyck, N. Van Dessel, K. Niewczas, V. Pandey
PoS NuFact2017 (2017) 072

Acknowledgements

This thesis is the outcome of a very long process of my doctorate studies. It has been a challenging yet rewarding journey in many aspects of academic and personal development. I was fortunate to meet many wonderful people who supported, encouraged, and inspired me along the way. As much as I am willing to try, acknowledging every person who contributed to this research is nearly impossible. To those who felt omitted, I apologize.

First and foremost, I would like to thank my supervisors, Natalie and Jan, for their unwavering support and mentoring throughout my academic career. Over the years, my research faced countless obstacles that required courage and effort to overcome. Their expertise, patience, and kindness allowed me to grow as a researcher and as a person. Jan, you were the first person who made me believe that my impact on science can be valuable. I am very grateful for all of the 10 years of our collaboration and friendship. Thanks to you, I still have hope that we are more than just a "quantum fluctuation". Natalie, you made me understand what it means to be an independent scientist and how to push my research beyond obstacles encountered on the way. Thank you very much for making me an "essential worker", a part of the group independently of my inhabitation.

I am grateful to the members of the doctoral committee and the referees of this thesis. Their time and efforts in tempering my physics knowledge allowed me to understand and learn many new things. I could only wish for more of such educative feedback in the future.

Studying neutrino-nucleus interactions is a broad subject that cannot be approached as a single-person effort but requires extensive collaboration and teamwork. I was fortunate to be a part of more than one scientific group that allowed me to expand my research horizons. I want to thank my dear nuclear friends, Raúl and Alexis, for their never-ending interest in my work and for helping me be equally devoted to theirs. Raúl, thank you for your academic guidance and all our captivating discussions that did not respect the boundaries of office walls. ¡Viva el Betis, manque pierda! Alexis, thank you for your patience with all my research issues and for teaching me to focus on essentials, not only in physics.

During my doctorate studies, I joined the NuWro group, where I enjoyed working with Tomasz, Cezary, Dmitry, Tomasz, Michał, and others. Thank you for our collaboration and meetings, which were always educative and inspiring. Many of us were the Polish Neutrino Group and the T2K Collaboration members. I thank Katarzyna, Justyna, Ewa, Magda, Jan, Kamil, and all other T2K and Hyper-Kamiokande collaborators for years of collective work on common research goals.

Despite the weird times and consequences of what surprised us all in March 2020, the primary place for doing physics has always been the laboratories and research institutes. My doctorate

studies followed a joint program between the University of Wrocław and Ghent University. I am happy I could be a part of these communities together. I am grateful to all my friends and colleagues from IFT, especially Anna, Mateusz, Piotr, Valeriya, Michał, Mateusz, Maciej, and Michał. Equally, I acknowledge the kindness and support of all my friends and colleagues from INW, especially Andres, Alexis, Nils, Ivan, Matthieu, Sam, Ward, Martina, Antoine, Christos, Ianthe, Celine, Sander, Basile, Corneel, Jannes, and Tom. Additionally, I want to thank José Manuel and his group at UCM for their warm welcome over my two research stays in Madrid. Working together with all of you was a charm.

This thesis would only be accomplished with the pillars of my strength: my parents, who have always supported me and encouraged me to move forward, no matter the circumstances. Their analytical thinking and broad horizons taught me everything that allowed me to reach this moment. Mamo, Tato, dziękuję bardzo, że jesteście.

I express my deepest sympathy and gratitude to everybody else who supported my research outside of the academic perspective. I want to thank my family, especially my brother, Maciej; my grandparents, Kazimiera, Stefan, and Adela; my aunts and uncles, Joanna, Piotr, Mira, Ewelina, Karsten, Krzysztof; and my cousins, Jakub, Filip, and Julia. I also want to express my gratitude to my friends Paweł and Kuba for always being there for me. Additionally, I would like to thank all my friends in Belgium and France who were not mentioned up to this point: Alba, Paula, Maren, Prem, Liesl, Meta, Vishvas, Tristan, Anastasija, Ksenia, Yulia, Aleksander, Sergey, Vlad, and Konstantin. As well as all other colleagues and friends who indirectly contributed to this research. Pani Karolino, dziękuję bardzo za Pani pomoc w najtrudniejszych chwilach, Pani cierpliwość i wsparcie, które pozwoliło mi dotrzeć do tych radosnych.

Those who ever met me surely noticed my devotion to sports. It is a vital aspect of life that lets me clear my mind and calm my insecurities. However unusual in the academic community, the impact of my sports activities on this work cannot be overstated. I want to thank my ice and inline hockey team, WTH Wrocław, especially Tomasz, Grzegorz, Tomasz, Tomáš, Artur, Radosław, Michał, Tymon, Tomasz, Michał, Sławomir, Aleksandr, Maciej, Atsushi, Daniel, Igor, Paweł. Likewise, I express my gratitude to my floorball teams of Politechnika Wrocławska, Floorball Wrocław, Black Cobra Gent, and our University of Wrocław team, especially coach Tomasz and Dominik, for dealing with my moods all these years.

Finally, most importantly, I want to express my heartfelt gratitude to my partner and muse, Anna. Such a simple text cannot tell how much I appreciate your love, understanding, and sacrifices to help me accomplish this thesis. I also had the privilege of collaborating with you on joint academic projects, where I could observe your dedication and high working standards. Thank you for showing me how it is done.

Contents

1	Introduction	3
1.1	Standardization of particle physics	3
1.2	Experimental study of neutrino properties	10
1.3	Theoretical picture of neutrino interactions	20
1.4	Monte Carlo neutrino event generators	29
1.5	Outline of the research	33
	References	34
2	Theoretical framework	41
2.1	Differential cross sections	41
2.2	Nuclear framework	49
2.3	Short-range correlations	59
2.4	Meson-exchange currents	73
	References	84
3	Cross sections for one- and two-nucleon knock-out reactions	87
3.1	Isobar degrees of freedom	87
3.2	Consistent modeling of two-body currents	104
3.3	Constraining the vector interaction	121
3.4	Numerical convergence	125
	References	130
4	Cascade model of final-state interactions	133
4.1	In-medium propagation of nucleons	133
4.2	Exclusive electron scattering simulations	137
4.3	Constraining the FSI model	142
4.4	Consequences for neutrino analyses	146
	References	150
5	Generator implementation philosophy	153
5.1	Single-pion production	153
5.2	Monte Carlo algorithms	157
5.3	Numerical tools	160

5.4 Implementation performance	161
References	171
6 Summary and outlook	173
6.1 Research synopsis	173
6.2 Future prospects	176
References	180
Appendices	181
A One-nucleon knock-out matrix elements	182
B Two-nucleon knock-out matrix elements	189
C Reduced matrix elements	193
References	201

1

Introduction

The advent of powerful particle accelerators has remarkably increased our capability to probe hadronic matter and the interactions of elementary particles. Among other advances, it also facilitated using high-luminosity neutrino fluxes, increasing the statistics obtained in neutrino detectors. It allows us to enter the precision era of neutrino experiments, probing effects that strain the Standard Model of particle physics. Thus, to facilitate this process, theoretical modeling of neutrino-nucleus reactions should provide state-of-art predictions for several essential interaction channels, accurately implemented in Monte Carlo event generators, to decrease the systematic uncertainties in experimental analyses.

1.1 Standardization of particle physics

Matter composed of various elementary particles held together by fundamental forces is a widely accepted picture of our observable surroundings. The modern understanding of this idea is rooted in the early-nineteenth-century atomic theory of an English chemist John Dalton, but some early beliefs originate from the very cradle of scientific thought—the Milesian school of philosophy. Although we commonly trace it back to the reductive arguments of Greek philosophers Leucippus and Democritus [1], it can be surprising how long humanity had to wait to obtain direct evidence for the existence of such indivisible constituents of matter. The path to this discovery commenced with the work of Robert Brown, a Scottish botanist, who, in 1828, described the random nature of traceable pollen particles moving in a fluid. This phenomenon only grabbed compelling public attention at the beginning of the twentieth century when Albert Einstein and Marian Smoluchowski independently formulated mathematical theories [2], explaining it as caused by the fact that any fluid is composed of tiny molecules in thermal equilibrium. In 1905, this explanation of the Brownian motion was validated experimentally by Jean Perrin [3], giving a solid argument

that elementary atoms and molecules form the world around us. However, another viable path led to studying physics on even smaller scales. A few years earlier, in 1897, Joseph John Thomson found evidence that electricity in gases transmits by individual particles of a universal mass-to-charge ratio [4], about one-thousandth of the one of hydrogen [5]. These entities, later called *electrons*, were the first discovered subatomic particles that remain elementary until now. These discoveries and the rapid development of special relativity and quantum mechanics opened a fruitful century of experimental particle physics that found a whole *zoo of particles* with different properties and substructures [6].

While one could understand elementary particles as actors on the physics stage, the fundamental forces are the ones that would write the script and govern their dynamics. Here, it has always been the role of theoretical physics to develop the mathematical description that would allow predicting the behavior of a particular system over time. An instinctive consequence of formulating such laws of physics is an urge to unify our understanding into a comprehensive first-principles picture. A primary example of this process is the mid-nineteenth-century James Clerk Maxwell's synthesis [7] that unified known electric and magnetic effects into a single electromagnetic interaction. With the other advancements in twentieth-century physics, more physicists proposed elegant forms of relating different phenomena through compact underlying theories. Notably, in 1928, Paul Dirac showed how to describe the dynamics of electrons (fermions) and photons (bosons) following the principles of both quantum mechanics and the special theory of

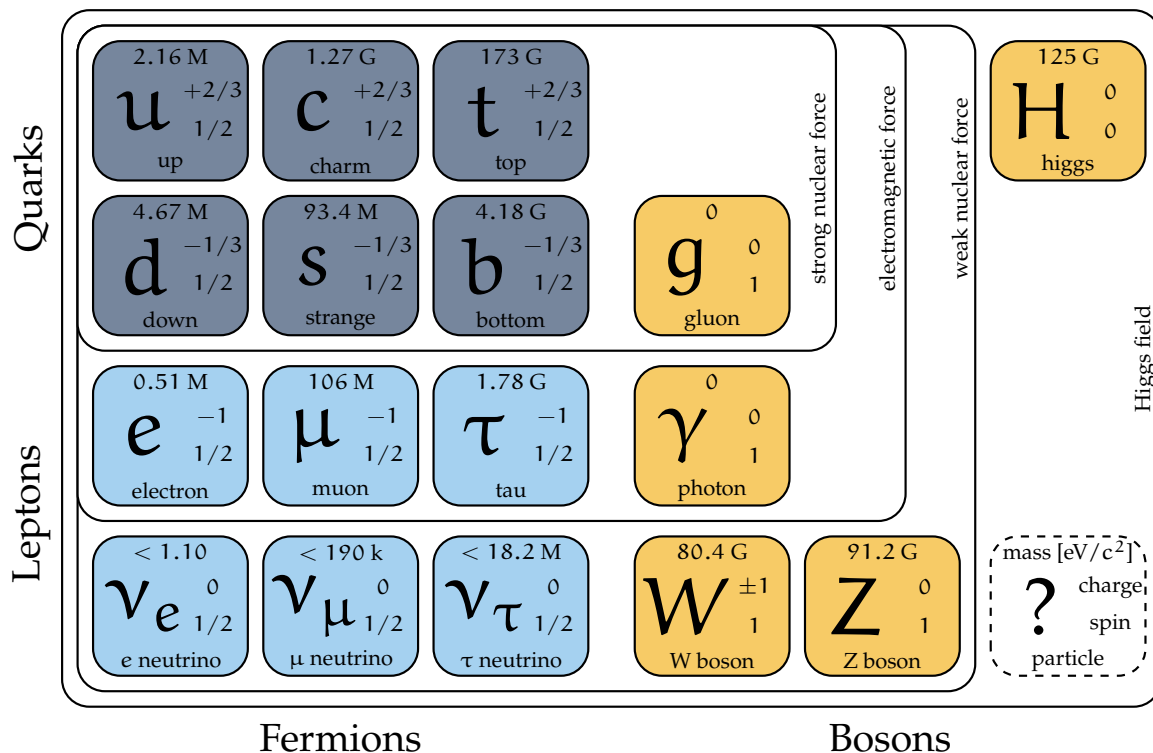


Figure 1.1: The Standard Model of elementary particles [6], with particles divided into matter-building fermions: quarks and leptons, and bosons, which are the force carriers of particular interactions. The frames represent types of fermions that participate in given interactions, together with an accompanying boson(s). The figure format was inspired by Ref. [8].

relativity [9]. Based on such a framework, an example of a quantum field theory, the theory by Sheldon Glashow [10], Abdus Salam [11], and Steven Weinberg [12] unified electromagnetic and weak interactions (governing nuclear decays) as both mediated by the exchange of gauge bosons. Together with a parallel construction for quarks (strongly interacting subcomponents of nucleons), having an additionally attributed *color*, the described theories form the Standard Model (SM) of elementary particles [13]. Although it is tempting to unify the interactions further, this is where the frontier of physics lies, with our present knowledge encapsulated in the most successful theory to date, schematically presented in Fig. 1.1.

Hunting for new particles

In modern times, performing high-energy experiments is crucial in searching for new particles or studying the underlying phenomena, as we must explore new, harder-to-access regions of phase space. There are two main philosophies to achieve such goals: the energy and the intensity frontiers. Experiments within the former aim to focus energy on single interactions that cause showers of various particles that are later analyzed, searching for the occurrence of specific particle decays. It proved notably successful in 2012 when the CMS and ATLAS experiments at CERN discovered the Higgs boson [14,15], a key ingredient in the mass-generating mechanism for elementary particles, especially for the W and Z bosons. Although a remarkable achievement, this concluded the shortlist of widely anticipated particles in the well-established formulation of the Standard Model, and it is still not entirely clear how this field will develop in the future. Still, the ongoing efforts on the new colliders: HL-LHC in CERN [16] and ILC in Japan [17], or more dedicated experiments, such as SHiP [18], might bring unexpected answers to the questions yet to be asked.

The other approach, the intensity frontier, aims at generating fluxes of an immense number of particles needed to study rare subatomic interactions. Here, observing significant discrepancies from the SM predictions, such as the Muon $g-2$ measurement anomaly [19], would point to the potential existence of yet undiscovered particles or other unexpected deviations. Such experiments also allow studying the properties of the tiniest fermions, called *neutrinos*, which are challenging to incorporate into the Standard Model consistently and span a promising investigation path. The existence of these particles was first postulated in 1930 by Wolfgang Pauli to explain the continuous spectrum of electrons emitted in beta decay experiments [20]. He reasoned that having an additional neutral particle in the process,

$$A^{Z,N} \rightarrow A^{Z+1,N-1} + e^- + \bar{\nu}_e \quad (1.1.1)$$

would allow continuous sharing of the reaction energy between the two particles ($\bar{\nu}$ are the antiparticles corresponding to neutrinos, called *antineutrinos*). As detected about 26 years later by Fredrick Reines and Clyde Cowan [21] via the inverse beta decay,

$$\bar{\nu}_e + A^{Z,N} \rightarrow A^{Z-1,N+1} + e^+. \quad (1.1.2)$$

neutrinos played a crucial role in formulating Enrico Fermi's theory of weak interactions [22]. Although highly elusive and therefore requiring large intensities to be studied, we now know that

neutrinos possess unexpected beyond-Standard-Model (BSM) properties that might be our most promising window to the new physics [6].

Extreme acceleration of particles can also happen without human intervention. High-energy particles of astronomical origin constantly bombard our planet, and we have many dedicated research programs to study them. It is the source of the most energetic particles known to humanity, such as the *Oh-My-God* particle [23], tens of times more energetic than the highest collision energy in the Large Hadron Collider at CERN. Many early neutrino detectors relied on this kind of particle source, and the first insights about their unusual properties appeared while studying neutrinos originating in the Sun. Namely, in the late 1960s, the Homestake experiment headed by Raymond Davis, Jr. reported an unexpectedly small flux of detected solar neutrinos [24]. A person who eagerly anticipated this observation was Bruno Pontecorvo, who, in 1969, published his explanation of this phenomenon through the theory of neutrino oscillations [25]. The idea, dated back to 1957 [26], was an analogy to the mixing of other neutral particles, where the particle state responsible for the weak interaction (characterized by the *flavor*) is not truly the one that propagates (characterized by the *mass*). This discrepancy causes obtaining specific probabilities for neutrinos to change their type while propagating through space. The conclusive evidence of this unique effect came through the Super-Kamiokande (SK) and SNO experiments, reported from 1998 to 2002 [27–29]. A fundamental consequence of neutrino oscillations is that they must have nonzero masses. Here, schematically compared to other elementary particles in Fig. 1.2.

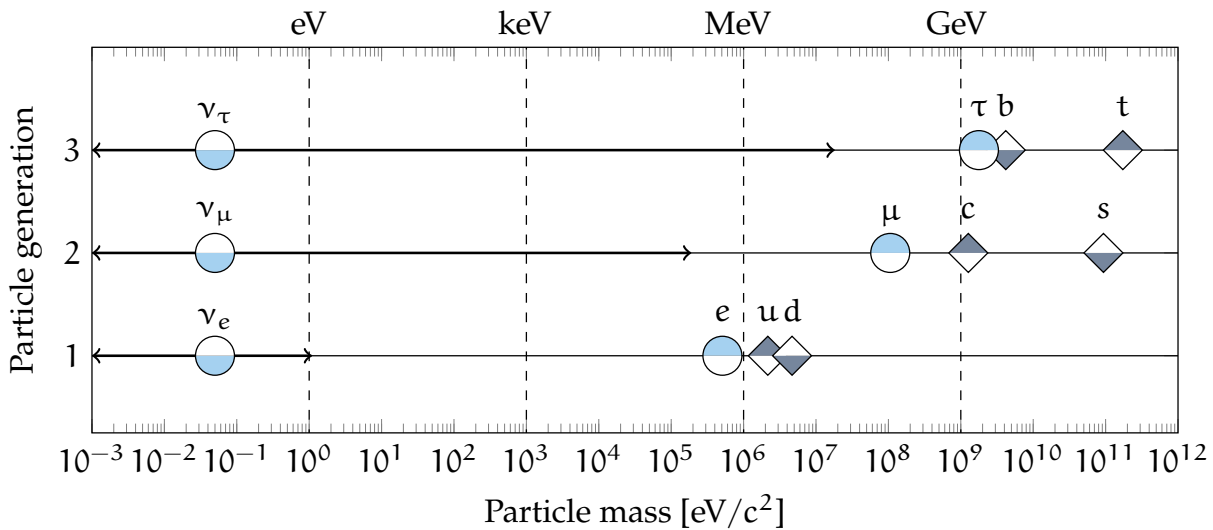


Figure 1.2: Masses of all known fundamental fermions [6] on a logarithmic scale. Each neutrino value represents one-third of the estimated total mass with an individual experimental bound. The figure format was inspired by Ref. [30].

(Un)usual neutrino properties

According to their well-established formulation within the Standard Model [6,31], neutrinos are the only electrically neutral elementary fermions, i.e., they have half-integer intrinsic angular momentum (spin). As presented in Fig. 1.1, they occur in three generations: ν_e , ν_μ , and ν_τ , which,

in the first order of perturbation expansion, do not participate in electromagnetic processes but interact only weakly. The neutrino label corresponds to the mass of the particular charged lepton produced in association: e , μ , or τ . As mentioned earlier, the primary source of electron neutrinos is the beta nuclear decay:

$$A^{Z,N} \rightarrow A^{Z+1,N-1} + e^- + \bar{\nu}_e \quad (1.1.3)$$

or

$$A^{Z,N} \rightarrow A^{Z-1,N+1} + e^+ + \nu_e. \quad (1.1.4)$$

For the muon neutrinos, the mass of the accompanying charged lepton (muon) is larger and so is the general energy scale of processes involving these particles. Muon neutrinos are produced in pion, or muon decays:

$$\pi^+ \rightarrow \mu^+ + \nu_\mu, \quad (1.1.5)$$

$$\mu^+ \rightarrow e^+ + \nu_e + \bar{\nu}_\mu, \quad (1.1.6)$$

which are unstable particles that are formed naturally in interactions of cosmic radiation entering the upper layers of our atmosphere. As for the third generation of fermions, the processes involving tau neutrinos require significantly more energy than those for the other species and therefore are the most challenging to observe in naturally occurring phenomena. They are produced by high-energy astronomical sources, such as core-collapse supernova explosions. Ultimately, we do not expect to discover any other than those three species of such light neutrinos because of the detailed analyses of the time of life of Z^0 bosons, which can decay according to

$$Z^0 \rightarrow \nu_\alpha + \bar{\nu}_\alpha. \quad (1.1.7)$$

As stated in Ref. [32], the number of neutrinos participating in the current formulation of the electroweak interactions is:

$$N_\nu = 2.9840 \pm 0.0082. \quad (1.1.8)$$

Deviations from this number would support potential BSM scenarios, which provide more exotic, so far non-observed particles.

In the theory of weak interactions, neutrinos couple with a Z^0 -boson in an elastic process where only their 4-momentum is changed (neutral current, NC) or with a W^\pm boson, additionally exchanging an electric charge (charged current, CC). We conventionally write the latter as

$$W^+ \rightarrow l^+ + \nu_l, \quad W^- \rightarrow l^- + \bar{\nu}_l, \quad (1.1.9)$$

where $l = e, \mu, \tau$ labels the flavor (mass) of the charged lepton. This leads to a clear, experimental distinction of ν and $\bar{\nu}$ as the Dirac particles corresponding to the charge of the produced charged lepton: positive and negative, respectively. Fig. 1.3 presents the first ever neutrino recorded in a bubble chamber experiment through an inelastic neutrino-nucleon scattering process, an example of a CC interaction. In 1957, two remarkable experiments led by Chien-Shiung Wu [34] and Leon Lederman [35] provided evidence that weak interactions can break parity symmetry and bring a universal sense of orientation in space. Then, in a subsequent experiment led by Maurice Goldhaber [36], neutrinos always showed a spin antiparallel to their momentum (negative helicity), implying that antineutrinos have their spin parallel to their momentum (positive helicity),



Figure 1.3: The first neutrino event in a hydrogen bubble chamber captured on film, taken at Argonne National Laboratory [33]. A neutrino coming from the left interacted with a proton to produce the three-pronged event consisting of μ^- (longest track), a proton (shortest track), and a pion π^+ .

i.e., neutrinos are always left-handed, and antineutrinos are always right-handed. In a massless particle limit, one can relate helicity to the more abstract concept of *chirality*, which provides a foundation for the weak neutrino interaction's vector-axial (V-A) structure. In simple terms, it contains a part that transforms under rotations as a vector (γ_μ) and gains a minus sign, which is of analogical structure to the electromagnetic interactions of electrons, and a part that does not change its sign, an axial-vector ($\gamma_\mu\gamma_5$) that depends on helicity and is characteristic to weak interactions. Mathematically, we include the chiral symmetry through a projection operator $P_L = (1 - \gamma_5)/2$ and obtain the whole interaction dynamics through the following Lagrangians:

$$\mathcal{L}_{CC} = \sum_l -\frac{g}{2\sqrt{2}} \bar{\nu}_l \gamma^\mu (1 - \gamma^5) l^- W_\mu^+ + \text{h.c.} \quad (1.1.10)$$

$$\mathcal{L}_{NC} = \sum_l -\frac{g}{4 \cos \theta_W} \bar{\nu}_l \gamma^\mu (1 - \gamma^5) \nu_l Z_\mu^0 + \text{h.c.} \quad (1.1.11)$$

The theory formulated in such a way satisfies a more complex charge-parity (CP) symmetry: the structure of weak interactions should not change under a simultaneous charge conjugation (particle/antiparticle) and a spatial reflection (mirror image), i.e., up to their helicity, left-handed neutrinos behave the same way as right-handed antineutrinos.

Neutrino masses, which characterize eigenstates of the free Hamiltonian, are too small to be determined with the current experimental methodology. Thus, we cannot distinguish them in either the production or detection of neutrinos, so we assume a mixing between the interacting and propagating states [37]. Therefore, the observed neutrino flavor eigenstates undergo a peculiar effect of oscillations. The diagonalization of neutrino masses is introduced by including the leptonic mixing matrix U in Eq. (1.1.10) and writing the propagating neutrino state as a superposition of the flavor states:

$$|\nu_j\rangle = \sum_{\alpha=e,\mu,\tau} U_{\alpha j} |\nu_\alpha\rangle, \quad (1.1.12)$$

where $\alpha = e, \mu, \tau$ and $i = 1, 2, 3$ label neutrinos with a specific flavor and mass, respectively. The mixing matrix is called the Pontecorvo-Maki-Nakagawa-Sakata (PMNS) matrix, and it is a unitary matrix parametrized through three θ mixing angles and a CP-violating δ phase as:

$$U = \begin{bmatrix} 1 & 0 & 0 \\ 0 & c_{23} & s_{23} \\ 0 & -s_{23} & c_{23} \end{bmatrix} \begin{bmatrix} c_{13} & 0 & s_{13}e^{-i\delta} \\ 0 & 1 & 0 \\ -s_{13}e^{i\delta} & 0 & c_{13} \end{bmatrix} \begin{bmatrix} c_{12} & s_{12} & 0 \\ -s_{12} & c_{12} & 0 \\ 0 & 0 & 1 \end{bmatrix}, \quad (1.1.13)$$

where $c_{ij} \equiv \cos \theta_{ij}$ and $s_{ij} \equiv \sin \theta_{ij}$. To understand what happens to neutrinos as they propagate through space, we describe the propagation of their mass eigenstates, of energy E_j and momentum p_j , as plane-wave solutions, a function of the time t and the distance L , in one direction:

$$|\nu_j(t, L)\rangle = e^{-i(E_j t - p_j L)} |\nu_j(0, 0)\rangle, \quad (1.1.14)$$

and formulate the oscillation probability as

$$\begin{aligned} P(\nu_\alpha \rightarrow \nu_\beta) &= |\langle \nu_\beta | \nu_\alpha(t, L) \rangle|^2 = \left| \sum_{j,k} U_{\alpha j}^* U_{\beta k} e^{-i(E_j t - p_j L)} \langle \nu_k | \nu_j \rangle \right|^2 \\ &= \left| \sum_j U_{\alpha j}^* U_{\beta j} e^{-i(E_j t - p_j L)} \right|^2 = \sum_{j,k} U_{\alpha j}^* U_{\beta j} U_{\alpha k} U_{\beta k}^* e^{-i((E_k - E_j)t - (p_k - p_j)L)}. \end{aligned} \quad (1.1.15)$$

Here, the derivation in fully correct description involves introducing wave packets and group velocity, which leads to the neutrino oscillation probability in a compact form:

$$\begin{aligned} P(\nu_\alpha \rightarrow \nu_\beta) &= \delta_{\alpha\beta} - 4 \sum_{j>k} \text{Re} \{ U_{\alpha j}^* U_{\beta j} U_{\alpha k} U_{\beta k}^* \} \sin^2 \left(\frac{\Delta m_{jk}^2 L}{4E} \right) \\ &\quad + 2 \sum_{j>k} \text{Im} \{ U_{\alpha j}^* U_{\beta j} U_{\alpha k} U_{\beta k}^* \} \sin^2 \left(\frac{\Delta m_{jk}^2 L}{2E} \right), \end{aligned} \quad (1.1.16)$$

where $\Delta m_{jk}^2 = m_j^2 - m_k^2$ is the difference of neutrino masses squared. The behavior of this formula depends on the neutrino energy spectrum and propagation distance, presented for two typical conditions in Fig. 1.4.

Due to their unusual properties, research on neutrinos serves as a promising path for discovering new physics, from the properties of neutrino oscillations to other beyond-Standard-Model phenomena. The list of unanswered questions connects many experimental conditions and origins of detected neutrinos. How many families of neutrinos do we have, and how do we interpret the number of Eq. (1.1.8)? How does this correspond to the parameters of the PMNS matrix, and do we expect deviations from the current oscillation model? Do we expect to see CP violation in the leptonic sector as we do for quarks? What is the absolute scale of neutrino masses, and what is their ordering relative to the flavor states in the PMNS matrix? How do neutrinos gain masses, and should we describe them according to Dirac or Majorana theory? Are there any other weakly-interacting heavy neutrinos? Answering any of these questions would change our perspective on modern physics, and therefore, we invest a lot of time and resources into investigating the fascinating field of neutrino physics.

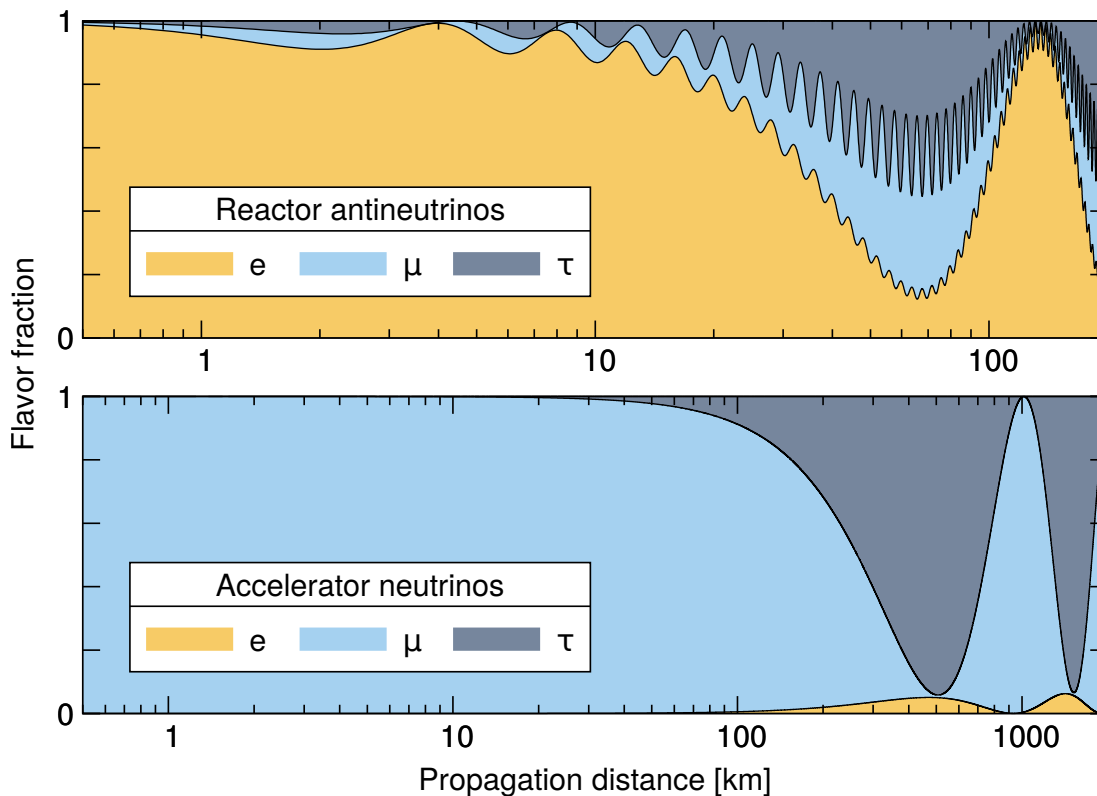


Figure 1.4: An abundance of the specific neutrino flavor in neutrino oscillations as a function of propagation distance in two typical experimental conditions: (top) electron antineutrinos in reactor experiments with the energy $E_\nu = 4$ MeV; (bottom) muon neutrinos in accelerator experiments with the energy $E_\nu = 1$ GeV. The figure format was inspired by Ref. [38].

1.2 Experimental study of neutrino properties

Research programs devoted to neutrino physics are diverse in their objectives, methodology, and sources of neutrinos. Having accepted that neutrinos can oscillate, the experimental studies of this phenomenon have become increasingly relevant. As multiple parameters enter the PMNS matrix and the general oscillation formula, it is important to find proper conditions to isolate and probe specific elements of the theory. Historically the experiments devoted to solar neutrinos came first: Homestake [24] and other radiochemical experiments such as SAGE [39] and GALLEX [40]. Their detection method relied on counting radioactive isotopes of nuclei that interacted with neutrinos. However clever, this method did not allow for measuring the direction of interacting neutrinos, failing to prove unambiguously they originate from the Sun. This issue changed with the introduction of Cherenkov light detectors, such as Kamiokande [41], and the ones that finally confirmed neutrino oscillations: SNO [28,29] and Super-Kamiokande [27]. Detecting this electromagnetic analogue of the sound shockwave enabled identifying highly energetic products of neutrino interactions and measuring their direction. The latest research on solar neutrinos, in the Borexino [42] or KamLAND [43] experiments, involves the third method of neutrino detection: liquid scintillators, which allow tracking of all

charged particles participating in the process. Although KamLAND mostly detected neutrinos from nuclear reactor sources, its long baseline allowed it to be sensitive to the solar oscillation parameters: θ_{12} , θ_{13} angles, and Δm_{21}^2 , which are accessible by studying low-energy electron neutrinos over large propagation distances [6].

Research on neutrinos from artificial sources divides into two main branches: electron antineutrinos from nuclear reactors and muon (anti)neutrinos obtained in proton accelerator facilities, with their oscillation characteristics depicted in Fig. 1.4. Reactor neutrinos have energies up to dozens of MeV and require medium-length baselines for detection, usually close to industrial power plants that create immense fluxes of these particles. Apart from the Japanese KamLAND experiment mentioned before, which has a significantly longer baseline than others, many countries with advanced nuclear energy infrastructures have developed such scintillator detectors: Double Chooz (France) [44], Daya Bay (China) [45], RENO (South Korea) [46], or the future JUNO (China) [47]. Their primary goal is to measure the θ_{13} angle, and the larger neutrino squared mass difference $|\Delta m_{31,32}^2|$, unfortunately not being sensitive to its absolute sign. Another setting to study the latter, together with the θ_{23} angle, is provided by accelerator-based experiments. They rely on high-energy proton interactions to produce charged pions that decay into muon neutrinos, with continuous energy distributions, typically of the order of a few GeV. Over their long baselines, they can usually measure both the muon neutrino disappearance and the electron neutrino appearance signals. The Japanese neutrino program has always relied on water-target Cherenkov light detectors, starting with the K2K project [48], through the current T2K [49] (both using SK as the far detector) and the future Hyper-Kamiokande [50]. Alternatively, one can use

Experiment	Dominant	Important
Solar experiments (Homestake, SAGE, GALLEX)	θ_{12}	$\Delta m_{21}^2, \theta_{13}$
Reactor long-baseline experiments (KamLAND)	Δm_{21}^2	θ_{12}, θ_{13}
Reactor medium-baseline experiments (Double Chooz, Daya Bay, RENO)	$\theta_{13}, \Delta m_{31,32}^2 $	
Atmospheric experiments (Super Kamiokande, ANTARES, IceCube)		$\theta_{23}, \theta_{13}, \Delta m_{31,32}^2 , \delta_{CP}$
Accelerator long-baseline, $\nu_{\mu}, \bar{\nu}_{\mu}$ disapp. (K2K, T2K, MINOS, NOvA, ICARUS)	$\theta_{23}, \Delta m_{31,32}^2 $	
Accelerator long-baseline, $\nu_e, \bar{\nu}_e$ appearance (T2K, MINOS, NOvA)	δ_{CP}	θ_{23}, θ_{13}

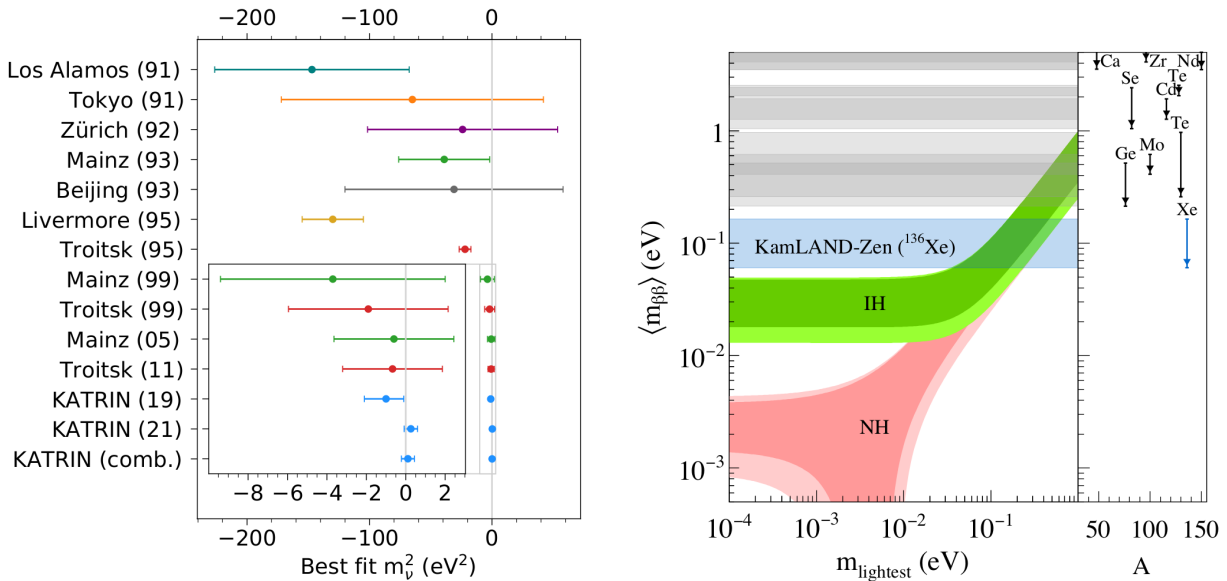
Table 1.1: Experiments contributing to the determination of the oscillation parameters [6].

scintillator methods as in the former MINOS [51] and the current NOvA [52] experiments. The other modern approaches use liquid Argon time-projection chambers (LArTPC), pioneered by ICARUS [53] and set to be used in the future DUNE [54] experiment. Finally, all of the parameters: θ_{23} , θ_{13} , and $|\Delta m_{31,32}^2|$, are measured by studying atmospheric neutrinos, e.g., in Super-

Kamiokande [55]. The high-energy neutrino telescopes, such as ANTARES [56] and IceCube [57] (or the future KM3NeT [58]), are also sensitive to these neutrino oscillations. Experiments capable of independently measuring neutrino and antineutrino signals may allow for observing hints of CP violation in the leptonic sector (δ_{CP}). We summarize the selected experimental studies in Table 1.1. At the time of this research, the latest global fits report, assuming the normal ordering of neutrino masses, the following parameter values [59]: $\theta_{12} = 33.41^{+0.75}_{-0.72}$, $\theta_{23} = 42.2^{+1.1}_{-0.9}$, $\theta_{13} = 8.58^{+0.11}_{-0.11}$, $\Delta m_{21}^2 = 7.41^{0.21}_{0.20} \times 10^{-5} \text{ eV}^2$, and $\Delta m_{31,31}^2 = +2.507^{0.026}_{0.027} \times 10^{-3} \text{ eV}^2$.

Over the last two decades, we have found several hints pointing to possible deviations from the well-established neutrino oscillation model. The hypothesis of sterile neutrinos provides a well-motivated minimal new physics extension that could impact this phenomenon. These particles may exist with some mixing with the active neutrinos and explain, e.g., why neutrinos have mass [60]. However, exploring the parameter space of the mixings and masses for these neutrinos presents a challenge since it spans several orders of magnitude [61]. Consequently, there are no definitive predictions, and a comprehensive scientific program is needed to investigate their potential existence.

Surprisingly, we can also study some neutrino properties in smaller-scale laboratory experiments. This research involves creative, indirect measurements of processes sensitive to the



(a) Comparison of historical best-fit values and uncertainties of direct neutrino mass measurements with the latest results of the KATRIN experiment. For more details, see Ref. [62] and the references therein.

(b) Sensitivity of the KamLAND-Zen detector in measuring the effective Majorana neutrino mass $\langle m_{\beta\beta} \rangle$, the parameter characterizing the $0\nu\beta\beta$ decay rate, as a function of the lightest neutrino mass. For more details, see Ref. [63].

Figure 1.5: Examples of experimental research on neutrino properties beyond the large-scale experimental programs on neutrino oscillation measurements.

investigated effects but not the strength of neutrino interaction with matter. As we learned that neutrinos have non-vanishing rest masses, it is tempting to measure these tiny values. Although we could infer them by studying the behavior of neutrinos from cosmological or artificial sources, the most straightforward method is to analyze beta decay spectra to understand the restrictions

of the process kinematics, which includes the effect involving neutrino mass. In Fig. 1.5a, we present the historical measurements and the ones coming from the leading tritium-decay project nowadays-KATRIN [64]. Another research direction of neutrino physics connected to beta decay experiments is searching for the hypothetical neutrinoless double-beta decay process ($0\nu\beta\beta$), a nuclear transition involving increasing proton number by two units and the emission of two electrons only. Detecting such an event would be of fundamental importance for particle physics [65], providing evidence that neutrinos follow the Majorana theory for neutral particles, i.e., they are their own antiparticles. For example, Fig. 1.5b presents an experimental sensitivity of the project KamLAND-Zen [63], a liquid Xenon scintillator. Finally, these advancements in particle detection technology allowed for the sprouting of many laboratory-sized experiments that try to search for new, weakly interacting particles, possibly other types of yet undiscovered neutrinos. It spans a vital branch of BSM physics investigations [6].

Accelerator-based neutrino experiments

The paramount environment to study the medium-energy characteristics of neutrino oscillation theory and the structure of neutrino-nucleus interactions is provided by accelerator-based neutrino sources. They rely on proton synchrotron facilities, such as J-PARC, Fermilab, or CERN, for the energetic input into the neutrino flux production. As presented in Fig. 1.6, the process initiates with the accelerated protons scattering off a heavy, fixed target, producing secondary particles such as pions or kaons. Then, a set of magnetic horns isolates particles with a selected charge:

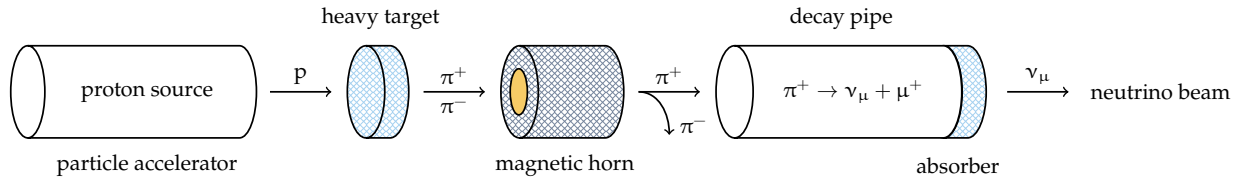


Figure 1.6: Neutrino production mechanism in an accelerator-based experiment.

positive to produce a neutrino-dominated flux or negative for an antineutrino-dominated one. Finally, neutrinos appear as products of decays happening in a dedicated tunnel, which ends with a beam dump meant to stop unwanted particles from propagating with the flux. The dominant decay channels of pions:

$$\pi^+ \rightarrow \mu^+ + \nu_\mu, \quad \pi^- \rightarrow \mu^- + \bar{\nu}_\mu, \quad (1.2.1)$$

and kaons:

$$K^+ \rightarrow \mu^+ + \nu_\mu (+\pi^0), \quad K^- \rightarrow \mu^- + \bar{\nu}_\mu (+\pi^0), \quad (1.2.2)$$

provide the bulk of neutrino flux of the desired helicity. However, this procedure involves two common types of contamination: the flux might include neutrinos of the opposite helicity or other flavors. The subsequent muon decay is the primary source of undesired neutrinos:

$$\mu^+ \rightarrow e^+ + \bar{\nu}_\mu + \nu_e, \quad \mu^- \rightarrow e^- + \nu_\mu + \bar{\nu}_e, \quad (1.2.3)$$

but kaons also have decay channels that contribute to the latter issue:

$$K^+ \rightarrow e^+ + \nu_e + \pi^0, \quad K^- \rightarrow e^- + \bar{\nu}_e + \pi^0. \quad (1.2.4)$$

Though one can reduce the contamination to a percent level, e.g., by adjusting the length of the decay pipe to prevent muons decay, the accelerator-based neutrino fluxes combine distributions of particles of different energies, helicities, and flavors. These flux uncertainties are the price for obtaining controlled, large-scale sources of neutrinos.

The oscillation program itself has a straightforward principle of operation: one counts the number of interacting neutrinos of a given energy over a specific propagation distance and confronts it with theoretical expectations. This approach is sufficient to infer the oscillation model parameters, even the CP-violating phase δ_{CP} after performing a joint neutrino and antineutrino analysis. However, considering how elusive neutrinos are, such a scientific program inevitably meets challenges that slow down the exploitation of this strategy. A defining one is that neutrino energy, one of the key parameters for the oscillation analyses, is known only as a broad distribution. Ideally, we could reconstruct the neutrino energy using the energy the final state particles deposit in the detectors. Unfortunately, determining the complete final state experimentally is usually impossible due to the limited detector acceptance. We rely on completing the missing information using Monte Carlo (MC) event generators that employ theoretical models to describe the neutrino interactions and carry out the neutrino energy reconstruction, which, however, faces further complications. As the probability of neutrinos interacting with matter is challengingly tiny, a large quantity of sensitive material must be accumulated to detect them with the desired statistics. This issue entails practical obstacles in all present and future generations of neutrino oscillation experiments. Due to its explosive nature, using the "easy-to-model" Hydrogen target is impossible, while using molecules containing complex nuclei instead, such as mineral oils (CH_x), water, or liquid Argon, significantly increases the modeling difficulty. In general, this is a model-dependent procedure, and it is essential to stress how the uncertainties in theoretical predictions propagate to the final neutrino measurements. We will exemplify this following a discussion from Ref. [66]. As depicted in Fig. 1.7, the total rate of observed neutrino events is a function of the reconstructed kinematical variables \mathbf{x} (e.g., reconstructed neutrino energy E_{ν}^{rec}). It is proportional to specific components, such as the neutrino flux $\Phi_{\nu_{\mu}}$ and the oscillation probability $P_{\nu_{\mu} \rightarrow \nu_{\alpha}}$ which

$$\begin{array}{cccccc}
 \mathbf{R}_{\nu_{\alpha}}(\mathbf{x}) & \sim & \Phi_{\nu_{\mu}}(E_{\nu}) & \times & P_{\nu_{\mu} \rightarrow \nu_{\alpha}}(\{\Theta\}, E_{\nu}) & \times & \sigma_{\nu_{\alpha}}(E_{\nu}, \mathbf{x}) & \times & \epsilon_{\text{det.}}(\mathbf{x}) \\
 \text{Event rate} & & \text{Incoming flux} & & \text{Oscillation probability} & & \text{Cross section} & & \text{Efficiency}
 \end{array}$$

Figure 1.7: The rate of detected neutrinos of a flavor α (ν_{α}) in neutrino oscillation experiments as a convolution of the crucial ingredients: the flux of produced muon neutrinos ($\Phi_{\nu_{\mu}}$), oscillation probability ($P_{\nu_{\mu} \rightarrow \nu_{\alpha}}$), neutrino-nucleus cross section ($\sigma_{\nu_{\alpha}}$), and the efficiency of a particular detector ($\epsilon_{\text{det.}}$). Here: E_{ν} is the "true" neutrino energy, $\{\Theta\}$ are the parameters of the oscillation model, and \mathbf{x} represents kinematical variables measured in the detector.

are functions of the "true" neutrino energy. To infer the oscillation model parameters $\{\Theta\}$ from the detected rate $\mathbf{R}_{\nu_{\alpha}}$, one needs an estimator for neutrino energy from the variables measured in the detector. The critical ingredient for a good estimator is the neutrino-nucleus cross section $\sigma_{\nu_{\alpha}}$ which strongly relies on nuclear theory. In recent years, several works have shown the impact of different nuclear effects on the neutrino energy reconstruction procedure [67–69]. However, most of these aspects have yet to find their way into Monte Carlo neutrino event generators and,

therefore, into the actual experimental analyses.

Despite many scientific and technical challenges, accelerator-based neutrino experiments provide a unique framework for studying these particles' properties extensively. Apart from the main oscillation programs mentioned before, the global community develops many research programs devoted to essential development on flux production and control, or detector technology. There are promising, modern ideas for neutrino production methods, such as the nuSTORM [70], ENUBET [71] or EMPHATIC [72] projects. There are also efforts to refine our particle detection methods, such as the WAGASCI [73] project or using liquid Argon in the ArgoNeuT [74], MicroBooNE [75] and SBND [76] detectors. The potential impact of these technological advancements on the future of the field cannot be overestimated. Finally, from a more theoretical point of view, the measurements of various kinds of neutrino-nucleus interaction cross sections facilitate the essential advancement in nuclear modeling computations needed for reducing the systematic uncertainties in oscillation analyses. The combined efforts of physicists from different backgrounds bring us closer to unraveling the mysteries of neutrino physics. Fig. 1.8 presents the field of accelerator-based neutrino experiments with a selection of active experimental collaborations which perform oscillation and neutrino-nucleus cross section analyses.

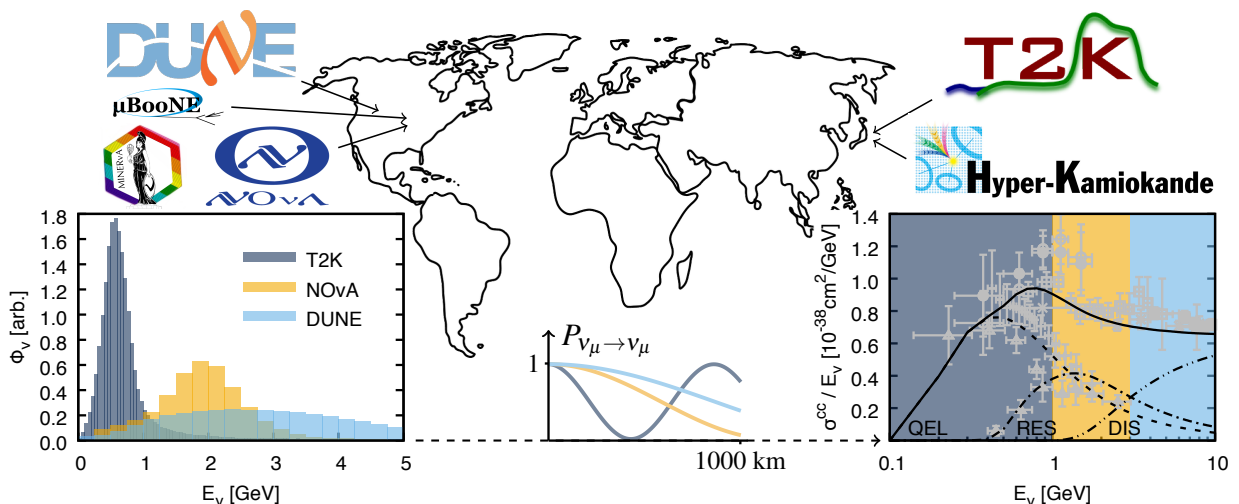


Figure 1.8: Experimental efforts in the worldwide quest for the understanding of neutrino-oscillations and neutrino-nucleus scattering, current: (gray) T2K [77], (yellow) NOvA [78], MINERvA [79], MicroBooNE [80], and future: Hyper-Kamiokande [81], (blue) DUNE [82]. (Bottom left) produced neutrino flux predictions; (bottom center) flux-averaged probability of non-oscillation as a function of the propagation distance; (bottom right) total charged current neutrino-nucleon cross section, where 'QEL' denotes quasielastic scattering, 'RES'—single-pion production, and 'SIS/DIS'—community slang for both shallow- and deep-inelastic scattering.

T2K experiment

An experimental collaboration initiated in 2006 [83], T2K ("Tokai-to-Kamioka") is a neutrino oscillation program that operates over a long baseline in Japan between the J-PARC accelerator-based neutrino source in Tokai and the Super-Kamiokande detector in Kamioka. It combines a

global effort of about 500 scientists from almost 80 international institutes. The original physics goals of the experiment grew on top of K2K experiences, focusing on discovering electron neutrino appearance signal (confirming that $\theta_{13} > 0$) and precision measurements of oscillation parameters in the muon neutrino disappearance case. This strategy quickly proved notably successful and evolved over a long data-taking period since 2010 [49]. However, T2K has not found evidence of sterile neutrino components in the disappearance signal, which was an auxiliary physics goal of the project. Fig. 1.9 presents a schematic view of the experiment, including the near-detector facilities that allow for monitoring the beam direction and other neutrino measurements needed to reduce systematic uncertainties. The T2K neutrino beam is produced using the accelerator facilities of J-PARC and flux modeling input based on the NA61/SHINE experiment data [84], which provided measurements with a graphite target replica. As for the far detector, T2K uses Super-Kamiokande, an enormous and well-understood Cherenkov light detector with many advantages for being used in that role. It has an excellent electron-muon separation ability, plotted in the top left part of Fig. 1.9, as well as reasonable energy resolution, control of backgrounds, and, although challenging experimentally, an ability to detect pions. However, the detector is not magnetized, which makes it unable to differentiate the charge of observed particles and, therefore, unable to separate neutrino from antineutrino signals. During the first 10 T2K experimental runs, until 2020,

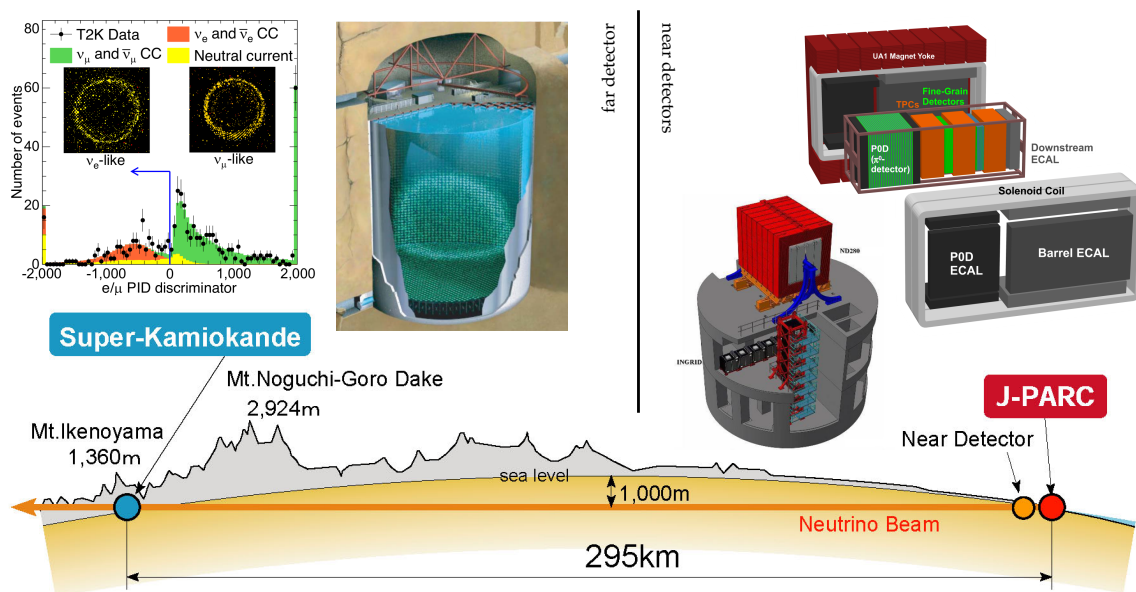


Figure 1.9: The 295-km-long baseline of the T2K experiment, spanning between the neutrino factory at J-PARC to the Super-Kamiokande far detector. (top left) the far detector facility and its ability to discriminate between electron and muon Cherenkov rings [85]; (top right) the off-axis near detector ND280 with its subcomponents, and the on-axis beam monitoring detector INGRID.

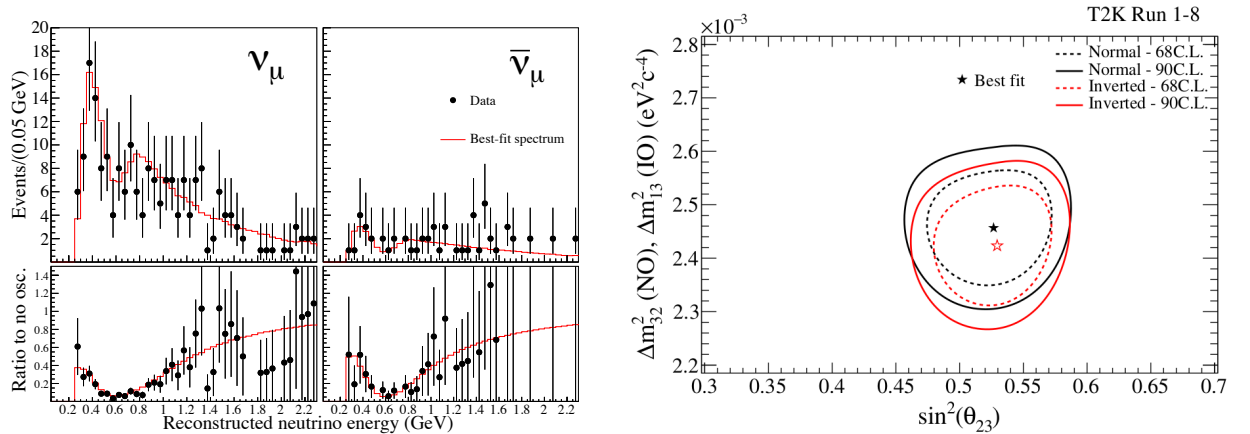
Super-Kamiokande managed to detect about 318 muon and 108 electron events in the neutrino-dominated flux and 137 muon and 16 electron events in the antineutrino-dominated one [86].

The critical component of a successful accelerator-based oscillation program is the near detector which allows for precise neutrino interaction measurements and control over the initial point of

flux propagation. In T2K, the near detector facilities are 280 meters from the target, hence its name: ND280. Contrary to the INGRID beam monitor, SK and ND280 are not aligned with the flux but are off-axis by 2.5 degrees. As presented in the bottom left (flux) and right (interaction) parts of Fig. 1.8, this method significantly narrows the flux energy distribution, emphasizing the quasielastic neutrino-nucleus interaction mechanism. This procedure constrains the detected final states below the pion-production threshold, optimizing the investigated physics to the capabilities of Super-Kamiokande. Assuming the neutrino interaction was a quasielastic process on a bound nucleon (inverse β -decay), we can use a simple kinematic energy reconstruction formula:

$$E_{\nu}^{\text{rec}} = \frac{2M_N E_l - m_l^2 + M_{N'}^2 - M_N^2}{2(M_N - E_l + p_l \cos \theta_l)}, \quad (1.2.5)$$

where the index l denotes the properties of a detected lepton, while M_N and $M_{N'}$ are the masses of an initial (off-shell) and a final nucleon, respectively. Provided reasonable control of uncertainties coming from the suppressed inelastic processes by controlling detected pions and the knowledge of the neutrino-nucleus interaction physics, this simple method is remarkably accurate. We can exemplify the success of this methodology with the outstanding precision in measuring the muon neutrino disappearance signal. In Fig. 1.10, we present the outcome of a T2K Run 1-8 oscillation analysis, wherein in the left panel, one can see a significant signal suppression compared to the non-oscillation expectation. From this observation, as depicted in Fig. 1.10b, one can derive oscillation model parameters, such as θ_{23} and the modulus $|\Delta m_{32}^2, 31}|$. Confronting the results of the bottom panels of Fig. 1.10a with the general picture presented in Fig. 1.4, one can see that the



(a) Reconstructed neutrino energy distributions for the ν_{μ} (left) and $\bar{\nu}_{\mu}$ (right) samples with the total predicted event rate shown in red. Ratios to the predictions under the no-oscillation hypothesis are shown in the bottom figures.

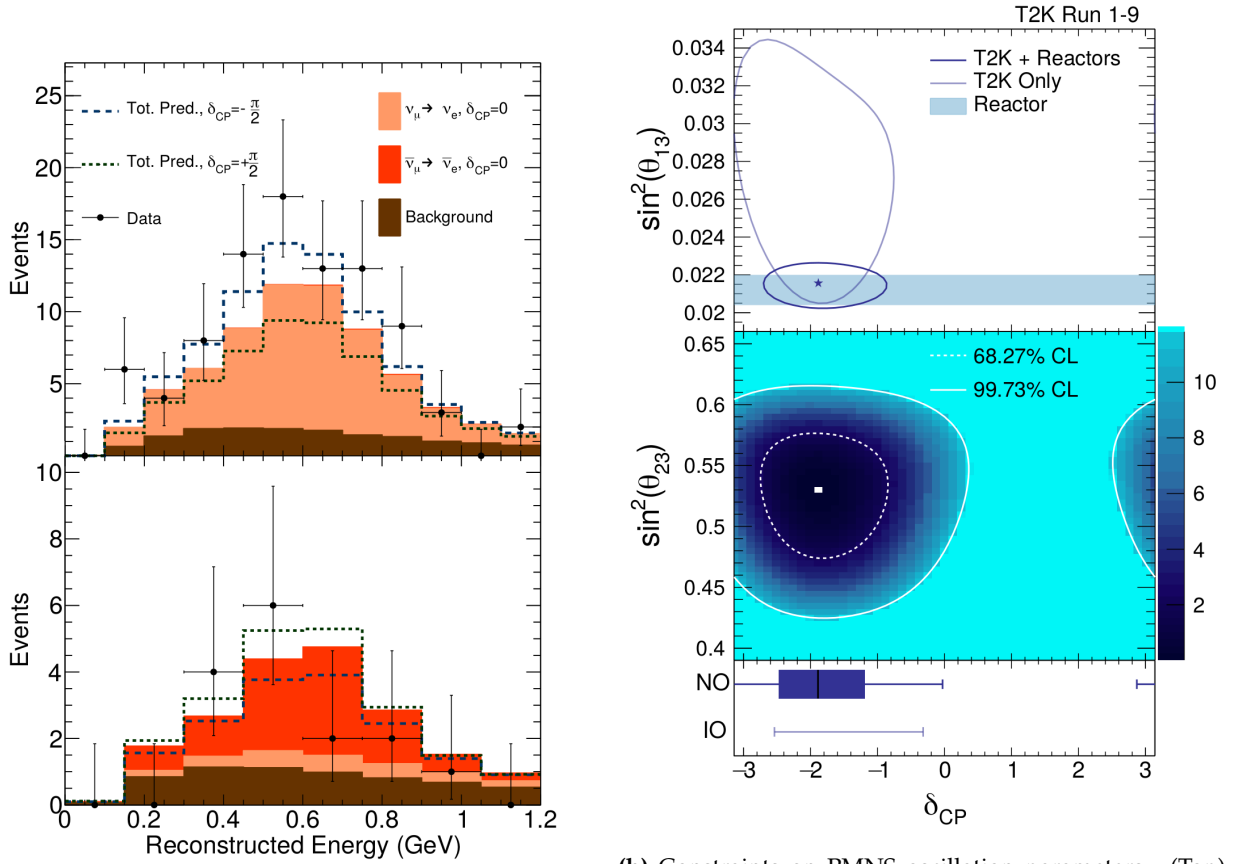
(b) The 68% (solid) and the 90% (dashed) constant $-2 \ln \mathcal{L}$ confidence regions in the $|\Delta m_{31,32}^2| - \sin^2 \theta_{23}$ plane for normal (black lines) and inverted (red lines) ordering using the reactor measurement prior on $\sin^2(2\theta_{13})$.

Figure 1.10: Constraints on PMNS matrix parameters $|\Delta m_{31,32}^2|$ (Δm_{32}^2 or Δm_{13}^2 assuming the normal or inverted ordering, respectively) and $\sin^2 \theta_{23}$ in neutrino oscillations measured by T2K. Figures and descriptions were adapted from Ref. [87].

minimum around the reconstructed energies of 0.6 GeV is the so-called first oscillation maximum, optimizing both the disappearance and appearance signals.

Since the birth of T2K and its early achievements, its scientific program has evolved and

pursued more challenging and progressive neutrino measurements. These advancements include significant stress, which the collaboration put on incorporating the theoretical progress in understanding the structure of neutrino-nucleus interactions and its impact on the systematic uncertainties in oscillation analyses. In this scope, the analyzers performed many ND280 cross section measurements with different event topologies, kinds of scattering neutrinos, and targets: hydrocarbon, water, and Iron, all of that trying to provide experimental data with as little model dependency as possible. Such an attitude popularized cleaner neutrino scattering experimental topologies, e.g., $CC0\pi$ (CCQE-like) with a charged lepton, nucleons but no pions in the final state, making no assumptions on pion absorption coming from interaction channels other than the quasielastic one. This approach strengthens the cooperation between the experimental and theoretical fields of neutrino-nucleus interactions, effectively communicating through the models implemented in MC neutrino event generators used in data analyses. Over the last ten years, this open-minded strategy and continuous data-taking have brought T2K into the precision era of neutrino measurements. An advent of it came with establishing constraints on the CP-violating δ_{CP} phase, excluding some of its values at the 3σ confidence level [85]. We present these results in Fig. 1.11, where the left panel contains the statistics of electron (anti)neutrino appearance measured in SK, and the right panel provides the results of the performed oscillation analysis. We expect to further develop this remarkable achievement in the future experiment Hyper-Kamiokande which is currently under construction. Upon completion in 2027, we expect it to provide a significant upgrade in experimental statistics that, combined with our acquired experience, might allow us to solve the puzzle of the CP violation in the leptonic sector [50].



(a) (Top) reconstructed neutrino energy spectra for the Super-Kamiokande samples containing electron-like events in neutrino-mode beam running; (bottom) the same quantity for the antineutrino beam mode. The solid-stacked histogram shows the predicted number of events in the $\delta_{CP} = 0$ scenario, separated according to whether the event was from an oscillated neutrino or antineutrino, or from a background process. The dashed lines show the total predicted number of events for the two most extreme CP-violating parametrizations of the oscillation formula.

(b) Constraints on PMNS oscillation parameters. (Top) 2D confidence intervals at the 68.27% confidence level for δ_{CP} vs. $\sin^2 \theta_{13}$ in the preferred normal neutrino mass ordering. (Middle) 2D confidence intervals at the 68.27% and 99.73% confidence level for δ_{CP} vs. $\sin^2 \theta_{23}$ from the T2K+Reactors fit in the normal mass ordering, with the color scale representing the value of negative two times the logarithm of the likelihood for each parameter value. (Bottom) 1D confidence intervals on δ_{CP} from the T2K+Reactors fit in both the normal (NO) and inverted (IO) orderings.

Figure 1.11: Constraints on matter-antimatter symmetry-violating phase δ_{CP} in neutrino oscillations measured by T2K. Figures and descriptions were adapted from Ref. [85].

1.3 Theoretical picture of neutrino interactions

Neutrinos are electrically neutral and couple to other particles only weakly. Thus, the only method of understanding whether and how they have interacted with matter is by analyzing the final states composed of directly detectable particles, such as muons, electrons, protons, pions, or nuclear clusters [88]. In accelerator-based neutrino oscillation experiments, the investigated events are neutrinos scattering off nuclear targets, which makes the theoretical predictions of neutrino-nucleus interactions vital for obtaining any physical conclusions [89]. The history of the developments in this field is inherently connected with electron-nucleus scattering physics, as the two processes share many similarities [90]. On the leptonic side, the electromagnetic interactions of electrons occur through the vector-structured current, equivalent to the one for neutrinos, which, with the axial-vector part on top, combine into the weak interaction. On the hadronic side, the initial nuclear state is the same in the two processes, while the transition and the final state slightly differ due to the charge provided in the charged-current interaction. These apparent similarities bring us to the conclusion that a prerequisite of a successful neutrino-nucleus interaction model is validation against electron scattering data. Therefore, both lepton-nucleus interaction dynamics must be studied exhaustively, and one should not overlook their physical resemblance.

The theoretical foundation for describing lepton-nucleus scattering processes was laid fairly soon after Dirac formulated his equation for the relativistic electron. In 1929, Sir Nevill Mott derived the cross-sectional formula for the scattering of Dirac particles by point-like nuclei [91]. Almost a century later, we still describe modern theories, which include sophisticated details of nuclear structure, relative to his basic quantum-mechanical definition. The fundamental variables defining the process of a lepton of energy E and momentum \vec{k} scattering to a lepton of energy E' and momentum \vec{k}' at a deflection angle θ' are the energy transfer $\omega = E - E'$ and the momentum transfer $\vec{q} = \vec{k} - \vec{k}'$. These quantities are "transferred" to the hadronic system, which is why nuclear physicists try to answer the question: what is the "response" of the target nucleus? However, to solve this problem, we must rely on a specific set of assumptions and approximations. Considering the strength of the interaction, especially the weak one, we can introduce the first theoretical concept—the *Born approximation*, which requires that only one boson is exchanged. Then, one can interpret ω and \vec{q} as the energy and momentum of the exchanged boson, and define an invariant quantity $Q^2 = -q^2 = \vec{q}^2 - \omega^2$, interpreted as its negative mass squared. For the electromagnetic case, the limit of $Q^2 \rightarrow 0$ means exchanging real, massless photons that require a different kinematical framework and will not be discussed here. Having established the one-boson exchange picture, the next step in obtaining a comprehensive theory is understanding the physical scales relevant to the lepton-nucleus scattering process and defining a suitable set of hadronic degrees of freedom. The resolution of the boson penetrating the nucleus is related to its De Broglie wavelength ($\lambda \propto 1/|\vec{q}|$). For accelerator-based neutrino oscillation experiments, the neutrino projectile energies are of the order of hundreds of MeV to a few GeV, which translates to size ranges starting from a few to tiny parts of femtometers. As presented in Fig. 1.12, this means that such lepton interactions require applying different formalisms: the coherent nucleus, e.g., Carbon with its radius of $\simeq 6$ fm, then individual nucleons with their radii below 1 fm, and finally the partonic (quark) substructure of nucleons for the most energetical processes. For interactions

with the same final states, a consistent transition between these frameworks is challenging and usually a subject of phenomenology.

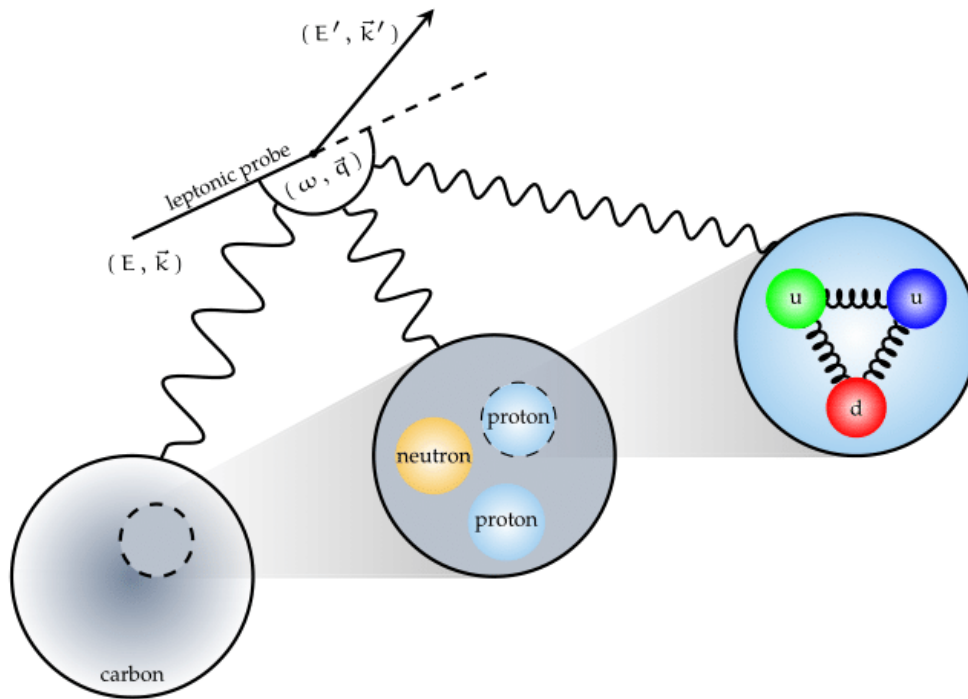


Figure 1.12: Hadronic degrees of freedom applied in modeling neutrino-nucleus interactions in the energy range suitable for accelerator-based neutrino oscillation experiments.

The most straightforward approach to lepton scattering off nuclei and individual nucleons is assuming a (quasi)elastic process. For nuclei, it results in a low-energetic deflection of the incoming lepton, while for bound nucleons, usually in the target nucleon knock-out. However, we cannot apply this logic to quark degrees of freedom, as their binding inside nucleons is significantly stronger than nucleons inside the nucleus, and they are not free particles asymptotically. Then, by transferring more energy to the hadronic system, we encounter the lightest mesons—pions ($m_\pi \simeq 135 - 140 \text{ MeV}/c^2$), the first particle to lift excess energy above the (quasi)elastic interaction. Production of pions starts already for leptons deflecting off the whole nuclei in a process called coherent pion production [92]. Next, pions are a common component of lepton-nucleon interaction as both a direct interaction yield (background terms in single-pion production) or a product of decaying nucleon resonances excited in the process, such as the $\Delta(1232)$ [93]. According to the meson-mediated interpretation of the strong nucleon-nucleon interaction, pions also appear as virtual particles in the nuclear medium. An interaction involving such a pion leads to knocking out both nucleons, whose interaction this pion mediates, and leaving the nucleus with two holes (2-particle-2-hole final state) [94]. Finally, we model interactions using partonic (quark) degrees of freedom following the deep-inelastic scattering (DIS) framework that leads to ripping the target nucleon apart and creating final states involving diverse hadrons [95]. The shallow-inelastic region (SIS) between the nucleon-based single-pion production (SPP) and the DIS formalism is an extremely difficult-to-model part of phase space that involves a smooth transition between the different scales of physics [96]. The assumption, dominant in the mechanisms

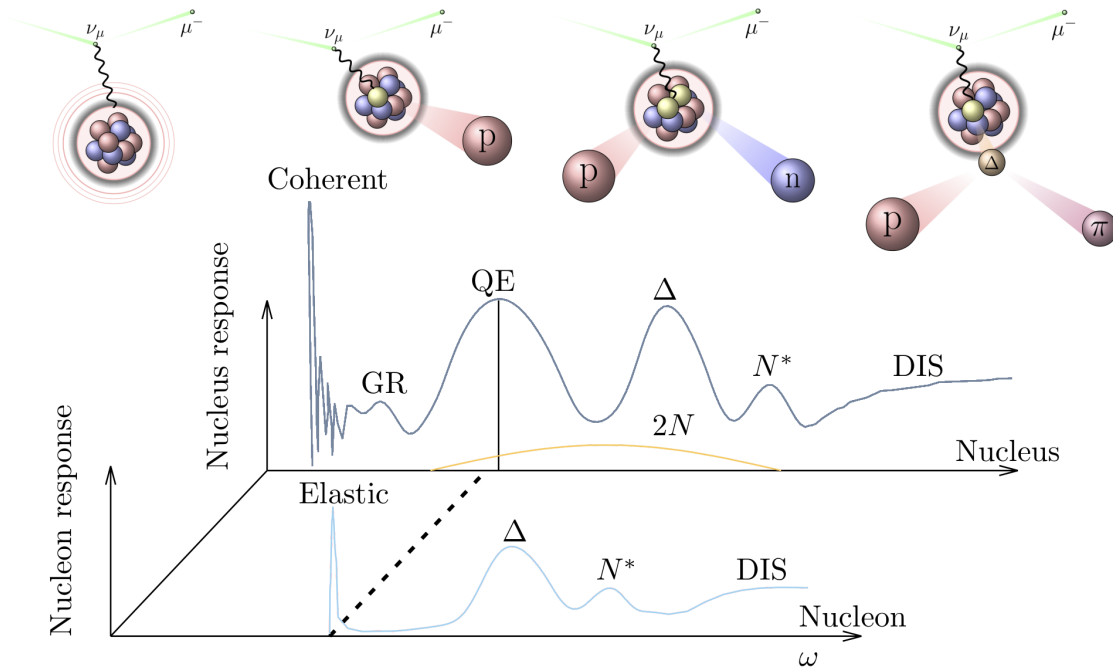


Figure 1.13: Magnitude of the nuclear response in neutrino scattering as a function of the energy transferred by the neutrino probe (ω). The particular dynamics are: "Coherent"—an elastic neutrino-nucleus scattering, "GR"—excitation of the target nucleus into its resonant states, "Elastic" and "QE"—(almost) elastic neutrino-nucleon interactions where the target is free or bound, respectively, " Δ " and " N^* "—excitations of the target nucleon into its resonant states, "DIS"—a collection of channels with partonic degrees of freedom; and "2N" represent multiple dynamics that cause two-nucleon knock-outs. Diagrams on top present different final states encountered in charged-current neutrino-nucleus scattering, where apart from a charged lepton and the residual nucleus, one can find (from left): no other particles, one nucleon, two nucleons, or one nucleon and one pion in the final state.

mentioned above, that the nuclear response is an incoherent sum of interactions happening on individual nucleons, i.e., that nucleons are the essential degrees of freedom, is called the *impulse approximation* (IA). In Fig. 1.13, we summarize the channels of lepton-nucleus interactions relative to their free nucleon target analogs. The presented intermediate-energy scattering physics is a complex many-body problem intersecting nuclear and particle physics. In this domain, bringing accurate theoretical predictions requires a proper understanding of free nucleon target interactions and nuclear dynamics of the hadronic system over the vast phase space of lepton scattering experiments.

Independently of a specific modeled interaction, it is essential and educative to understand the kinematics based on the final particles detected in the process. We can perform this exercise by evaluating the number of independent variables needed to describe a particular interaction phase space. As presented in Table 1.2, there are several particles and effects that we need to take into account. In an example process, the initial state consists of an interacting leptonic probe and the target nucleus, while the final state includes the scattered lepton, which we sum over its possible spins, an undetected, excited remnant system, and an arbitrary number of N detected hadrons. All these particles and hadronic systems constitute $16 + 4N$ unknown variables, 4 for

Unknown particle 4-vectors	Variables	Physical effects	Variables
Initial lepton	4	Particles on-shell	$-(3 + N)$
Target nucleus	4	4-momentum conservation	-4
Final lepton	4	Target rest-frame	-3
Remnant nucleus	4	Fixed projectile direction	-2
Outgoing hadrons	4N	Fixed incoming energy	-1
	16 + 4N		$-13 - N$
			3 + 3N

Table 1.2: Counting the number of independent variables describing lepton-nucleus interactions while detecting N hadronic particles in the process, summing over the spin of the outgoing lepton, and leaving the remnant nucleus undetected.

every four-momentum involved. Then, we can think of particular equations constraining the process that will reduce the number of independent variables. All on-shell particles have a known relation between their energy and momentum ($E^2 = p^2 + m^2$), which reduces the number by $3 + N$. Note that the undetected remnant nucleus is a hadronic system whose excitation is an additional degree of freedom and cannot be constrained this way. The following constraints come from the energy and momentum conservation laws, contributing to eliminating 4 variables. Finally, there are methods to optimize the scattering conditions: working in the target rest frame, fixing the coordinate system relative to the projectile, and selecting the incoming lepton energy. They allow us to reduce the number of variables by 6 to the final number of $3 + 3N$ independent variables needed to obtain complete information about each scattering event. This formula shows that the process phase space grows by 3 dimensions with every additional detected particle in the final state, which explains the increasing difficulty in modeling more complex lepton-nucleus scattering processes.

To further illustrate this, we look at the most crucial quantity—the cross section (σ), directly proportional to the interaction probability for the given set of independent variables. We commonly write it in its differential forms, where every derivative is responsible for behavior over a specific degree of freedom. For example, a differential cross section $d^2\sigma/d\Omega$ is proportional to the probability of finding an outgoing particle in the (two-dimensional) solid angle Ω . Table 1.3 presents example formulas for cross sections of different scattering channels discussed before. Note that the dimensionality of these formulas is always lower by 1 degree from the total number of independent variables for each process. It stems from one more global symmetry, which states that a rotation of the whole system should leave the cross section unchanged, effectively eliminating one ϕ angle. In the table, we can see how the effects described before play a role in the dimensionality of each formula: an excited final state leading to one more, and every particle detected leading to 3 additional variables. Moreover, we interpret the particular cross sections differently, depending on the investigated dynamics of the interaction. For example, if we model lepton-nucleus scattering with two nucleons knocked-out to the continuum, the 8-dimensional formula is called the *exclusive* cross section due to the complete information about each event.

Target	Process	Properties	Example formula
Free nucleon	(Quasi)elastic	$N = 0$, all particles on-shell	$\frac{d\sigma}{dQ^2}$
	Inelastic	$N = 0$, excited hadronic system	$\frac{d^2\sigma}{dQ^2 dW}$
	SPP	$N = 1$, all particles on-shell	$\frac{d^4\sigma}{dQ^2 dW d\Omega_\pi}$
Nucleus	Inclusive	$N = 0$, all hadrons integrated	$\frac{d^2\sigma}{d\Omega'}$
	1p1h	$N = 1$, detected one nucleon	$\frac{d^5\sigma}{dE' d\Omega' d\Omega_{N'}}$
	2p2h	$N = 2$, detected two nucleons	$\frac{d^8\sigma}{dE' d\Omega' dE_{N'} d\Omega_{N'} d\Omega_{N''}}$
	SPP	$N = 2$, detected nucleon and π	$\frac{d^8\sigma}{dE' d\Omega' dE_\pi d\Omega_\pi d\Omega_{N'}}$

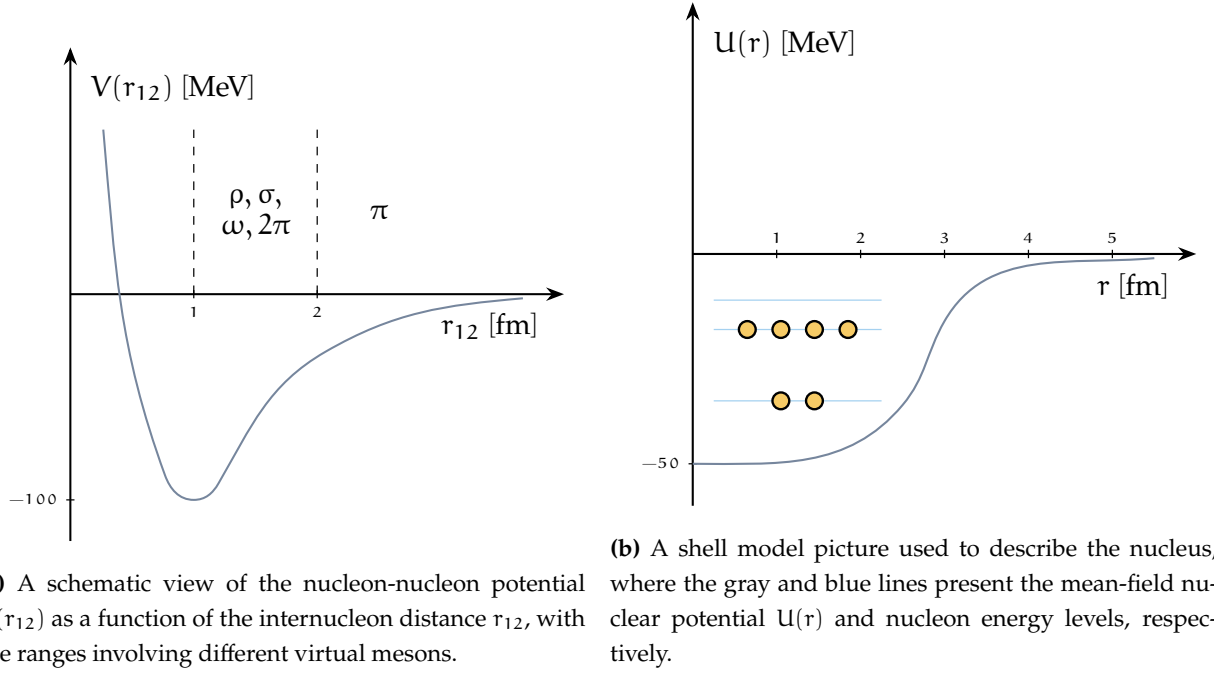
Table 1.3: The dimensionality of cross section formulas for the most basic lepton scattering scenarios, off the free nucleon or on the nucleus.

Integrating over one of the nucleons, which experimentally means detecting only one of them, we calculate the *semi-inclusive* (*semi-exclusive*) cross section. Finally, by integrating over all hadrons and detecting only the final lepton, we examine the *inclusive* cross section. As discussed in Section II, the phase space of independent variables needed to describe a particular event grows with 3 dimensions for every particle detected in the final state. It is a common approach to tabularize models, which are too computationally demanding to be explicitly implemented in the generators. Analogously, for 1-particle-1-hole (quasielastic) processes, one nucleon detected in the final state leads to an exclusive cross section. This discussion shows that providing theoretical predictions for lepton-nucleus interactions requires calculations across a multidimensional phase space of potential event kinematics with different occurrence probabilities.

Many-body nuclear problem

One can perceive the lepton-nucleus scattering process in three different yet interconnected stages: the properties of the initial nuclear state, the (one-boson) interaction dynamics, and the final state interactions of knocked-out nucleons and produced pions. As the middle one is the very subject of this thesis, at this point, we will focus on the more philosophical aspects of nuclear modeling. Fig. 1.14a presents a typical behavior of the nucleon-nucleon strong interaction potential, with a hard repulsive core while approaching $r_{12} \rightarrow 0$ and an attractive dip around $r_{12} \simeq 1$ fm. Comparing these values to the size of nucleons (≈ 1 fm), we conclude that treating bound nucleons independently in an averaged mean-field-like potential is justified. This approach, called the *independent-particle model* (IPM), involves a standard approximation to study intermediate-energy nuclear processes. As the simplest possible IPM-like solution, one can think of a Fermi gas of nucleons (FG) [97], parametrized through the Fermi momentum:

$$p_F = (3\pi^2 \rho_{\text{avg}})^{1/3}, \quad (1.3.1)$$



(a) A schematic view of the nucleon-nucleon potential $V(r_{12})$ as a function of the internucleon distance r_{12} , with the ranges involving different virtual mesons.

(b) A shell model picture used to describe the nucleus, where the gray and blue lines present the mean-field nuclear potential $U(r)$ and nucleon energy levels, respectively.

Figure 1.14: Nucleon-nucleon physics on the scale of (left) individual particles and (right) the nucleus.

where ρ_{avg} is the average nuclear density for a given nucleus. In this model, nucleons compactly occupy energetic levels below the Fermi energy ($E_F = \sqrt{p_F^2 + M_N^2}$) and are subject to the motion of random nature. However successful in reproducing specific basic properties of inclusive reactions, this model fails to grasp the complexity of nuclear behavior, leading to many inconsistencies. The more appropriate approach to obtaining a realistic model is to derive the mean-field nuclear potential explicitly. The nucleons embedded within are subject to averaged-out forces assuming that direct nucleon-nucleon correlations are merely a subsequent correction. Supposing we work in a non-relativistic framework, these nucleons are solutions ϕ_a to the one-body Schrödinger equation:

$$(T + U(r)) \phi_a(r) = \epsilon_a \phi_a(r), \quad (1.3.2)$$

where T describes the kinetic energy, $U(r)$ the average field, and ϵ the single-particle energy. Then, we write the model Hamiltonian for the A independent nucleons as

$$H_0 = \sum_{i=1}^A (T_i + U(r_i)) = \sum_{i=1}^A h_0(i), \quad (1.3.3)$$

its eigenfunctions as

$$\Phi_{\alpha_1, \dots, \alpha_A}(r_1, \dots, r_A) = \prod_{i=1}^A \phi_{\alpha_i}(r_i), \quad (1.3.4)$$

and the corresponding energy eigenvalue as

$$E_0 = \sum_{i=1}^A \epsilon_{\alpha_i}(r_i). \quad (1.3.5)$$

However, such a wave function Φ does not fulfill the Pauli exclusion principle yet, and therefore, we write it in a Slater determinant form:

$$\Phi_{\alpha_1, \dots, \alpha_A}(r_1, \dots, r_A) = \frac{1}{\sqrt{A!}} \begin{vmatrix} \phi_{\alpha_1}(r_1) & \dots & \phi_{\alpha_1}(r_A) \\ \vdots & \ddots & \vdots \\ \phi_{\alpha_A}(r_1) & \dots & \phi_{\alpha_A}(r_A) \end{vmatrix}. \quad (1.3.6)$$

Here, we note that we do not know the mean-field potential $U(r)$ explicitly, and to obtain it from the chosen parametrization of nucleon-nucleon interaction, one has to start from the more general Hamiltonian:

$$H = \sum_{i=1}^A T_i + \frac{1}{2} \sum_{i=1}^A V_{ij}, \quad (1.3.7)$$

restricted to two-body interactions only, for educative purposes. Now, we can include the potential $U(r)$ again to obtain the following:

$$H = \sum_{i=1}^A (T_i + U(r_i)) + \left(\frac{1}{2} \sum_{i=1}^A V_{ij} - \sum_{i=1}^A U(r_i) \right) = H_0 + H_{\text{res}} = \sum_{i=1}^A h_0(i) + H_{\text{res}}, \quad (1.3.8)$$

where H_0 describes the motion of A nucleons, independent of each other in the same average field. The smaller the effect of H_{res} , the better the assumption of an average, independent field becomes. For determining $U(r)$, starting from a known V_{ij} and a Slater determinant A -nucleon wave function that is a good approximation to the total ground state wave function for the full Hamiltonian H , we rely on the Hartree-Fock method [98]. Solving a radial potential in a spherically-symmetric system inevitably leads to discrete energy levels in the shell model, depicted in Fig. 1.14b. The resulting single-nucleon wave functions are the essential input to further theoretical calculations. One can also use the described philosophy of nuclear modeling in the relativistic approaches, where one solves a Dirac equation with scalar-vector potentials [99].

After establishing basic knowledge of the nuclear states involved in lepton-nucleus scattering, we can look at the other side of this process and the fate of the resulting final states. The simplest solution is to assume that the outgoing hadrons are not subject to reinteractions, which we call the *plane-wave impulse approximation* (PWIA). This picture is a potent tool, allowing for decent theoretical consistency on the level of lepton scattering off bound nucleons, leaving the final-state interactions (FSI) of outgoing nucleons and produced pions as a separate modeling task. As shown explicitly in Ref. [100], PWIA allows for the *factorization* of the lepton-nucleus cross section as a formula involving scattering off individual off-shell nucleons folded with the probability of finding such targets in the nucleus. Under these assumptions, for the quasielastic process, we can write an inclusive cross section in the general form of

$$\frac{d^2\sigma}{d\omega d|\vec{q}|} = K \int dE d^3\vec{p} S(E, |\vec{p}|) L_{\mu\nu} H^{\mu\nu}, \quad (1.3.9)$$

where K combines lepton-specific prefactors, and $S(E, |\vec{p}|)$ is called the *hole spectral function*. $L_{\mu\nu}$ and $H^{\mu\nu}$ are tensors describing dynamics of the leptonic and single-nucleon hadronic parts of the interaction, respectively. Note that the property allowing for such an $L_{\mu\nu} H^{\mu\nu}$ separation stems directly from applying the one-boson exchange Born approximation and is a fundamental

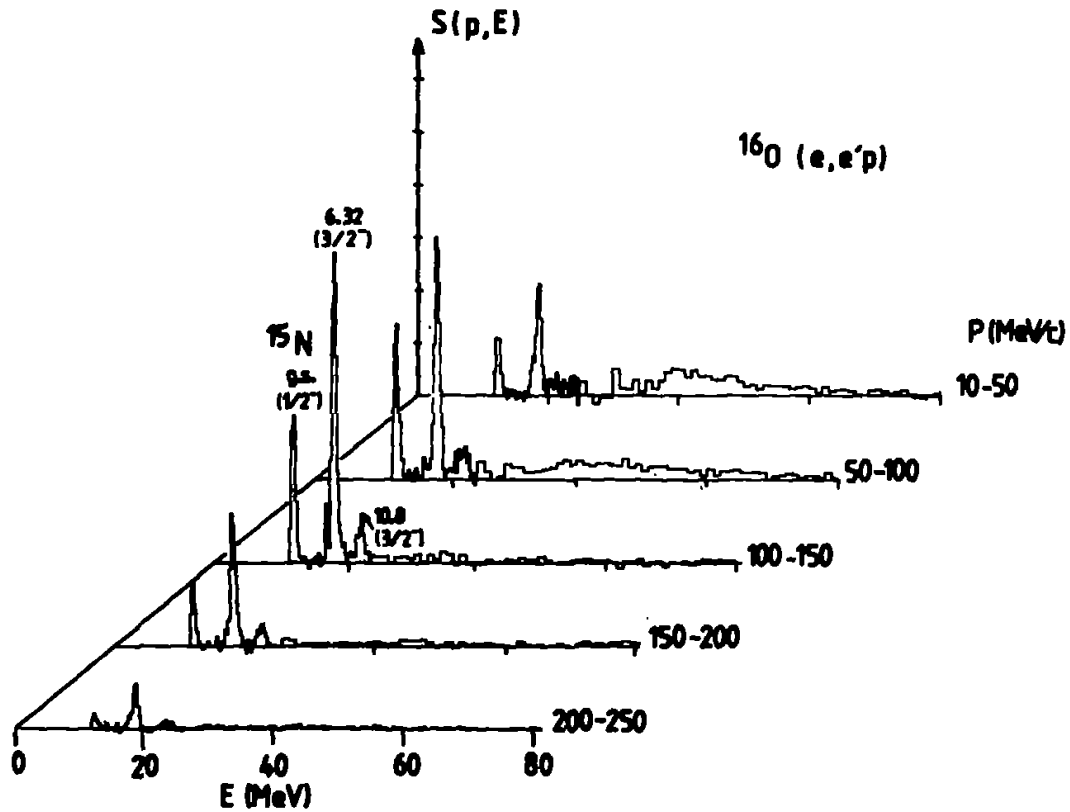


Figure 1.15: Proton separation energy spectra for the $^{16}\text{O}(e, e'p)$ reaction, with different recoil momentum bins [101].

property of any processes discussed here. The arguments of the spectral function $S(E, |\vec{p}|)$, which provides the nuclear information for our calculation, are related to the hole state left after the nucleon knock-out: the remnant nucleus excitation (separation) energy E and its recoil momentum magnitude $|\vec{p}|$. The spectral function does not depend on the direction of \vec{p} because we interpret it as the Fermi motion that is rudimentary random. In Fig. 1.15, we present an example of experimental measurement of the function S in exclusive electron scattering on Oxygen, with a dominant role of the shell structure of the nucleus, especially the so-called $1p_{1/2}$ and $1p_{3/2}$ states. However, one can see a part of the signal distributed between the highlighted shells, which we have not incorporated in the framework mentioned above. The lowering and spreading of the single-particle strength are caused by the nucleon-nucleon correlations, a relevant correction to the mean-field nuclear picture. Known attempts to model this phenomenon involve: using spectroscopic factors that reduce the shell normalization [102], dedicated calculations carried out in the local-density approximation [103], or dynamic mechanisms with additional diagrams and phenomenological interactions [104].

The PWIA theoretical picture, incoherently combined with models that carry out inelastic hadron-nucleus FSI, proved reasonably accurate [105]. However, one should pay attention to the importance of the final-nucleon distortion, which, modeled in a consistent quantum-mechanical way, also affects the kinematics of the outgoing lepton. It is vital for successful electron scattering data comparison (even for inclusive analyses) and leads to non-trivial effects

in neutrino interactions [106]. Schematically presented in Fig. 1.16, the approximation in which the knocked-out nucleon is subject to nuclear potential is called the *distorted-wave impulse approximation* (DWIA). Here, the fundamental approach considers outgoing nucleons in terms of continuum states of the used nuclear potential. Apart from non-relativistic solutions, the same holds for relativistic models, such as the *relativistic mean field* (RMF). Nevertheless, it is not trivial how to consistently combine this approach with the effects of inelastic nucleon-nucleus interactions. One can rely on phenomenology and incorporate these effects through optical potentials or the Glabuer approach [107]. However, these models cannot describe the diverse multiplicity of final states but only provide the averaged reduction in the investigated channel. Combining the quantum-mechanical consistency in modeling the lepton-nucleus interaction with the experimentally-desired predictions for the different kinds of exclusive final states is challenging and of great interest in the community [108].

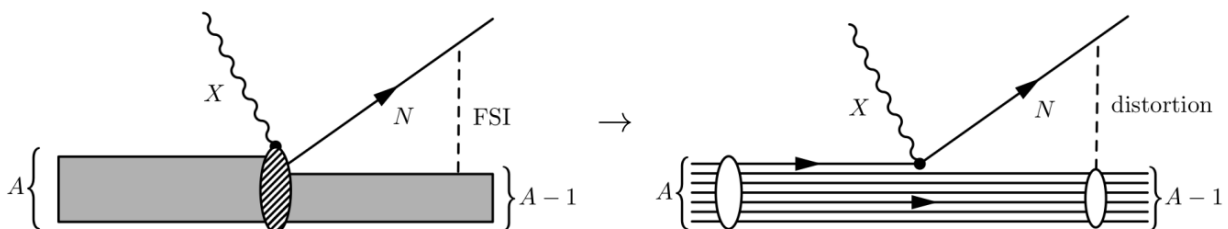


Figure 1.16: (Left) a complete description of the lepton-induced one-nucleon knock-out, (right) the distorted-wave impulse approximation that considers the distortion of the outgoing nucleon wave function. Diagrams adapted from Ref. [109].

Constraints

The crucial component of any successful intermediate-energy lepton-nucleus scattering theory lies in understanding the process involving individual nucleon targets. Over the years, this has been extensively studied in electron scattering experiments to constrain electromagnetic form factors of nucleons. This relates to both the elastic properties [110] and nucleon resonances [111]. We use the acquired knowledge to model neutrino interactions, keeping in mind that the change in the nucleon type requires certain modifications, i.e., a rotation in nucleon isospin space. Then, there are no easy ways to directly constrain the nucleon response to the axial-vector part of the neutrino interaction. Due to poor experimental knowledge, these axial-vector form factors are among the largest sources of uncertainty for neutrino oscillation measurements. However, this may change with modern, clever approaches, such as the latest measurement by the MINERvA experiment [112]. Additionally, we must model these nucleon targets as bound in a nuclear medium and their interactions in an off-shell manner. Although there are a few theoretical and numerical solutions, such as the De Forest prescription for the quasielastic process [113] or the Oset-Salcedo in-medium effects for $\Delta(1232)$ resonances [114], understanding the physics of combining the dynamics of particle projectiles and nuclei is challenging.

Constraining the nuclear dynamics itself also requires tremendous efforts and extensive comparisons to electron scattering data. An educative example of probing nuclear structure comes

from spectral functions, which we extract in specific kinematics that reduce the effect of final-state interactions to isolate the initial nuclear dynamics according to the plane-wave impulse approximation [115]. However, no matter the efforts, such a result will only provide an approximate picture of the nucleus, as trails of FSI will always remain. Also, the phenomenological nature of the nucleon-nucleon correlations involved does not specify the true dynamical effects and makes any interpretation above 1p1h inclusive scattering unclear. Using optical potentials helps to correct our understanding of processes happening in the nuclear medium [116], but their consistent application to PWIA models still needs to be resolved [117]. Alternatively, one can think of other methods of building nuclear dynamics from first principles and incorporating the nucleon-nucleon potential without any mean-field approximations. The *ab initio* approach provides extraordinary results for inclusive reactions [118] but struggles with enormous numerical demands. Nevertheless, no matter the method used and the approximations applied, studying lepton-nucleus scattering requires careful analyses of experimental data and humble interpretations of nuclear effects.

1.4 Monte Carlo neutrino event generators

In the energy region covered by accelerator-based neutrino experiments, we generally consider knowing the neutrino-nucleus scattering cross section with a precision not exceeding 20% [89]. This number provides the general scale of tensions between the theoretical calculations and experimental analyses. Monte Carlo neutrino event generators are the tools that span the bridge connecting the two fields. As described in Section 1.2, they are essential experimental means to understand the neutrino-nucleus interaction systematics and carry out experimental analyses, serving as a theoretical prediction in the experimental format. The generators use the probabilistic MC method to mimic experimental events distributed throughout the phase space according to differential cross sections governing particular neutrino-nucleus scattering dynamics. This idea assumes that, provided large enough statistics, repeated random sampling that introduces randomness in individual model components results in distributions describing a complex process. In practice, we perform these calculations in two steps. In the first one, we integrate the cross sections to obtain global normalization factors, which also provide the balance between particular interaction channels. In the second step, we use the accept-or-reject algorithm to generate events with complete experimental kinematics relative to respective maximum differential cross section values. The numerical speed of this process relies on the sampling efficiency (ratio of accepted to generated events) and the dimensionality of the simulated phase space. The generators commonly used in the accelerator-based neutrino experiments community are: NuWro [119], NEUT [120], GENIE [121], and GiBUU [122]. Moreover, recent approaches include developing the ACHILLES [123] generator and adapting the INCL cascade model [88] to simulate certain neutrino reactions. Although these codes differ in details of the algorithmic structure and the physical models applied, they follow the basic principle of the Monte Carlo method to generate events in a format suitable for experimental analyses.

As shown in Fig. 1.17, Monte Carlo neutrino event generators rely on the plane-wave impulse approximation to factorize the modeling framework. This approach might look oversimplified,

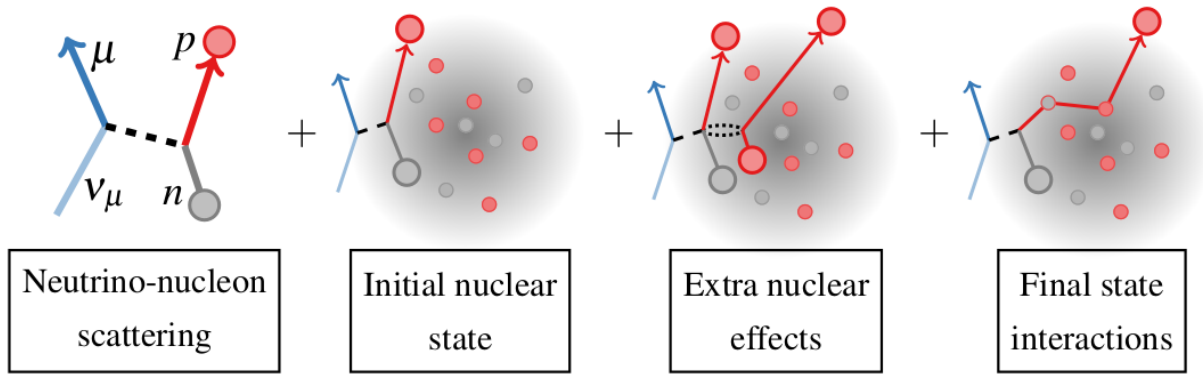


Figure 1.17: Neutrino-nucleus scattering in the factorized scheme, as modeled by Monte Carlo neutrino event generators.

considering the theoretical advancements described before. However, these models originate in the electron scattering community, and there are significant philosophical differences between electron and neutrino scattering experiments, which force their analyses to tackle different problems. In electron scattering, we control the projectile energy, and as the interaction probability is relatively high, we can allow ourselves to investigate isolated parts of the phase space. Constraining ω and \vec{q} variables, we gain access to the full leptonic kinematics and provide meaningful inclusive or exclusive data. In neutrino experiments, we know the incoming energy only as a distribution, and the acquired statistics drastically limit our precision. This means that MC generators must be able to provide predictions for all interaction channels relevant to the broad incoming neutrino fluxes, describing all possible final state topologies. In other words, they need to model neutrino-nucleus interactions in their full exclusive complexity, which is an extremely demanding computational task.

NuWro

Since 2005, the theoretical group of the University of Wroclaw has developed NuWro as a comprehensive Monte Carlo lepton-nucleus event generator [119], optimizing it for use in accelerator-based neutrino oscillation experiments, i.e., the few-GeV energy region. Depending on the energy transferred from the interacting leptonic probe to the hadronic system, NuWro provides quasielastic (QE) [124], hyperon production (HYP) [125], single-pion production (RES), and more inelastic channels (DIS) [126] for scattering off free nucleons. After including complex nuclear targets, additional channels such as two-body processes (MEC) [127], coherent pion production (COH) [92], and neutrino scattering off atomic electrons (LEP) [128] are included. The framework utilizes various nuclear models to provide predictions for the dynamics of target nucleons (e.g., global or local Fermi gas, spectral functions [129,130], or a momentum-dependent nuclear potential [124]. Finally, FSI are simulated by an intranuclear cascade that propagates the outgoing nucleons [105] and produced pions [131] through the residual nucleus. Fig. 1.18 provides a schematic blueprint of the physics implemented in NuWro.

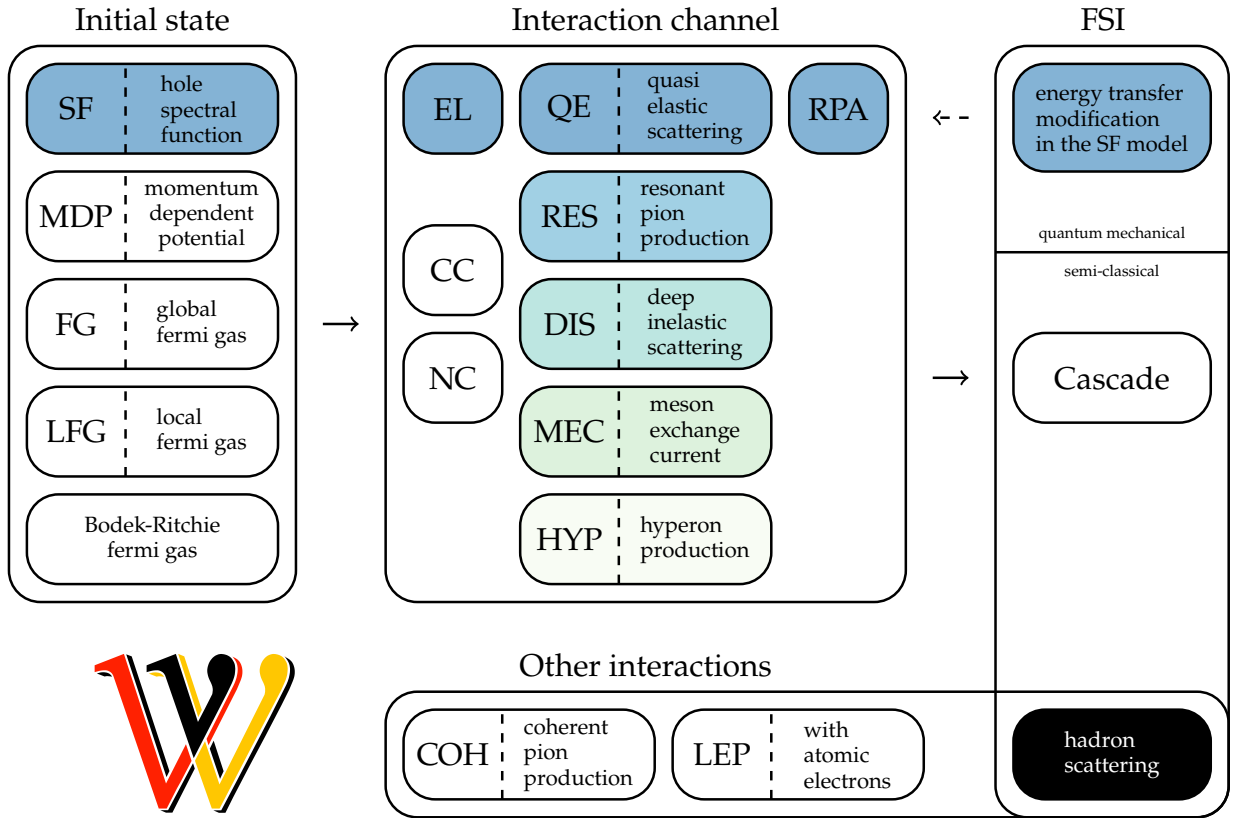


Figure 1.18: The physics blueprint of the NuWro Monte Carlo neutrino event generator according to the factorized scheme of modeling neutrino-nucleus interactions.

As discussed before, we rely on the PWIA picture to model the lepton-nucleus interaction. In the quasielastic interaction channel, this approximation factorizes the one nucleon knock-out processes into the interaction on a single off-shell nucleon convoluted with a particular hole spectral function (SF). The approach relies on the calculation by O. Benhar *et al.* [129] that considers the electron scattering input to the single-particle wave functions and adds the correlated part evaluated within the local density approximation. Additionally, in this model, the prescription by A. Ankowski *et al.* [117] is applied to go beyond the factorized picture and account for the effects of distorting the final nucleon wave function by an optical potential. Alternatively, the target nucleons can be treated as constituting the ideal Fermi gas, parametrized through nuclear density or its average value and referred to as local (LFG) or global Fermi gas (FG), respectively. Finally, the primary interaction vertex is constrained by the conserved vector current (CVC) and partially conserved axial current (PCAC) hypotheses. The default set of vector form factors is provided by the BBBA05 parametrization [110], while the axial form factor has a dipole shape with $g_A = 1.267$, and the axial mass parameter $M_A = 1.03 \text{ GeV}/c^2$. However, other popular form factor parametrizations are also available.

The NuWro single-pion production model combines the contribution from the $\Delta(1232)$ resonance excitation [132] with a non-resonant background obtained by extrapolating the DIS contribution to lower values of invariant hadronic mass W , blended incoherently in the region

$W \in (1.3, 1.6)$ GeV/ c^2 [126]. The generated events follow the double-differential cross sections $d^2\sigma/dQ^2dW$ for both the resonant and non-resonant parts. On top of that, for the former, the model obtains the pion angular distributions (Ω_π) using the parametrized ones measured by the BNL bubble chamber experiment [133], while for the non-resonant part, obtains the kinematics using the PYTHIA6 hadronization routines [134]. Alternatively, one can use the parametrization obtained by the ANL experiment [135]. This model has been exhaustively compared to numerous pion production datasets obtaining adequate accuracy of theoretical predictions [136,137]. Unfortunately, due to many physical similarities and their competition for the same part of the phase space, it is experimentally challenging to distinguish the RES and MEC interactions [138], especially in inclusive neutrino scattering processes. The NuWro implementation of two-nucleon knock-out dynamics relies on tabularized inclusive nuclear responses. We provide the models by the Valencia [139] and Granada (SuSA parametrization) [140] groups and can reproduce their $d^2\sigma/d\omega d|\vec{q}|$ differential cross sections. However, this solution lacks essential information about the dynamics of the outgoing nucleons; for that, we use the phase space model of Ref. [141]. Additionally, we have implemented a different, Transverse-Enhancement model of GENIE [142], which increases transverse quasielastic responses to account for the 2p2h strength. Finally, NuWro contains an independent Valencia-model-based data-driven solution [127], which maximizes the accuracy in reproducing T2K and MINERvA inclusive data under an assumption of all discrepancies originating in the 2p2h dynamics.

Modeling final-state interactions is a challenging many-body problem that bears a tension between numerical efficiency and the accuracy of nuclear calculations. NuWro solution is based on seminal papers by N. Metropolis *et al.* [143,144], which describe an algorithm of the space-like cascade model, and apply up-to-date physics ingredients. In this approach, mean-free paths are attributed to the particles propagated in straight lines with steps of Δx through a continuous medium. Such Monte Carlo sampling uses the standard non-interaction probability formula:

$$P(\Delta x) = \exp(-\Delta x/\lambda), \quad (1.4.1)$$

where $\lambda = (\rho\sigma)^{-1}$ is the mean-free path calculated locally, expressed in nuclear density ρ and an effective interaction cross section σ . The maximal step of $\Delta x = 0.2$ fm is sufficient to grasp the structure of commonly used density profiles. By default, the nucleons constituting the nuclear medium originate from the LFG model and meet its Pauli blocking rules (applied on an event-by-event basis). The cascade terminates when all the moving hadrons leave the nucleus or do not have enough kinetic energy and are stuck in nuclear potential (with the nucleon separation energy of their Fermi energy plus 7 MeV). The remnant nucleus is left in an excited state, and we do not attempt to model its deexcitation. Additionally, we utilize the pion-nucleon interaction dynamics from the model of L.L. Salcedo *et al.* [145]. This aspect and the formation zone effect for the inelastic scattering channels have been presented and compared to data in Ref. [131].

Constraints

As we venture into the precision era of neutrino measurements, Monte Carlo neutrino events generators are expected to provide efficient theoretical predictions resulting from sophisticated and accurate neutrino-nucleus scattering models. Hence, applying our knowledge of nuclear

physics to all relevant interaction channels is crucial. So far, the quasielastic interactions have focused the community's attention, allowing us to implement various solutions beyond the Fermi gas picture [146,147]. In this scope, T2K started using the spectral function formalism in their latest oscillation analyses [86]. However, such a model is practical once its implementation involves direct access to its internal degrees of freedom with a set of parameters we can reweight while evaluating systematics in the analyses. This fact puts significant tension on any implementations that rely on pre-computed assets without the ability to alter the model parameters in real-time. As we try to implement models beyond the PWIA, comprehensive solutions require computational resources that are not currently attainable. We must significantly improve efficiency and the general philosophy of model implementations in Monte Carlo generators. Without such progress and using frameworks that can consistently account for the final nucleon distortion, Pauli blocking, and unitarity, we will not be able to provide percent-level accuracy on neutrino-nucleus interaction predictions.

The second challenge that the Monte Carlo neutrino event generators approach stems mainly from the experimental development and the shift of emphasis to the exclusive neutrino measurements. As discussed in Section 1.3, the phase space of independent variables needed to describe a particular event grows with 3 dimensions for every particle detected in the final state. It is a common approach to tabularize models, which are too computationally demanding to be explicitly implemented in the generators. Unfortunately, tables with more than three dimensions become considerably unmanageable, and one needs to find more efficient implementation schemes. On top of that, comparison to exclusive data requires reasonable control of the inelastic FSI of outgoing hadrons. It is still not firmly established how to merge two frameworks: the quantum-mechanically consistent lepton-nucleus scattering, where the outgoing nucleon is subject to averaged nuclear potential, and the inelastic final-state modeling governed by in-medium nucleon-nucleon interactions. Without the latter, generating the multiplicity of hadrons in the final state, which we observe in neutrino measurements, is impossible.

1.5 Outline of the research

This research involves a novel, multidirectional approach to tackle the problems of neutrino-nucleus interactions in the context of accelerator-based neutrino oscillation experiments. On the theoretical side, we use the nuclear model of *J. Ryckebusch, N. Jachowicz, et al.*, developed at Ghent University, Belgium. This framework involves a non-relativistic, mean-field-based model for both the initial and final hadronic states, combined with one- and two-body nuclear currents [148–150]. Additionally, it utilizes the *continuum random phase approximation* (CRPA) to account for long-range correlations through collective nucleon treatment in low-energy lepton-nucleus scattering [151]. Then, on the Monte Carlo event generators side, we use NuWro as an implementation framework that allows for meaningful comparisons to neutrino data. Having expertise in both ends, we attempt to study the dynamics of two nucleon knock-out channels and implement it in the MC generator as precisely and efficiently as possible. The ultimate goal of this research is to bring state-of-the-art nuclear models closer to being used by the accelerator-based neutrino experiments community, especially for the needs of the T2K experiment.

What will we address in this thesis?

This thesis focuses on the in-medium dynamics of nucleon pairs and their responses to electromagnetic and weak probes. In Chapter 2, we will describe the theoretical foundations of the framework, which we have analytically and numerically validated, and adjusted to our specific needs. Then, using the updated model, we will attempt to quantify the contribution of short-range correlated nucleon pairs to interactions resulting in 1p1h and 2p2h hadronic final states. We will approach this task by employing a dynamic model with phenomenological correlations that modify one-body nuclear currents. Subsequently, we will investigate explicit two-body currents with meson-exchange currents in which no nucleon resonance occurs. In Chapter 3, we will extend our model to incorporate meson-exchange currents involving isobar degrees of freedom. We will constrain the complete model of one- and two-nucleon knock-outs via one- and two-body nuclear currents through electron scattering data and present its capabilities of providing inclusive, semi-inclusive, and exclusive cross section predictions. In Chapter 4, we will investigate the role of short-range nucleon-nucleon correlations for inelastic final-state interactions modeled within the intranuclear cascade model. We will exhaustively compare this model to exclusive ($e, e'p$) experimental data, focusing on the measurements of proton transparency. In the last study, in Chapter 5, we will describe a novel Monte Carlo algorithm for improving the implementation efficiency of sophisticated interaction models. We will exemplify this approach by implementing the Ghent model for the single-pion production off the nucleon target. Finally, we will also show how the obtained 2p2h inclusive cross section model can be implemented in NuWro and compared it to experimental neutrino data, therefore completing the bridge between the theoretical and experimental sides of accelerator-based neutrino research.

References

- [1] B. Pullman, *The atom in the history of human thought* (Oxford University Press, Oxford, England, 1998).
- [2] S. G. Brush, *Archive for History of Exact Sciences* **5**, 1 (1968).
- [3] Jean Baptiste Perrin – Nobel Lecture, <https://www.nobelprize.org/prizes/physics/1926/perrin/lecture/>, Nobel Prize Outreach AB 2023, Accessed: 23.01.2023.
- [4] J. J. Thomson, *Phil. Mag. Ser. 5* **44**, 293 (1897).
- [5] F. Lenz, *Phys. Rev.* **82**, 554 (1951).
- [6] R. L. Workman *et al.* *PTEP* **2022**, 083C01 (2022).
- [7] J. C. Maxwell, *Phil. Trans. Roy. Soc. Lond.* **155**, 459 (1865).
- [8] Matic Lubej, <https://www-f9.ijs.si/~lubej/>, Personal Homepage, Accessed: 28.11.2022.
- [9] P. A. M. Dirac, *Proc. Roy. Soc. Lond. A* **117**, 610 (1928).
- [10] S. L. Glashow, *Nucl. Phys.* **10**, 107 (1959).
- [11] A. Salam and J. C. Ward, *Nuovo Cim.* **11**, 568 (1959).
- [12] S. Weinberg, *Phys. Rev. Lett.* **19**, 1264 (1967).

- [13] A. Pais and S. B. Treiman, *Phys. Rev. Lett.* **35**, 1556 (1975).
- [14] G. Aad *et al.* *Phys. Lett. B* **716**, 1 (2012).
- [15] S. Chatrchyan *et al.* *Phys. Lett. B* **716**, 30 (2012).
- [16] I. Zurbano Fernandez *et al.* **10/2020**, edited by I. Béjar Alonso, O. Brüning, P. Fessia, *et al.* **10.23731/CYRM-2020-0010** (2020).
- [17] H. Baer *et al.* arXiv:1504.04956 (2013).
- [18] M. Anelli *et al.* arXiv:1504.04956 (2015).
- [19] A. Keshavarzi, K. S. Khaw, and T. Yoshioka, *Nucl. Phys. B* **975**, 115675 (2022).
- [20] W. Pauli, *Phys. Today* **31N9**, 27 (1978).
- [21] C. L. Cowan, F. Reines, F. B. Harrison, *et al.* *Science* **124**, 103 (1956).
- [22] E. Fermi, *Z. Phys.* **88**, 161 (1934).
- [23] D. J. Bird *et al.* *Astrophys. J.* **441**, 144 (1995).
- [24] R. Davis Jr., D. S. Harmer, and K. C. Hoffman, *Phys. Rev. Lett.* **20**, 1205 (1968).
- [25] V. N. Gribov and B. Pontecorvo, *Phys. Lett. B* **28**, 493 (1969).
- [26] B. Pontecorvo, *Sov. Phys. JETP* **6**, 429 (1957).
- [27] Y. Fukuda *et al.* *Phys. Rev. Lett.* **81**, 1562 (1998).
- [28] Q. R. Ahmad *et al.* *Phys. Rev. Lett.* **87**, 071301 (2001).
- [29] Q. R. Ahmad *et al.* *Phys. Rev. Lett.* **89**, 011301 (2002).
- [30] A. de Gouvea, in *Theoretical Advanced Study Institute in Elementary Particle Physics: Physics in $D \geq 4$* (Nov. 2004), pp. 197–258.
- [31] P. Lipari, in *1st CERN-CLAF School of High-Energy Physics* (May 2001), pp. 115–199.
- [32] S. Schael *et al.* *Phys. Rept.* **427**, 257 (2006).
- [33] First neutrino event in a hydrogen bubble chamber, *Physics Today* **24**, 21 (2971).
- [34] C. S. Wu, E. Ambler, R. W. Hayward, *et al.* *Phys. Rev.* **105**, 1413 (1957).
- [35] R. L. Garwin, L. M. Lederman, and M. Weinrich, *Phys. Rev.* **105**, 1415 (1957).
- [36] M. Goldhaber, L. Grodzins, and A. W. Sunyar, *Phys. Rev.* **109**, 1015 (1958).
- [37] E. K. Akhmedov, *JHEP* **09**, 116 (2007).
- [38] P. Vogel, L. Wen, and C. Zhang, *Nature Commun.* **6**, 6935 (2015).
- [39] J. N. Abdurashitov *et al.* *J. Exp. Theor. Phys.* **95**, 181 (2002).
- [40] W. Hampel *et al.* *Phys. Lett. B* **447**, 127 (1999).
- [41] K. S. Hirata *et al.* *Phys. Rev. Lett.* **63**, 16 (1989).
- [42] C. Arpesella *et al.* *Phys. Lett. B* **658**, 101 (2008).
- [43] S. Abe *et al.* *Phys. Rev. C* **84**, 035804 (2011).
- [44] Y. Abe *et al.* *Phys. Rev. Lett.* **108**, 131801 (2012).
- [45] F. P. An *et al.* *Phys. Rev. Lett.* **108**, 171803 (2012).
- [46] J. K. Ahn *et al.* *Phys. Rev. Lett.* **108**, 191802 (2012).

- [47] F. An *et al.* J. Phys. G **43**, 030401 (2016).
- [48] M. H. Ahn *et al.* Phys. Rev. D **74**, 072003 (2006).
- [49] K. Abe *et al.* Phys. Rev. Lett. **107**, 041801 (2011).
- [50] K. Abe *et al.* arXiv:1805.04163 (2018).
- [51] P. Adamson *et al.* Phys. Rev. Lett. **110**, 251801 (2013).
- [52] P. Adamson *et al.* Phys. Rev. Lett. **116**, 151806 (2016).
- [53] C. Rubbia *et al.* JINST **6**, P07011 (2011).
- [54] B. Abi *et al.* JINST **15**, T08008 (2020).
- [55] K. Abe *et al.* Phys. Rev. D **97**, 072001 (2018).
- [56] A. Albert *et al.* JHEP **06**, 113 (2019).
- [57] M. G. Aartsen *et al.* Phys. Rev. Lett. **120**, 071801 (2018).
- [58] S. Adrian-Martinez *et al.* J. Phys. G **43**, 084001 (2016).
- [59] I. Esteban *et al.* <https://www.nu-fit.org>, NuFIT v5.2.
- [60] B. Dasgupta and J. Kopp, Physics Reports **928**, Sterile neutrinos, 1 (2021).
- [61] P. D. Bolton, F. F. Deppisch, and P. S. Bhupal Dev, JHEP **03**, 170 (2020).
- [62] M. Aker *et al.* Nature Phys. **18**, 160 (2022).
- [63] A. Gando *et al.* Phys. Rev. Lett. **117**, [Addendum: Phys.Rev.Lett. 117, 109903 (2016)], 082503 (2016).
- [64] M. Aker *et al.* J. Phys. G **49**, 100501 (2022).
- [65] F. T. Avignone III, S. R. Elliott, and J. Engel, Rev. Mod. Phys. **80**, 481 (2008).
- [66] K. Mahn, C. Marshall, and C. Wilkinson, Ann. Rev. Nucl. Part. Sci. **68**, 105 (2018).
- [67] T. Leitner and U. Mosel, Phys. Rev. C **81**, 064614 (2010).
- [68] J. Nieves, F. Sanchez, I. Ruiz Simo, *et al.* Phys. Rev. D **85**, 113008 (2012).
- [69] A. Nikolakopoulos, M. Martini, M. Ericson, *et al.* Phys. Rev. C **98**, 054603 (2018).
- [70] L. A. Ruso *et al.* In 2022 Snowmass Summer Study (Mar. 2022).
- [71] A. Branca *et al.* PoS **ICHEP2022**, 611 (2023).
- [72] M. Pavin *et al.* Phys. Rev. D **106**, 112008 (2022).
- [73] P. Giorgio, PoS **LeptonPhoton2019**, 142 (2019).
- [74] C. Anderson *et al.* Phys. Rev. Lett. **108**, 161802 (2012).
- [75] R. Acciarri *et al.* JINST **12**, P02017 (2017).
- [76] A. M. Szec, JINST **11**, C02018 (2016).
- [77] K. Abe *et al.* Nucl. Instrum. Meth. A **659**, 106 (2011).
- [78] D. Ayres *et al.* **10**.2172/935497 (2007).
- [79] L. Aliaga *et al.* Nucl. Instrum. Meth. A **743**, 130 (2014).
- [80] R. Acciarri *et al.* JINST **12**, P02017 (2017).
- [81] K. Abe *et al.* PTEP **2015**, 053C02 (2015).

- [82] R. Acciarri *et al.* arXiv:1601.05471 (2016).
- [83] K. Nishikawa *et al.* http://j-parc.jp/researcher/Hadron/en/pac_0606/pdf/p11-Nishikawa.pdf, Tokai-to-Kamioka (T2K) Long Baseline Neutrino Oscillation Experiment Proposal, Accessed: 1.03.2023.
- [84] N. Abgrall *et al.* Eur. Phys. J. C **76**, 617 (2016).
- [85] K. Abe *et al.* Nature **580**, [Erratum: Nature 583, E16 (2020)], 339 (2020).
- [86] K. Abe *et al.* arXiv:2303.03222 (2023).
- [87] K. Abe *et al.* Phys. Rev. Lett. **121**, 171802 (2018).
- [88] A. Ershova *et al.* Phys. Rev. D **106**, 032009 (2022).
- [89] L. Alvarez-Ruso *et al.* Prog. Part. Nucl. Phys. **100**, 1 (2018).
- [90] J. E. Amaro, M. B. Barbaro, J. A. Caballero, *et al.* J. Phys. G **47**, 124001 (2020).
- [91] N. F. Mott, Proc. R. Soc. **124**, 425 (1929).
- [92] C. Berger and L. M. Sehgal, Phys. Rev. D **79**, 053003 (2009).
- [93] S. L. Adler, Annals Phys. **50**, 189 (1968).
- [94] J. Ryckebusch, V. Van der Sluys, M. Waroquier, *et al.* Phys. Lett. B **333**, 310 (1994).
- [95] M. Gluck, E. Reya, and A. Vogt, Z. Phys. C **67**, 433 (1995).
- [96] C. Andreopoulos *et al.* In NuSTEC Workshop on Shallow- and Deep-Inelastic Scattering (July 2019).
- [97] A. V. Butkevich and S. P. Mikheyev, Phys. Rev. C **72**, 025501 (2005).
- [98] K. L. G. Heyde, The nuclear shell model (Springer Berlin, Heidelberg, 1990).
- [99] J. D. Walecka, Annals Phys. **83**, 491 (1974).
- [100] S. Frullani and J. Mougey, Adv. Nucl. Phys. **14**, 1 (1984).
- [101] J. Mougey, Nucl. Phys. A **335**, 35 (1980).
- [102] J. M. Udias, P. Sarriguren, E. Moya de Guerra, *et al.* Phys. Rev. C **48**, 2731 (1993).
- [103] O. Benhar, A. Fabrocini, S. Fantoni, *et al.* Nucl. Phys. A **579**, 493 (1994).
- [104] J. Ryckebusch, V. Van der Sluys, K. Heyde, *et al.* Nucl. Phys. A **624**, 581 (1997).
- [105] K. Niewczas and J. T. Sobczyk, Phys. Rev. C **100**, 015505 (2019).
- [106] A. Nikolakopoulos, N. Jachowicz, N. Van Dessel, *et al.* Phys. Rev. Lett. **123**, 052501 (2019).
- [107] M. C. Martinez, P. Lava, N. Jachowicz, *et al.* Phys. Rev. C **73**, 024607 (2006).
- [108] A. Nikolakopoulos, R. González-Jiménez, N. Jachowicz, *et al.* Phys. Rev. C **105**, 054603 (2022).
- [109] T. Van Cuyck, Short-range correlations and meson-exchange currents in neutrino-nucleus scattering, PhD thesis (Ghent University, 2017).
- [110] R. Bradford, A. Bodek, H. S. Budd, *et al.* Nucl. Phys. B Proc. Suppl. **159**, edited by F. Cavanna, J. G. Morfin, and T. Nakaya, 127 (2006).
- [111] D. Drechsel, S. S. Kamalov, and L. Tiator, Eur. Phys. J. A **34**, 69 (2007).

- [112] T. Cai *et al.* *Nature* **614**, 48 (2023).
- [113] T. De Forest, *Nucl. Phys. A* **392**, 232 (1983).
- [114] E. Oset and L. L. Salcedo, *Nucl. Phys. A* **468**, 631 (1987).
- [115] L. Jiang *et al.* *Phys. Rev. D* **105**, 112002 (2022).
- [116] R. González-Jiménez, M. B. Barbaro, J. A. Caballero, *et al.* *Phys. Rev. C* **101**, 015503 (2020).
- [117] A. M. Ankowski, O. Benhar, and M. Sakuda, *Phys. Rev. D* **91**, 033005 (2015).
- [118] A. Lovato, S. Gandolfi, J. Carlson, *et al.* *Phys. Rev. Lett.* **117**, 082501 (2016).
- [119] Nuwro official repository, <https://github.com/NuWro/nuwro>.
- [120] Y. Hayato and L. Pickering, *Eur. Phys. J. ST* **230**, 4469 (2021).
- [121] C. Andreopoulos *et al.* *Nucl. Instrum. Meth. A* **614**, 87 (2010).
- [122] O. Buss, T. Gaitanos, K. Gallmeister, *et al.* *Phys. Rept.* **512**, 1 (2012).
- [123] J. Isaacson, W. I. Jay, A. Lovato, *et al.* *Phys. Rev. D* **107**, 033007 (2023).
- [124] C. Juszczak, J. A. Nowak, and J. T. Sobczyk, *Eur. Phys. J. C* **39**, 195 (2005).
- [125] C. Thorpe, J. Nowak, K. Niewczas, *et al.* *Phys. Rev. C* **104**, 035502 (2021).
- [126] C. Juszczak, J. A. Nowak, and J. T. Sobczyk, *Nucl. Phys. B Proc. Suppl.* **159**, edited by F. Cavanna, J. G. Morfin, and T. Nakaya, 211 (2006).
- [127] T. Bonus, J. T. Sobczyk, M. Siemaszko, *et al.* *Phys. Rev. C* **102**, 015502 (2020).
- [128] D. Zhuridov, J. T. Sobczyk, C. Juszczak, *et al.* *J. Phys. G* **48**, 055002 (2021).
- [129] O. Benhar, N. Farina, H. Nakamura, *et al.* *Phys. Rev. D* **72**, 053005 (2005).
- [130] A. M. Ankowski and J. T. Sobczyk, *Phys. Rev. C* **77**, 044311 (2008).
- [131] T. Golan, C. Juszczak, and J. T. Sobczyk, *Phys. Rev. C* **86**, 015505 (2012).
- [132] K. M. Graczyk, D. Kielczewska, P. Przewlocki, *et al.* *Phys. Rev. D* **80**, 093001 (2009).
- [133] T. Kitagaki *et al.* *Phys. Rev. D* **34**, 2554 (1986).
- [134] T. Sjostrand, S. Mrenna, and P. Z. Skands, *JHEP* **05**, 026 (2006).
- [135] G. M. Radecky *et al.* *Phys. Rev. D* **25**, [Erratum: *Phys.Rev.D* 26, 3297 (1982)], 1161 (1982).
- [136] R. González-Jiménez, K. Niewczas, and N. Jachowicz, *Phys. Rev. D* **97**, 013004 (2018).
- [137] A. Nikolakopoulos, R. González-Jiménez, K. Niewczas, *et al.* *Phys. Rev. D* **97**, 093008 (2018).
- [138] K. Niewczas and J. T. Sobczyk, *Phys. Rev. C* **93**, 035502 (2016).
- [139] J. Nieves, I. Ruiz Simo, and M. J. Vicente Vacas, *Phys. Rev. C* **83**, 045501 (2011).
- [140] G. D. Megias, J. E. Amaro, M. B. Barbaro, *et al.* *Phys. Rev. D* **94**, 093004 (2016).
- [141] J. T. Sobczyk, *Phys. Rev. C* **86**, 015504 (2012).
- [142] T. Katori, *AIP Conf. Proc.* **1663**, edited by H. Da Motta, J. G. Morfin, and M. Sakuda, 030001 (2015).
- [143] N. Metropolis, R. Bivins, M. Storm, *et al.* *Phys. Rev.* **110**, 185 (1958).
- [144] N. Metropolis, R. Bivins, M. Storm, *et al.* *Phys. Rev.* **110**, 204 (1958).
- [145] L. L. Salcedo, E. Oset, M. J. Vicente-Vacas, *et al.* *Nucl. Phys. A* **484**, 557 (1988).

- [146] S. Dolan, G. D. Megias, and S. Bolognesi, *Phys. Rev. D* **101**, 033003 (2020).
- [147] S. Dolan, A. Nikolakopoulos, O. Page, *et al.* *Phys. Rev. D* **106**, 073001 (2022).
- [148] T. Van Cuyck, N. Jachowicz, R. González-Jiménez, *et al.* *Phys. Rev. C* **94**, 024611 (2016).
- [149] T. Van Cuyck, N. Jachowicz, R. González-Jiménez, *et al.* *Phys. Rev. C* **95**, 054611 (2017).
- [150] N. Jachowicz and A. Nikolakopoulos, *Eur. Phys. J. ST* **230**, 4339 (2021).
- [151] V. Pandey, N. Jachowicz, J. Ryckebusch, *et al.* *Phys. Rev. C* **89**, 024601 (2014).

2

Theoretical framework

Our modeling aims to provide quantitative predictions for the probability of lepton-nucleus interactions with a given final state. Such an observable which can be measured experimentally is called the cross section, typically denoted as σ . Depending on the analysis, we usually express this quantity in the differential form, e.g., $d^2\sigma/d\Omega$, which is proportional to the probability of finding an outgoing particle in the solid angle Ω . We focus on processes where one or two nucleons are knocked-out from the target nucleus due to an interaction with electron or muon-neutrino projectiles. Our methodology includes the dynamics governed by both one-body and two-body nuclear currents. This chapter will discuss the framework we revised and tailored to suit our needs in providing neutrino-nucleus scattering predictions.

2.1 Differential cross sections

Describing the dynamics of intermediate energy leptons scattering off atomic nuclei is a complex multidimensional problem involving several approximations and sophisticated modeling. Here, we employ the Born picture, where an incoming electron or neutrino, denoted by $k_i = (\epsilon_i, \vec{k}_i)$, exchanges only one boson with the hadronic system and turns into the observed final lepton, denoted by $k_f = (\epsilon_f, \vec{k}_f)$. We will investigate the circumstances under which this interaction leads to the following processes: the one-nucleon knockout

$$e + A \rightarrow e' + R + N, \quad (2.1.1)$$

$$\nu_\mu + A \rightarrow \mu^- + R + N, \quad (2.1.2)$$

and the two-nucleon knockout

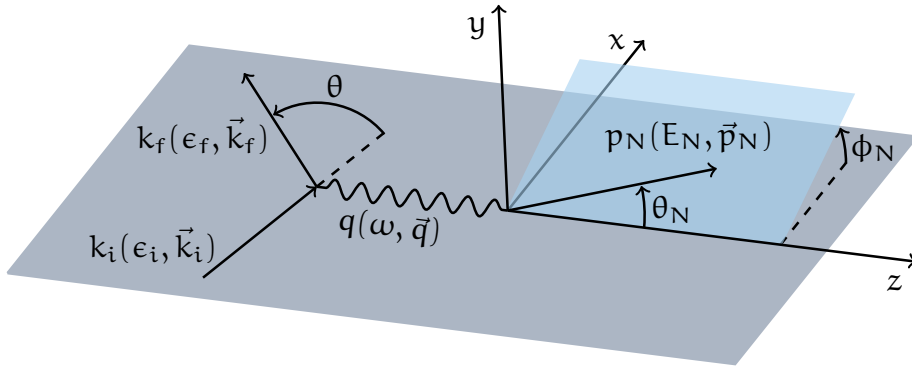
$$e + A \rightarrow e' + R + N_a + N_b, \quad (2.1.3)$$

$$\nu_\mu + A \rightarrow \mu^- + R + N_a + N_b, \quad (2.1.4)$$

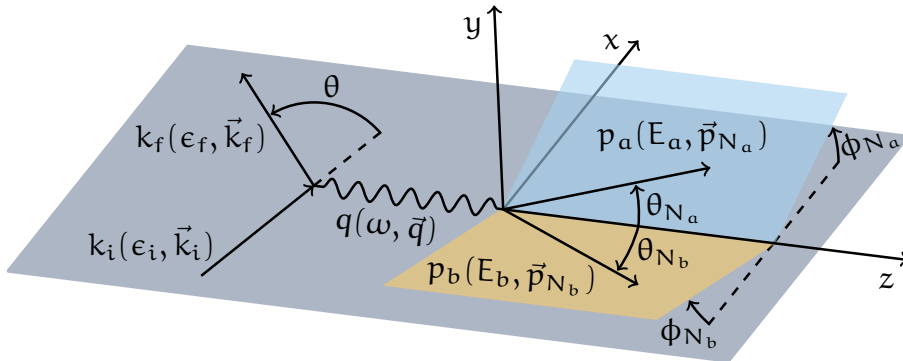
where $R = (A - 1)^*$, $(A - 2)^*$, respectively. The asterisk denotes an excited nuclear remnant, which we consider unstable by an excess energy up to tens of MeV. We denote the initial and final hadronic states as $P_A = (E_A, \vec{P}_A)$ and $P_R = (E_R, \vec{P}_R)$, while the outgoing nucleons are $p_N = (E_N, \vec{p}_N)$ (one-nucleon case) or $p_{N_a} = (E_{N_a}, \vec{p}_{N_a})$, $p_{N_b} = (E_{N_b}, \vec{p}_{N_b})$ (two-nucleon case). Working in the laboratory frame, we consider the target nucleus to be at rest and write $P_A = (M_A, 0)$. Then, we define the four-momentum transfer $q = (\omega, \vec{q})$ through

$$\omega = E_i - E_f, \quad \vec{q} = \vec{k}_i - \vec{k}_f, \quad (2.1.5)$$

and the invariant quantity $Q^2 = -q^2 = (k_i - k_f)^2$. As presented in Fig. 2.1, we work in the coordinate system with \vec{q} along the z-axis and the (lepton) scattering plane coinciding with the xz plane. Fig. 2.1a and Fig. 2.1b present the angles definition for each outgoing particle in the one- and two-nucleon knock-out, respectively.



(a) Kinematics of lepton-induced one-nucleon knock-out processes.



(b) Kinematics of lepton-induced two-nucleon knock-out processes.

Figure 2.1: Schematic view of the kinematical variables used in this work.

To derive convenient differential cross section prescriptions, we begin with the most general,

relativistic formula in the Bjorken and Drell convention [1]:

$$\begin{aligned} d\sigma = & \frac{m_i}{\epsilon_i} \frac{m_f}{\epsilon_f} \frac{d\vec{k}_f}{(2\pi)^3} \frac{d\vec{p}_R}{(2\pi)^3} \left(\prod_x \frac{M_x}{E_x} \frac{d\vec{p}_x}{(2\pi)^3} \right) \\ & \times (2\pi)^4 \delta^{(4)}(k_i + P_A - k_f - P_R - (\sum_x p_x)) \overline{\sum_{i,f}} |\mathcal{M}_{fi}|^2, \end{aligned} \quad (2.1.6)$$

where x iterates over one (N) or two (N_a, N_b) knocked-out nucleons. This formula is differential over the phase space of all outgoing particles, with the δ function ensuring four-momentum conservation. The \mathcal{M}_{fi} is a Lorentz scalar containing all the interaction dynamics, averaged over the initial and summed over the final states. By default, this formula considers on-shell Dirac fermions and their plane-wave normalization factors, e.g., m/ϵ . In our model, the initial and final leptons are on-shell, whereas the knocked-out nucleons are subject to the nuclear potential and independently obtain explicit normalization factors relative to their plane-wave states. To complete our description, we examine the nuclei involved in the process, and for the target nucleus, we trivially obtain a factor of $M_A/E_A = 1$. For the excited remnant, we define the effective mass as $M_R^* = M_R + E_{\text{exc}}$, where the excitation energy E_{exc} is low enough to write $E_R/M_R^* \simeq 1$. Under the described assumptions, the obtained formula is universal, and we will exploit it for investigations of both the 1p1h and 2p2h processes.

By integrating the four-momentum-conserving δ function, we can reduce the number of differentials, especially in the variables not accessible experimentally. Thus, we proceed by integrating over the recoil of the nucleus and obtain

$$d\sigma = \frac{1}{(2\pi)^2} \frac{m_i}{\epsilon_i} \frac{m_f}{\epsilon_f} d\vec{k}_f \left(\prod_x \frac{M_x}{E_x} \frac{d\vec{p}_x}{(2\pi)^3} \right) \delta(\epsilon_i + M_A - \epsilon_f - E_R - (\sum_x E_x)) \overline{\sum_{i,f}} |\mathcal{M}_{fi}|^2. \quad (2.1.7)$$

We can also use the remaining function to integrate the magnitude of the momentum of an outgoing nucleon. However, this requires using the following property

$$\delta(f(x)) = \sum_{x_0} \frac{\delta(x - x_0)}{\left| \frac{df}{dx}(x_0) \right|}, \quad (2.1.8)$$

where the values of x_0 are the roots of the $f(x)$ function. For the one-nucleon knock-out case, we expand the δ function as

$$\delta \left(\epsilon_i + M_A - \epsilon_f - \sqrt{(\vec{q} - \vec{p}_N)^2 + (M_{A-1}^*)^2} - \sqrt{\vec{p}_N^2 + M_N^2} \right) \quad (2.1.9)$$

to integrate over the $d|\vec{p}_N|$ variable. This results in

$$d\sigma = \frac{m_i}{\epsilon_i} \frac{m_f}{\epsilon_f} \frac{p_N M_N}{(2\pi)^5} f_{1p1h}^{-1} d\vec{k}_f d\Omega_N \overline{\sum_{i,f}} |\mathcal{M}_{fi}|^2, \quad (2.1.10)$$

where we define the nucleus recoil factor as

$$f_{1p1h} = \left| 1 + \frac{E_N}{E_{A-1}} \left(1 - \frac{\vec{p} \cdot \vec{q}}{p_N^2} \right) \right|. \quad (2.1.11)$$

We proceed analogically in the two-nucleon knock-out case, aiming to integrate over the $d\vec{p}_{N_b}$ variable. It leads to the following expansion

$$\delta \left(\epsilon_i + M_A - \epsilon_f - \sqrt{(\vec{q} - \vec{p}_{N_a} - \vec{p}_{N_b})^2 + (M_{A-1}^*)^2} - E_{N_a} - \sqrt{\vec{p}_{N_b}^2 + M_N^2} \right). \quad (2.1.12)$$

Then, we again use Eq. (2.1.8) and obtain

$$d\sigma = \frac{m_i}{\epsilon_i} \frac{m_f}{\epsilon_f} \frac{M_N}{E_{N_a}} \frac{p_{N_b} M_N}{(2\pi)^8} f_{2p2h}^{-1} d\vec{k}_f d\vec{p}_{N_a} d\Omega_{N_b} \sum_{i,f} |\mathcal{M}_{fi}|^2, \quad (2.1.13)$$

with the recoil factor

$$f_{2p2h} = \left| 1 + \frac{E_{N_b}}{E_{A-2}} \left(1 - \frac{\vec{p}_{N_b} \cdot (\vec{q} - \vec{p}_{N_a})}{p_{N_b}^2} \right) \right|. \quad (2.1.14)$$

In the ideal case of all momentum being transferred to the outgoing nucleon(s) and the residual nucleus not having any recoil, the factors f_{1p1h} and f_{2p2h} approach unity.

The matrix element \mathcal{M}_{fi} encapsulates the dynamics of the lepton-nucleus scattering and dictates the physical meaning of this process. We use the Feynman rules in momentum space to evaluate its properties, as presented in Fig. 2.2. We employ the following propagators

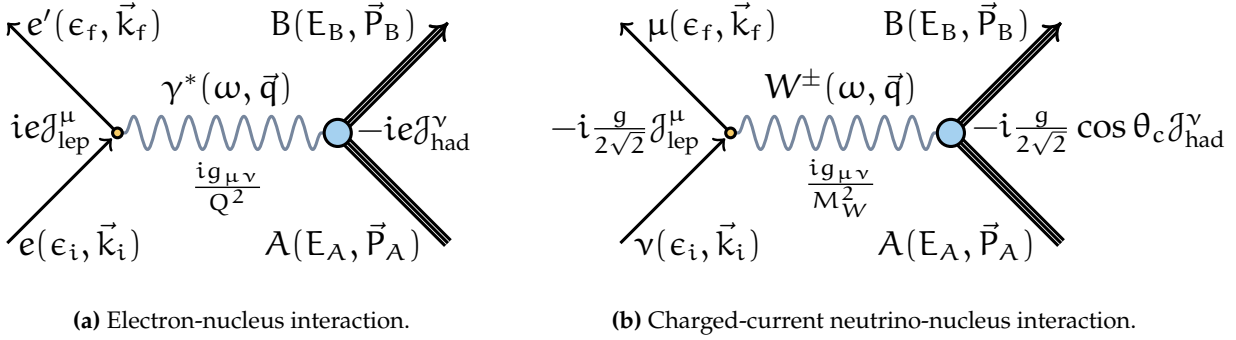


Figure 2.2: Feynman diagrams for leptons scattering off atomic nuclei. The final hadronic system, denoted as B, contains both the residual nucleus and the outgoing nucleons.

$$\mathcal{P}_{\mu\nu}^{\gamma} = \frac{ig_{\mu\nu}}{Q^2}, \quad \mathcal{P}_{\mu\nu}^{W} = \frac{i \left(g_{\mu\nu} - \frac{q_{\mu} q_{\nu}}{M_W^2} \right)}{M_W^2 + Q^2} \simeq \frac{ig_{\mu\nu}}{M_W^2} \quad (2.1.15)$$

for the virtual photon and W boson, respectively. For the latter, we note that the mass of the W boson is significantly higher than the energies accessible in the modeled environment ($M_W \simeq 80.4 \text{ GeV}/c^2$), so we make a static approximation that recovers the Fermi theory of weak interactions. Thus, we also introduce the Fermi coupling constant G_F , which relates to the weak coupling constant g as $G_F/\sqrt{2} = g^2/8M_W^2$. Finally, for the matrix elements, we obtain the following expressions

$$\mathcal{M}_{fi}^{\gamma}(q) = -i \frac{e^2}{2Q^2} \mathcal{J}_\nu^{\text{lep}}(q) \mathcal{J}_{\text{had}}^\nu(q), \quad (2.1.16)$$

$$\mathcal{M}_{fi}^W(q) = -i \frac{G_F}{\sqrt{2}} \cos \theta_c \mathcal{J}_\nu^{\text{lep}}(q) \mathcal{J}_{\text{had}}^\nu(q), \quad (2.1.17)$$

where we define the lepton and hadron current as

$$\mathcal{J}_\nu^{\text{lep}}(\mathbf{q}) \equiv \bar{u}(\mathbf{k}_f, s_f) \hat{\mathcal{J}}_\nu^{\text{lep}} u(\mathbf{k}_i, s_i) = \bar{u}(\mathbf{k}_f, s_f) \gamma_\nu (1 + h\gamma^5) u(\mathbf{k}_i, s_i), \quad (2.1.18)$$

$$\mathcal{J}_\nu^{\text{had}}(\mathbf{q}) \equiv \langle \Psi_f | \hat{\mathcal{J}}_\nu^{\text{had}} | \Psi_i \rangle. \quad (2.1.19)$$

The incoming and outgoing leptons are described by Dirac spinors $u(\mathbf{k}_i, s_i)$ and $\bar{u}(\mathbf{k}_f, s_f)$, respectively. The Standard Model describes their interaction exactly, assuming the helicity h taking values: $-(+)$ for (anti)neutrinos and averaging out to zero for electrons. Note that we absorb the factor $1/2$ of the spin-projection operator $(1 + h\gamma^5)/2$ into the weak coupling constant but write it explicitly in the electron case. The hadronic current $\hat{\mathcal{J}}_\nu^{\text{had}}(\mathbf{q})$, evaluated between the initial and final nuclear states $|\Psi_i\rangle$ and $\langle\Psi_f|$, is subject to modeling.

Once we square the matrix elements \mathcal{M}_{fi} , it is convenient to introduce bilinear products of the currents and define the leptonic $L_{\mu\nu}$ and hadronic $W^{\mu\nu}$ tensors. Thus, for the processes discussed here, we obtain

$$\overline{\sum_{i,f} |\mathcal{M}_{fi}^\gamma(\mathbf{q})|^2} = \frac{e^4}{4Q^4} L_{\mu\nu}(\mathbf{q}) W^{\mu\nu}(\mathbf{q}), \quad (2.1.20)$$

$$\overline{\sum_{i,f} |\mathcal{M}_{fi}^W(\mathbf{q})|^2} = \frac{G_F^2}{2} \cos^2 \theta_c L_{\mu\nu}(\mathbf{q}) W^{\mu\nu}(\mathbf{q}). \quad (2.1.21)$$

The explicit calculation of the leptonic tensor is straightforward [2] and leads to

$$\begin{aligned} L_{\mu\nu}(\mathbf{q}) &= \overline{\sum_{i,f} \left(\mathcal{J}_\mu^{\text{lep}}(\mathbf{q}) \right)^\dagger \mathcal{J}_\nu^{\text{lep}}(\mathbf{q})} \\ &= \frac{2}{m_i m_f} (k_{i,\mu} k_{f,\nu} + k_{f,\nu} k_{i,\mu} - g_{\mu\nu} k_i \cdot k_f + g_{\mu\nu} m_i m_f - i h \epsilon_{\mu\nu\alpha\beta} k_i^\alpha k_f^\beta). \end{aligned} \quad (2.1.22)$$

As for the hadronic tensor, we obtain

$$W_{1p1h}^{\mu\nu}(\mathbf{q}) = \frac{1}{2J_i + 1} \sum_{M_i} \sum_{J_R, M_R} \sum_{m_{s_N}} (\mathcal{J}_{\text{had}}^\mu(\mathbf{q}))^\dagger \mathcal{J}_{\text{had}}^\nu(\mathbf{q}), \quad (2.1.23)$$

$$W_{2p2h}^{\mu\nu}(\mathbf{q}) = \frac{1}{2J_i + 1} \sum_{M_i} \sum_{J_R, M_R} \sum_{m_{s_{N_a}}} \sum_{m_{s_{N_b}}} (\mathcal{J}_{\text{had}}^\mu(\mathbf{q}))^\dagger \mathcal{J}_{\text{had}}^\nu(\mathbf{q}), \quad (2.1.24)$$

where (J_i, M_i) and (J_R, M_R) are the quantum numbers of the initial and residual nucleus, respectively. Here, we will only consider processes with $J_i = 0$, with no need for summation over M_i . We do sum over the spin projection of the outgoing nucleon(s), e.g. m_{s_N} , which introduces an additional summation in the 2p2h case. Without any loss of kinematical generality, this commonly used description wraps the process of the one-boson exchange scattering of relativistic leptons on nuclear targets leading to one- and two-nucleon knock-out.

Language of responses

Working in the coordinate systems, presented in Fig. 2.1, with the z -axis along the direction of the momentum transfer, brings additional means to simplify the formulas describing the lepton-nucleus scattering process. As shown in Ref. [3], one can introduce a base for hadronic system

responses corresponding to specific components of the current: 0—Coulomb, 1,2—transverse, and 3—longitudinal. Then, we can write the contraction of the leptonic and hadronic tensors as

$$L_{\mu\nu}(q)W^{\mu\nu}(q) = 2\frac{\epsilon_i\epsilon_f}{m_i m_f} [\mathcal{V}_{CC}\mathcal{W}_{CC} + \mathcal{V}_{CL}\mathcal{W}_{CL} + \mathcal{V}_{LL}\mathcal{W}_{LL} + \mathcal{V}_T\mathcal{W}_T + \mathcal{V}_{TT}\mathcal{W}_{TT} + \mathcal{V}_{TC}\mathcal{W}_{TC} + \mathcal{V}_{TL}\mathcal{W}_{TL} + \text{h}(\mathcal{V}_{T'}\mathcal{W}_{T'} + \mathcal{V}_{TC'}\mathcal{W}_{TC'} + \mathcal{V}_{TL'}\mathcal{W}_{TL'})], \quad (2.1.25)$$

where \mathcal{W}_x are the hadronic responses and \mathcal{V}_x are the corresponding kinematic factors, as defined in Table 2.1. The hadronic system is spherically symmetric; therefore, we express the responses

Kinematic factors	Nuclear responses
$\mathcal{V}_{CC} = 1 + \zeta \cos \theta$	$\mathcal{W}_{CC} = \mathcal{J}_0 ^2$
$\mathcal{V}_{CL} = -\left(\frac{\omega}{ \vec{q} }(1 + \zeta \cos \theta) + \frac{m_f^2}{\epsilon_f \vec{q} }\right)$	$\mathcal{W}_{CL} = 2\Re(\mathcal{J}_0 \mathcal{J}_3^\dagger)$
$\mathcal{V}_{LL} = 1 + \zeta \cos \theta - 2\frac{\epsilon_i \epsilon_f}{ \vec{q} ^2} \zeta^2 \sin^2 \theta$	$\mathcal{W}_{LL} = \mathcal{J}_3 ^2$
$\mathcal{V}_T = 1 - \zeta \cos \theta + \frac{\epsilon_i \epsilon_f}{ \vec{q} ^2} \zeta^2 \sin^2 \theta$	$\mathcal{W}_T = \mathcal{J}_{+1} ^2 + \mathcal{J}_{-1} ^2$
$\mathcal{V}_{TT} = -\frac{\epsilon_i \epsilon_f}{ \vec{q} ^2} \zeta^2 \sin^2 \theta$	$\mathcal{W}_{TT} = 2\Re(\mathcal{J}_{+1} \mathcal{J}_{-1}^\dagger)$
$\mathcal{V}_{TC} = -\frac{\sin \theta}{\sqrt{2} \vec{q} } \zeta(\epsilon_i + \epsilon_f)$	$\mathcal{W}_{TC} = 2\Re(\mathcal{J}_0(\mathcal{J}_{+1}^\dagger - \mathcal{J}_{-1}^\dagger))$
$\mathcal{V}_{TL} = \frac{\sin \theta}{\sqrt{2} \vec{q} ^2} \zeta(\epsilon_i^2 - \epsilon_f^2 + m_f^2)$	$\mathcal{W}_{TL} = 2\Re(\mathcal{J}_3(\mathcal{J}_{+1}^\dagger - \mathcal{J}_{-1}^\dagger))$
$\mathcal{V}_{T'} = \frac{\epsilon_i + \epsilon_f}{ \vec{q} }(1 - \zeta \cos \theta) - \frac{m_f^2}{\epsilon_f \vec{q} }$	$\mathcal{W}_{T'} = \mathcal{J}_{+1} ^2 - \mathcal{J}_{-1} ^2$
$\mathcal{V}_{TC'} = -\frac{\sin \theta}{\sqrt{2}} \zeta$	$\mathcal{W}_{TC'} = 2\Re(\mathcal{J}_0(\mathcal{J}_{+1}^\dagger + \mathcal{J}_{-1}^\dagger))$
$\mathcal{V}_{TL'} = \frac{\omega \sin \theta}{\sqrt{2} \vec{q} ^2} \zeta$	$\mathcal{W}_{TL'} = 2\Re(\mathcal{J}_3(\mathcal{J}_{+1}^\dagger + \mathcal{J}_{-1}^\dagger))$

Table 2.1: Kinematic factors and nuclear responses for the electron and charged-current neutrino scattering off the nucleus.

in the spherical basis $\vec{e}_z, \vec{e}_{\pm 1} = \mp(\vec{e}_x \pm i\vec{e}_y)/\sqrt{2}$ as $\vec{\mathcal{J}} = -\mathcal{J}_{-1}\vec{e}_{+1} - \mathcal{J}_{+1}\vec{e}_{-1} + \mathcal{J}_z\vec{e}_z$. Additionally, we include the dependence on the outgoing lepton mass through the following correction

$$\zeta \equiv \frac{|\vec{k}_f|}{\epsilon_f} = \sqrt{1 - \frac{m_f^2}{\epsilon_f^2}}. \quad (2.1.26)$$

Utilizing these tools, we can write our general 1p1h and 2p2h differential cross section formulas as

$$\begin{aligned} \frac{d\sigma^X}{d\epsilon_f d\Omega_f d\Omega_N} &= \frac{|\vec{p}_N| M_N}{(2\pi)^3} f_{1p1h}^{-1} \zeta \sigma^X \\ &\times [\mathcal{V}_{CC}\mathcal{W}_{CC} + \mathcal{V}_{CL}\mathcal{W}_{CL} + \mathcal{V}_{LL}\mathcal{W}_{LL} + \mathcal{V}_T\mathcal{W}_T + \mathcal{V}_{TT}\mathcal{W}_{TT} \\ &+ \mathcal{V}_{TC}\mathcal{W}_{TC} + \mathcal{V}_{TL}\mathcal{W}_{TL} + \text{h}(\mathcal{V}_{T'}\mathcal{W}_{T'} + \mathcal{V}_{TC'}\mathcal{W}_{TC'} + \mathcal{V}_{TL'}\mathcal{W}_{TL'})] \end{aligned} \quad (2.1.27)$$

and

$$\begin{aligned} \frac{d\sigma^X}{d\epsilon_f d\Omega_f dT_{N_a} d\Omega_{N_a} d\Omega_{N_b}} &= \frac{|\vec{p}_{N_a}|M_N|\vec{p}_{N_b}|M_N}{(2\pi)^6} f_{2p2h}^{-1} \zeta \sigma^X \\ &\times [\mathcal{V}_{CC}\mathcal{W}_{CC} + \mathcal{V}_{CL}\mathcal{W}_{CL} + \mathcal{V}_{LL}\mathcal{W}_{LL} + \mathcal{V}_T\mathcal{W}_T + \mathcal{V}_{TT}\mathcal{W}_{TT} \\ &+ \mathcal{V}_{TC}\mathcal{W}_{TC} + \mathcal{V}_{TL}\mathcal{W}_{TL} + \mathfrak{h}(\mathcal{V}_{T'}\mathcal{W}_{T'} + \mathcal{V}_{TC'}\mathcal{W}_{TC'} + \mathcal{V}_{TL'}\mathcal{W}_{TL'})], \end{aligned} \quad (2.1.28)$$

where we combine the normalization differences between the electron and neutrino case in Mott-like prefactors σ^X , defined as

$$\sigma^\gamma = \frac{1}{2} \left(\frac{e^2 \epsilon_f}{2\pi Q^2} \right)^2, \quad (2.1.29)$$

$$\sigma^W = \left(\frac{G_F \cos \theta_c \epsilon_f}{2\pi} \right)^2. \quad (2.1.30)$$

In these expressions, the functions \mathcal{V}_x again contain all the lepton kinematic information, while the response functions \mathcal{W}_x include the nuclear dynamics.

Finally, in the context of electron scattering and the vector-current contribution to neutrino scattering, we can further simplify our expressions utilizing the conserved vector current (CVC) hypothesis [4], which states that in the momentum space, we obtain

$$q_\mu \mathcal{J}^\mu(q) = 0, \quad (2.1.31)$$

and, in our coordinate system,

$$\mathcal{J}_3(q) = \frac{\omega}{|\vec{q}|} \mathcal{J}_0(q). \quad (2.1.32)$$

Additionally, the scattered electron has a negligible mass $m_e \simeq 0$, leading to $\zeta \simeq 1$. Combining all this knowledge, we write the differential cross sections for electron scattering as

$$\frac{d\sigma^\gamma}{d\epsilon_f d\Omega_f d\Omega_N} = \frac{|\vec{p}_N|M_N}{(2\pi)^3} f_{1p1h}^{-1} \sigma^{\text{Mott}} [\mathcal{V}_L^e \mathcal{W}_{CC} + \mathcal{V}_T^e \mathcal{W}_T + \mathcal{V}_{TT}^e \mathcal{W}_{TT} + \mathcal{V}_{TL}^e \mathcal{W}_{TL}] \quad (2.1.33)$$

and

$$\begin{aligned} \frac{d\sigma^\gamma}{d\epsilon_f d\Omega_f dT_{N_a} d\Omega_{N_a} d\Omega_{N_b}} &= \frac{|\vec{p}_{N_a}|M_N|\vec{p}_{N_b}|M_N}{(2\pi)^6} f_{2p2h}^{-1} \sigma^{\text{Mott}} \\ &\times [\mathcal{V}_L^e \mathcal{W}_{CC} + \mathcal{V}_T^e \mathcal{W}_T + \mathcal{V}_{TT}^e \mathcal{W}_{TT} + \mathcal{V}_{TL}^e \mathcal{W}_{TL}]. \end{aligned} \quad (2.1.34)$$

We define the new kinematic factors in Table 2.2. Within these approximations, the new prefactor

Electromagnetic kinematic factors			
\mathcal{V}_L^e	$= \frac{Q^4}{ \vec{q} ^4}$	\mathcal{V}_T^e	$= \frac{Q^2}{2 \vec{q} ^2} + \tan^2 \frac{\theta}{2}$
\mathcal{V}_{TT}^e	$= -\frac{Q^2}{2 \vec{q} ^2}$	\mathcal{V}_{TL}^e	$= -\frac{Q^2}{\sqrt{2} \vec{q} ^3} (\epsilon_i + \epsilon_f) \tan^2 \frac{\theta}{2}$

Table 2.2: CVC-constrained kinematic factors for electron scattering off the nucleus.

is the commonly used Mott cross section

$$\sigma^{\text{Mott}} = \left(\frac{\alpha \cos \frac{\theta}{2}}{2\epsilon_i \sin^2 \frac{\theta}{2}} \right)^2, \quad (2.1.35)$$

where $\alpha = e^2/4\pi$ is the fine structure constant.

We can use the experience from the electron scattering case to better understand the relevance of specific nuclear responses in neutrino scattering. We notice that the kinematical factor \mathcal{V}_{CC} is present in the formulation of the \mathcal{V}_{CL} and \mathcal{V}_{LL} . Assuming that the final lepton has negligible mass, we write

$$\mathcal{V}_{CC} + \mathcal{V}_{CL} + \mathcal{V}_{LL} \simeq \left(1 - \frac{\omega}{|\vec{q}|} + \frac{\omega^2}{|\vec{q}|^2}\right) \mathcal{V}_{CC}. \quad (2.1.36)$$

Thus, knowing how particular responses enter the cross section, we combine the Coulomb and longitudinal components into an approximate nuclear response

$$\mathcal{W}_L \equiv \left| \mathcal{J}_0 - \frac{\omega}{|\vec{q}|} \mathcal{J}_3 \right|^2 = \mathcal{W}_{CC} - \frac{\omega}{|\vec{q}|} \mathcal{W}_{CL} + \frac{\omega^2}{|\vec{q}|^2} \mathcal{W}_{LL}. \quad (2.1.37)$$

This formula, in certain circumstances, encapsulates enough physics to provide meaningful results while maintaining presentation clarity.

Multipole expansion

The ten nuclear response functions we present in Table 2.1 contain complete hadronic information about the lepton-nucleus interaction process. All of them are functions of the four-dimensional hadronic current $\hat{\mathcal{J}}_{\nu}^{\text{had}}(\vec{q})$ and correspond to the particular matrix elements in momentum space

$$\hat{\mathcal{J}}_{\nu}^{\text{had}} = \langle \Psi_f | \hat{\mathcal{J}}_{\nu}^{\text{had}}(\vec{q}) | \Psi_i \rangle. \quad (2.1.38)$$

However, our non-relativistic approach we perform the numerical calculations in coordinate space, to which we move using the Fourier transform

$$\hat{\mathcal{J}}_{\nu}^{\text{had}}(\vec{q}) = \int d\vec{x} e^{i\vec{q}\cdot\vec{x}} \hat{\mathcal{J}}_{\nu}^{\text{had}}(\vec{x}). \quad (2.1.39)$$

Additionally, as the mean-field nuclear potential is spherically symmetric and we consider nucleon wave functions as its bound or continuum energy eigenstates, we wish to utilize this symmetry to separate the angular dependency of calculations. For this purpose, we use the Rayleigh formula

$$e^{i\vec{q}\cdot\vec{x}} = \sqrt{4\pi} \sum_{J=0}^{\infty} i^J \sqrt{2J+1} j_J(|\vec{q}||\vec{x}|) Y_{J0}(\Omega_x), \quad (2.1.40)$$

which factorizes the problem into the Bessel functions $j_J(|\vec{q}||\vec{x}|)$ and the spherical harmonics $Y_{JM}(\Omega_x)$. The summation over multipoles J is in principle infinite but, in our applications, convergent, so we can safely truncate it, achieving the desired level of precision. As presented in Ref. [5], this framework introduces well-known multipole operators: Coulomb ($\hat{\mathcal{C}}_{JM}^{\text{Coul}}(|\vec{q}|)$), longitudinal ($\hat{\mathcal{L}}_{JM}^{\text{long}}(|\vec{q}|)$), electric ($\hat{\mathcal{J}}_{JM}^{\text{elec}}(|\vec{q}|)$), and magnetic ($\hat{\mathcal{J}}_{JM}^{\text{magn}}(|\vec{q}|)$), in the following way

$$\begin{aligned} \hat{\rho}(\vec{q}) &= +\sqrt{4\pi} \sum_{J \geq 0} i^J \hat{\mathcal{C}}_{J0}^{\text{Coul}}(|\vec{q}|), \\ \hat{\mathcal{J}}_3(\vec{q}) &= -\sqrt{4\pi} \sum_{J \geq 0} i^J \hat{\mathcal{L}}_{J0}^{\text{long}}(|\vec{q}|), \\ \hat{\mathcal{J}}_{\pm}(\vec{q}) &= -\sqrt{2\pi} \sum_{J \geq 1} i^J \left(\hat{\mathcal{J}}_{J\pm 1}^{\text{elec}}(|\vec{q}|) \pm \hat{\mathcal{J}}_{J\pm 1}^{\text{magn}}(|\vec{q}|) \right), \end{aligned} \quad (2.1.41)$$

where $\hat{J} \equiv \sqrt{2J+1}$. Therefore, we define the multipole operators as

$$\begin{aligned}\hat{\mathcal{C}}_{JM}^{\text{Coul}}(|\vec{q}|) &= \int d\vec{x} (j_J(|\vec{q}||\vec{x}|) Y_{JM}(\Omega_x)) \hat{\rho}(\vec{x}), \\ \hat{\mathcal{L}}_{JM}^{\text{long}}(|\vec{q}|) &= \frac{i}{q} \int d\vec{x} \left[\vec{\nabla} (j_J(|\vec{q}||\vec{x}|) Y_{JM}(\Omega_x)) \right] \cdot \hat{\mathcal{J}}(\vec{x}), \\ \hat{\mathcal{J}}_{JM}^{\text{elec}}(|\vec{q}|) &= \frac{1}{q} \int d\vec{x} \left[\vec{\nabla} \times \left(j_J(|\vec{q}||\vec{x}|) \vec{y}_{J(J,1)}^M(\Omega_x) \right) \right] \cdot \hat{\mathcal{J}}(\vec{x}), \\ \hat{\mathcal{J}}_{JM}^{\text{magn}}(|\vec{q}|) &= \int d\vec{x} \left(j_J(|\vec{q}||\vec{x}|) \vec{y}_{J(J,1)}^M(\Omega_x) \right) \cdot \hat{\mathcal{J}}(\vec{x}),\end{aligned}\tag{2.1.42}$$

where $\hat{\rho}(\vec{x})$ and $\hat{\mathcal{J}}(\vec{x})$ are the time and space components of the nuclear current, respectively. Apart from the spherical harmonics $Y_{LM}(\Omega_x)$, we also use the vector spherical harmonics

$$\vec{y}_{J(l,1)}^M(\Omega_x) \equiv \sum_{m,i} \langle l, m; 1, i | J, M \rangle Y_{lm}(\Omega_x) \vec{e}_i.\tag{2.1.43}$$

It is convenient to introduce one more multipole operator $\hat{\mathcal{O}}_{JM}^\kappa(|\vec{q}|)$, defined as

$$\hat{\mathcal{O}}_{JM}^\kappa(|\vec{q}|) = \int d\vec{x} \left(j_{J+\kappa}(|\vec{q}||\vec{x}|) \vec{y}_{J(J+\kappa,1)}^M(\Omega_x) \right) \cdot \hat{\mathcal{J}}(\vec{x}).\tag{2.1.44}$$

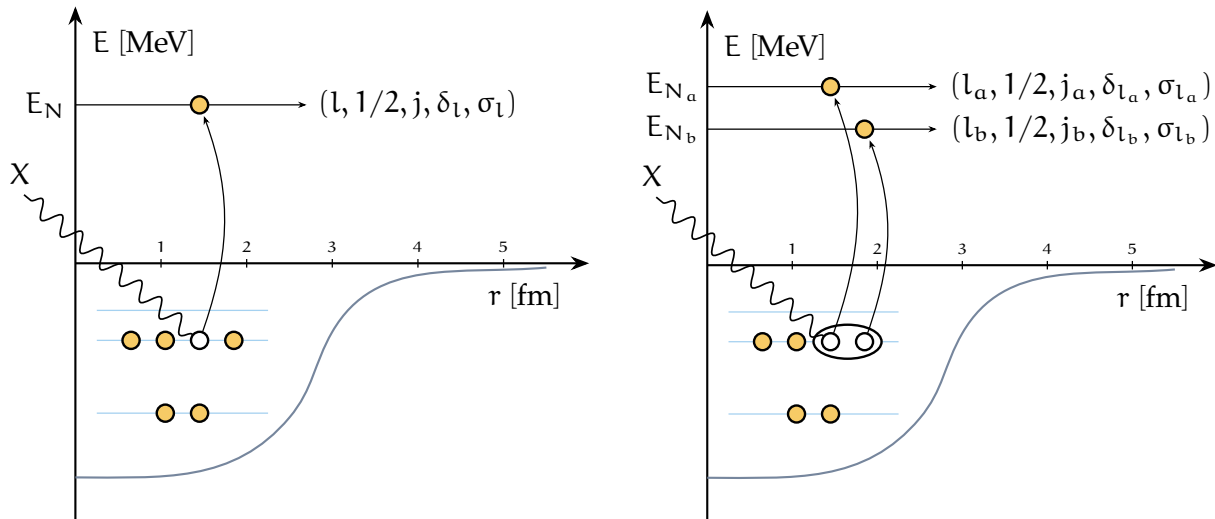
Then, we can simplify the longitudinal, electric, and magnetic operators and write in the following form

$$\begin{aligned}\hat{\mathcal{L}}_{JM}^{\text{long}}(|\vec{q}|) &= i \sum_{\kappa=\pm 1} \left(\frac{J + \delta_{\kappa,+1}}{2J+1} \right)^{\frac{1}{2}} \hat{\mathcal{O}}_{JM}^\kappa(|\vec{q}|) \\ \hat{\mathcal{J}}_{JM}^{\text{elec}}(|\vec{q}|) &= i \sum_{\kappa=\pm 1} (-1)^{\delta_{\kappa,+1}} \left(\frac{J + \delta_{\kappa,-1}}{2J+1} \right)^{\frac{1}{2}} \hat{\mathcal{O}}_{JM}^\kappa(|\vec{q}|) \\ \hat{\mathcal{J}}_{JM}^{\text{magn}}(|\vec{q}|) &= \hat{\mathcal{O}}_{JM}^{\kappa=0}(|\vec{q}|).\end{aligned}\tag{2.1.45}$$

Finally, we see how the essence of our nuclear calculations lies in evaluating the $\hat{\mathcal{C}}_{JM}^{\text{Coul}}$ and $\hat{\mathcal{O}}_{JM}^\kappa$ operators for particular hadronic processes leading to one- and two-nucleon knock-outs.

2.2 Nuclear framework

In the context of this thesis, we construct the nuclear description based on the Ghent model [6–11]. As such, the cornerstone of our nuclear model is an independent-particle picture of nuclear dynamics. We assume the protons and neutrons are moving according to the Schrödinger equation in a mean-field (MF) potential. We determine this through a Hartree-Fock calculation based on an effective Skyrme-type nucleon-nucleon force SkE2 [12]. The original Skyrme interaction is a well-established parametrization that accurately reflects the ground-state and low-lying excited state characteristics of spherical nuclei [13]. As presented in Fig. 2.3, our model describes the outgoing nucleons as continuum states of the same potential, guaranteeing that the initial and final states are orthogonal. Thus, the final nucleons are asymptotically free but are still under the influence of the mean-field potential of the residual hadronic system. It is an example of



(a) One-nucleon knock-out process, where the interacting boson ejects a nucleon to the continuum, and the residual nucleus remains in a one-hole state: h^{-1} .

(b) Two-nucleon knock-out process, where the interacting boson ejects two nucleons to the continuum, and the residual nucleus remains in a two-hole state: $(hh')^{-1}$.

Figure 2.3: Lepton-induced nucleon knock-out from ^{12}C as interpreted in the shell model picture. We characterize the continuum states by their angular quantum numbers and additional phase shifts: δ and σ .

a distorted-wave calculation in the so-called *spectator approach*, which is quantum mechanically consistent, yet lacks the inelastic final-state nucleon-nucleus interaction properties.

The Ghent model has a long history of describing electron- and neutrino-nucleus cross sections, and other nuclear dynamics phenomena. This research has always stressed the methodology to overcome the limitations of the IPM, especially its lack of an exhaustive treatment of nucleon-nucleon correlations. For one-nucleon knock-out processes, the Ghent framework accounts for long-range correlations and collective nucleon treatment through the CRPA methodology. These corrections are significant for lower projectile energies, where long-range nuclear physics dominates the narrative. Early studies involve photo-induced (γ, N) and electron-induced ($e, e'N$) reactions on ^{16}O [14–16]. Refs. [17–19] describe the extension of this framework to NC and CC neutrino-induced processes at energies relevant to supernova research. Most of the further research was motivated by the demands from accelerator-based neutrino experiments [20–25] and novel projects involving neutrino scattering off ^{40}Ar nuclei [26–29].

For intermediate projectile energies, our model has two methods of incorporating nuclear correlations: attributed to nuclear states and the dynamics of the hadronic current. The former effectively introduces short-range nucleon-nucleon correlations (SRC) using one-body currents modified with central, tensor, and spin-isospin correlation functions. Such modeling produces the expected depletion of single-particle strength, dynamically acting like spectroscopic factors, and provides information about the redistribution of nucleons into higher regions of momentum space. The latter, concerning the lepton interaction, involves two-body meson-exchange currents (MEC) through the seagull, pion-in-flight, and Δ diagrams, allowing us to go beyond the impulse approximation picture. The abovementioned directions push our understanding of the electron- and neutrino-nucleus interactions beyond the first approximation in the structure of

the initial nuclear state and the interaction with the projectile, respectively. This framework is essential to generate consistent predictions for the two-nucleon knock-out reactions, which have grown in relevance for accelerator-based neutrino oscillation analyses in the past decade [30]. The path of the Ghent research on this topic commenced with MEC photo-induced (γ, pp) and (γ, pn) reactions [6]. Then, introducing SRC led to modeling electron-induced ($e, e'pp$) and ($e, e'pn$) [8,31]. Over the years, this framework has been employed in various analyses of exclusive $^{16}\text{O}(e, e'pp)$ [32,33], semi-inclusive $^{16}\text{O}(e, e'p)$ [34,35], along with inclusive $^{12}\text{C}(e, e')$ and $^{40}\text{Ca}(e, e')$ [7] electron scattering. Finally, this research progressed to studying neutrino-induced interactions, as described in Refs. [4,10,11].

In this work, we analyze the properties of our model by examining the following lepton-nucleus scattering cross sections. In one-nucleon knock-out processes, we compute exclusive cross sections

$$\begin{aligned} \frac{d\sigma^X}{d\epsilon_f d\Omega_f d\Omega_N} &= \frac{|\vec{p}_N| E_N}{(2\pi)^3} f_{1p1h}^{-1} \zeta \sigma^X \\ &\times [\mathcal{V}_{CC} \mathcal{W}_{CC} + \mathcal{V}_{CL} \mathcal{W}_{CL} + \mathcal{V}_{LL} \mathcal{W}_{LL} + \mathcal{V}_T \mathcal{W}_T + \mathcal{V}_{TT} \mathcal{W}_{TT} \\ &+ \mathcal{V}_{TC} \mathcal{W}_{TC} + \mathcal{V}_{TL} \mathcal{W}_{TL} + \hbar (\mathcal{V}_{T'} \mathcal{W}_{T'} + \mathcal{V}_{TC'} \mathcal{W}_{TC'} + \mathcal{V}_{TL'} \mathcal{W}_{TL'})], \end{aligned} \quad (2.2.1)$$

where X denotes either an electromagnetic (γ) or a weak (W) boson, and the inclusive ones

$$\frac{d\sigma^W}{d\epsilon_f d\Omega_f} = 4\pi\sigma^W \zeta [\mathcal{V}_{CC} \mathcal{W}_{CC} + \mathcal{V}_{CL} \mathcal{W}_{CL} + \mathcal{V}_{LL} \mathcal{W}_{LL} + \mathcal{V}_T \mathcal{W}_T + \hbar \mathcal{V}_{T'} \mathcal{W}_{T'}], \quad (2.2.2)$$

$$\frac{d\sigma^\gamma}{d\epsilon_f d\Omega_f} = 4\pi\sigma^{\text{Mott}} [\mathcal{V}_L^e \mathcal{W}_{CC} + \mathcal{V}_T^e \mathcal{W}_T] \quad (2.2.3)$$

for the neutrino and electron interactions, respectively. The equivalent formulas also describe the inclusive cross sections for two-nucleon knock-out reactions, while

$$\begin{aligned} \frac{d\sigma^X}{d\epsilon_f d\Omega_f dT_{N_a} d\Omega_{N_a} d\Omega_{N_b}} &= \frac{|\vec{p}_{N_a}| E_{N_a} |\vec{p}_{N_b}| E_{N_b}}{(2\pi)^6} f_{2p2h}^{-1} \zeta \sigma^X \\ &\times [\mathcal{V}_{CC} \mathcal{W}_{CC} + \mathcal{V}_{CL} \mathcal{W}_{CL} + \mathcal{V}_{LL} \mathcal{W}_{LL} + \mathcal{V}_T \mathcal{W}_T + \mathcal{V}_{TT} \mathcal{W}_{TT} \\ &+ \mathcal{V}_{TC} \mathcal{W}_{TC} + \mathcal{V}_{TL} \mathcal{W}_{TL} + \hbar (\mathcal{V}_{T'} \mathcal{W}_{T'} + \mathcal{V}_{TC'} \mathcal{W}_{TC'} + \mathcal{V}_{TL'} \mathcal{W}_{TL'})] \end{aligned} \quad (2.2.4)$$

provides the exclusive one. The semi-inclusive cross section arises from integrating over the solid angle of one of the outgoing nucleons

$$\frac{d\sigma^X}{d\epsilon_f d\Omega_f dT_N d\Omega_N} = \int d\Omega_{N'} \frac{d\sigma^X}{d\epsilon_f d\Omega_f dT_N d\Omega_N d\Omega_{N'}}. \quad (2.2.5)$$

We summarize these formulas, the analytical steps of obtaining the matrix elements in the second quantization picture and integrating them over their angular dependency in Appendix A and Appendix B for the 1p1h and 2p2h processes, respectively.

Nucleon wave functions

Solving a many-body nuclear system for single-particle wave functions is a challenging problem. As introduced in Section 1.3, we use them to build a Slater determinant, describing the uncorrelated ground state of the investigated nucleus. We rely on the self-consistent Hartree-Fock

equation to obtain the appropriate mean-field potential U , based on the Skyrme SkE2 force

$$V = \sum_{i<j} V_{ij}^{[2]} + \sum_{i<j<k} V_{ijk}^{[3]}, \quad (2.2.6)$$

which includes two-body and three-body interaction terms. In this work, all nuclei are spherically symmetric, which allows us to separate the variables in single-nucleon states as

$$\Psi_{nl\frac{1}{2}jm}(\vec{r}) = \phi(|\vec{r}|)_{nlj} \mathcal{Y}_{j(l,\frac{1}{2})}^m(\Omega_r), \quad (2.2.7)$$

where \mathcal{Y} represents the spin spherical harmonics. Then, we use the same MF potential to calculate the bound and continuum nucleon wave functions using radial equations of the form

$$(T + U(|\vec{r}|))\phi(|\vec{r}|)_{nlj} = \epsilon_{nlj}\phi(|\vec{r}|)_{nlj}. \quad (2.2.8)$$

Then, we form the asymptotically free outgoing nucleon state as a sum over partial wave contributions from each positive-energy solution. This approach allows us to account for the distortion of the outgoing nucleon and ensures orthogonality between the interacting states.

We construct the Slater determinants of the target and residual nuclei using bound single-nucleon wave functions obtained from Eq. (2.2.8) ($\epsilon < 0$). One can find exhaustive descriptions of this procedure in many textbooks, e.g., Ref. [36]. Here, we will focus on regular solutions, which provide the following asymptotic behavior

$$\begin{aligned} \phi(|\vec{r}|)_{nlj} &\xrightarrow{|\vec{r}| \rightarrow 0} r^l, \\ \phi(|\vec{r}|)_{nlj} &\xrightarrow{|\vec{r}| \gg |\vec{r}_A|} \sim 0, \end{aligned} \quad (2.2.9)$$

where $|\vec{r}_A|$ is the nuclear radius. In Fig. 2.4, we present the calculations for Carbon and Oxygen nuclei that we use throughout this work. One can see that the shape differences between the two nuclei and isospin types are negligible. Thus, we expect the total number of nucleons (normalization) will dominate the nuclear response strength differences, keeping its properties somewhat universal between the two nuclei.

For calculating the continuum states ($\epsilon > 0$), we rely on the observation that at a considerable distance ($|\vec{r}| \gg |\vec{r}_A|$), the nuclear potential fades away, and the wave functions tend to the solutions of the Coulomb equation. Therefore, we expect them to behave asymptotically like the Bessel functions and write

$$\begin{aligned} \phi(|\vec{r}|)_{nlj} &\xrightarrow{|\vec{r}| \rightarrow 0} r^l \\ \phi(|\vec{r}|)_{nlj} &\xrightarrow{|\vec{r}| \gg |\vec{r}_A|} \sim \frac{\sin(|\vec{p}_N||\vec{r}| - \eta \ln(2|\vec{p}_N||\vec{r}|) - \pi l/2 + \delta_l + \sigma_l)}{|\vec{p}_N||\vec{r}|}, \end{aligned} \quad (2.2.10)$$

where we relate the energy and momentum using the reduced mass μ_N as

$$\epsilon = \frac{|\vec{p}_N|^2}{2\mu_N}, \quad \mu_N = \frac{A}{A-1}M_N. \quad (2.2.11)$$

The δ_l and σ_l are the central and Coulomb phase shifts, and the factor η accounts for the Coulomb part of the single-particle potential

$$\eta = (Z-1) \frac{e^2 \mu_N}{|\vec{p}_N|}. \quad (2.2.12)$$

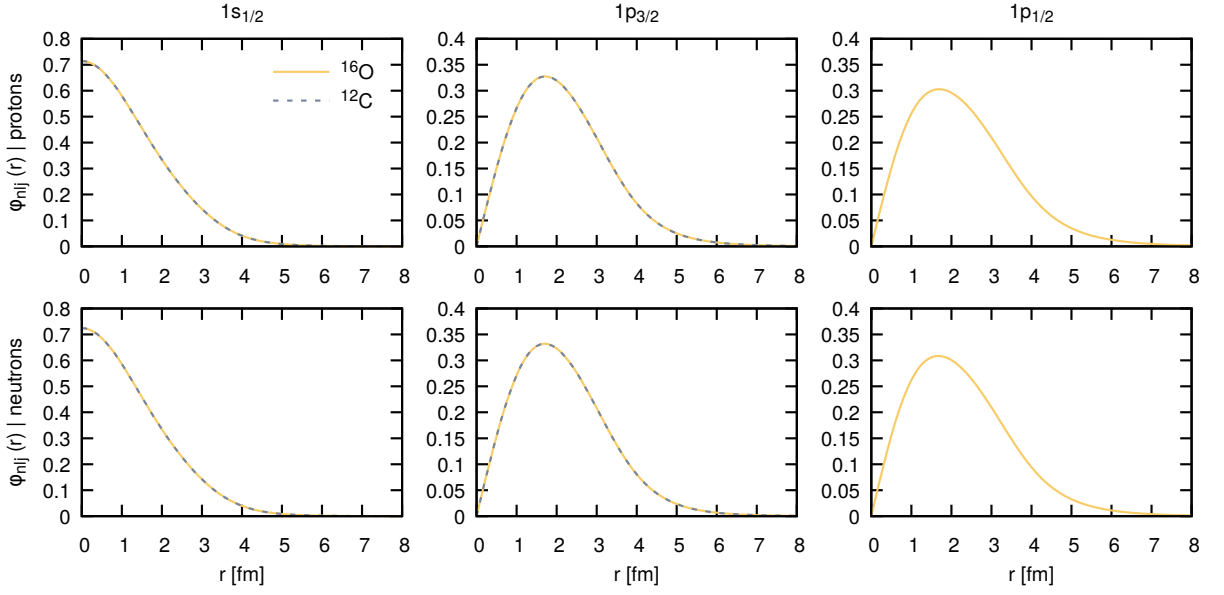


Figure 2.4: Radial part of the single-nucleon wave functions of Carbon and Oxygen nuclei, calculated with the Ske2 potential through the Hartree-Fock procedure.

Note that for neutrons $\sigma_l = \eta = 0$. Finally, applying the proper normalization, we obtain the radial wave functions by enforcing the following asymptotic behavior

$$\phi(|\vec{r}|)_{nlj} \xrightarrow{|\vec{r}| \gg |\vec{r}_A|} \sqrt{\frac{2M_N |\vec{p}_N|}{\pi}} \frac{\sin(|\vec{p}_N| |\vec{r}| - \eta \ln(2|\vec{p}_N| |\vec{r}|) - \pi l/2 + \delta_l + \sigma_l)}{|\vec{p}_N| |\vec{r}|}. \quad (2.2.13)$$

Once we employ a partial wave expansion for the emitted nucleon, we will obtain a distorted wave function in terms of the continuum eigenstates of the MF potential.

Impulse approximation

Within the impulse approximation picture, we treat the nuclear many-body current as a sum of one-body operators

$$\hat{j}(\vec{r})_V^{\text{had}} \simeq \hat{j}(\vec{r})_V^{\text{IA}} = \sum_{j=1}^A \hat{j}(\vec{r}_j)_V^{[1]} \delta^{(3)}(\vec{r} - \vec{r}_j). \quad (2.2.14)$$

We schematically present the one-body currents in Fig. 2.5a, while in Fig. 2.5b, we show a two-body correction to the IA not considered in this subsection. Appendix A summarizes the essential kinematical calculus concerning one-nucleon knock-out reactions in our framework. Therefore, here, we focus on the theoretical structure of Feynman diagrams and the non-relativistic prescriptions for nuclear currents.

We use the standard prescriptions for obtaining nuclear current operators in the coordinate space for electron-nucleus interactions. As shown in, e.g., Ref. [5], the operators involve the charge density

$$\hat{\rho}_V^{\text{IA}}(\vec{r}) = \sum_{j=1}^A G_D(Q^2) \delta^{(3)}(\vec{r} - \vec{r}_j) e(j) \quad (2.2.15)$$



Figure 2.5: Graphical representation of the diagrams involved in the one-nucleon knock-out process we investigate in this work.

and the current with convection and magnetization parts

$$\begin{aligned}
\hat{j}_V^{IA}(\vec{r}) &= \hat{j}_V^{\text{con}}(\vec{r}) + \hat{j}_V^{\text{mag}}(\vec{r}) \\
&= \sum_{j=1}^A \frac{G_D(Q^2)}{2M_N i} \left[\delta^{(3)}(\vec{r} - \vec{r}_j) \vec{\nabla} - \overleftarrow{\nabla} \delta^{(3)}(\vec{r} - \vec{r}_j) \right] e(j) \\
&\quad + \sum_{j=1}^A \frac{G_D(Q^2)}{2M_N} \left(\vec{\nabla} \times \sigma_j \right) \delta^{(3)}(\vec{r} - \vec{r}_j) \mu(j),
\end{aligned} \tag{2.2.16}$$

where we define

$$e(j) = \frac{1}{2}(1 + \tau_z(j)), \tag{2.2.17}$$

$$\mu(j) = 2.793 \frac{1}{2}(1 + \tau_z(j)) - 1.913 \frac{1}{2}(1 + \tau_z(j)), \tag{2.2.18}$$

and

$$\tau_z |p\rangle = +|p\rangle, \quad \tau_z |n\rangle = -|n\rangle. \tag{2.2.19}$$

Additionally, we introduced a dipole form factor $G_D(Q^2) = (1 + Q^2/M_V^2)^{-2}$, with $M_V = 843 \text{ MeV}/c^2$ to account for the realistic charge distribution. In our framework, the value of the electric coupling strength has been absorbed in the cross section prefactor. Note that all of the currents presented in this subsection are functions of Q^2 as they involve Q^2 -dependent form factors.

Provided appropriate involvement of Pauli, Dirac, and axial form factors, one can extend this formalism to CC neutrino reactions. Here, we employ the axial currents described in Ref. [37] and obtain

$$\hat{\rho}_V^{IA}(\vec{r}) = \sum_{j=1}^A F_1^Y(Q^2) \delta^{(3)}(\vec{r} - \vec{r}_j) \tau_{\pm}(j), \tag{2.2.20}$$

$$\begin{aligned}
\hat{j}_V^{IA}(\vec{r}) &= \hat{j}_V^{\text{con}}(\vec{r}) + \hat{j}_V^{\text{mag}}(\vec{r}) \\
&= \sum_{j=1}^A \frac{F_1^Y(Q^2)}{2M_N i} \left[\delta^{(3)}(\vec{r} - \vec{r}_j) \vec{\nabla} - \overleftarrow{\nabla} \delta^{(3)}(\vec{r} - \vec{r}_j) \right] \tau_{\pm}(j) \\
&\quad + \sum_{j=1}^A \frac{F_1^Y(Q^2) + F_2^Y(Q^2)}{2M_N} \left(\vec{\nabla} \times \sigma_j \right) \delta^{(3)}(\vec{r} - \vec{r}_j) \tau_{\pm}(j),
\end{aligned} \tag{2.2.21}$$

and

$$\hat{\rho}_A^{IA}(\vec{r}) = \sum_{j=1}^A \frac{G_A(Q^2)}{2M_N i} \sigma_j \cdot \left[\delta^{(3)}(\vec{r} - \vec{r}_j) \vec{\nabla} - \overleftarrow{\nabla} \delta^{(3)}(\vec{r} - \vec{r}_j) \right] \tau_{\pm}(j), \quad (2.2.22)$$

$$\hat{j}_A^{IA}(\vec{r}) = \sum_{j=1}^A G_A(Q^2) \sigma_j \delta^{(3)}(\vec{r} - \vec{r}_j) \tau_{\pm}(j). \quad (2.2.23)$$

The isospin rules are now

$$\tau_+ |n\rangle = +|p\rangle, \quad \tau_+ |p\rangle = 0, \quad (2.2.24)$$

$$\tau_- |p\rangle = -|n\rangle, \quad \tau_- |n\rangle = 0. \quad (2.2.25)$$

To obtain the equations above, we used the fact that the vector part of the weak currents has identical structure to the isovector part of the electromagnetic ones. Thus, we use the isovector form factors

$$F_i^V(Q^2) = F_{i,p}(Q^2) - F_{i,n}(Q^2), \quad (2.2.26)$$

which we define in terms of the Pauli ($F_{1,x}(Q^2)$) and Dirac ($F_{2,x}(Q^2)$) form factors given by

$$F_{1,x}(Q^2) = \frac{1}{1+\tau} (G_{E,x}(Q^2) + \tau G_{M,x}(Q^2)), \quad (2.2.27)$$

$$F_{2,x}(Q^2) = \frac{1}{1+\tau} (G_{E,x}(Q^2) - G_{M,x}(Q^2)), \quad (2.2.28)$$

where $\tau = Q^2/4M_N^2$. The electric and magnetic Sachs form factors $G_{E,x}(Q^2)$, $G_{M,x}(Q^2)$ for protons are given by

$$G_{E,p}(Q^2) = G_D(Q^2), \quad G_{M,p}(Q^2) = \lambda_p G_D(Q^2), \quad (2.2.29)$$

where $\lambda_p = 2.793$, and for neutrons by

$$G_{E,n}(Q^2) = \lambda_n G_D(Q^2), \quad G_{M,n}(Q^2) = -\frac{\tau}{1+5.6\tau} \lambda_n G_D(Q^2), \quad (2.2.30)$$

where $\lambda_n = -1.913$. Additionally, we substitute the dipole form factors $G_D(Q^2)$ in each of the form factors above with the BBBA05 parametrization [38], which is a fit to the world neutrino data. Finally, for the axial part, we use a dipole form factor

$$G_A(Q^2) = -\frac{1.262}{\left(1 + \frac{Q^2}{M_A^2}\right)} \quad (2.2.31)$$

with $M_A = 1.03 \text{ GeV}/c^2$.

In our framework, we need to evaluate multipole operators $\hat{C}_{JM}^{\text{Coul}}$ and \hat{O}_{JM}^{κ} for each of the densities and currents, respectively. This information is sufficient to construct the time-like and spherical components of the nuclear transition current, which we use to obtain electron- and neutrino-nucleus cross sections.

The strength of this model lies at lower energies, where careful calculation models the detailed aspects of a nuclear response. Therefore, we present hadronic responses evaluated in the IA, which we can compare to available inclusive electron scattering data. We calculate the responses

for fixed momentum transfer values $|\vec{q}| = 300, 400, 550$ MeV/c, which are distinct enough to grasp the differences in particular model components. We leave the intermediate steps of obtaining nuclear matrix elements and angular integrations for Appendix A and summarize the $1p1h$ reduced matrix elements in Appendix C. Fig. 2.6 presents the hadronic responses in inclusive electron scattering compared to experimental results. The basic version of our model compares reasonably well to the data, except for the overestimation in the longitudinal response for lower energies and slight underestimation for higher energies in the transverse channel. We need to address these issues using methodology beyond the IA.

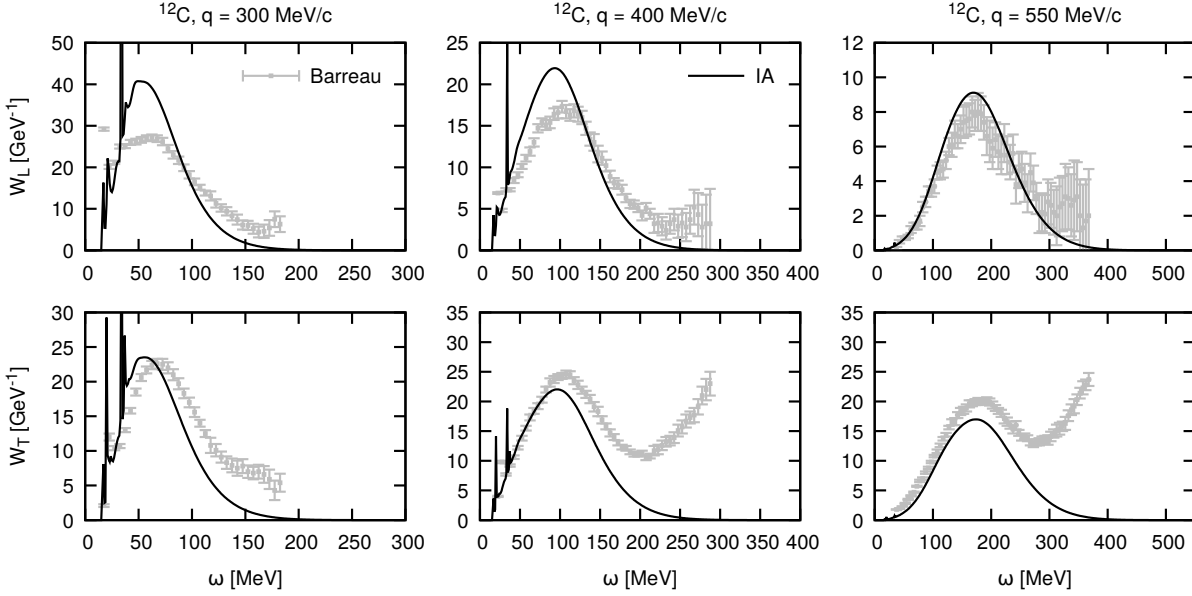


Figure 2.6: Inclusive hadronic responses for fixed momentum transfer values in electron scattering off the ^{12}C nucleus confronted with the experimental results of Ref. [39]. The black lines present the impulse approximation calculation.

Fig. 2.7 presents analogical results for the neutrino case. Here, we point out the separation between the vector and axial contributions, noting the axial terms' domination of the longitudinal current in \mathcal{W}_{LL} and partially \mathcal{W}_{CL} . Moreover, in the transverse responses, one can notice how the \mathcal{W}_T includes the vector and axial contributions, while the interference yields the $\mathcal{W}_{T'}$ response. Electron and neutrino distributions generally present similar features, with a visible increase in strength owing to low-lying continuum states below $\omega \simeq 50$ MeV.

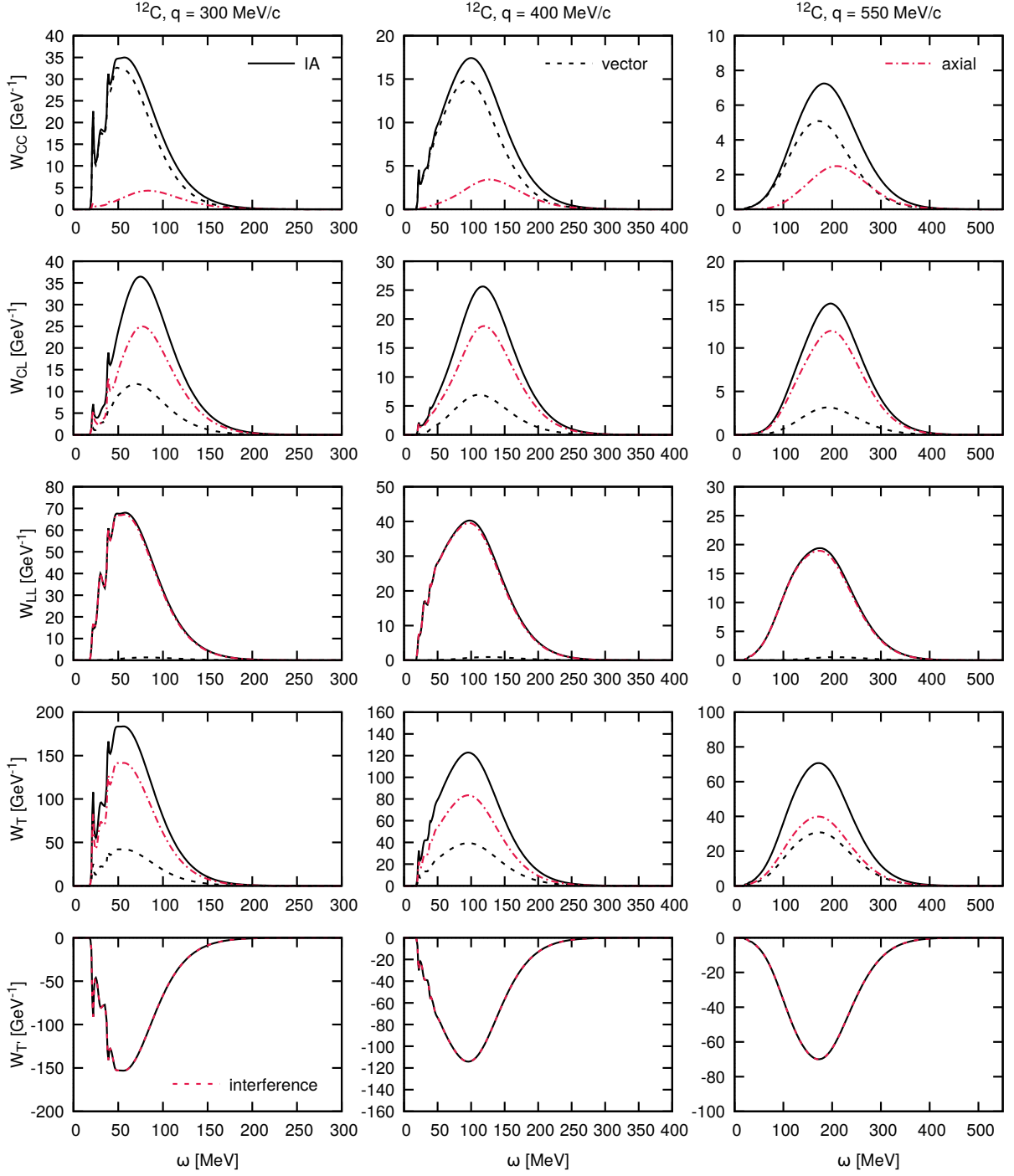


Figure 2.7: Inclusive hadronic responses for fixed momentum transfer values in neutrino scattering off the ^{12}C nucleus. The black, solid lines present the impulse approximation calculation, while the black dashed, red dot-dashed, and red dashed lines provide the separation into the vector and axial contributions, and the interference term, respectively.

Careful analysis of the axial current of Eq. (2.2.23) points out the lack of pseudoscalar coupling of the form [37]

$$\hat{\partial}_{A(\text{PS})}^{\text{IA}}(\vec{r}) = \sum_{i=1}^A G_A(Q^2) \nabla_i \frac{\sigma_i \cdot \nabla_i}{\nabla_i^2 - m_\pi^2} \delta^{(3)}(\vec{r} - \vec{r}_i) \tau_{\pm}(i). \quad (2.2.32)$$

This current contributes to the longitudinal current \mathcal{J}_3 and, therefore, to the \mathcal{W}_{CL} and \mathcal{W}_{LL} hadronic responses. Fig. 2.8 presents the responses together with the \mathcal{W}_L function, that combines \mathcal{W}_{CC} , \mathcal{W}_{CL} , and \mathcal{W}_{LL} proportionally to their relative contribution to the cross section. One can

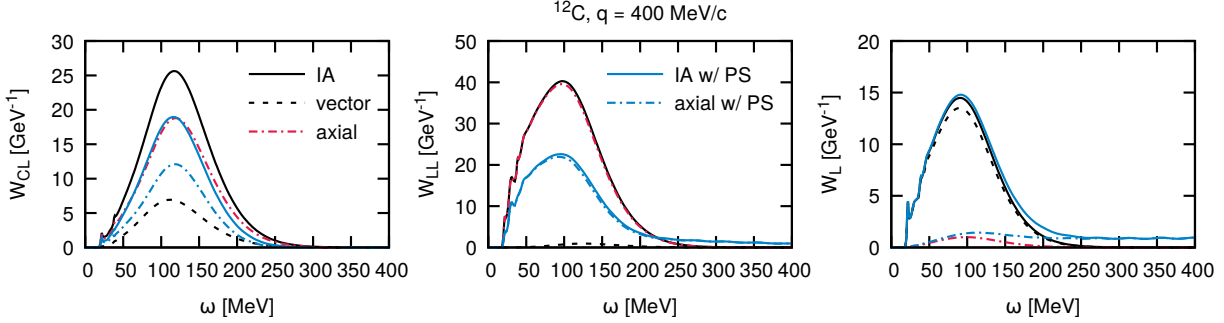


Figure 2.8: Inclusive hadronic responses for fixed momentum transfer $|\vec{q}| = 400$ MeV/c in neutrino scattering off the ^{12}C nucleus. The black, solid lines present the impulse approximation calculation, while the black dashed and red dot-dashed lines provide the separation into the vector and axial contributions, respectively. The blue lines present results that include the pseudoscalar coupling.

see that the form of the pseudoscalar current requires additional regularization for higher energy transfer values, but considering the kinematical conditions, its effect is negligible. Thus, we do not include this component in further calculations, significantly simplifying the modeling process.

Our model is non-relativistic, which leads to inevitable kinematical consequences. Trying to counterweight these effects, we modify the energy transfer in the following manner

$$\omega \rightarrow \omega \left(1 + \frac{\omega}{2M_N} \right), \quad (2.2.33)$$

restoring the relativistic energy-momentum relation. This correction constrains the high-energy behavior of the responses and brings the quasielastic peak to the proper relativistic position

$$\omega_{QE} = \frac{|\vec{q}|^2}{2M_N} \rightarrow \frac{Q^2}{2M_N}. \quad (2.2.34)$$

These necessary relativistic corrections allow us to provide meaningful cross section results at higher energies, as presented in Fig. 2.9, exemplifying the effect of shifting of the quasielastic peak and constraining the behavior for high ω and $\theta_{e'}$ values. In Fig. 2.10, we present the effect of using distorted nucleon waves in the calculation. Here, one can see that for both investigated nuclei, this method lowers down the cross section and, for forward scattering, shifts the peak to lower values of ω . Finally, we can perform a similar calculation for neutrino scattering in Fig. 2.11. Here, we investigate an additional effect of *charge change*, which corresponds to solving the outgoing nucleon wave functions after they change their isospin, e.g., from neutron to proton. However logical, this approach does not respect the unitarity between the initial and final hadronic systems. Thus, we refrain from using it in future calculations due to its negligible effect. These example results conclude the description of the fundamental methodology constituting our model.

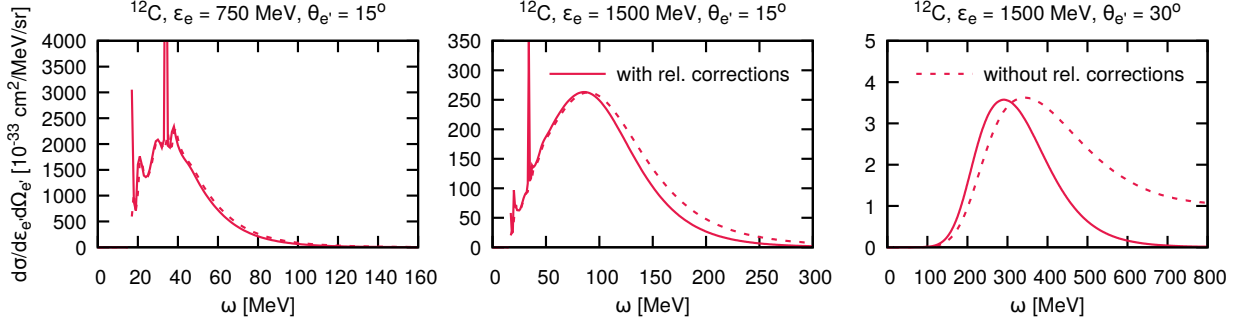


Figure 2.9: Inclusive cross sections for electron scattering off the ^{12}C nucleus for fixed outgoing electron angle $\theta_{e'}$ = 15° , 30° and the incoming neutrino energies ϵ_e = 750, 1500 MeV. The dashed and solid lines correspond to the calculations with and without relativistic corrections, respectively.

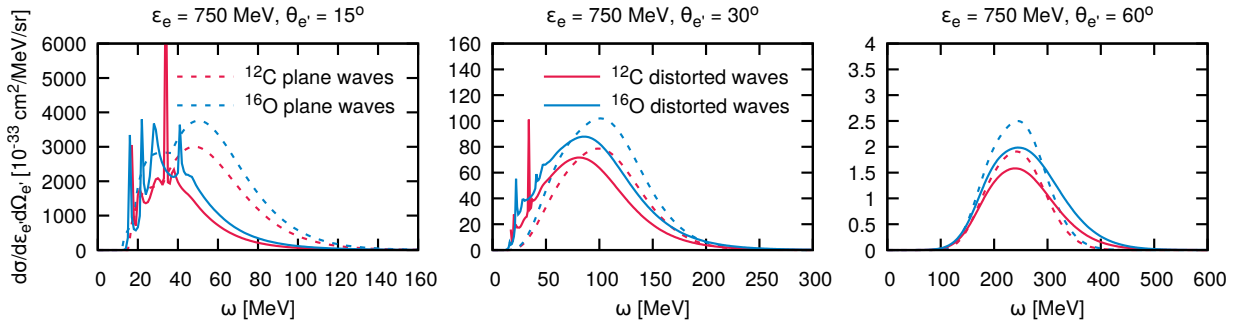


Figure 2.10: Inclusive cross sections for electron scattering off the ^{12}C (red lines) and ^{16}O (blue lines) nuclei for fixed outgoing electron angle $\theta_{e'}$ = 15° , 30° , 60° . The dashed and solid lines correspond to the plane and distorted wave calculations, respectively.

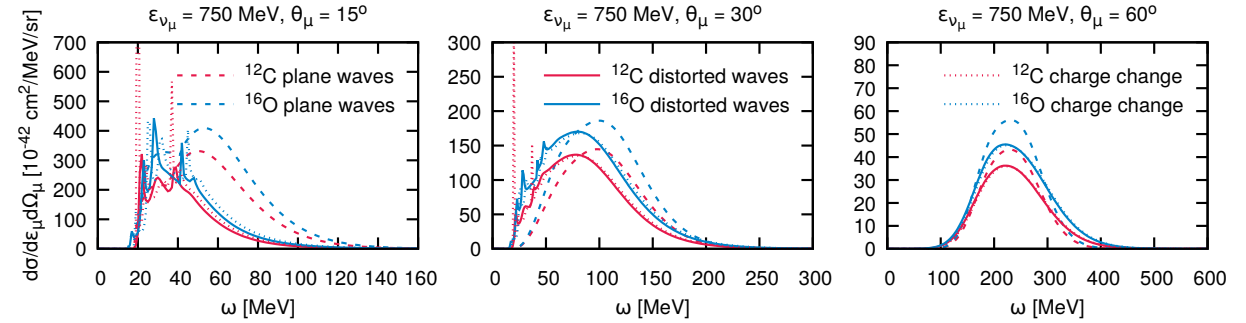


Figure 2.11: Inclusive cross sections for muon neutrino scattering off the ^{12}C (red lines) and ^{16}O (blue lines) nuclei for fixed outgoing muon angle θ_μ = 15° , 30° , 60° . The dashed and solid (dotted) lines correspond to the plane and distorted wave (charge change) calculations, respectively.

2.3 Short-range correlations

The force that binds nucleons within the nucleus is both repulsive at short distances and attractive at longer ones, compared to the size of nucleons and their typical mean-free paths. We have already employed this property to treat the nucleus as a group of nucleons moving independently

within a mean-field potential rather than a fully correlated many-body system. While such an IPM provides a straightforward explanation for the nuclear binding energies and other basic phenomena, it has limitations in its ability to account for local internucleon correlations. Long-range correlations, which cover the entire nucleus, can redistribute energy across all nuclear components, resulting in collective excitations like giant resonances. Short-range correlations, on the other hand, occur when two nucleons have strongly overlapping wave functions for short periods of time. Such behavior leads to significant deviations from the IPM properties. As a result, the nuclear wave function contains a high-momentum component, absent in single-particle wave functions, as well as reduced occupation probability of valence shells, known as spectroscopic strength [40]. This redistribution of strength, relative to the theoretical IPM results, constitutes a genuine part of the nuclear ground state.

To impose correlations on an independent-particle model, one can define a two-body density function

$$\rho^{[2]}(\vec{r}_1, \vec{r}_2) = \rho^{[1]}(\vec{r}_1)\rho^{[1]}(\vec{r}_2)g(\vec{r}_1, \vec{r}_2) \simeq \rho^{[1]}(\vec{r}_1)\rho^{[1]}(\vec{r}_2)g(|\vec{r}_{21}|), \quad (2.3.1)$$

where $\vec{r}_{21} = \vec{r}_2 - \vec{r}_1$ and $g(|\vec{r}_{21}|)$ is the correlation function. Such a formula provides the probability of finding particles at \vec{r}_1 and \vec{r}_2 in coincidence. In the default model, the two-body density is expressed as a product of two single-body densities, which are recovered by imposing $g(|\vec{r}_{21}|) = 1$. Fig. 2.12 presents first-principle numerical calculations of correlation functions in infinite nuclear

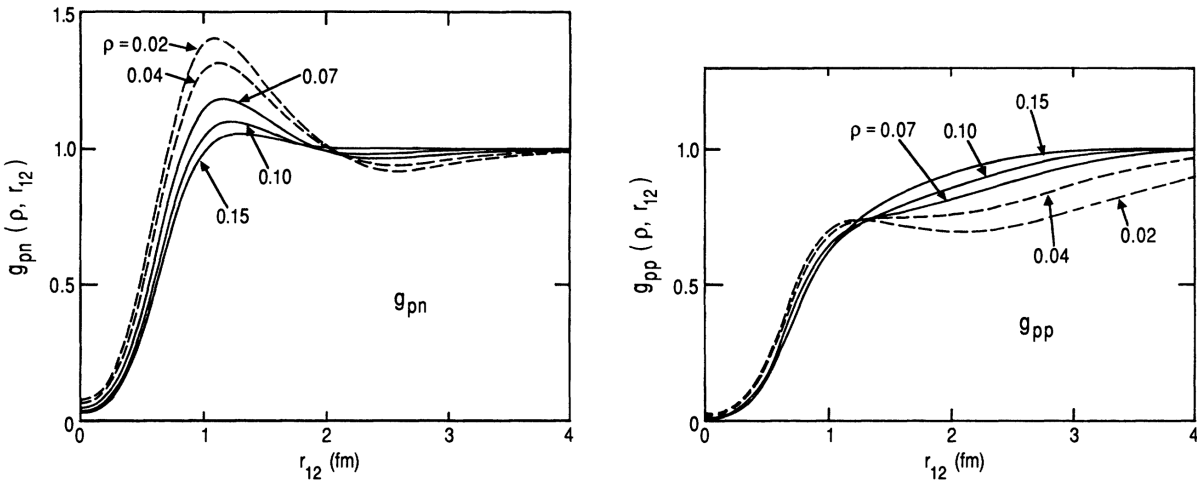


Figure 2.12: The pair distribution functions $g(|\vec{r}_{21}|)$ for (left) proton-neutron and (right) proton-proton pairs as a function of the local nuclear density. The results originate from variational Monte Carlo calculations in infinite nuclear matter, as presented in Ref. [41].

matter. For small internucleon distances, $g(|\vec{r}_{21}|)$ has a hard repulsive core representing the repulsive nature of the nuclear force at short distances. For larger $|\vec{r}_{21}|$, the function rises above one before approaching an asymptotic value of $g(|\vec{r}_{21}|) \rightarrow 1$, indicating that nucleons are not correlated beyond the range of the nuclear force. Since the range of correlations is generally limited to 2 fm, which is shorter than the radius of most nuclei, it is considered a universal nuclear property, supporting the approximation of Eq. (2.3.1).

Since the pioneering work on photoabsorption on SRC pairs by K. Gottfried in 1958 [42],

many research groups have investigated the influence of nucleon correlations on photo- and electro-induced cross sections [43–48]. Modern approaches invest efforts to obtain consistent models that also provide neutrino results. An example of similar philosophy in treating SRC corrections is the extended factorization formalism by N. Rocco *et al.* [49,50]. However, other works of M. Martini *et al.* [51] and J. Nieves *et al.* [52] also contain explicit SRC-like effects utilizing different pionic correlation currents. In sophisticated ab-initio calculations on ^{12}C [53,54], these effects are included inherently. The formalism we present in this work is an extension of the model by Ryckebusch *et al.*, which has been extensively compared to various inclusive [7], semi-inclusive [34,35], and exclusive [8,31] electron scattering data. This model was further developed to study the general nuclear properties of nuclei [55–57], but here, we continue the work of Refs. [4,11], which extended the calculations to the case of neutrino-nucleus scattering.

Formalism

While calculating nuclear transitions, independent particle models treat nuclear wave functions as Slater determinants $|\Phi\rangle$. We correct this picture by obtaining correlated wave functions $|\Psi\rangle$ after applying a many-body correlation operator $\hat{\mathcal{G}}$ as

$$|\Psi\rangle = \frac{1}{\sqrt{\mathcal{N}}}\hat{\mathcal{G}}|\Phi\rangle, \quad (2.3.2)$$

with the normalization constant $\mathcal{N} = \langle\Phi|\hat{\mathcal{G}}^\dagger\hat{\mathcal{G}}|\Phi\rangle$. Nucleon-nucleon potentials, which we intend to reflect in this procedure, are usually parametrized with several terms, with the central and tensor components dominating the short-range part. Thus, we approximate the correlation operator with

$$\hat{\mathcal{G}} \simeq \hat{\mathcal{S}} \left(\prod_{i<j}^A [1 + \hat{l}(i,j)] \right), \quad (2.3.3)$$

where $\hat{\mathcal{S}}$ is the symmetrization operator, and

$$\begin{aligned} \hat{l}(i,j) &= -\hat{g}(i,j) + \hat{s}(i,j) + \hat{t}(i,j) \\ &= -f_c(|\vec{r}_{ij}|) + f_{\sigma\tau}(|\vec{r}_{ij}|)(\sigma_i \cdot \sigma_j)(\tau_i \cdot \tau_j) + f_{t\tau}(|\vec{r}_{ij}|)\hat{S}_{ij}(\tau_i \cdot \tau_j), \end{aligned} \quad (2.3.4)$$

with the tensor operator

$$\hat{S}_{ij} = \frac{3}{|\vec{r}_{ij}|^2}(\sigma_i \cdot \vec{r}_{ij})(\sigma_j \cdot \vec{r}_{ij}) - (\sigma_i \cdot \sigma_j). \quad (2.3.5)$$

For the central correlations, our default choice is the calculation by C. Gearhart and W. Dickhoff [58]. It was derived using Green's function methods for nuclear matter with the Reid potential [59]. This function $f_c(|\vec{r}_{21}|)$, related to $g(|\vec{r}_{21}|)$ as

$$g(|\vec{r}_{21}|) = 1 - f_c(|\vec{r}_{21}|), \quad (2.3.6)$$

goes to zero for $|\vec{r}_{21}| > 2$ fm and has a hard core at short distances, ensuring nucleons repel each other when they get too close. The same function has been successfully employed to describe semi-inclusive [31] and exclusive [60,61] reactions. For the spin-isospin $f_{\sigma\tau}(|\vec{r}_{21}|)$ and tensor $f_{t\tau}(|\vec{r}_{21}|)$ functions, we use the results by S. Piper *et al.* [62]. These functions are significantly

weaker for smaller internucleon distances than the central function $f_c(|\vec{r}_{21}|)$. However, they extend to larger distances making them increasingly relevant. Ref. [55] provides arguments and evidence to support this choice of correlation functions. Fig. 2.13 summarizes our choice of these numerical inputs to the SRC calculations. To investigate the sensitivity of our model to the choice

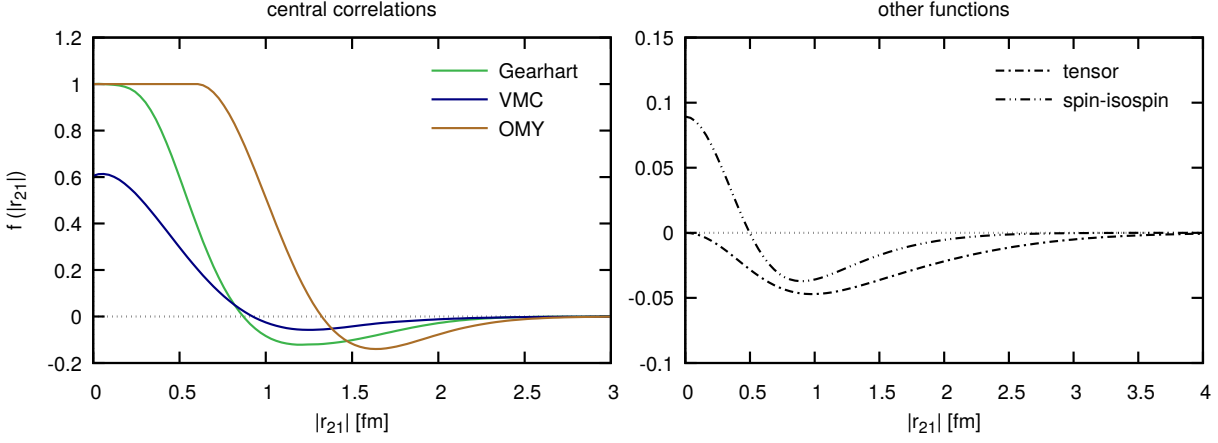


Figure 2.13: The correlation functions used in the presented calculations. (Left) central correlation functions $f_c(|\vec{r}_{21}|)$: C. Gearhart *et al.* [58], VMC [62], and OMY [63]. (Right) the spin-isospin $f_{\sigma\tau}(|\vec{r}_{21}|)$ and tensor $f_{t\tau}(|\vec{r}_{21}|)$ correlation functions of Ref. [62].

of the central correlation function, we investigate two additional solutions, denoted as VMC and OMY. The former is a result of a variational Monte Carlo calculation of Ref. [62] using the Argonne v_{14} nucleon-nucleon potential [64] and the Urbana VII three-nucleon interaction [65]. This result presents a significantly softer core, so we expect it to provide weaker SRC strength in our calculations. The latter function, OMY [63], resembles the Gearhart correlation function in shape but has an extended hard core. Although it should not be considered realistic, it is relevant in our investigations as it provides an upper limit for the effect of SRCs [8].

In our formalism, we write the matrix elements of a generic operator $\hat{\Omega}$ between correlated states as

$$\langle \Psi_f | \hat{\Omega} | \Psi_i \rangle = \frac{1}{\sqrt{\mathcal{N}_f \mathcal{N}_i}} \langle \Phi_f | \hat{\Omega}^{\text{eff}} | \Phi_i \rangle, \quad (2.3.7)$$

with the effective operator $\hat{\Omega}^{\text{eff}}$ incorporating the SRC influence as

$$\hat{\Omega}^{\text{eff}} = \hat{g}^\dagger \hat{\Omega} \hat{g} = \left(\prod_{i < j}^A [1 + \hat{l}(i, j)] \right)^\dagger \hat{s}^\dagger \hat{\Omega} \hat{s} \left(\prod_{k < l}^A [1 + \hat{l}(k, l)] \right). \quad (2.3.8)$$

This method shifts the complexity of calculations from the wave functions to the matrix element, thereby reducing the numerical cost of the formalism. This approach translates to the actual lepton-nucleus calculations through the hadronic current operator and the matrix elements of the form

$$\langle \Psi_f | \hat{j}_\nu^{\text{had}} | \Psi_i \rangle = \frac{1}{\sqrt{\mathcal{N}_f \mathcal{N}_i}} \langle \Phi_f | \hat{j}_\nu^{\text{eff}} | \Phi_i \rangle. \quad (2.3.9)$$

In the IA, we separate the current into a sum over single-particle interactions

$$\hat{j}_v^{\text{had}} \simeq \hat{j}_v^{\text{IA}} = \sum_{i=1}^A \hat{j}_v^{[1]}(i). \quad (2.3.10)$$

Including correlations in the IA framework would ideally involve a variety of operators ranging from one- to A-body. However, further approximations are necessary due to the complexity of such an approach. To simplify the process, we focus on the universal features of SRCs, which are primarily short-range and localized within the range of nucleon size. Hence, we limit the operator expansion to linear terms in the correlation functions and obtain

$$\hat{j}_v^{\text{eff}} \simeq \sum_{i=1}^A \hat{j}_v^{[1]}(i) + \sum_{i<j}^A \hat{j}_v^{[1],\text{SRC}}(i,j) + \left[\sum_{i<j}^A \hat{j}_v^{[1],\text{SRC}}(i,j) \right]^\dagger \quad (2.3.11)$$

with

$$\hat{j}_v^{[1],\text{SRC}}(i,j) = \left[\hat{j}_v^{[1]}(i) + \hat{j}_v^{[1]}(j) \right] \hat{i}(i,j). \quad (2.3.12)$$

In Fig. 2.14, we present the schematic representation of the SRC influence on the lepton-induced one- and two-nucleon knock-out processes, which we investigate in this work. We summarize

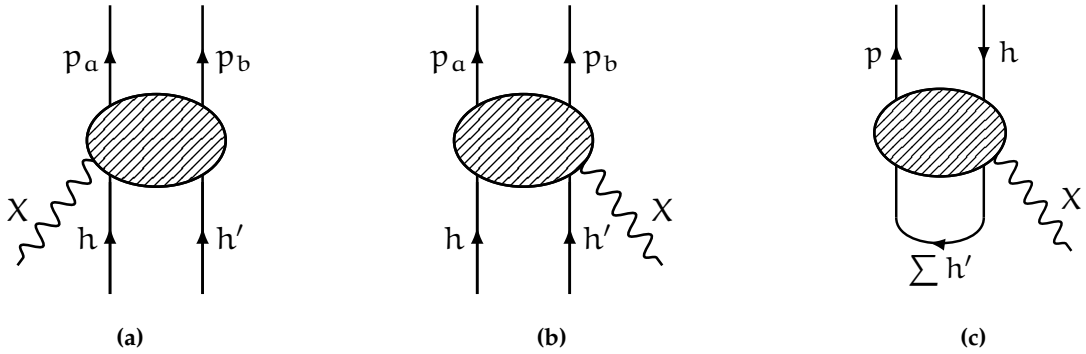


Figure 2.14: Graphical representation of the diagrams involved in the two-nucleon (a),(b) and one-nucleon (c) knock-out process induced with the short-range correlations dynamics.

the matrix elements and cross section formulas for the 1p1h and 2p2h cases in Appendix A and Appendix B, respectively. Then, we wrap the reduced matrix elements for vector and axial operators involving central, spin-isospin, and tensor correlations in Appendix C.

Inclusive electron scattering

While presenting the current status of the model, we focus on inclusive processes, where we have easy access to electron scattering data allowing us to constrain the general features of our calculations. We commence with Fig. 2.15, where we compare SRC-modified hadronic responses with the inclusive electron data of Ref. [39]. The effect of correlations brings us closer to data, especially in the longitudinal response, where the strength is more substantial. There, SRCs provides a reduction of 1p1h result similar to the expected effect of spectroscopic factors while dynamically pushing the signal to the 2p2h channel for higher energies. The latter phenomenon is

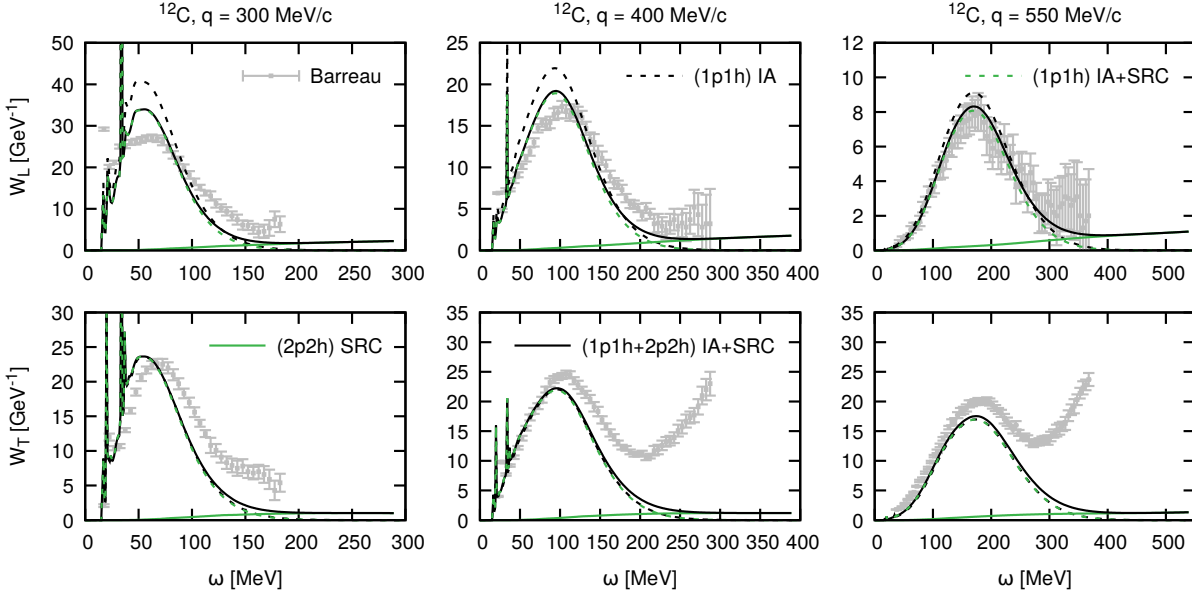


Figure 2.15: Inclusive hadronic responses for fixed momentum transfer values in electron scattering off the ^{12}C nucleus confronted with the experimental results of Ref. [39]. The black and green dashed lines present the 1p1h results with and without the short-range correlations corrections, respectively. The solid green line shows the 2p2h calculation, while the solid black line is the full calculation.

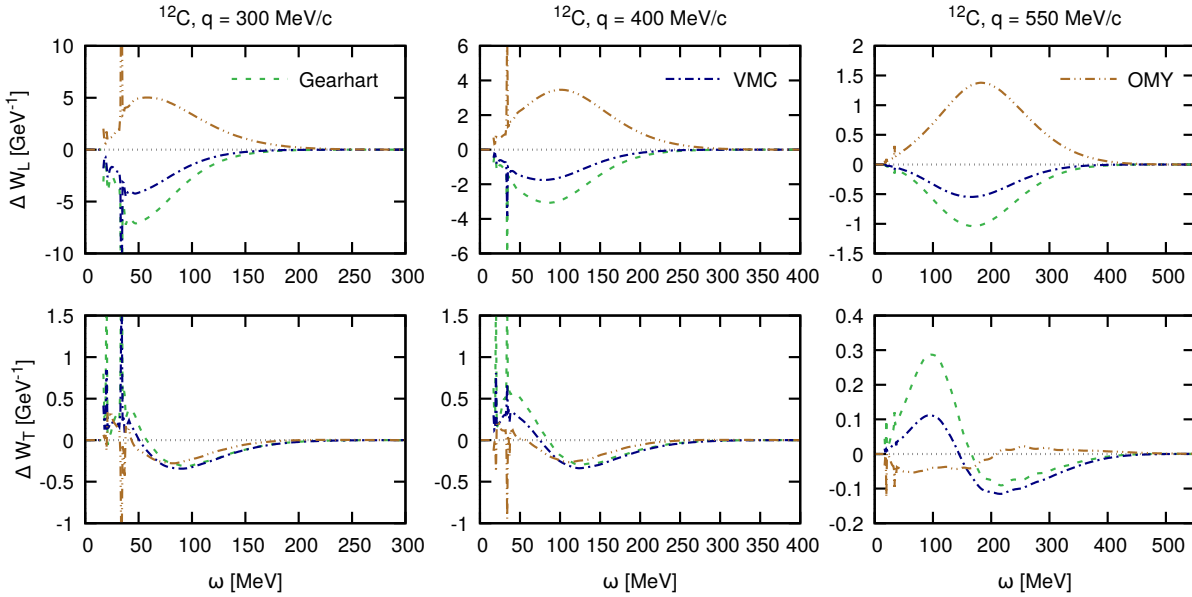


Figure 2.16: Corrections to the 1p1h hadronic responses for fixed momentum transfer values in electron scattering off the ^{12}C nucleus. Different curves correspond to the choice of the central correlation function, as described in the text.

common for both investigated responses. In Fig. 2.16, we focus on the 1p1h responses presenting the difference between the SRC calculation and the IA result. Here, we distinguish between the results obtained with different choices of central correlation functions. As expected, the VMC result is similar, yet weaker than the default Gearhart one, which reflects its softer core. The

OMY calculation has the highest magnitude but yields a different sign of correction than other solutions, contrary to our understanding of SRC effects. This discrepancy could also suggest an implementation issue, as the 1p1h corrections are sensitive to the minus sign in matrix elements. The 2p2h results presented in Fig. 2.17 genuinely exemplify the dominance of OMY responses over other correlation functions, which we consider rather unrealistic. Calculations using Gearhart and

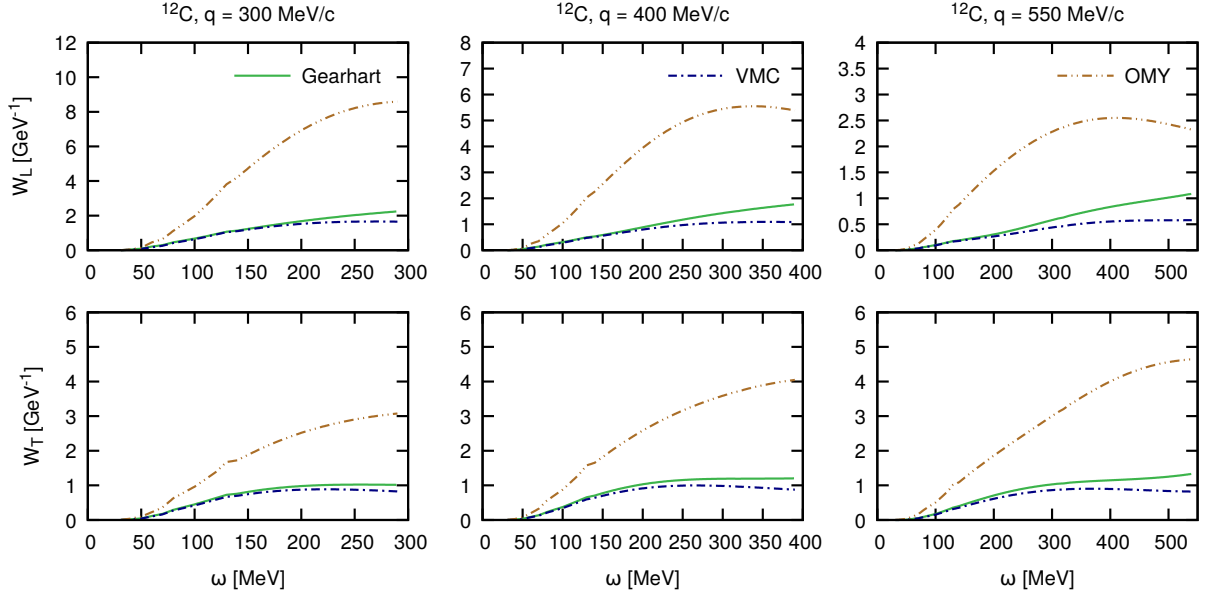


Figure 2.17: 2p2h hadronic responses for fixed momentum transfer values in electron scattering off the ^{12}C nucleus. Different curves correspond to the choice of the central correlation function, as described in the text.

VMC functions present very similar features, with the former providing more strength for higher energy transfers. This comparison shows reasonable control over this interaction dynamics.

The model for lepton-nucleus scattering can be meaningful once it produces accurate cross section results. For this purpose, we calculate electron scattering results for different kinematics, focusing on the region relevant to accelerator-based neutrino experiments. In Fig. 2.18, we present 1p1h and 2p2h cross sections for different fixed values of the angle of the outgoing electron. Note that kinematical conditions tend to emphasize similar phase-space regions for both interaction channels. Additionally, we show the contributions coming from the longitudinal and transverse parts. Here, we see an increasing effect of the former for higher angles that emphasize transverse kinematics. This is especially important for the long tail of the 2p2h distributions, dominating the bottom right panel. The low-energy fluctuations in these distributions come from the significant increase in strength once the final nucleons resonate with the energy eigenstates of continuum nuclear states. Regarding 2p2h interactions, the computational resources needed to calculate these specific points, which total cross section contribution is marginal, are beyond our current capabilities. Finally, we will investigate more general properties of SRC-corrected inclusive electron-nucleus cross sections, gathered in Fig. 2.19.

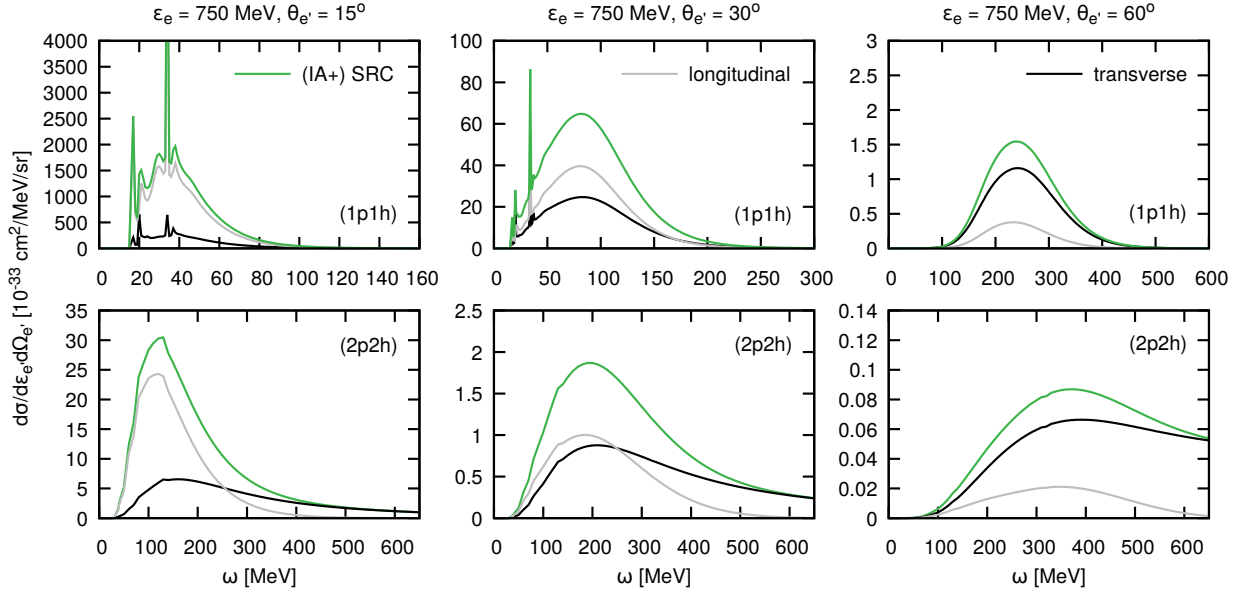


Figure 2.18: Inclusive cross sections for electron scattering off the ^{12}C nucleus for fixed outgoing electron angle $\theta_{e'} = 15^\circ, 30^\circ, 60^\circ$. The gray and black lines correspond to the longitudinal and transverse contributions, respectively. The green line shows the final calculation involving short-range correlations.

We find that proton-neutron pair emission dominates in this process for both ^{12}C and ^{16}O nuclei. In electron scattering, this channel corresponds to interactions on quasi-deuteron target nucleon pairs that are the leading component of the beyond-IPM nuclear picture. The A -dependence of these pairs is in agreement with the results of Refs. [4,66], where an asymptotic tendency of $A^{1.44}$ was observed. Additionally, the emission of proton-proton pairs has a A -dependence below the standard combinatoric pair fractions. The ratio between the SRC-induced emission of proton-neutron and proton-proton pairs varies between 4 to 6, changing with energy, depending on the dominance of the longitudinal or transverse contributions to particular kinematical conditions.

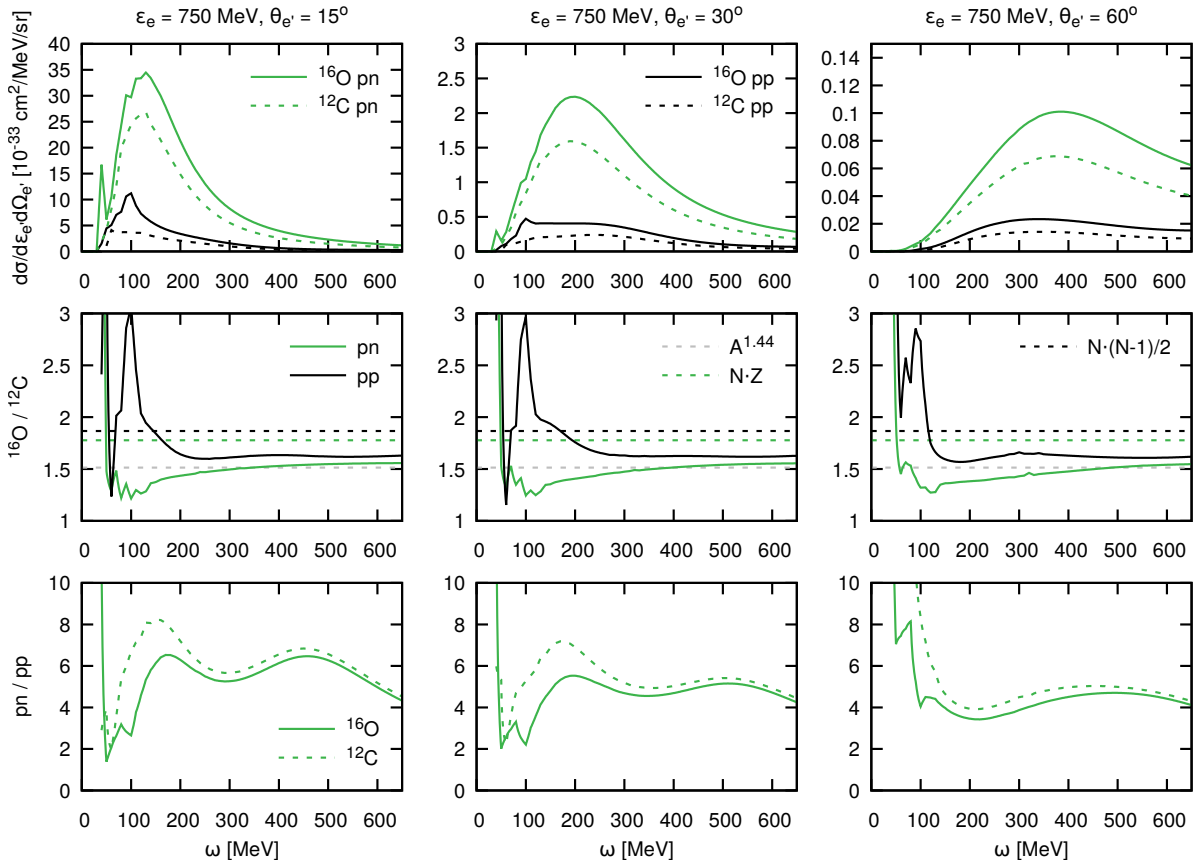


Figure 2.19: Contribution of the different outgoing nucleon pairs to the inclusive electron scattering cross sections induced by short-range correlations. (Top) the separation between proton-neutron and proton-proton final pairs presented with the green and black lines, respectively. Here, the solid lines show the scattering off ^{16}O , while the dashed lines show the scattering off the ^{12}C nucleus. (Middle) $^{16}\text{O}/^{12}\text{C}$ ratio of the inclusive cross sections for proton-neutron (green) and proton-proton (black) pairs. The dashed lines present different ratios of nuclear constituents. (Bottom) ratio of different outgoing nucleon pair contributions to the investigated cross sections, where the solid and dashed lines correspond to the ^{16}O and ^{12}C target nuclei, respectively.

Inclusive neutrino scattering

We present our results for neutrino-nucleus interactions for the same conditions as in the electron part to provide meaningful comparisons. Here, we gather all non-transverse neutrino responses into the longitudinal one, incorporating \mathcal{W}_{CL} and \mathcal{W}_{LL} in \mathcal{W}_L , according to their relative cross section influence. Fig. 2.20 presents the results of hadronic responses to neutrino probes for fixed momentum transfer values. The general features of the distributions are similar to the

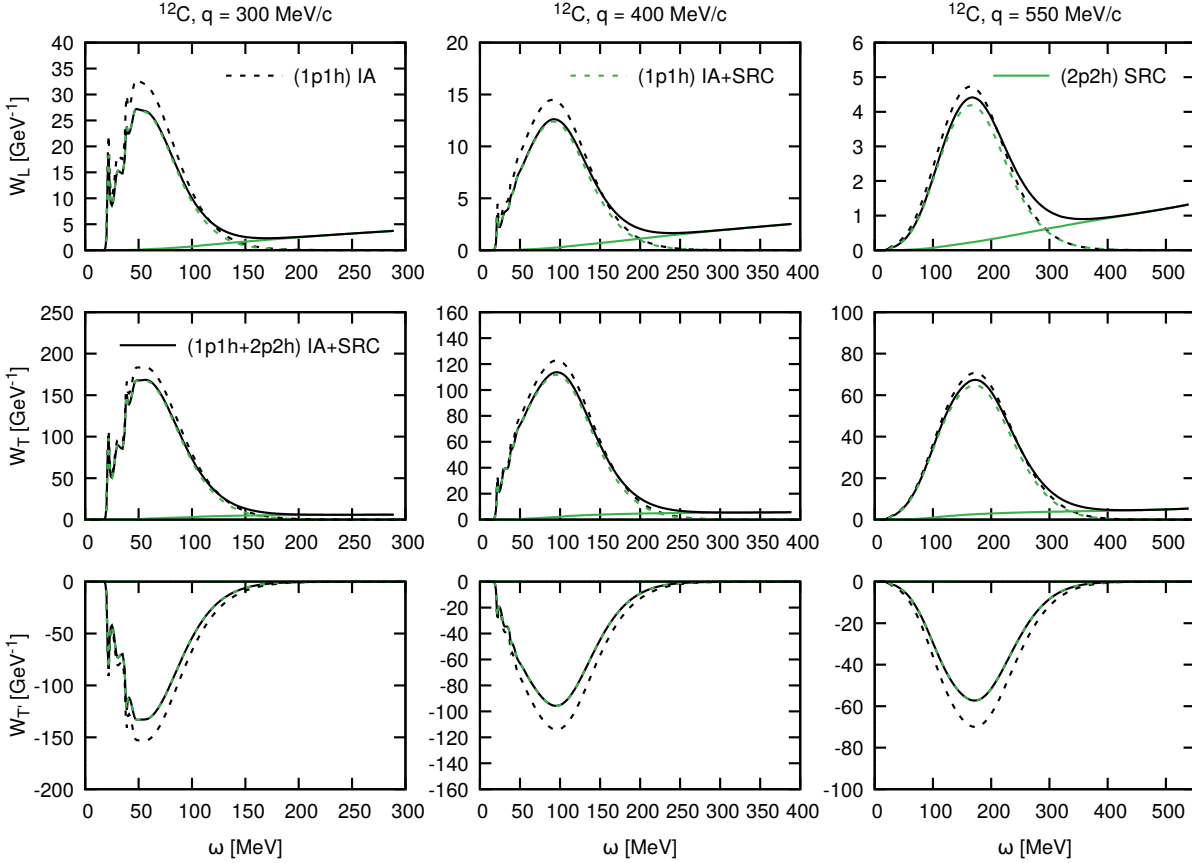


Figure 2.20: Inclusive hadronic responses for fixed momentum transfer values in neutrino scattering off the ^{12}C nucleus. The black and green dashed lines present the 1p1h results with and without the short-range correlations corrections, respectively. The solid green line shows the 2p2h calculation, while the solid black line is the full calculation.

electron ones, with a stronger 1p1h reduction in the transverse responses and an increased relative longitudinal importance of the 2p2h reaction. Two-nucleon final states do not contribute to the \mathcal{W}_T hadronic response. We present the corrections to the 1p1h responses in Fig. 2.21. Contrary to the electron case, here, the difference between the calculations using Gearhart and VMC central correlation functions are significant, both higher than the OMY result. Then, Fig. 2.22 presents the 2p2h contribution to the hadronic responses. Here, we see very similar properties to the electron case of Fig. 2.17, with the OMY calculation dominating the picture, providing unrealistic strength.

In Fig. 2.23, we demonstrate the capability of our model to produce neutrino-nucleus inclusive cross sections. In the neutrino case, the longitudinal-transversal separation is significantly more

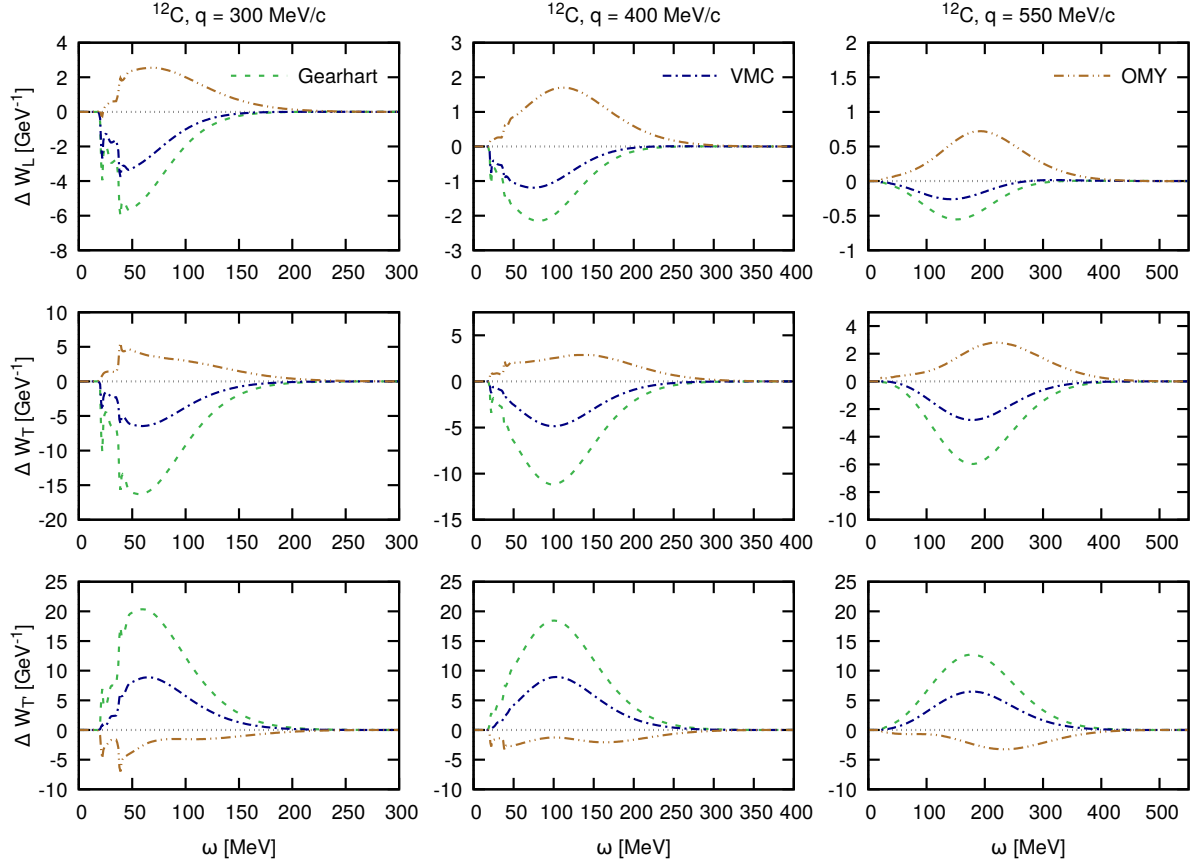


Figure 2.21: Corrections to the 1p1h hadronic responses for fixed momentum transfer values in neutrino scattering off the ^{12}C nucleus. Different curves correspond to the choice of the central correlation function, as described in the text.

dramatic, with the $\theta_\mu = 60^\circ$ results almost entirely provided by the transverse part. We attribute this effect to the influence of the axial current, which generally tends to be more transversal. Finally, we wish to investigate the general properties of SRC-induced two-nucleon knock-out, its A -dependence, and the effect of different isospins of target nucleon pairs. We summarize these properties in Fig. 2.24. In the neutrino case, the outgoing proton-proton and proton-neutron pairs correspond to the initial proton-neutron and neutron-neutron, respectively. As the core of nuclear response depends on the initial isospin configurations, we decided to provide different labeling, keeping the fixed color scheme relative to the initial nucleon pairs, as compared to Fig. 2.19. We see that these calculations yield the expected A -dependence of $A^{1.44}$ for the initial deuteron-like nucleon pairs. The other configuration, proton-neutron emission, scales according to the number of initial neutron-neutron pairs in each nucleus. The ratio of outgoing proton-proton to proton-neutron pairs varies between 3 and 4, with more minor fluctuations than in the electron case. We conclude that the transition from electron to neutrino interactions provides good numerical results.

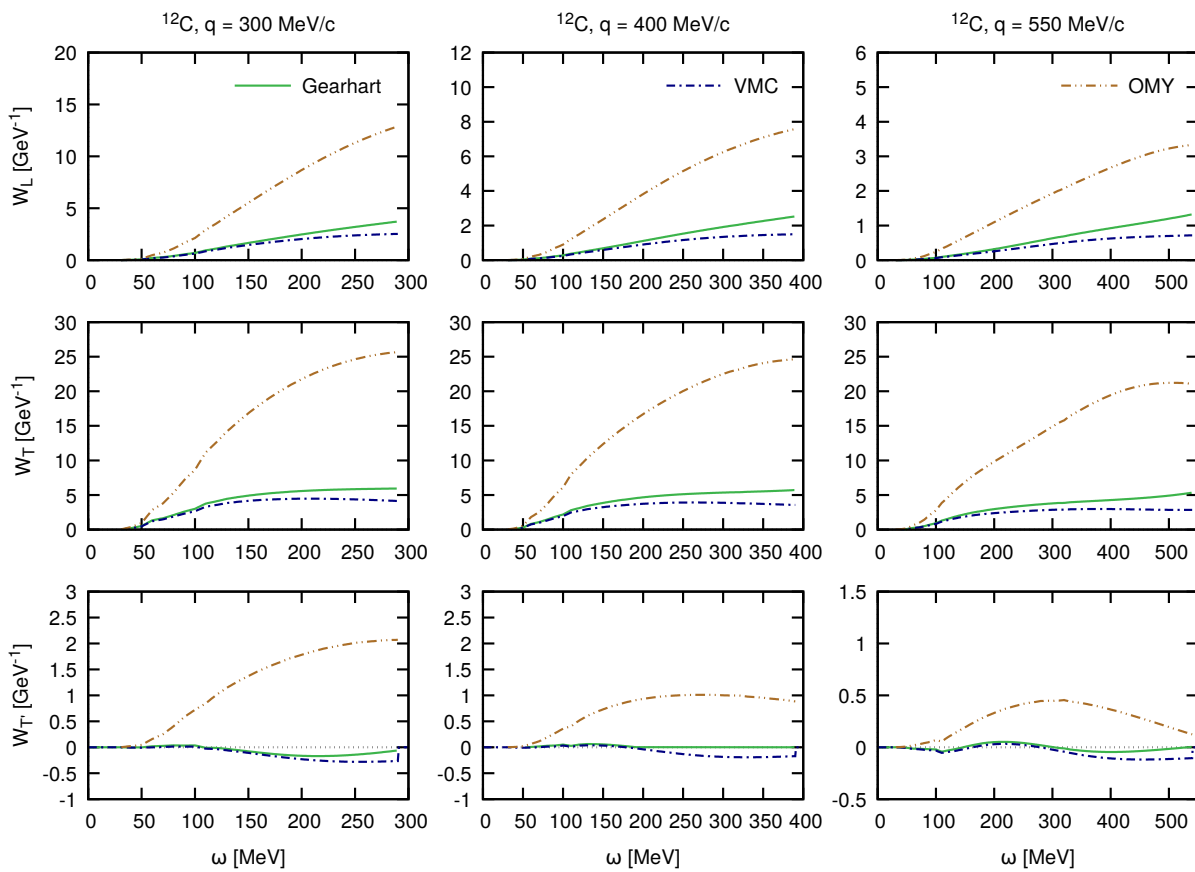


Figure 2.22: 2p2h hadronic responses for fixed momentum transfer values in neutrino scattering off the ^{12}C nucleus. Different curves correspond to the choice of the central correlation function, as described in the text.

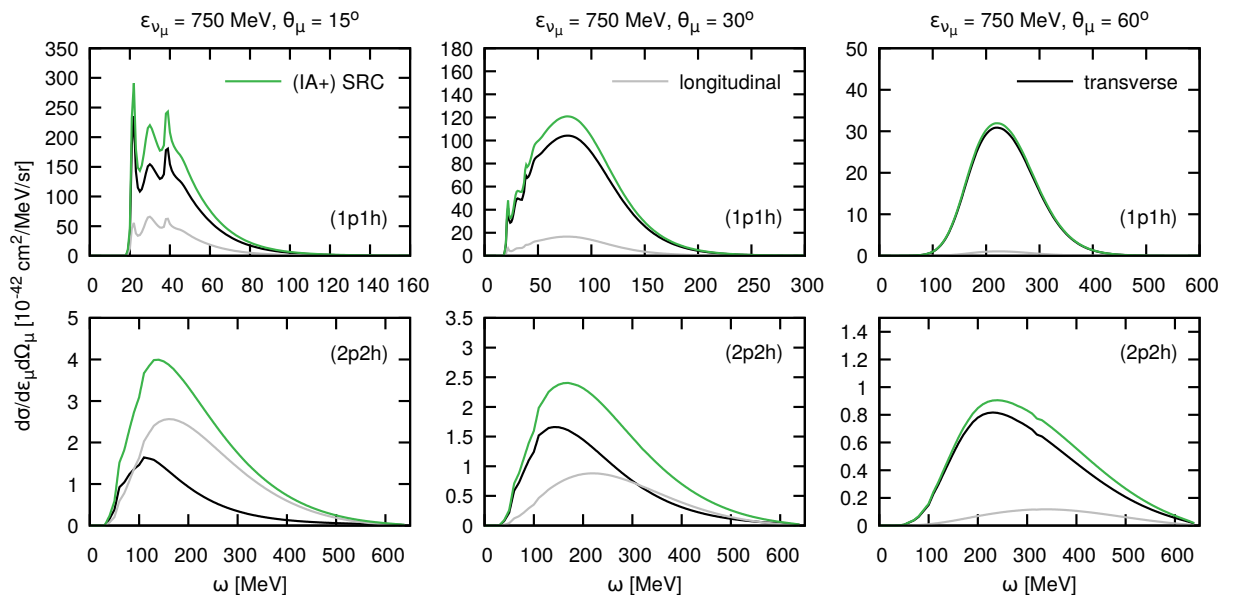


Figure 2.23: Inclusive cross sections for neutrino scattering off the ^{12}C nucleus for fixed outgoing muon angle $\theta_\mu = 15^\circ, 30^\circ, 60^\circ$. The gray and black lines correspond to the longitudinal and transverse contributions, respectively. The green line shows the final calculation involving short-range correlations.

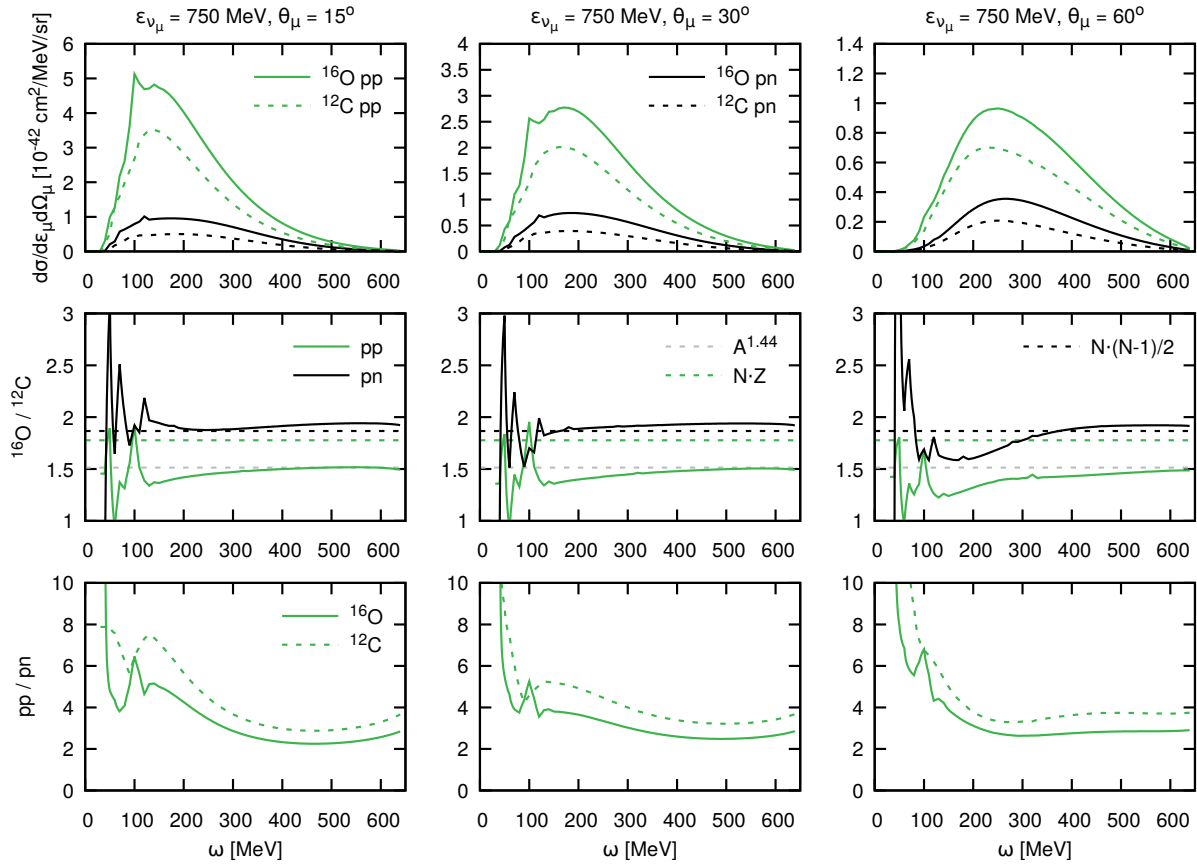


Figure 2.24: Contribution of the different outgoing nucleon pairs to the inclusive neutrino scattering cross sections induced by short-range correlations. (Top) the separation between proton-proton and proton-neutron final pairs presented with the green and black lines, respectively. Here, the solid lines show the scattering off ^{16}O , while the dashed lines show the scattering off the ^{12}C nucleus. (Middle) $^{16}\text{O}/^{12}\text{C}$ ratio of the inclusive cross sections for proton-proton (green) and proton-neutron (black) pairs. The dashed lines present different ratios of nuclear constituents. (Bottom) ratio of different outgoing nucleon pair contributions to the investigated cross sections, where the solid and dashed lines correspond to the ^{16}O and ^{12}C target nuclei, respectively.

2.4 Meson-exchange currents

The nuclear force, which holds the nucleus together, results from the strong force that binds quarks to form nucleons. The standard approach is to explain the nuclear force through exchanging virtual mesons, such as π , ρ , and ω [67]. When an electroweak boson interacts with a pair of nucleons, correlated through meson exchange, it can knock out one or both of the particles from the nucleus. This interaction is called a two-body current or MEC. We can construct several types of such currents by coupling the incoming boson to different mesons or vertices. In this work, we consider only the diagrams which include the lightest meson—pion ($m_\pi \simeq 135$ MeV). For the heavier mesons ($m_\rho \simeq 775$ MeV, $m_\omega \simeq 782$ MeV), the effective interaction has a much shorter range, and the short-range repulsion between the nucleons strongly dampens the expectation values of the associated operators. As explained in the previous section, we implement the short-range effects in an effective approach.

Before moving to the core of this work in Chapter 3, in this section, we investigate meson-exchange currents in which no nucleon resonance occurs. They are commonly known as the *seagull* and *pion-in-flight* currents. We construct the former by coupling the boson to a πNN vertex and the produced virtual pion to another nucleon leg. The latter involves coupling directly to a pion exchanged between two nucleons. Fig. 2.25 schematically presents the investigated MEC diagrams for lepton-induced one- and two-nucleon knock-out reactions. The diagrams we show

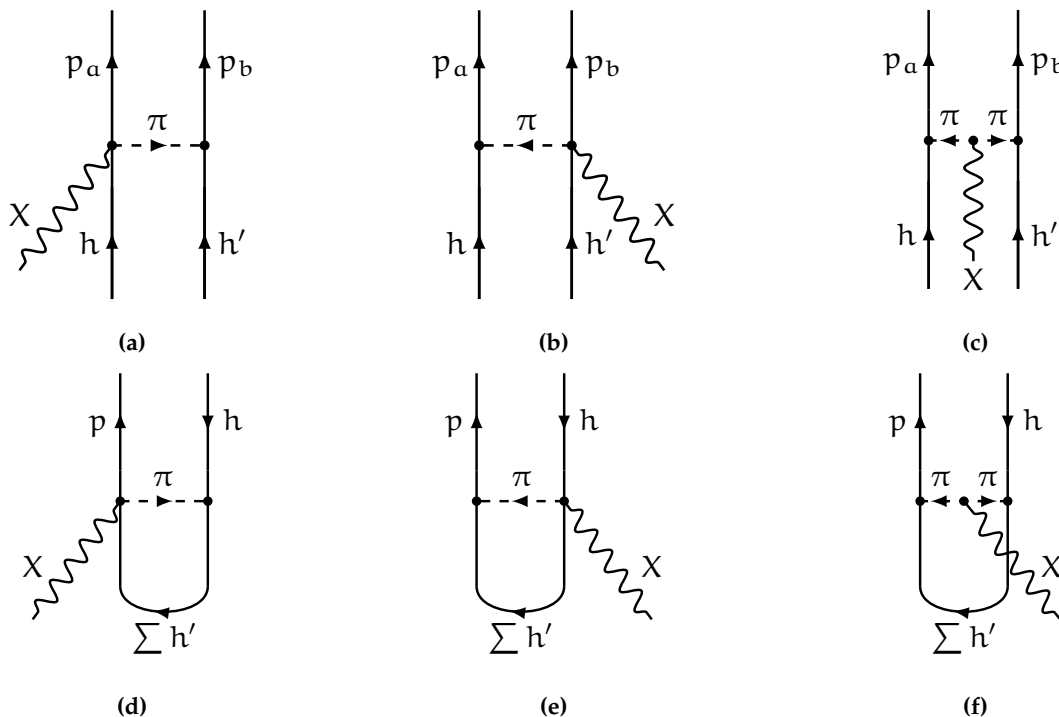


Figure 2.25: Graphical representation of the diagrams involved in the two-nucleon (top) and one-nucleon (bottom) knock-out process induced with the meson-exchange currents dynamics: (a), (b) 2p2h seagull, (c) 2p2h pion-in-flight, (d), (e) 1p1h seagull, and (f) 1p1h pion-in-flight currents.

in Fig. 2.26 are called *correlation currents*. As explained in Ref. [68], these are not genuine two-body currents but merely a product of a one-body current and a potential. Hence, while adding them

to Fermi-gas-based models can be justified, they should not be considered in mean-field-based approaches like ours.

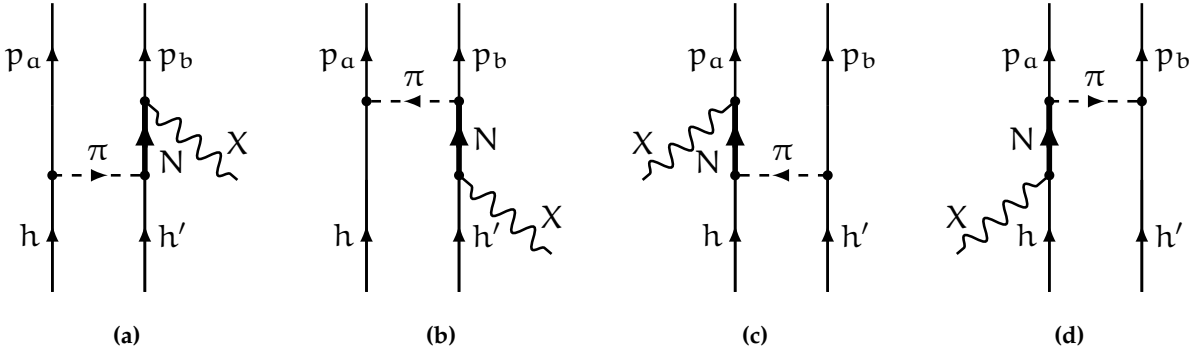


Figure 2.26: Graphical representation of the diagrams not included explicitly in the two-nucleon knock-out process.

The role of meson-exchange currents in electron- and neutrino-nucleus interactions has been studied in many theoretical approaches. Early works include research of Refs. [69–72]. Then, the effect of MECs in the transverse response for electron scattering was investigated by M. Dekker *et al.* [73], J. Amaro *et al.* [74,75], and A. De Pace *et al.* [76]. The development of models describing 2p2h neutrino reactions was motivated by the unexpected results of the MiniBooNE collaboration [77,78]. For these reactions, the models by M. Martini *et al.* [51] and J. Nieves *et al.* [52] include two-body currents, also mediated through Δ -resonances, to adequately describe inclusive neutrino cross sections. These currents also contribute to the calculations in the extended factorization approach by N. Rocco *et al.* [49,50] and are included in the *ab initio* formalism of Ref. [54]. Finally, current efforts involve extensions of the relativistic Fermi gas by I. Ruiz Simo *et al.* [79–81] and incorporating them into the SuSAv2 framework [82,83], as well as fully relativistic shell model calculations for the two-nucleon knock-out [84,85]. Recently, corrections to the electromagnetic one-nucleon knock-out responses were calculated by R. González-Jiménez *et al.* [86]. We base our presented model on calculations of Refs. [6–8] and their extension to neutrino interactions [4,10].

Vector currents

We consider single-pion exchange diagrams to describe the seagull and pion-in-flight meson-exchange currents, as depicted in Fig. 2.25. We use the pseudovector πNN coupling [67] in the low-energy limit

$$\mathcal{L}_{\pi NN} = i \frac{f_{\pi NN}}{m_\pi} (\boldsymbol{\sigma} \cdot \vec{q})(\boldsymbol{\tau} \cdot \vec{\pi}), \quad (2.4.1)$$

where the coupling constant is set via $f_{\pi NN}^2/4\pi = 0.08$, and m_π is the mass of the pion. For electron scattering interactions, the purely space-like vector currents are expressed as equations [8]

$$\hat{J}_V^{[2],\text{sea}}(\vec{q}) = -i \left(\frac{f_{\pi NN}}{m_\pi} \right)^2 (\mathcal{J}_V)_z \left(\frac{\sigma_1(\sigma_2 \cdot \vec{q}_2)}{|\vec{q}_2|^2 + m_\pi^2} - \frac{\sigma_2(\sigma_1 \cdot \vec{q}_1)}{|\vec{q}_1|^2 + m_\pi^2} \right) \quad (2.4.2)$$

and

$$\hat{J}_V^{[2],\text{pif}}(\vec{q}) = i \left(\frac{f_{\pi\text{NN}}}{m_\pi} \right)^2 (\mathcal{J}_V)_z \frac{(\sigma_1 \cdot \vec{q}_1)(\sigma_2 \cdot \vec{q}_2)}{(|\vec{q}_1|^2 + m_\pi^2)(|\vec{q}_2|^2 + m_\pi^2)} (\vec{q}_1 - \vec{q}_2), \quad (2.4.3)$$

where the momenta $\vec{q}_1 + \vec{q}_2 = \vec{q}$ are defined as

$$\vec{q}_1 = \vec{p}_a - \vec{h}, \quad \vec{q}_2 = \vec{p}_b - \vec{h}', \quad (2.4.4)$$

and \mathcal{J}_V is the two-body isovector operator

$$\mathcal{J}_V = (\vec{\tau}_1 \times \vec{\tau}_2). \quad (2.4.5)$$

The combined seagull and pion-in-flight currents of Eq. (2.4.2) and Eq. (2.4.3) satisfy the continuity equation with the one-pion-exchange potential [87]

$$V_\pi(\vec{q}) = - \left(\frac{f_{\pi\text{NN}}}{m_\pi} \right)^2 \frac{(\sigma_1 \cdot \vec{q})(\sigma_2 \cdot \vec{q})}{m_\pi^2 + |\vec{q}|^2} (\tau_1 \cdot \tau_2). \quad (2.4.6)$$

To obtain the prescriptions for CC neutrino interactions, we follow the conservation of vector current and perform a rotation in a isospin space [88]. Thus, we replace the third component of the \mathcal{J}_V operator by

$$(\mathcal{J}_V)_z \rightarrow (\mathcal{J}_V)_\pm = ((\mathcal{J}_V)_x \pm i(\mathcal{J}_V)_y). \quad (2.4.7)$$

We implicitly assume that the total meson-exchange current is a sum over all target nucleon pairs

$$\hat{J}_V^{[2],\text{MEC}}(\vec{q}) = \sum_{i < j}^A \hat{J}_V^{[2],\text{MEC}}(\vec{q}, \vec{q}_i, \vec{q}_j). \quad (2.4.8)$$

In order to consider the inner structure of hadrons in our currents, it is necessary to introduce form factors. A standard regularization procedure at the πNN vertex involves a monopole form factor

$$\Gamma_\pi(|\vec{q}|^2) = \frac{\Lambda_\pi^2 - m_\pi^2}{|\vec{q}|^2 + \Lambda_\pi^2}, \quad (2.4.9)$$

with a cutoff mass $\Lambda_\pi = 1250$ MeV. One can interpret this choice as if the nucleon emitted a *heavy pion* of mass Λ_π , which is then converted into a pion [89]. Thus, we write the seagull current as

$$\hat{J}_V^{[2],\text{sea}}(\vec{q}) = -i \left(\frac{f_{\pi\text{NN}}}{m_\pi} \right)^2 (\mathcal{J}_V)_z F_1^Y(Q^2) \left(\Gamma_\pi^2(|\vec{q}_2|^2) \frac{\sigma_1(\sigma_2 \cdot \vec{q}_2)}{|\vec{q}_2|^2 + m_\pi^2} - \Gamma_\pi^2(|\vec{q}_1|^2) \frac{\sigma_2(\sigma_1 \cdot \vec{q}_1)}{|\vec{q}_1|^2 + m_\pi^2} \right) \quad (2.4.10)$$

with each pion vertex multiplied by Γ_π , ensuring CVC. For the pion-in-flight diagram, we obtain

$$\hat{J}_V^{[2],\text{pif}}(\vec{q}) = i \left(\frac{f_{\pi\text{NN}}}{m_\pi} \right)^2 (\mathcal{J}_V)_z F_1^Y(Q^2) \Gamma_\pi(|\vec{q}_1|^2) \Gamma_\pi(|\vec{q}_2|^2) \frac{(\sigma_1 \cdot \vec{q}_1)(\sigma_2 \cdot \vec{q}_2)}{(|\vec{q}_1|^2 + m_\pi^2)(|\vec{q}_2|^2 + m_\pi^2)} (\vec{q}_1 - \vec{q}_2). \quad (2.4.11)$$

In both currents, we have also regularized the $\chi\pi\text{NN}$ and $\chi\pi\pi$ vertices, relying on the vector meson dominance model [68]. As discussed in Ref. [4], these couplings could be multiplied by two distinct form factors: $F_{\text{sea}}(Q^2)$ and $F_{\text{pif}}(Q^2)$, respectively. However, as argued in Ref. [89], these form factors should be equal, and in this case, the vertices should contain the isovector nucleon form factor $F_1^Y(Q^2)$.

Axial currents

Out of the meson-exchange currents discussed in the previous subsection, only the seagull current has an axial counterpart. Contrary to the vector current, in the low-energy limit, the axial seagull current is purely time-like [4] and reads

$$\hat{\rho}_A^{[2],\text{sea}}(\vec{q}) = \frac{i}{g_A} \left(\frac{f_{\pi\text{NN}}}{m_\pi} \right)^2 (J_V)_\pm \left(\frac{\sigma_2 \cdot \vec{q}_2}{|\vec{q}_2|^2 + m_\pi^2} - \frac{\sigma_1 \cdot \vec{q}_1}{|\vec{q}_1|^2 + m_\pi^2} \right), \quad (2.4.12)$$

where $g_A = 1.26$ is the axial coupling constant. To account for the inner structure of hadrons, we regularize the πNN vertices using the same monopole form factors as in the vector seagull current case. However, constraining the currents at the electroweak vertices is more challenging as it relies on the partially-conserved axial current hypothesis. This procedure is not unambiguous in the low energy limit and requires additional assumptions. Our model considers three solutions described in Ref. [4] in detail, which read

$$\hat{\rho}_A^{[2],\text{sea1}}(\vec{q}) = i \left(\frac{f_{\pi\text{NN}}}{m_\pi} \right)^2 (J_V)_\pm G_A(Q^2) \left(\Gamma^2(|\vec{q}_2|^2) \frac{\sigma_2 \cdot \vec{q}_2}{|\vec{q}_2|^2 + m_\pi^2} - \Gamma_\pi^2(|\vec{q}_1|^2) \frac{\sigma_1 \cdot \vec{q}_1}{|\vec{q}_1|^2 + m_\pi^2} \right), \quad (2.4.13)$$

$$\begin{aligned} \hat{\rho}_A^{[2],\text{sea2}}(\vec{q}) = \frac{i}{g_A} \left(\frac{f_{\pi\text{NN}}}{m_\pi} \right)^2 (J_V)_\pm & \left(F_\pi(|\vec{q}_1|^2) \Gamma^2(|\vec{q}_2|^2) \frac{\sigma_2 \cdot \vec{q}_2}{|\vec{q}_2|^2 + m_\pi^2} \right. \\ & \left. - F_\pi(|\vec{q}_2|^2) \Gamma_\pi^2(|\vec{q}_1|^2) \frac{\sigma_1 \cdot \vec{q}_1}{|\vec{q}_1|^2 + m_\pi^2} \right), \end{aligned} \quad (2.4.14)$$

and

$$\begin{aligned} \hat{\rho}_A^{[2],\text{axi}}(\vec{q}) = \frac{i}{g_A} \left(\frac{f_{\pi\text{NN}}}{m_\pi} \right)^2 (J_V)_\pm & \left(F_\pi(|\vec{q}_2|^2) \Gamma^2(|\vec{q}_2|^2) \frac{\sigma_2 \cdot \vec{q}_2}{|\vec{q}_2|^2 + m_\pi^2} \right. \\ & \left. - F_\pi(|\vec{q}_1|^2) \Gamma_\pi^2(|\vec{q}_1|^2) \frac{\sigma_1 \cdot \vec{q}_1}{|\vec{q}_1|^2 + m_\pi^2} \right). \end{aligned} \quad (2.4.15)$$

In these formulations, to comply with PCAC, we have introduced an additional pion form factor

$$F_\pi(|\vec{q}|^2) = \frac{m_\rho^2}{|\vec{q}|^2 + m_\rho^2}. \quad (2.4.16)$$

The first current, Eq. (2.4.13), denoted as *sea1*, corresponds to the straightforward axial version of Eq. (2.4.10) by adjusting the coupling and introducing the axial form factor $G_A(Q^2)$ in its standard dipole parametrization. This expression, derived using the soft-pion approximation [90], has been used in neutrino-deuteron studies of Ref. [88]. Note that it does not rely on the PCAC hypothesis in its construction. The second current, Eq. (2.4.15), denoted as *sea2*, is a non-relativistic reduction of the current used in calculations by I. Ruiz Simo *et al.* [80]. To understand this formulation, we refer to the form factor of Eq. (2.4.16), which follows the ρ -meson dominance of the $\pi\pi\text{NN}$ vertex and was introduced to preserve the one-body version of PCAC. We use the same form factor to regularize the axial $W\pi\text{NN}$ vertex. Finally, we constrain the πNN vertices in the same way as for the previous currents. Using this brings us very close to the prescriptions of Ref. [80], as our vector currents, up to the usage of the $\Gamma_\pi(\vec{q})$ form factor, correspond to the non-relativistic limits of the currents used therein.

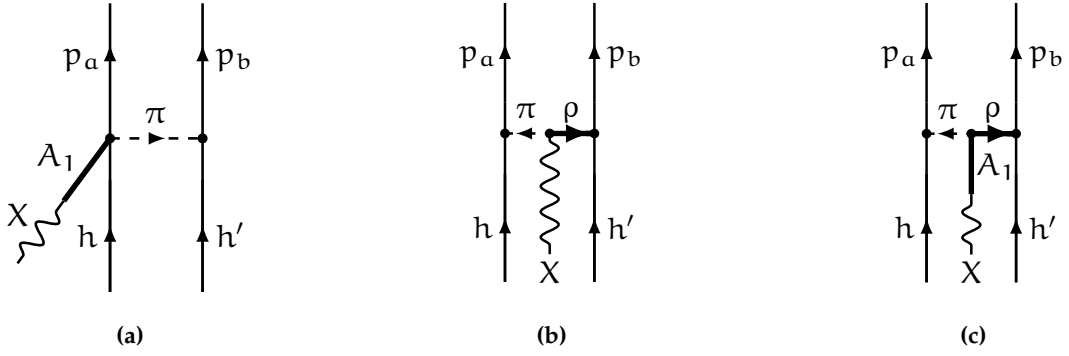


Figure 2.27: Diagrams included in the axial density $\rho_A^{[2],axi}$, derived in Ref. [90].

The axial current, denoted as *axi* was introduced in Ref. [90] and comprises three diagrams shown in Fig. 2.27. The first diagram is an axial version of the seagull current, including an exchange term. The other two diagrams have a structure similar to a pion-in-flight current but with one of the pions replaced by a ρ -meson. The coupling of the W -boson at the $\pi\rho$ vertex in these diagrams is either a contact coupling or an A_1 -pole. The two diagrams with a $\pi - \rho$ exchange have no vector equivalent, and their range can be considered similar to that of the vector diagrams since one of the mesons is a pion. The combination of these three currents satisfies the two-nucleon version of the PCAC relation when we take their divergence. Finally, we multiply the πNN vertices in the current by the appropriate $\Gamma_\pi(\vec{q})$ form factors to account for the finite structure of the hadrons. This current has the same operator structure as the two axial seagull currents, but because it includes more diagrams, we contend that it is the optimal choice for our model.

To study the contribution of meson-exchange currents to the lepton-induced one- and two-nucleon knock-out reactions, we will use the vector seagull and pion-in-flight currents, and the axial density *axi*. In Appendix A and Appendix B, we summarize the matrix elements and cross section formulas for the 1p1h and 2p2h cases. Then, we wrap the reduced matrix elements for vector and axial operators in Appendix C.

Inclusive electron scattering

Comparing to electron scattering data has to be an essential cross-check for any viable neutrino-nucleus scattering model. Here, we will use the Rosenbluth decomposition of Ref. [39], which allows us to access the longitudinal and transverse inclusive strength for different fixed values of $|\vec{q}|$. In Fig. 2.28, we present the 1p1h and 2p2h hadronic responses of ^{12}C calculated using the meson-exchange currents mentioned earlier. The impact of these corrections on inclusive responses is tiny. Thus, to learn more, we present the separated 1p1h and 2p2h results in Fig. 2.29 and Fig. 2.30, respectively. In the former, which shows the corrections relative to the bare IA result, the seagull and pion-in-flight contributions enter with a different sign. Therefore, to a large extent, their influence cancels, reducing the responses for the lowest energies and increasing their strength in the higher energy regions. The negative relative sign in the seagull and pion-in-flight currents is also visible in the 2p2h responses, where they experience a substantial destructive interference.

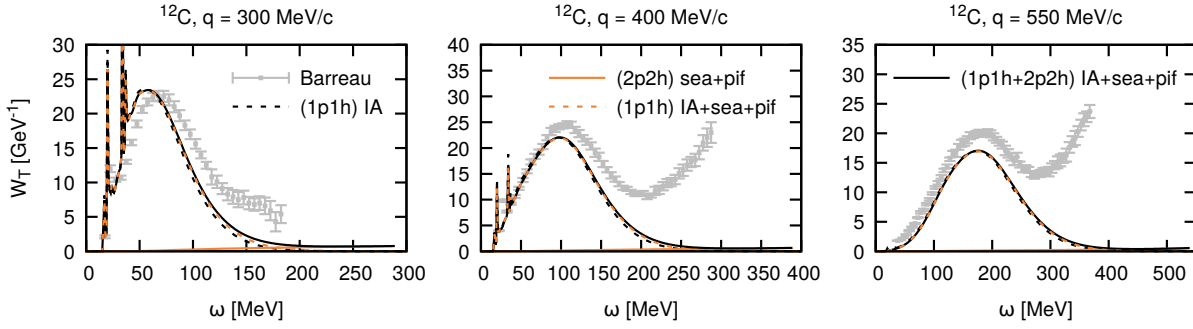


Figure 2.28: Inclusive hadronic responses for fixed momentum transfer values in electron scattering off the ^{12}C nucleus confronted with the experimental results of Ref. [39]. The black and orange dashed lines present the 1p1h results with and without the meson-exchange currents corrections, respectively. The solid orange line shows the 2p2h calculation, while the solid black line is the full calculation.

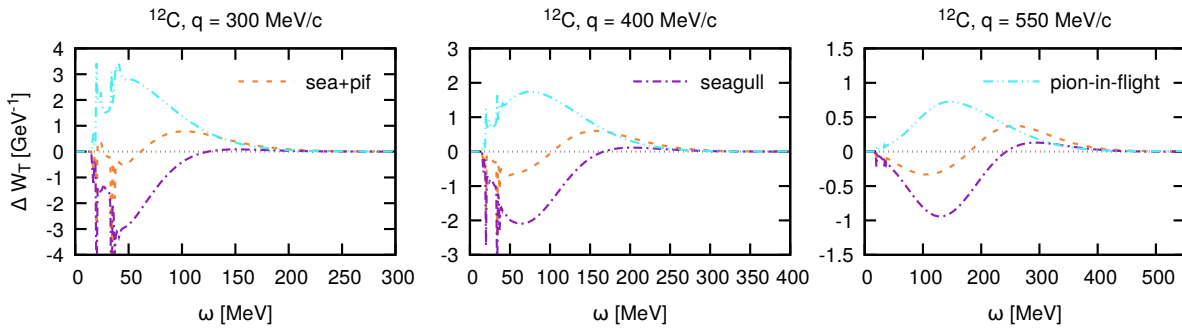


Figure 2.29: Corrections to the 1p1h hadronic responses for fixed momentum transfer values in electron scattering off the ^{12}C nucleus. Different curves correspond to the contributions of seagull and pion-in-flight diagrams.

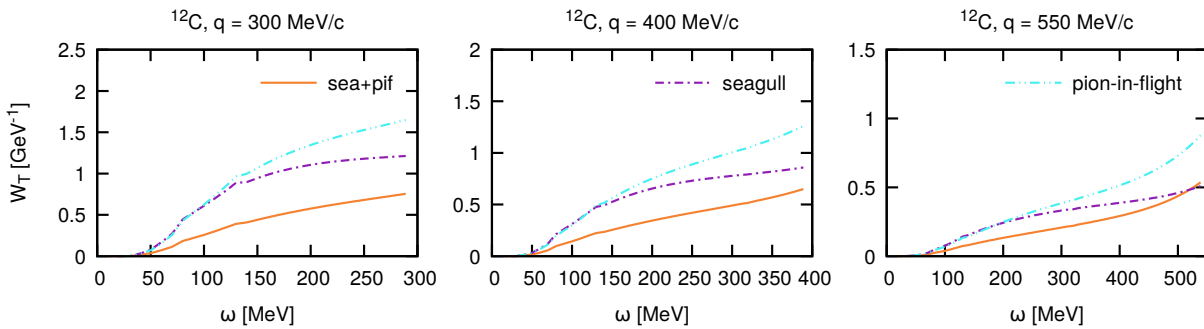


Figure 2.30: 2p2h hadronic responses for fixed momentum transfer values in electron scattering off the ^{12}C nucleus. Different curves correspond to the contributions of seagull and pion-in-flight diagrams.

This phenomenon explains the tiny contribution to the inclusive responses in electron scattering.

As discussed in the previous subsections, the non-relativistic vector seagull and pion-in-flights currents are entirely space-like. In Fig. 2.31, we present inclusive electron scattering cross sections for different fixed angles of the outgoing electron $\theta_{e'}$ = 15° , 30° , 60° . Here, we see that the 2p2h contribution is purely transverse and becomes less constrained the more transverse the kinematics

is. Finally, in Fig. 2.32, we summarize the A -dependence of our calculation. The isospin rules

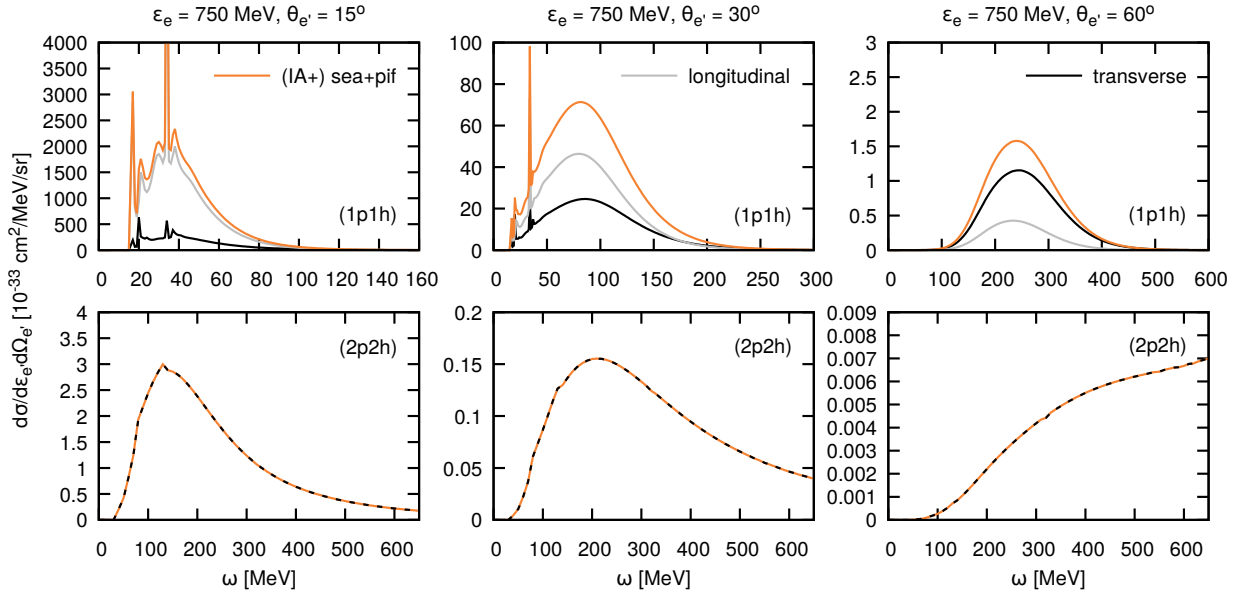


Figure 2.31: Inclusive cross sections for electron scattering off the ^{12}C nucleus for fixed outgoing electron angle $\theta_{e'}$ = 15° , 30° , 60° . The gray and black lines correspond to the longitudinal and transverse contributions, respectively. The orange line shows the final calculation involving meson-exchange currents.

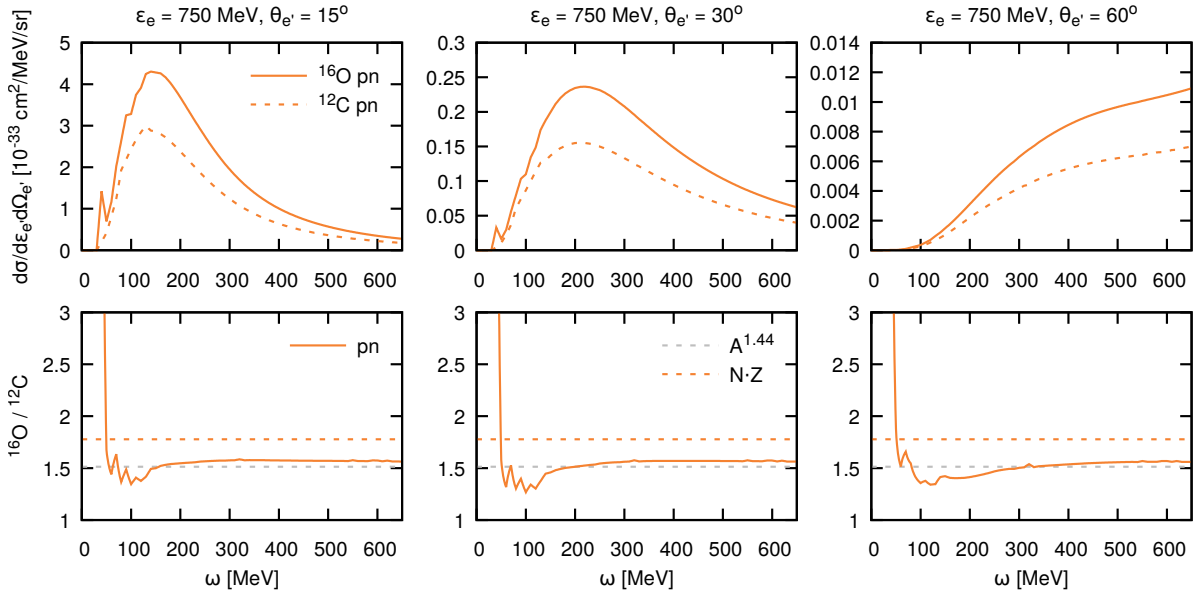


Figure 2.32: Differences due to nuclear targets involved in the inclusive electron scattering cross sections induced by meson-exchange currents. (Top) the solid lines show the scattering off ^{16}O , while the dashed lines show the scattering off the ^{12}C nucleus. (Bottom) $^{16}\text{O}/^{12}\text{C}$ ratio of the inclusive cross sections for the outgoing proton-neutron pairs. The dashed lines present different ratios of nuclear constituents.

in electron scattering allow only interactions on initial proton-neutron pairs for the seagull and pion-in-flight currents. Similarly to the SRC-induced case, the strength of interaction on these

deuteron-like configurations asymptotically scales like target nuclei mass number A to the power of 1.44.

Inclusive neutrino scattering

In this subsection, we present our model of neutrino-nucleus interactions under the same conditions as the electron part. Here, we find non-zero results only in the \mathcal{W}_L and \mathcal{W}_T responses. Fig. 2.33 shows the inclusive neutrino-induced responses with the effect of the seagull and pion-in-flight currents. Contrary to the electron case, here we find a sizeable contribution of the seagull

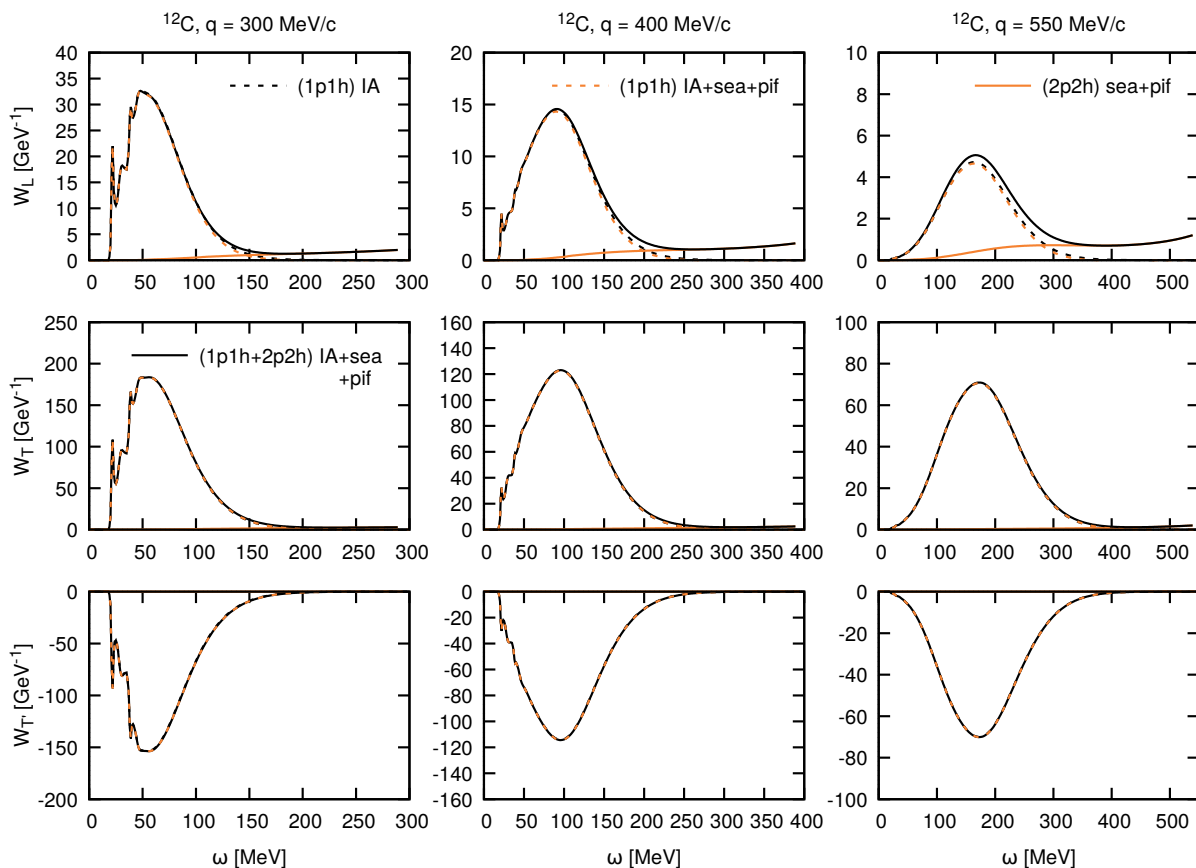


Figure 2.33: Inclusive hadronic responses for fixed momentum transfer values in neutrino scattering off the ^{12}C nucleus. The black and orange dashed lines present the 1p1h results with and without the meson-exchange currents corrections, respectively. The solid orange line shows the 2p2h calculation, while the solid black line is the full calculation.

axial current in the longitudinal response. In Fig. 2.34, we present the IA 1p1h corrections stemming from including MECs in the calculation. In the longitudinal response \mathcal{W}_L , we compare different prescriptions for the axial density, finding *axi* and *sea1* to be comparable in strength while *sea2* is significantly stronger. This effect is consistent with the 2p2h responses in Fig. 2.35. The *sea2* calculation dominates the lower energy regions, allowing it to interfere stronger with the IA result in the 1p1h process. Note that we have not explicitly imposed CVC, and the longitudinal pion-in-flight result comes from the \mathcal{W}_{LL} response. Moreover, we do not observe any contributions to the \mathcal{W}_T , 2p2h responses, which are sensitive to the vector-axial interference. This effect

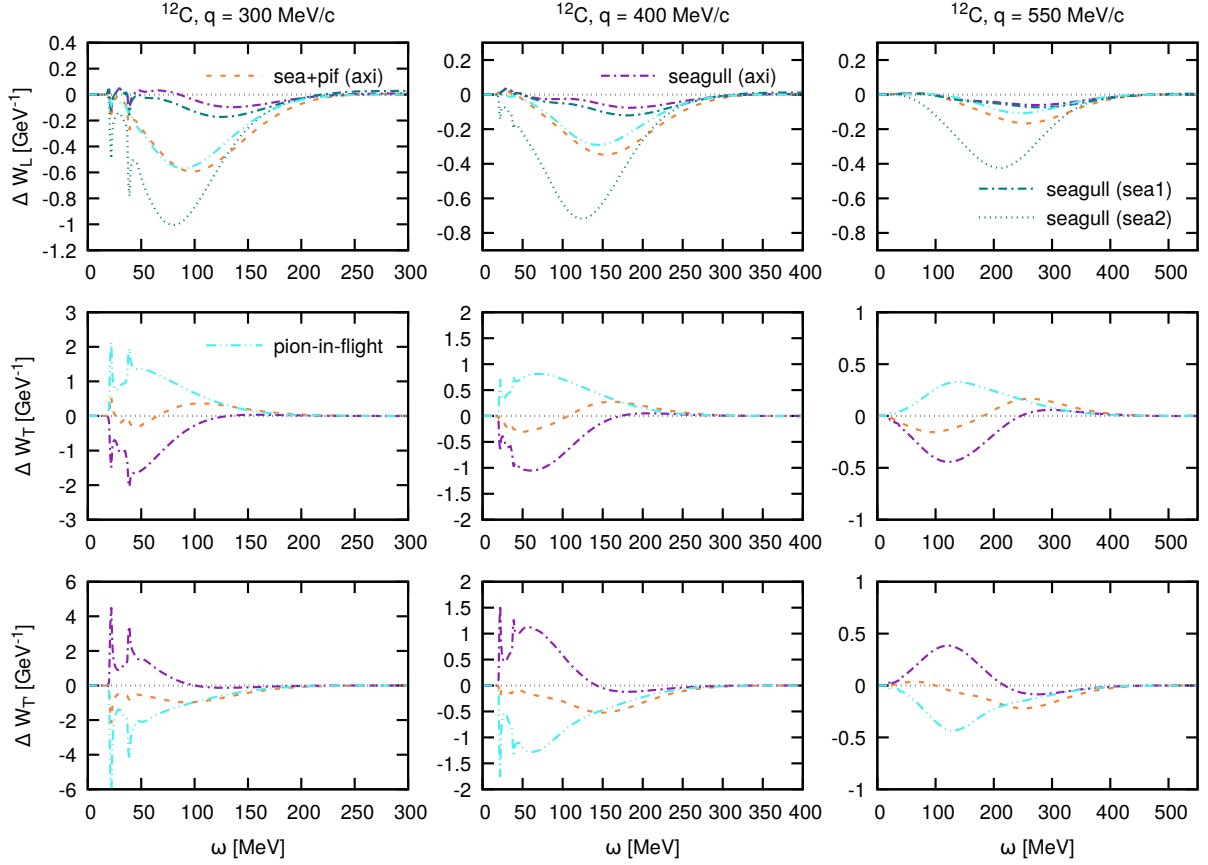


Figure 2.34: Corrections to the 1p1h hadronic responses for fixed momentum transfer values in neutrino scattering off the ^{12}C nucleus. Different curves correspond to the contributions of seagull and pion-in-flight diagrams. The dotted and dot-dashed lines present results of using different prescriptions for the axial seagull current, as described in the text.

originates from the vector contributions being purely space-like and the axial—entirely time-like.

In Fig. 2.31, we demonstrate the capability of our model to produce inclusive neutrino-nucleus scattering cross sections for the fixed values of the outgoing muon angle θ_μ . Here, we see that the 2p2h contributions contain both vector and axial parts, which reflects our model's components. Finally, we summarize all cross section properties in Fig. 2.37, focusing on outgoing proton-proton and proton-neutron pairs. The A -dependence of interactions on initial proton-neutron pairs is consistent with all previous results and asymptotically reaches $A^{1.44}$. On the other hand, the interactions on neutron-neutron pairs, which lead to proton-neutron emission, scale significantly differently from other processes and combinatoric expectations. We find the ratio of outgoing nucleon configuration to be within a range of 3 to 5. This is about factor ~ 2.5 higher than in the electron case but similar to the ratio we found in the SRC-induced processes. These conclusions finish the discussion on the basic aspects of our model. Moving forward to the next chapter, we will enhance our model by integrating meson-exchange currents involving diagrams with explicit Δ -isobar degrees of freedom.

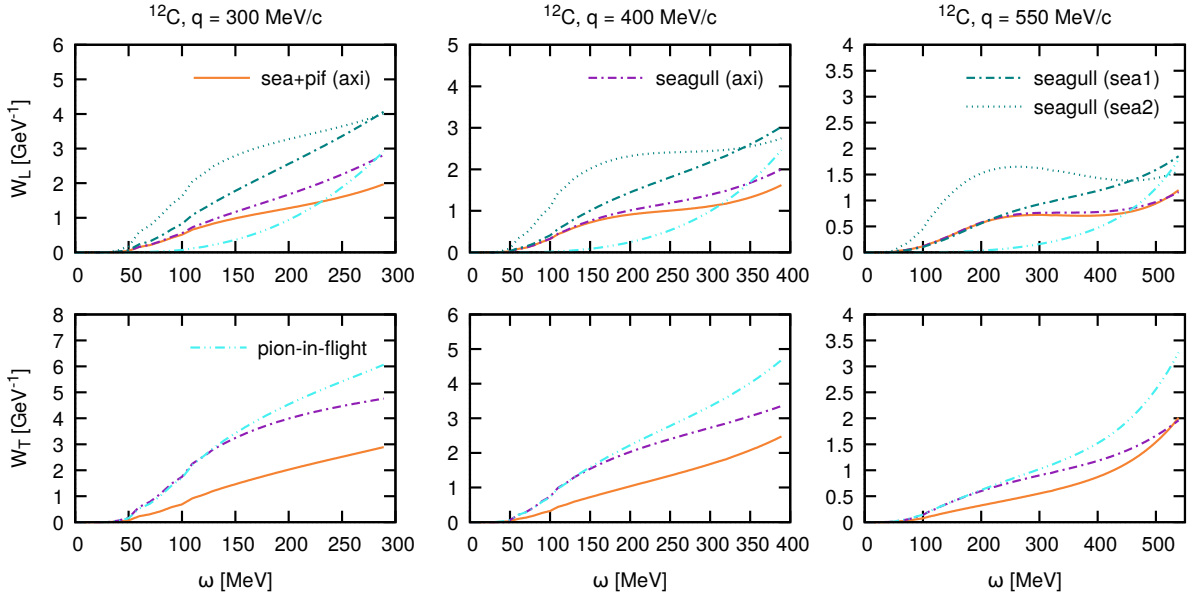


Figure 2.35: 2p2h hadronic responses for fixed momentum transfer values in neutrino scattering off the ^{12}C nucleus. Different curves correspond to the contributions of seagull and pion-in-flight diagrams. The dotted and dot-dashed lines present results of using different prescriptions for the axial seagull current, as described in the text.

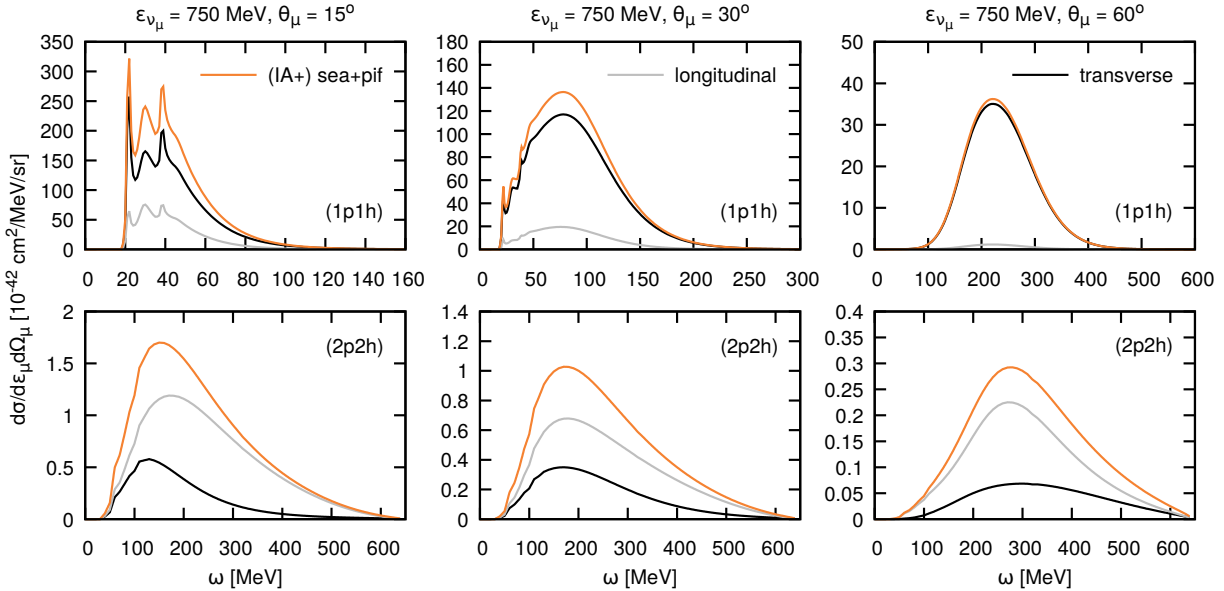


Figure 2.36: Inclusive cross sections for neutrino scattering off the ^{12}C nucleus for fixed outgoing muon angle $\theta_\mu = 15^\circ, 30^\circ, 60^\circ$. The gray and black lines correspond to the longitudinal and transverse contributions, respectively. The orange line shows the final calculation involving meson-exchange currents.

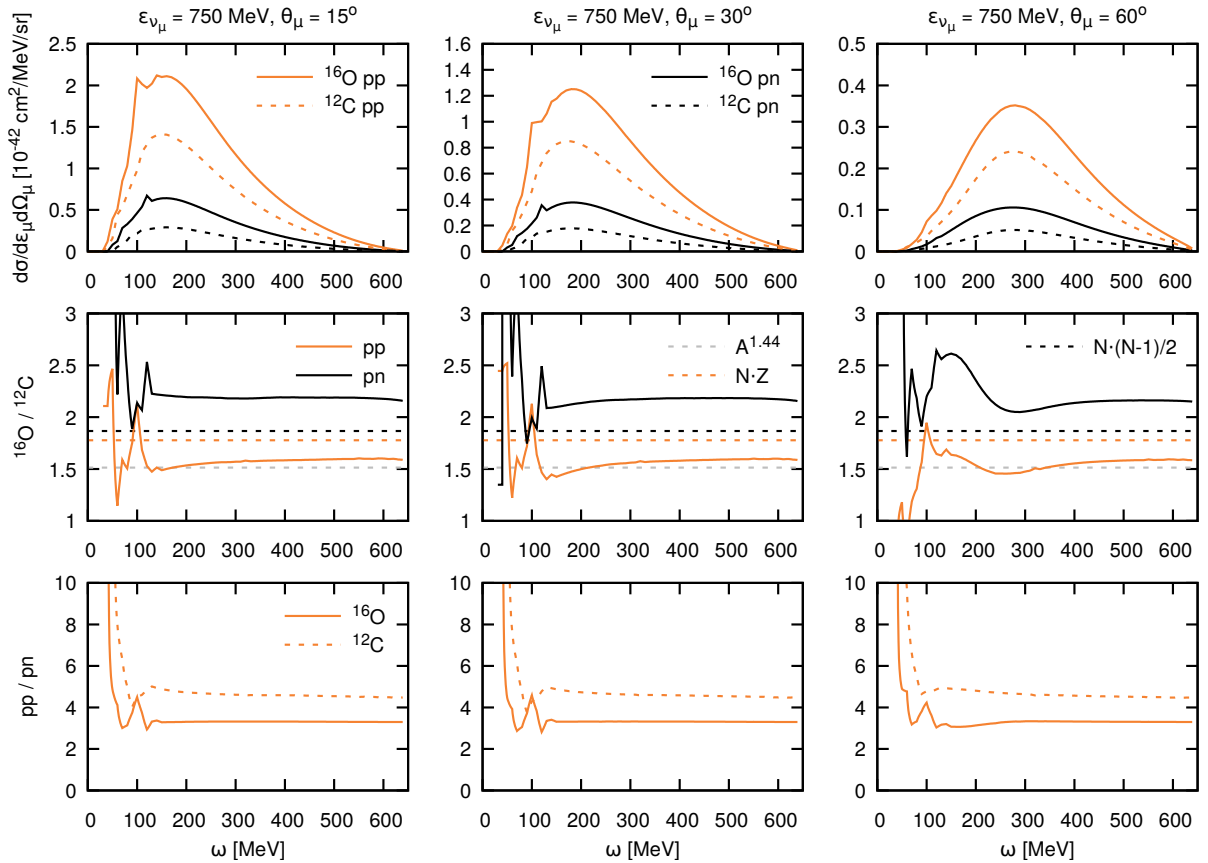


Figure 2.37: Contribution of the different outgoing nucleon pairs to the inclusive neutrino scattering cross sections induced by meson-exchange currents. (Top) the separation between proton-proton and proton-neutron final pairs presented with the orange and black lines, respectively. Here, the solid lines show the scattering off ^{16}O , while the dashed lines show the scattering off the ^{12}C nucleus. (Middle) $^{16}\text{O}/^{12}\text{C}$ ratio of the inclusive cross sections for proton-proton (green) and proton-neutron (black) pairs. The dashed lines present different ratios of nuclear constituents. (Bottom) ratio of different outgoing nucleon pair contributions to the investigated cross sections, where the solid and dashed lines correspond to the ^{16}O and ^{12}C target nuclei, respectively.

References

- [1] J. D. Bjorken and S. D. Drell, *Relativistic Quantum Mechanics*, International Series In Pure and Applied Physics (McGraw-Hill, New York, 1965).
- [2] K. Niewczas, *Impact of Correlated Nucleon Pairs on Neutrino-Nucleus Interactions*, MSc thesis (University of Wrocław, 2016).
- [3] T. Donnelly, *Progress in Particle and Nuclear Physics* **13**, 183 (1985).
- [4] T. Van Cuyck, *Short-range correlations and meson-exchange currents in neutrino-nucleus scattering*, PhD thesis (Ghent University, 2017).
- [5] J. D. Walecka, *Theoretical nuclear and subnuclear physics*, Vol. 16 (1995).
- [6] J. Ryckebusch, M. Vanderhaeghen, L. Machenil, *et al.* *Nucl. Phys. A* **568**, 828 (1994).
- [7] V. Van der Sluys, J. Ryckebusch, and M. Waroquier, *Phys. Rev. C* **51**, 2664 (1995).
- [8] J. Ryckebusch, V. Van der Sluys, K. Heyde, *et al.* *Nucl. Phys. A* **624**, 581 (1997).
- [9] J. Ryckebusch, D. Debruyne, W. Van Nespen, *et al.* *Phys. Rev. C* **60**, 034604 (1999).
- [10] T. Van Cuyck, N. Jachowicz, R. González-Jiménez, *et al.* *Phys. Rev. C* **94**, 024611 (2016).
- [11] T. Van Cuyck, N. Jachowicz, R. González-Jiménez, *et al.* *Phys. Rev. C* **95**, 054611 (2017).
- [12] M. Waroquier, G. Wenes, and K. Heyde, *Nucl. Phys. A* **404**, 298 (1983).
- [13] D. Vautherin and D. M. Brink, *Phys. Rev. C* **5**, 626 (1972).
- [14] J. Ryckebusch, *Photon and electron-induced one-nucleon emission within a selfconsistent HF-RPA model*, PhD thesis (Ghent University, 1988).
- [15] J. Ryckebusch, M. Waroquier, K. Heyde, *et al.* *Nucl. Phys. A* **476**, 237 (1988).
- [16] J. Ryckebusch, K. Heyde, D. Van Neck, *et al.* *Nucl. Phys. A* **503**, 694 (1989).
- [17] N. Jachowicz, *Many-body description of neutrino-nucleus interactions*, PhD thesis (Ghent University, 2000).
- [18] N. Jachowicz, S. Rombouts, K. Heyde, *et al.* *Phys. Rev. C* **59**, 3246 (1999).
- [19] N. Jachowicz, K. Heyde, J. Ryckebusch, *et al.* *Phys. Rev. C* **65**, 025501 (2002).
- [20] V. Pandey, *Quasielastic electroweak scattering cross sections in kinematics relevant for accelerator-based neutrino-oscillation experiments*, PhD thesis (Ghent University, 2016).
- [21] V. Pandey, N. Jachowicz, J. Ryckebusch, *et al.* *Phys. Rev. C* **89**, 024601 (2014).
- [22] V. Pandey, N. Jachowicz, T. Van Cuyck, *et al.* *Phys. Rev. C* **92**, 024606 (2015).
- [23] V. Pandey, N. Jachowicz, M. Martini, *et al.* *Phys. Rev. C* **94**, 054609 (2016).
- [24] A. Nikolakopoulos, M. Martini, M. Ericson, *et al.* *Phys. Rev. C* **98**, 054603 (2018).
- [25] A. Nikolakopoulos, N. Jachowicz, N. Van Dessel, *et al.* *Phys. Rev. Lett.* **123**, 052501 (2019).
- [26] N. van Dessel, *Modeling neutrino-argon interactions in the low to medium energy regime*, PhD thesis (Ghent University, 2020).
- [27] N. Van Dessel, N. Jachowicz, R. González-Jiménez, *et al.* *Phys. Rev. C* **97**, 044616 (2018).
- [28] N. Van Dessel, N. Jachowicz, and A. Nikolakopoulos, *Phys. Rev. C* **100**, 055503 (2019).

- [29] N. Van Dessel, A. Nikolakopoulos, and N. Jachowicz, *Phys. Rev. C* **101**, 045502 (2020).
- [30] L. Alvarez-Ruso *et al.* *Prog. Part. Nucl. Phys.* **100**, 1 (2018).
- [31] S. Janssen, J. Ryckebusch, W. Van Nespen, *et al.* *Nucl. Phys. A* **672**, 285 (2000).
- [32] R. Starink *et al.* *Phys. Lett. B* **474**, 33 (2000).
- [33] J. Ryckebusch and W. Van Nespen, *Eur. Phys. J. A* **20**, 435 (2004).
- [34] K. G. Fissum *et al.* *Phys. Rev. C* **70**, 034606 (2004).
- [35] M. Iodice *et al.* *Phys. Lett. B* **653**, 392 (2007).
- [36] K. L. G. Heyde, *The nuclear shell model* (Springer Berlin, Heidelberg, 1990).
- [37] V. Dmitrasinovic and T. Sato, *Phys. Rev. C* **58**, 1937 (1998).
- [38] R. Bradford, A. Bodek, H. S. Budd, *et al.* *Nucl. Phys. B Proc. Suppl.* **159**, edited by F. Cavanna, J. G. Morfin, and T. Nakaya, 127 (2006).
- [39] P. Barreau, M. Bernheim, J. Duclos, *et al.* *Nuclear Physics A* **402**, 515 (1983).
- [40] L. Lapikas, *Nucl. Phys. A* **553**, edited by R. Bock, H. Emling, E. Grosse, *et al.* 297c (1993).
- [41] V. R. Pandharipande and S. C. Pieper, *Phys. Rev. C* **45**, 791 (1992).
- [42] K. Gottfried, *Nucl. Phys.* **5**, 5557 (1958).
- [43] G. Co' and A. M. Lallena, *Phys. Rev. C* **57**, 145 (1998).
- [44] J. E. Amaro, A. M. Lallena, G. Co', *et al.* *Phys. Rev. C* **57**, 3473 (1998).
- [45] G. Co' and A. M. Lallena, *Annals Phys.* **287**, 101 (2001).
- [46] M. Anguiano, G. Co, A. M. Lallena, *et al.* *Annals Phys.* **296**, 235 (2002).
- [47] M. Anguiano, G. Co', and A. M. Lallena, *J. Phys. G* **29**, 1119 (2003).
- [48] C. Giusti, H. Muther, F. D. Pacati, *et al.* *Phys. Rev. C* **60**, 054608 (1999).
- [49] N. Rocco, A. Lovato, and O. Benhar, *Phys. Rev. Lett.* **116**, 192501 (2016).
- [50] N. Rocco, C. Barbieri, O. Benhar, *et al.* *Phys. Rev. C* **99**, 025502 (2019).
- [51] M. Martini, M. Ericson, G. Chanfray, *et al.* *Phys. Rev. C* **80**, 065501 (2009).
- [52] J. Nieves, I. Ruiz Simo, and M. J. Vicente Vacas, *Phys. Rev. C* **83**, 045501 (2011).
- [53] A. Lovato, S. Gandolfi, J. Carlson, *et al.* *Phys. Rev. Lett.* **117**, 082501 (2016).
- [54] A. Lovato, J. Carlson, S. Gandolfi, *et al.* *Phys. Rev. X* **10**, 031068 (2020).
- [55] M. Vanhalst, J. Ryckebusch, and W. Cosyn, *Phys. Rev. C* **86**, 044619 (2012).
- [56] J. Ryckebusch, W. Cosyn, and M. Vanhalst, *J. Phys. G* **42**, 055104 (2015).
- [57] C. Colle, O. Hen, W. Cosyn, *et al.* *Phys. Rev. C* **92**, 024604 (2015).
- [58] C. Gearhart, PhD thesis (Washington University, 1994).
- [59] R. V. Reid Jr., *Annals Phys.* **50**, 411 (1968).
- [60] K. I. Blomqvist *et al.* *Phys. Lett. B* **421**, 71 (1998).
- [61] C. J. G. Onderwater *et al.* *Phys. Rev. Lett.* **81**, 2213 (1998).
- [62] S. C. Pieper, R. B. Wiringa, and V. R. Pandharipande, *Phys. Rev. C* **46**, 1741 (1992).
- [63] T. Ohmura, M. Morita, and M. Yamada, *Prog. Theor. Phys.* **15**, 222 (1956).

- [64] R. B. Wiringa, R. A. Smith, and T. L. Ainsworth, *Phys. Rev. C* **29**, 1207 (1984).
- [65] R. Schiavilla, V. R. Pandharipande, and R. B. Wiringa, *Nucl. Phys. A* **449**, 219 (1986).
- [66] M. Vanhalst, W. Cosyn, and J. Ryckebusch, *Phys. Rev. C* **84**, 031302 (2011).
- [67] T. E. O. Ericson and W. Weise, *Pions and Nuclei* (Clarendon Press, Oxford, UK, 1988).
- [68] I. S. Towner, *Phys. Rept.* **155**, 263 (1987).
- [69] D. O. Riska and G. E. Brown, *Phys. Lett. B* **38**, 193 (1972).
- [70] E. Ivanov and E. Truhlik, *Nucl. Phys. A* **316**, 437 (1979).
- [71] J. W. Van Orden and T. W. Donnelly, *Annals Phys.* **131**, 451 (1981).
- [72] W. M. Alberico, M. Ericson, and A. Molinari, *Annals Phys.* **154**, 356 (1984).
- [73] M. J. Dekker, P. J. Brussaard, and J. A. Tjon, *Phys. Lett. B* **266**, 249 (1991).
- [74] J. E. Amaro, A. M. Lallena, G. Co, *et al.* *Phys. Lett. B* **277**, 249 (1992).
- [75] J. E. Amaro, A. M. Lallena, and G. Co, *Nucl. Phys. A* **578**, 365 (1994).
- [76] A. De Pace, M. Nardi, W. M. Alberico, *et al.* *Nucl. Phys. A* **726**, 303 (2003).
- [77] A. A. Aguilar-Arevalo *et al.* *Phys. Rev. D* **81**, 092005 (2010).
- [78] J. Nieves, I. Ruiz Simo, and M. J. Vicente Vacas, *Phys. Lett. B* **707**, 72 (2012).
- [79] I. Ruiz Simo, J. E. Amaro, M. B. Barbaro, *et al.* *Phys. Rev. C* **94**, 054610 (2016).
- [80] I. Ruiz Simo, J. E. Amaro, M. B. Barbaro, *et al.* *J. Phys. G* **44**, 065105 (2017).
- [81] I. Ruiz Simo, J. E. Amaro, M. B. Barbaro, *et al.* *Phys. Lett. B* **762**, 124 (2016).
- [82] G. D. Megias, J. E. Amaro, M. B. Barbaro, *et al.* *Phys. Rev. D* **94**, 013012 (2016).
- [83] G. D. Megias, J. E. Amaro, M. B. Barbaro, *et al.* *Phys. Rev. D* **94**, 093004 (2016).
- [84] V. L. Martinez-Consentino, I. R. Simo, and J. E. Amaro, *Phys. Rev. C* **104**, 025501 (2021).
- [85] V. L. Martinez-Consentino, J. E. Amaro, and I. Ruiz Simo, *Phys. Rev. D* **104**, 113006 (2021).
- [86] T. Franco-Munoz, R. González-Jiménez, and J. M. Udías, arXiv:2203:09996 (2022).
- [87] M. Vanderhaeghen, L. Machenil, J. Ryckebusch, *et al.* *Nuclear Physics A* **580**, 551 (1994).
- [88] G. Shen, L. E. Marcucci, J. Carlson, *et al.* *Phys. Rev. C* **86**, 035503 (2012).
- [89] J. F. Mathiot, *Phys. Rept.* **173**, 63 (1989).
- [90] I. S. Towner, *Nucl. Phys. A* **542**, [Erratum: *Nucl.Phys.A* 569, 834–834 (1994)], 631 (1992).

3

Cross sections for one- and two-nucleon knock-out reactions

Multinucleon knock-out contribution has proved vital in understanding neutrino-nucleus scattering experiments. A complete model of such interactions should involve several relevant many-body diagrams and be capable of providing inclusive, semi-inclusive, and exclusive cross section predictions. We perform calculations in a non-relativistic framework with explicit (N, Δ, π) degrees of freedom combined with the dynamically evaluated short-range nucleon correlations. We focus on the aspects of the modeling affected by the Δ -resonance propagator prescriptions and numerical input for the nucleon correlation functions. To understand the reliability of our description, we validate our calculations through a comparison with inclusive electron scattering data. This chapter constitutes the core of the first direction of our work—the microscopic modeling part [1].

3.1 Isobar degrees of freedom

Nucleon resonances are short-living excited states that involve an altered internal structure of their parent baryon. The possibility of exciting nucleons to their resonant states provides significant strength in scattering experiments [2]. This behavior is vivid in electro- and neutrino-induced single-pion production reactions on nuclear targets, where the resonant reactions dominate the non-resonant background [3]. One can interpret meson-exchange current diagrams to be created once an electroweakly produced pion is captured on another nucleon in the nuclear medium. Thus, the currents involving nucleon resonances should be significantly more relevant than seagull or pion-in-flight, which we investigated in Chapter 2. The most prominent resonance we should consider is the isobaric $\Delta(1232)$, and including its effect in the calculations is a prerequisite for a

reliable two-nucleon knock-out model. In the following discussion, we consider this resonance as a separate baryonic species in addition to the nucleon. Moreover, we assume that the exact intrinsic structure of the Δ -resonance is not resolved: whether it arises from pion-nucleon dynamics or quark physics is not relevant.

This section investigates meson-exchange currents, which include nucleon excitations, limiting ourselves to the $\Delta(1232)$ isobar. They are commonly known as Δ -currents. We construct them by coupling an electroweak probe to a $NN\Delta$ vertex and the pion, produced in the subsequent Δ decay, to another nucleon leg. The former coupling can happen before or after the pion exchange, resulting in a *resonant* or *non-resonant* Δ propagator, respectively. Out of all π -related two-body currents investigated in our modeling, the Δ -current is the only one in which we consider strong medium dependence. However, we only consider diagrams where the Δ is attached to a boson line. Fig. 3.1 schematically presents the investigated MEC diagrams for lepton-induced two-nucleon knock-out reactions. Similarly, Fig. 3.2 shows the two-body current corrections to one-nucleon knock-out processes obtained with Δ -currents.

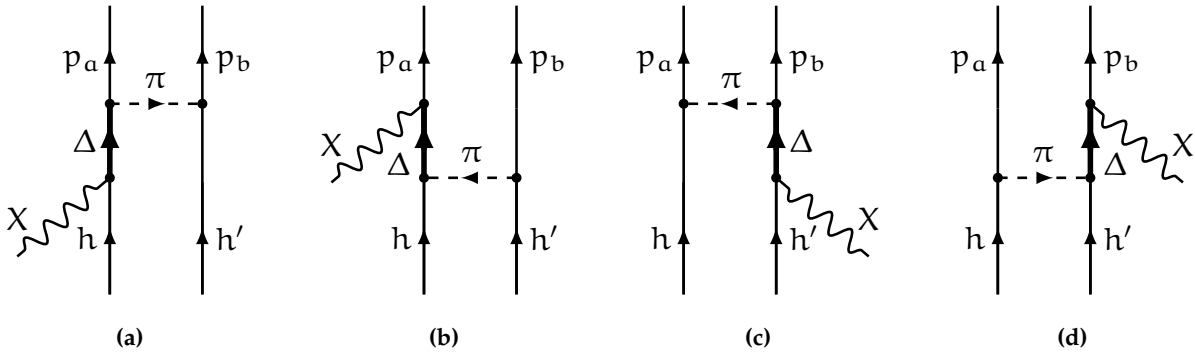


Figure 3.1: Graphical representation of the two-body Δ -mediated currents in the two-nucleon knock-out process: (a), (c) external boson coupling before the meson-exchange, (b), (d) external boson coupling after the meson-exchange.

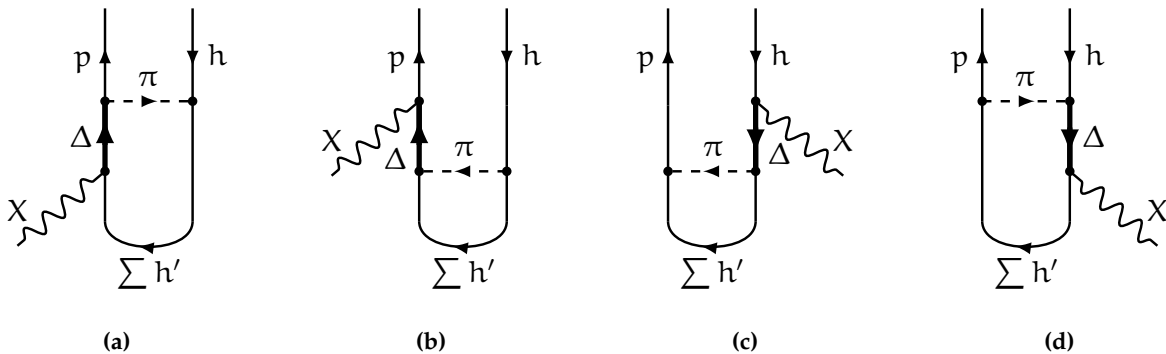


Figure 3.2: Graphical representation of the contribution of the two-body Δ -mediated currents to the one-nucleon knock-out process: (a), (c) external boson coupling before the meson-exchange, (b), (d) external boson coupling after the meson-exchange.

Several theoretical approaches have investigated the significance of the Δ -mediated meson-exchange currents in electron- and neutrino-induced two-nucleon knock-out reactions on nuclei.

The cornerstone of this research path is the work on low-energy photoabsorption and electron scattering involving two-nucleon systems, as described in a few seminal papers [4,5]. Later, such models started incorporating explicit Δ degrees of freedom, e.g., [6,7]. This progress led to the development of models, such as M. Dekker *et al.* [8,9], J. Amaro *et al.* [10,11], and A. De Pace *et al.* [12], which accurately described MEC-induced transverse response enhancement in electron scattering. The fundamental research on electromagnetic meson-exchange currents is summarized in Refs. [2,13,14]. For neutrino reactions, Δ -currents are included in models implemented in Monte Carlo neutrino event generators, such as those by M. Martini *et al.* [15], J. Nieves *et al.* [16], and SuSAv2 [17,18]. They are also essential ingredients in the extended factorization framework of N. Rocco *et al.* [19], as well as in the relativistic Fermi gas calculations by I. Ruiz Simo *et al.* [20,21] and the similar relativistic shell model approach [22]. We base our presented model on electromagnetic calculations of Refs. [23–26] and, in this section, extend their results to neutrino interactions.

Vector currents

We consider single-pion exchange diagrams involving the $\Delta(1232)$ isobar, as depicted in Fig. 3.1. In the electron-induced reaction, we encounter the πNN , $\pi N\Delta$, and $\gamma N\Delta$ vertices, which we evaluate using the standard methodology in the low energy limit [2]. For the πNN vertex, we use the pseudovector coupling

$$\mathcal{L}_{\pi NN} = i \frac{f_{\pi NN}}{m_\pi} (\boldsymbol{\sigma} \cdot \vec{q})(\boldsymbol{\tau} \cdot \vec{\pi}), \quad (3.1.1)$$

matching the seagull and pion-in-flight currents studied in Chapter 2. To handle the Δ -resonance, we introduce the spin and isospin $1/2 \rightarrow 3/2$ transition operators \vec{S} and \vec{T} , respectively. Per analogy to the πNN vertex, we use the effective Lagrangians of the form [26]

$$\mathcal{L}_{\pi N\Delta} = i \frac{f_{\pi N\Delta}}{m_\pi} (\vec{S}^\dagger \cdot \vec{q}) (\vec{T}^\dagger \cdot \vec{\pi}), \quad (3.1.2)$$

$$\mathcal{L}_{\gamma N\Delta} = i \frac{f_{\gamma N\Delta}}{m_\pi} G_{\gamma N\Delta}(Q^2) (\vec{S}^\dagger \times \vec{q}) \cdot \vec{A} \vec{T}_z^\dagger, \quad (3.1.3)$$

where $f_{\pi N\Delta}^2/4\pi = 0.37$ and $f_{\gamma N\Delta} = 0.12$. The electromagnetic form factor $G_{\gamma N\Delta}(Q^2)$ is parametrized as [27]

$$G_{\gamma N\Delta}(Q^2) = \frac{1}{(1 + Q^2/\Lambda_1^2)^2} \frac{1}{\sqrt{1 + Q^2/\Lambda_2^2}}, \quad (3.1.4)$$

where $\Lambda_1 = 0.84$ GeV/c and $\Lambda_2 = 1.2$ GeV/c. Note that this form factor decreases with Q^2 faster than the nucleon dipole form [28,29]. Finally, similarly to other meson-exchange currents in our model, we regularize the πNN and $\pi N\Delta$ vertices with monopole form factors

$$\Gamma_\pi(|\vec{q}|^2) = \frac{\Lambda_\pi^2 - m_\pi^2}{|\vec{q}|^2 + \Lambda_\pi^2}, \quad (3.1.5)$$

where $\Lambda_\pi = 1250$ MeV/c. With the Lagrangians mentioned above, we derive the expression of the Δ -currents in momentum space as

$$\begin{aligned} \hat{j}_V^{[2],\Delta}(\vec{q}) &= \frac{i}{9} \frac{f_{\pi NN} f_{\pi N\Delta} f_{\pi N\gamma}}{m_\pi^3} G_{\gamma N\Delta}(Q^2) \\ &\times \left\{ (G_\Delta^{\text{res}} + G_\Delta^{\text{nres}}) \left((\mathcal{J}_V)_z \left[\Gamma_\pi^2(|\vec{q}_1|^2)(\sigma_2 \times \vec{q}_1) \frac{(\vec{\sigma}_1 \cdot \vec{q}_1)}{|\vec{q}_1|^2 + m_\pi^2} - \Gamma_\pi^2(|\vec{q}_2|^2)(\sigma_1 \times \vec{q}_2) \frac{(\vec{\sigma}_2 \cdot \vec{q}_2)}{|\vec{q}_2|^2 + m_\pi^2} \right] \times \vec{q} \right. \right. \\ &+ 4(\tau_2)_z \Gamma_\pi^2(|\vec{q}_2|^2)(\vec{q}_2 \times \vec{q}) \frac{(\vec{\sigma}_2 \cdot \vec{q}_2)}{|\vec{q}_2|^2 + m_\pi^2} + 4(\tau_1)_z \Gamma_\pi^2(|\vec{q}_1|^2)(\vec{q}_1 \times \vec{q}) \frac{(\vec{\sigma}_1 \cdot \vec{q}_1)}{|\vec{q}_1|^2 + m_\pi^2} \left. \right) \\ &+ (G_\Delta^{\text{res}} - G_\Delta^{\text{nres}}) \left(2i(\mathcal{J}_V)_z \left[\Gamma_\pi^2(|\vec{q}_1|^2) \vec{q}_1 \frac{(\vec{\sigma}_1 \cdot \vec{q}_1)}{|\vec{q}_1|^2 + m_\pi^2} - \Gamma_\pi^2(|\vec{q}_2|^2) \vec{q}_2 \frac{(\vec{\sigma}_2 \cdot \vec{q}_2)}{|\vec{q}_2|^2 + m_\pi^2} \right] \times \vec{q} \right. \\ &\left. \left. - 2i(\tau_2)_z \Gamma_\pi^2(|\vec{q}_2|^2)((\sigma_1 \times \vec{q}_2) \times \vec{q}) \frac{(\vec{\sigma}_2 \cdot \vec{q}_2)}{|\vec{q}_2|^2 + m_\pi^2} - 2i(\tau_1)_z \Gamma_\pi^2(|\vec{q}_1|^2)((\sigma_2 \times \vec{q}_1) \times \vec{q}) \frac{(\vec{\sigma}_1 \cdot \vec{q}_1)}{|\vec{q}_1|^2 + m_\pi^2} \right) \right\}, \end{aligned} \quad (3.1.6)$$

where we used the following identities

$$(\vec{S} \cdot \vec{A})(\vec{S}^\dagger \cdot \vec{B}) = \frac{2}{3}(\vec{A} \times \vec{B}) - i\frac{1}{3}((\vec{\sigma} \times \vec{A}) \times \vec{B}), \quad (3.1.7)$$

$$\tau_2^\alpha T_1^\alpha (T_1^\dagger)_z = \frac{2}{3}(\tau_2)_z - i\frac{1}{3}(\tau_1 \times \tau_2)_z. \quad (3.1.8)$$

G_Δ^{res} and G_Δ^{nres} are the Δ propagators in the resonant (Fig. 3.2a and Fig. 3.2c) and the non-resonant (Fig. 3.2b and Fig. 3.2d) cases, respectively. We defer the discussion of their properties to the next-to-next subsection. To obtain the prescriptions for CC neutrino interactions, we follow the conservation of vector current and perform a rotation in isospin space [30]. Thus, we replace the third component of the \vec{T} operator as

$$\vec{T}_z \rightarrow \vec{T}_\pm = (\vec{T}_x \pm i\vec{T}_y). \quad (3.1.9)$$

Note that this results in the following substitutions: $(\mathcal{J}_V)_z \rightarrow (\mathcal{J}_V)_\pm$ and $(\tau)_z \rightarrow 2(\tau)_\pm$.

A common approach in the low-energy nuclear studies is to assume the Δ -resonance in the static limit ($G_\Delta^{\text{res}} \simeq G_\Delta^{\text{nres}} \simeq 1/(M_\Delta - M_N)$). Using this approximation, we obtain the following current

$$\begin{aligned} \hat{j}_V^{[2],\Delta,\text{st}}(\vec{q}) &= i\frac{2}{9} \frac{f_{\pi NN} f_{\pi N\Delta} f_{\pi N\gamma}}{m_\pi^3(M_\Delta - M_N)} G_{\gamma N\Delta}(Q^2) \\ &\times \left\{ (\mathcal{J}_V)_z \left[\Gamma_\pi^2(|\vec{q}_1|^2)(\sigma_2 \times \vec{q}_1) \frac{(\vec{\sigma}_1 \cdot \vec{q}_1)}{|\vec{q}_1|^2 + m_\pi^2} - \Gamma_\pi^2(|\vec{q}_2|^2)(\sigma_1 \times \vec{q}_2) \frac{(\vec{\sigma}_2 \cdot \vec{q}_2)}{|\vec{q}_2|^2 + m_\pi^2} \right] \times \vec{q} \right. \\ &\left. + 4(\tau_2)_z \Gamma_\pi^2(|\vec{q}_2|^2)(\vec{q}_2 \times \vec{q}) \frac{(\vec{\sigma}_2 \cdot \vec{q}_2)}{|\vec{q}_2|^2 + m_\pi^2} + 4(\tau_1)_z \Gamma_\pi^2(|\vec{q}_1|^2)(\vec{q}_1 \times \vec{q}) \frac{(\vec{\sigma}_1 \cdot \vec{q}_1)}{|\vec{q}_1|^2 + m_\pi^2} \right\}, \end{aligned} \quad (3.1.10)$$

which recovers the result of Ref. [23].

Axial currents

Contrary to the seagull meson-exchange currents, the non-relativistic Δ -currents are space-like in both the vector and axial case [13]. To obtain the low-energy limit prescription for the axial

current, we refer to the discussion by I. Towner [13], who proposes the following structure

$$\begin{aligned} \hat{j}_{A,i}^{[2],\Delta,\text{Towner}}(\vec{q}) = & -\frac{1}{9} \frac{f_{\pi N\Delta}^2}{m_\pi^2 (M_\Delta - M_N)} g_A \frac{2m_\rho^2}{|\vec{q}|^2 + 2m_\rho^2} \\ & \times \left\{ (\mathcal{J}_V)_i \left[(\sigma_2 \times \vec{q}_1) \frac{(\vec{\sigma}_1 \cdot \vec{q}_1)}{|\vec{q}_1|^2 + m_\pi^2} - (\sigma_1 \times \vec{q}_2) \frac{(\vec{\sigma}_2 \cdot \vec{q}_2)}{|\vec{q}_2|^2 + m_\pi^2} \right] \right. \\ & \left. + 4(\tau_2)_i \vec{q}_2 \frac{(\vec{\sigma}_2 \cdot \vec{q}_2)}{|\vec{q}_2|^2 + m_\pi^2} + 4(\tau_1)_i \vec{q}_1 \frac{(\vec{\sigma}_1 \cdot \vec{q}_1)}{|\vec{q}_1|^2 + m_\pi^2} \right\}, \end{aligned} \quad (3.1.11)$$

where g_A is the axial coupling and m_ρ is the mass of the ρ meson. This result has been derived from the meson-isobar-nucleon Lagrangian—containing π , ρ , and A_1 mesons—originating from the hard-pion model of E. Ivanov and E. Truhlik [5]. Here, the external boson coupling is constrained by the axial form factor

$$g_A(|\vec{q}|^2) = g_A \frac{2m_\rho^2}{|\vec{q}|^2 + 2m_\rho^2}, \quad (3.1.12)$$

which assumes the A_1 -meson dominance of the coupling and $m_{A_1}^2 \simeq 2m_\rho^2$. This formulation of the current satisfies the two-body version of the PCAC hypothesis [13].

To adapt the current of Eq. (3.1.11) to our framework, we notice that it corresponds to the static limit of Eq. (3.1.10). Thus, we retain the complete Δ -propagator formulation and obtain a robust axial current

$$\begin{aligned} \hat{j}_A^{[2],\Delta}(\vec{q}) = & -\frac{1}{2} \frac{1}{9} \frac{f_{\pi N\Delta}^2}{m_\pi^2} G_A(Q^2) \\ & \times \left\{ (G_\Delta^{\text{res}} + G_\Delta^{\text{nres}}) \left((\mathcal{J}_V)_\pm \left[\Gamma_\pi^2(|\vec{q}_1|^2) (\sigma_2 \times \vec{q}_1) \frac{(\vec{\sigma}_1 \cdot \vec{q}_1)}{|\vec{q}_1|^2 + m_\pi^2} - \Gamma_\pi^2(|\vec{q}_2|^2) (\sigma_1 \times \vec{q}_2) \frac{(\vec{\sigma}_2 \cdot \vec{q}_2)}{|\vec{q}_2|^2 + m_\pi^2} \right] \right. \right. \\ & + 4(2\tau_2)_\pm \Gamma_\pi^2(|\vec{q}_2|^2) \vec{q}_2 \frac{(\vec{\sigma}_2 \cdot \vec{q}_2)}{|\vec{q}_2|^2 + m_\pi^2} + 4(2\tau_1)_\pm \Gamma_\pi^2(|\vec{q}_1|^2) \vec{q}_1 \frac{(\vec{\sigma}_1 \cdot \vec{q}_1)}{|\vec{q}_1|^2 + m_\pi^2} \left. \right) \\ & + (G_\Delta^{\text{res}} - G_\Delta^{\text{nres}}) \left(2i(\mathcal{J}_V)_\pm \left[\Gamma_\pi^2(|\vec{q}_1|^2) \vec{q}_1 \frac{(\vec{\sigma}_1 \cdot \vec{q}_1)}{|\vec{q}_1|^2 + m_\pi^2} - \Gamma_\pi^2(|\vec{q}_2|^2) \vec{q}_2 \frac{(\vec{\sigma}_2 \cdot \vec{q}_2)}{|\vec{q}_2|^2 + m_\pi^2} \right] \right. \\ & \left. \left. - 2i(2\tau_2)_\pm \Gamma_\pi^2(|\vec{q}_2|^2) (\sigma_1 \times \vec{q}_2) \frac{(\vec{\sigma}_2 \cdot \vec{q}_2)}{|\vec{q}_2|^2 + m_\pi^2} - 2i(2\tau_1)_\pm \Gamma_\pi^2(|\vec{q}_1|^2) (\sigma_2 \times \vec{q}_1) \frac{(\vec{\sigma}_1 \cdot \vec{q}_1)}{|\vec{q}_1|^2 + m_\pi^2} \right) \right\}, \end{aligned} \quad (3.1.13)$$

where we introduced the Q^2 -dependent version of the axial form factor, in its standard dipole form, by the following substitution: $g_A(|\vec{q}|^2) \rightarrow G_A(Q^2)$. This method is consistent with the prescriptions of Ref. [30]. In what follows, we refer to this solution as *axi1*, while we call the current involving $g_A(|\vec{q}|^2)$ —*axi2*.

Δ -resonance propagator

Defining field properties for particles with spins greater than one-half and nonvanishing mass, presents several challenges. The non-uniqueness and gauge freedom lead to inevitable complexity of such a description. While the Dirac equation provides a good description of spin-1/2 fermions, the next most complex case, spin-3/2, still has ambiguities. Calculating diagrams involving a spin-3/2 (Δ)-isobar requires understanding its propagator and in-medium properties, usually expressed in the Rarita-Schwinger formalism [31]. The natural prescription for our non-relativistic

framework is the *static approximation*. However, this approach lacks the characteristic resonant behavior. This subsection will discuss various methods of extending the Δ -propagation prescription to account for its relativistic nature.

In the diagrams presented in Fig. 3.1, we encounter two Δ propagators, which correspond to the isobar interacting with an external boson at either the beginning or the end of its excitation. As schematically shown in Fig. 3.3, neglecting the produced pion's fate, we can discuss these processes as the direct and crossed $\Delta(1232)$ -pole diagrams of single-pion production, respectively. To describe the isobar dynamics, we adopt the following propagators

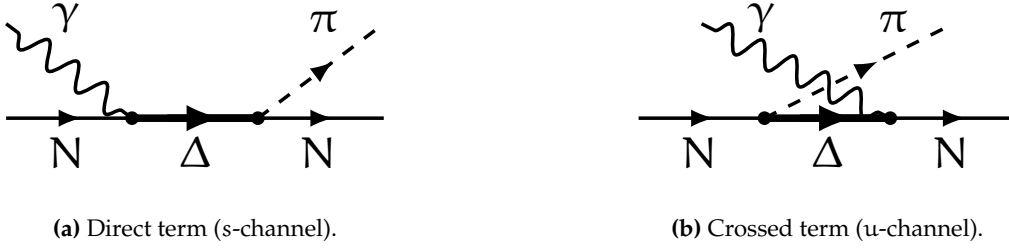


Figure 3.3: Graphical representation of the Δ -resonance excitation with an external photon, and its de-excitation.

$$G_{\Delta}^{\text{res}} = \frac{1}{M_{\Delta} - \sqrt{s} - i/2\Gamma_{\Delta}^{\text{res}} + V_{\Delta}}, \quad G_{\Delta}^{\text{nr}} = \frac{1}{M_{\Delta} - \sqrt{u}}, \quad (3.1.14)$$

where \sqrt{s} and \sqrt{u} are the intrinsically available energies in the resonant and non-resonant cases, respectively. $\Gamma_{\Delta}^{\text{res}}$ is the free Δ -resonance width [32]

$$\Gamma_{\Delta}^{\text{res}} = \frac{1}{3} \frac{f_{\pi N \Delta}^2}{4\pi} \frac{|\vec{p}_{\pi}|^3}{m_{\pi}^3} \frac{M_N + E_{\pi}}{\sqrt{s}}, \quad (3.1.15)$$

expressed in center-of-momentum frame variables. Additionally, we correct the resonant propagator with a potential V_{Δ} , which brings in-medium effects into the formula.

Modeling in-medium properties of nucleon resonances and their impact on various lepton-nucleus interaction channels, especially single-pion production [33], is a relevant topic in the community. Typical values for the Δ self-energy in the medium, also denoted as Σ_{Δ} , are $V_{\Delta}^{\text{Chen\&Lee}} = -40 - i30$ [MeV], as used in the calculations of Ref. [25]. E. Oset and L. Salcedo calculated this quantity for pion photo-production in a Fermi gas as a function of photon energy [34]. To use that, we introduce the effective energy transfer

$$\omega_{\gamma} = \omega + \frac{q^2}{2M_N}, \quad (3.1.16)$$

which mimics the real photon energy in electron scattering interactions. However, this potential is a function of (ρ/ρ_0) , with the nuclear density ρ relative to the saturation value ρ_0 . For nuclei, that are finite-sized hadronic systems, it is argued that using the value of $\rho = 0.75\rho_0$ is more accurate. Here, we follow the description of J. Ryckebusch *et al.* [26] and take $\rho = \rho_0$. Fig. 3.4 presents the solutions to describe the imaginary part of the Δ potential as a function of the effective energy transfer and the impact of these in-medium effects on the real and imaginary parts of the

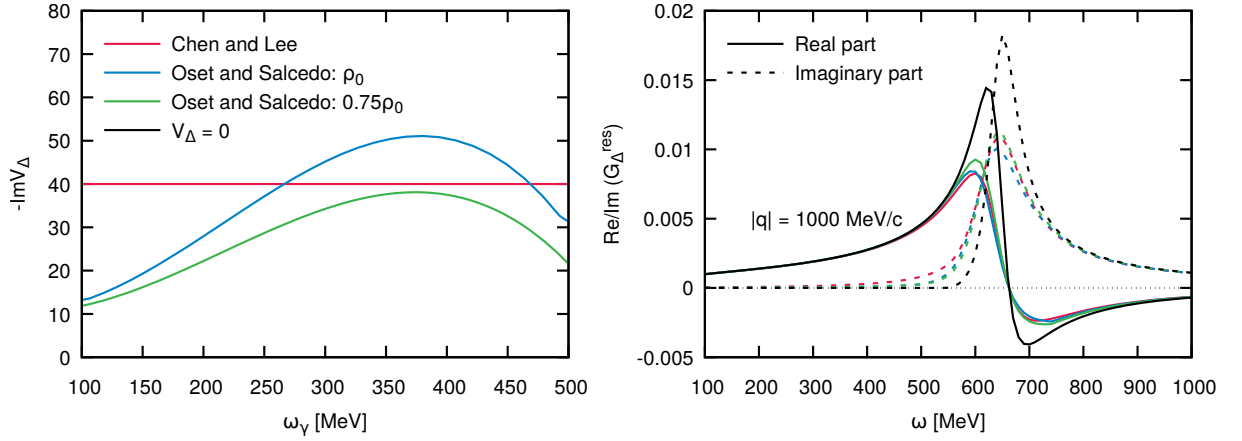


Figure 3.4: (Left) parametrizations of the Δ -resonance nuclear potential V_Δ and (right) their impact on the real and imaginary parts of the propagator G_Δ^{res} .

Δ propagator G_Δ^{res} . We see that, while the prescriptions provide similar results, their general effect is a significant suppression. One can also find other parametrizations of the Δ self-energy in the literature, such as the ones by J. Nieves *et al.* [35] or M. Hjorth-Jensen *et al.* [36]. The former provides a significantly higher real part than the descriptions mentioned above.

Calculating the propagators G_Δ^{res} and G_Δ^{hres} requires evaluating Mandelstam variables s and u , respectively. For this purpose, we need to understand the kinematics of the investigated processes. In the direct term of Fig. 3.3a, the external boson transfers energy (ω) and momentum (\vec{q}) directly to the nucleon state. Thus, assuming the target nucleon, of binding energy ϵ_h , to be at rest, we obtain

$$s = q^2 + (M_N - \epsilon_h)^2 + 2\omega(M_N - \epsilon_h). \quad (3.1.17)$$

As discussed before, one could derive an effective quantity [37]

$$s_\gamma = (M_N - \epsilon_h)^2 + 2\omega_\gamma(M_N - \epsilon_h), \quad (3.1.18)$$

which translates the properties of this process to the real photon equivalent. However, we found this correction negligible ($s - s_\gamma \approx 0.015q^2$) and will use the prescription of Eq. (3.1.17) [26]. The evaluation of the $u = (q - p_{N_a})^2$ variable is more complex, as we do not have access to the isobar state's dynamics before the interaction. Ref. [26], similarly to the calculation of s , assumes the Δ is at rest and receives the whole momentum transferred to the system ($\vec{p}_{N_a} \simeq \vec{q}$). However, this solution is prone to diverge at $\sqrt{u} = M_\Delta$, and we must introduce dynamical information into the formalism to deal with this issue. The momentum conservation of the final state nucleons is

$$\vec{P}_{hh'} + \vec{q} = \vec{p}_{N_a} + \vec{p}_{N_b} \quad (3.1.19)$$

where $\vec{P}_{hh'}$ is the momentum of the nucleons COM system. Following the rational reasoning of the approximation by K. Gottfried [38], which introduces quasi-deuteron back-to-back kinematics of two-nucleon states, we put $|\vec{P}_{hh'}| \approx 0$. In our framework, we calculate the propagators at the level of the inclusive cross section, with only the ω and \vec{q} variables available. Thus, to average

over the momenta of the final nucleons, we put ($\vec{p}_{N_a} \simeq \vec{q}/2$) and get

$$u = \left(\sqrt{M_N^2 + |\vec{q}|^2/4} \right)^2 - \left(\frac{|\vec{q}|^2}{4} \right). \quad (3.1.20)$$

This formula is well-constrained and significantly more realistic than the approach used in Ref. [26].

To improve the treatment of relativistic effects in the Δ -resonance excitation process, starting from the static isobar model, one needs to account for the poles of the form $(M_\Delta^2 - s)^{-1}$ and $(M_\Delta^2 - u)^{-1}$ in the direct and crossed channels, respectively [2]. As J. Dekker *et al.* presented [9], one should treat the propagators, resembling the relativistic Breit-Wigner distribution, as

$$G_\Delta^{\text{res}} = \frac{2M_\Delta}{M_\Delta^2 - s - iM_\Delta\Gamma_\Delta^{\text{res}} + 2M_\Delta V_\Delta}, \quad G_\Delta^{\text{nres}} = \frac{2M_\Delta}{M_\Delta^2 - u}. \quad (3.1.21)$$

In Fig. 3.5, we present the final results of the resonant and non-resonant propagators for two values of momentum transfer $|\vec{q}| = 200, 1000 \text{ MeV}/c$. We see that the corrections in the s -channel

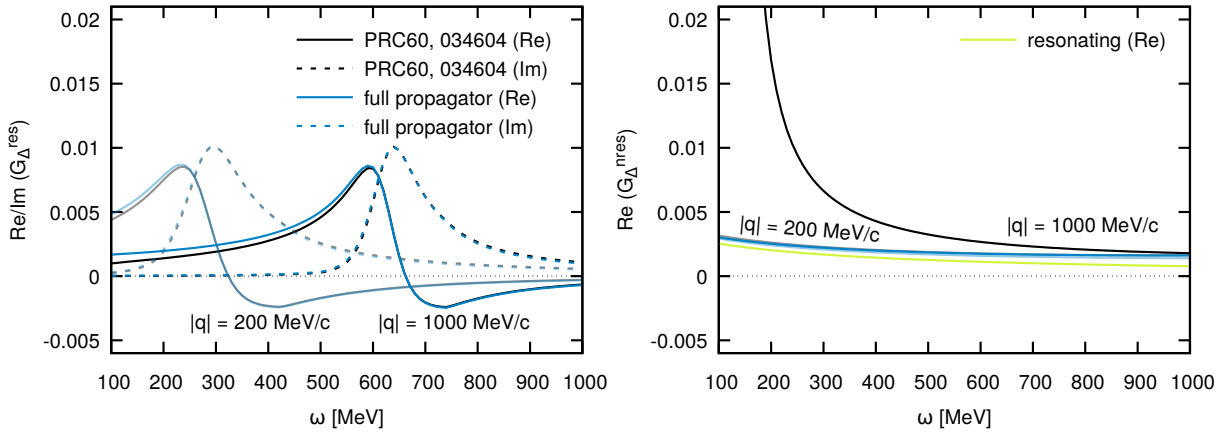


Figure 3.5: Δ -isobar propagators for the fixed values of the momentum transfer $|\vec{q}| = 200, 1000 \text{ MeV}/c$, compared to the calculations of Ref. [26]. (Left) the real and imaginary parts in the resonant case; (right) the real part of the non-resonant propagator.

are minor, while the ones in the u -channel avoid the divergence at low ω .

Finally, we will address the approximations used in the previous studies with our framework: in Ref. [23], the propagators are treated in a *static* way, obtaining

$$G_\Delta^{\text{res}} = \frac{1}{M_\Delta - M_N}, \quad G_\Delta^{\text{nres}} = 0, \quad (3.1.22)$$

limiting the number of contributing spin and isospin structures, as presented in Eq. (3.1.10). The resonating approach proposed by J. Dekker *et al.* [9] extended the model's applicability [24] and introduced the *resonant* prescription for the Δ isobar

$$G_\Delta^{\text{res}} + G_\Delta^{\text{nres}} = \frac{1}{M_\Delta - M_N - \omega - i/2\Gamma_\Delta^{\text{res}}} + \frac{1}{M_\Delta - M_N + \omega} \quad (3.1.23)$$

$$G_\Delta^{\text{res}} - G_\Delta^{\text{nres}} = 0. \quad (3.1.24)$$

However, these calculations are limited to the same number of terms as the static one. In the past, the complete calculation has been presented in Ref. [26]. Nowadays, there are many discussions about the quantum-mechanical consistency of simultaneously using two-nucleon knock-out and single-pion production models for inclusive lepton-induced processes. It has been argued by A. De Pace *et al.* that to avoid double-counting of the Δ -resonance strength; one needs to remove the imaginary part of the propagator [39]. We refer to this approach as the *real part only* and analyze its significance in the following subsections. To study the contribution of Δ -currents to the lepton-induced one- and two-nucleon knock-out reactions, we will use different propagator prescriptions and the axial current *axi1*. In Appendix A and Appendix B, we summarize the matrix elements and cross section formulas for the 1p1h and 2p2h cases. Then, we wrap the reduced matrix elements for vector and axial operators in Appendix C.

Inclusive electron scattering

To ensure the reliability of any neutrino-nucleus scattering model, it is essential to compare it against electron scattering data. In this section, we benchmark our model with the Δ -currents only. To achieve this, we repeat the analyses of Chapter 2 and use the data of Ref. [40], which provides inclusive electron scattering measurements. This method permits separate longitudinal and transverse inclusive strength access for various fixed values of $|\vec{q}|$. Fig. 3.6 presents the Δ -currents-modified 1p1h and 2p2h responses in electron scattering off Carbon. As our current

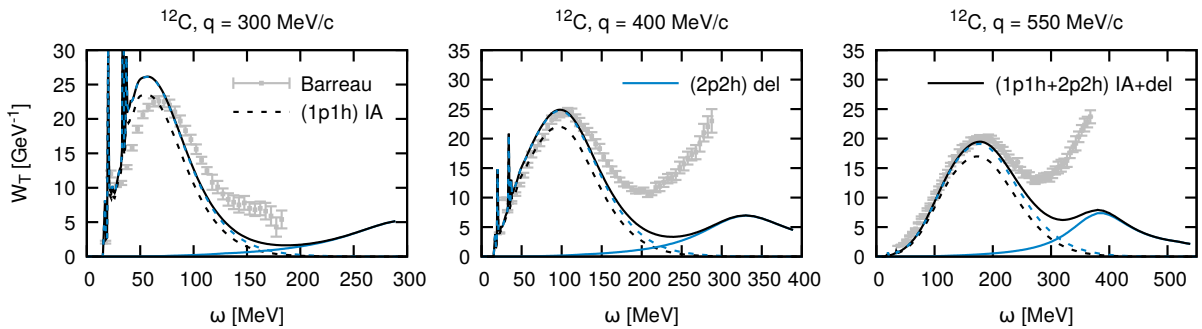


Figure 3.6: Inclusive hadronic responses for fixed momentum transfer values in electron scattering off the ^{12}C nucleus confronted with the experimental results of Ref. [40]. The black and blue dashed lines present the 1p1h results with and without the Δ -currents corrections, respectively. The solid blue line shows the 2p2h calculation, while the solid black line is the full calculation.

formulation is purely space-like, inclusive electron scattering obtains Δ -current contributions only in the transverse part. Here, we observe a visible enhancement in the 1p1h responses, similar for all three kinematics, and a characteristic resonance peak structure in the 2p2h responses, which becomes more pronounced with increasing $|\vec{q}|$. We describe this behavior in detail in Fig. 3.7 and Fig. 3.8, respectively. In the former, we see the low- ω nature is similar for different Δ -current prescriptions, while in the latter, we see the difference starting from $\sim 150 \text{ MeV}$. At $|\vec{q}| = 550 \text{ MeV}/c$, the resonating approach significantly enhances the 1p1h response, which corresponds to the 2p2h strength peaking earlier than in other models, and is consistent with the results of Ref. [24]. The most visible aspect of Fig. 3.8 is the substantial reduction of the 2p2h response due to removing

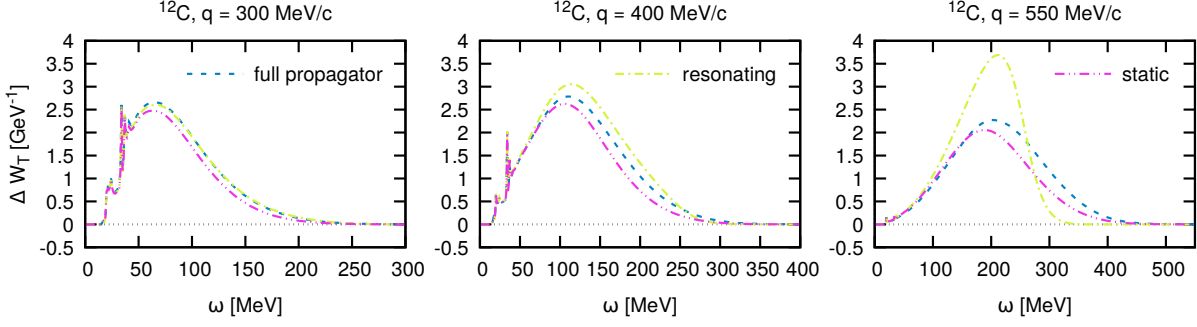


Figure 3.7: Corrections to the 1p1h hadronic responses for fixed momentum transfer values in electron scattering off the ^{12}C nucleus. Different curves correspond to the choice of the Δ -propagator approximation, as described in the text.

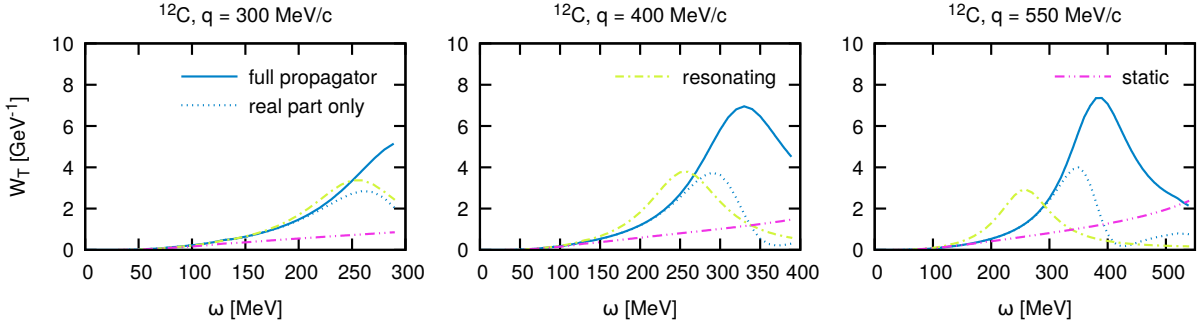


Figure 3.8: 2p2h hadronic responses for fixed momentum transfer values in electron scattering off the ^{12}C nucleus. Different curves correspond to the choice of the Δ -propagator approximation, as described in the text.

the imaginary part of the Δ propagator, especially for the higher values of the momentum transfer. Finally, the characteristic ratio of the full and the static approaches is consistent with the results of M. Dekker *et al.* [9] and A. De Pace *et al.* [12]. Still, the latter find the static model to start diverging at lower values of ω in the transverse channel. This is surprising, as our results are consistent with the older analysis by J. Amaro *et al.* [11].

We continue our investigations by combining the information from nuclear responses into inclusive (e, e') cross sections for fixed angles of the outgoing electron. In Fig. 3.9, we present the 1p1h and 2p2h cross sections for the incoming energy $\epsilon_e = 750$ MeV, representing a typical energy scale for accelerator neutrino experiments, such as T2K. As expected, the effect of Δ -mediated two-body currents is purely transverse. We summarize the cross section properties in Fig. 3.10, distinguishing the contributions from the proton-neutron and proton-proton initial nucleon pairs. One can see a significant dominance of the interaction strength coming from the former targets. As in all SRC and other MEC results, the A -dependence of the electron-induced proton-neutron emission is consistent with the power law of $A^{1.44}$. The contribution of proton-proton emission, as well as the target pair's contribution ratio, changes across the investigated dynamics. We infer that the energy dependence of the different isospin-configuration-sensitive terms of Eq. (3.1.6) differs. Thus, it is perilous to draw general conclusions about the nature of

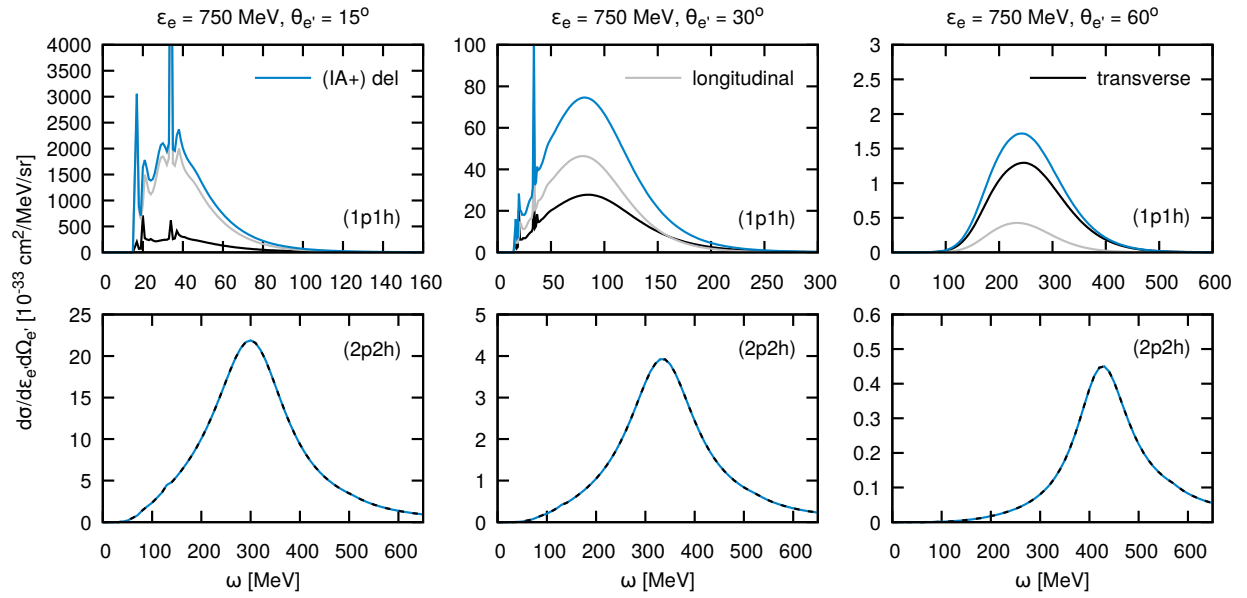


Figure 3.9: Inclusive cross sections for electron scattering off the ^{12}C nucleus for fixed outgoing electron angle $\theta_{e'}$ = 15° , 30° , 60° . The gray and black lines correspond to the longitudinal and transverse contributions, respectively. The blue line shows the final calculation involving Δ -currents.

these processes and universal laws other than the A -dependence of the proton-neutron emission. I. Ruiz Simo *et al.* reported the pp/pn ratio of the bottom row in Fig. 3.10 to be between 12 to 6 [41], with increasing energy of the interaction and its longitudinal character. This tension between the two models requires a dedicated study.

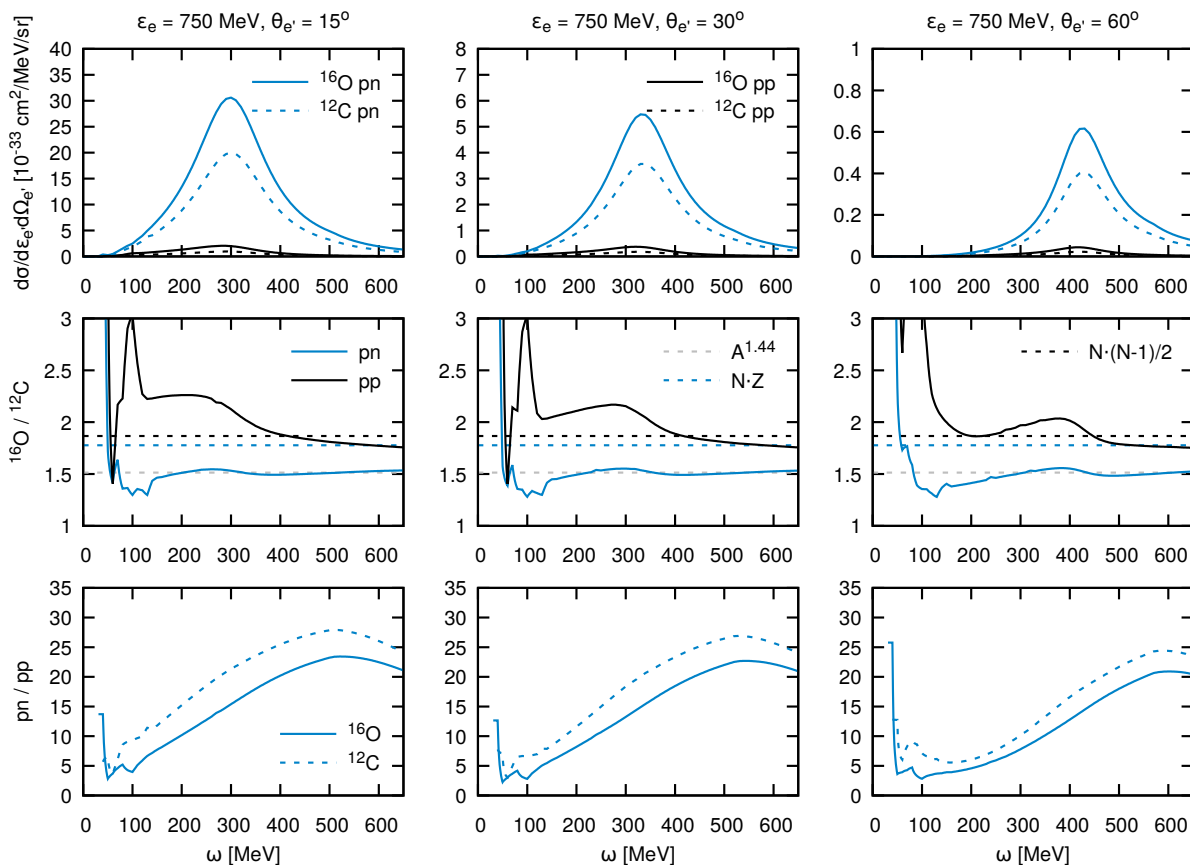


Figure 3.10: Contribution of the different outgoing nucleon pairs to the inclusive electron scattering cross sections induced by Δ -currents. (Top) the separation between proton-neutron and proton-proton final pairs presented with the blue and black lines, respectively. Here, the solid lines show the scattering off ^{16}O , while the dashed lines show the scattering off the ^{12}C nucleus. (Middle) $^{16}\text{O}/^{12}\text{C}$ ratio of the inclusive cross sections for proton-neutron (green) and proton-proton (black) pairs. The dashed lines present different ratios of nuclear constituents. (Bottom) ratio of different outgoing nucleon pair contributions to the investigated cross sections, where the solid and dashed lines correspond to the ^{16}O and ^{12}C target nuclei, respectively.

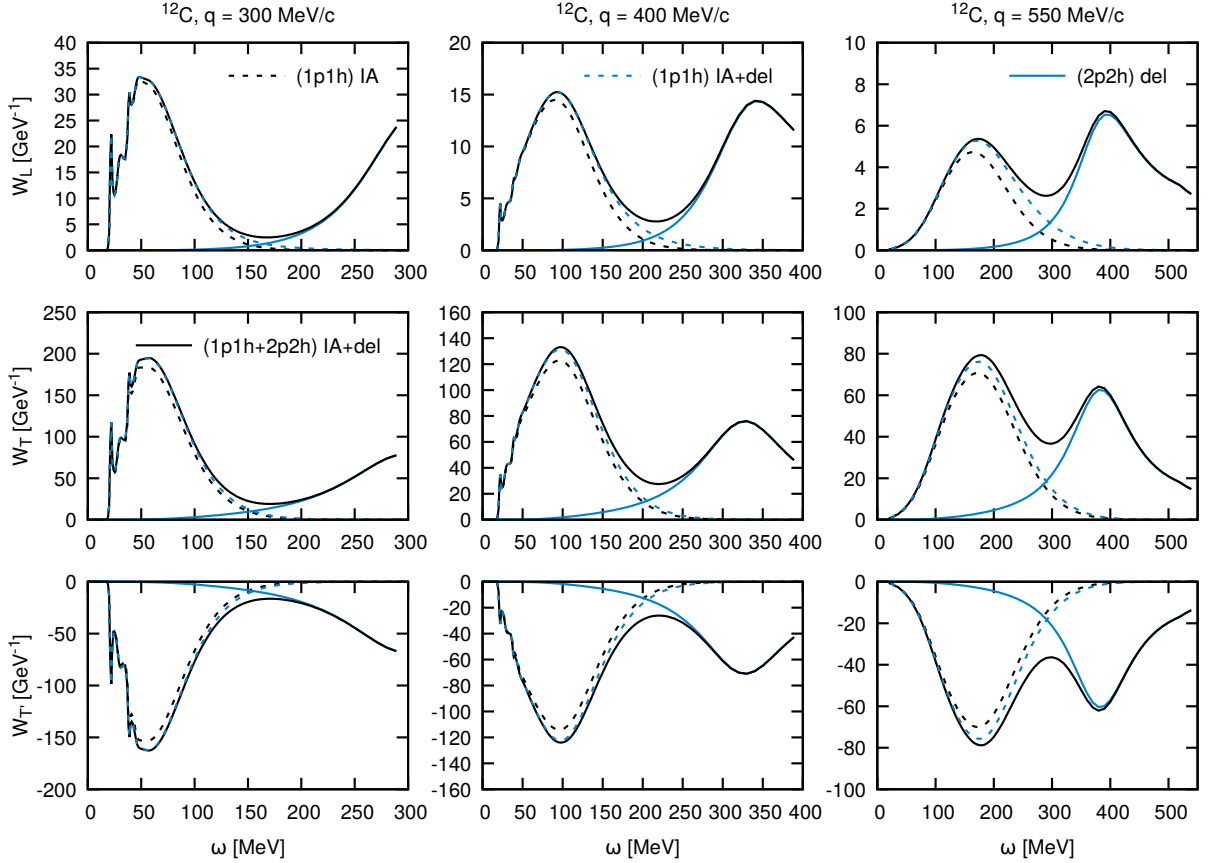


Figure 3.11: Inclusive hadronic responses for fixed momentum transfer values in neutrino scattering off the ^{12}C nucleus. The black and blue dashed lines present the 1p1h results with and without the Δ -current corrections, respectively. The solid blue line shows the 2p2h calculation, while the solid black line is the full calculation.

Inclusive neutrino scattering

In this subsection, for the first time in the framework of the Ghent model, we present the neutrino-induced two-nucleon knock-out results mediated by the Δ -currents. Fig. 3.11 illustrates the calculations of the longitudinal, transverse, and asymmetric transverse responses for different values of the momentum transfer $|\vec{q}|$. These results are similar yet stronger than their electron counterparts, with an enhancement in the 1p1h strength and a peak in the 2p2h part. Note that we access kinematics in the top right panel where the 2p2h response is larger than the 1p1h one. In Fig. 3.12 and Fig. 3.13, we present the Δ -current 1p1h corrections to the IA picture and the 2p2h responses, respectively. The properties of these results, which stem from the modeling of the Δ -isobar propagation, are equivalent to our previous studies of electron-induced reactions. Here, we investigate the different prescriptions for the axial current: *axi1* (default) and *axi2*. One can see that the Q^2 -dependent form factor of Eq. (3.1.13) (blue curve) exhibits the most physical behavior, and we expect it to be more reliable.

Focusing on the cross sections, in Fig. 3.14, we present the results for the inclusive muon neutrino-induced processes for the fixed value of the outgoing muon angle θ_μ . Here, the 2p2h

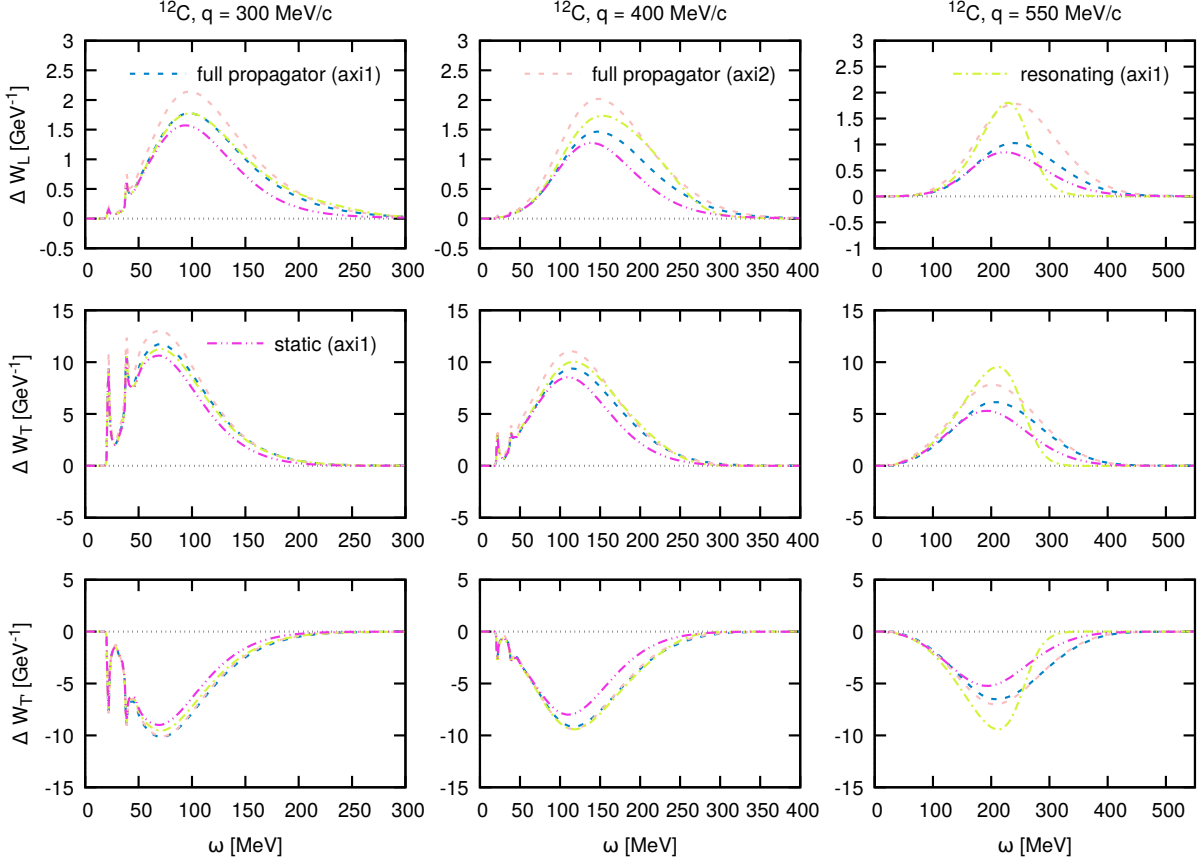


Figure 3.12: Corrections to the 1p1h hadronic responses for fixed momentum transfer values in neutrino scattering off the ^{12}C nucleus. Different curves correspond to the choice of the Δ -propagator approximation, as described in the text. The dashed blue and salmon lines present results of using different prescriptions for the axial current, as described in the text.

longitudinal (axial) part of the interaction provides significant strength at more forward scattering kinematics. Concluding these calculations, we present a summary of cross section properties in Fig. 3.15, emphasizing the resulting proton-proton and proton-neutron pairs. Our analysis reveals that the A -dependence of interactions on initial proton-neutron pairs aligns with previous findings and approaches $A^{1.44}$. In this case, the target nucleon pair's contributions ratio is between 4 to 6. This is consistent with the conclusions of I. Ruiz Simo *et al.* [21] that reported a value not exceeding 6. This good agreement adds to the validation of the constructed model.

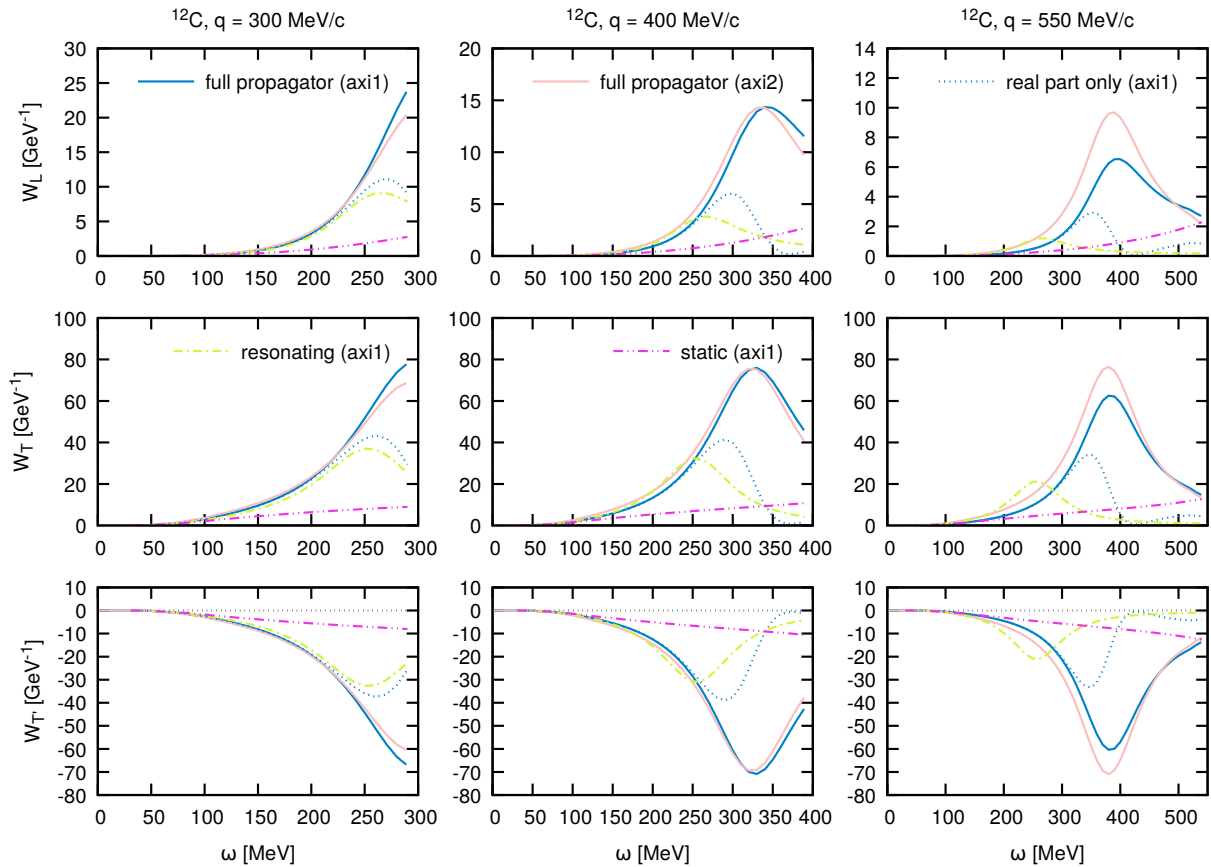


Figure 3.13: 2p2h hadronic responses for fixed momentum transfer values in neutrino scattering off the ^{12}C nucleus. Different curves correspond to the choice of the Δ -propagator approximation, as described in the text. The solid blue and salmon lines present results of using different prescriptions for the axial current, as described in the text.

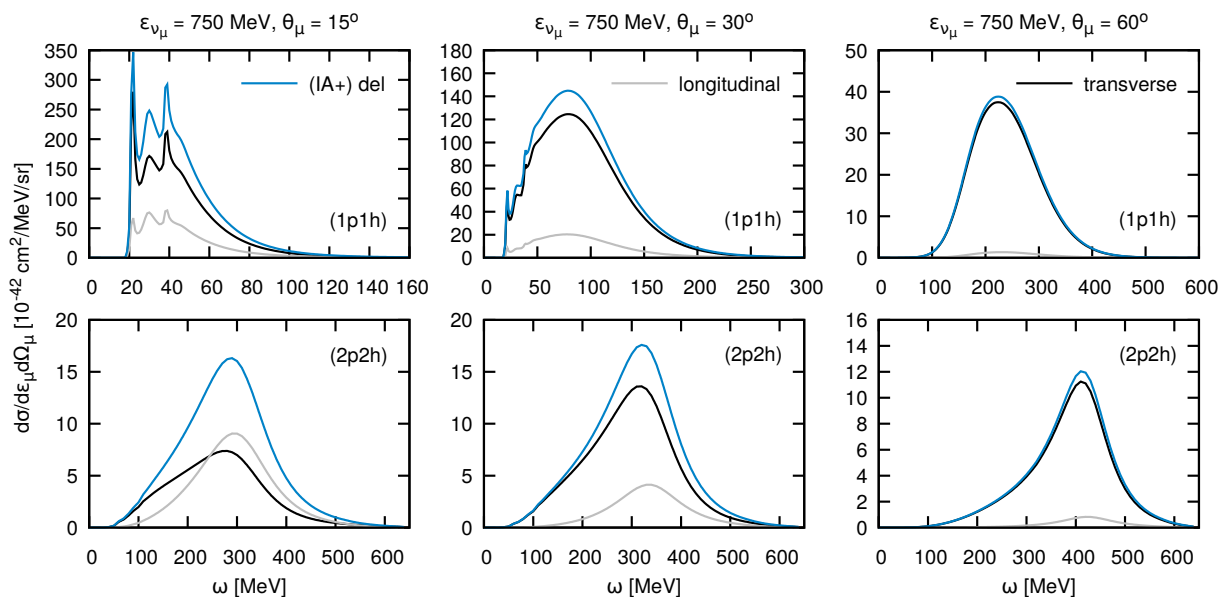


Figure 3.14: Inclusive cross sections for neutrino scattering off the ^{12}C nucleus for fixed outgoing muon angle $\theta_\mu = 15^\circ, 30^\circ, 60^\circ$. The gray and black lines correspond to the longitudinal and transverse contributions, respectively. The blue line shows the final calculation involving Δ -currents.

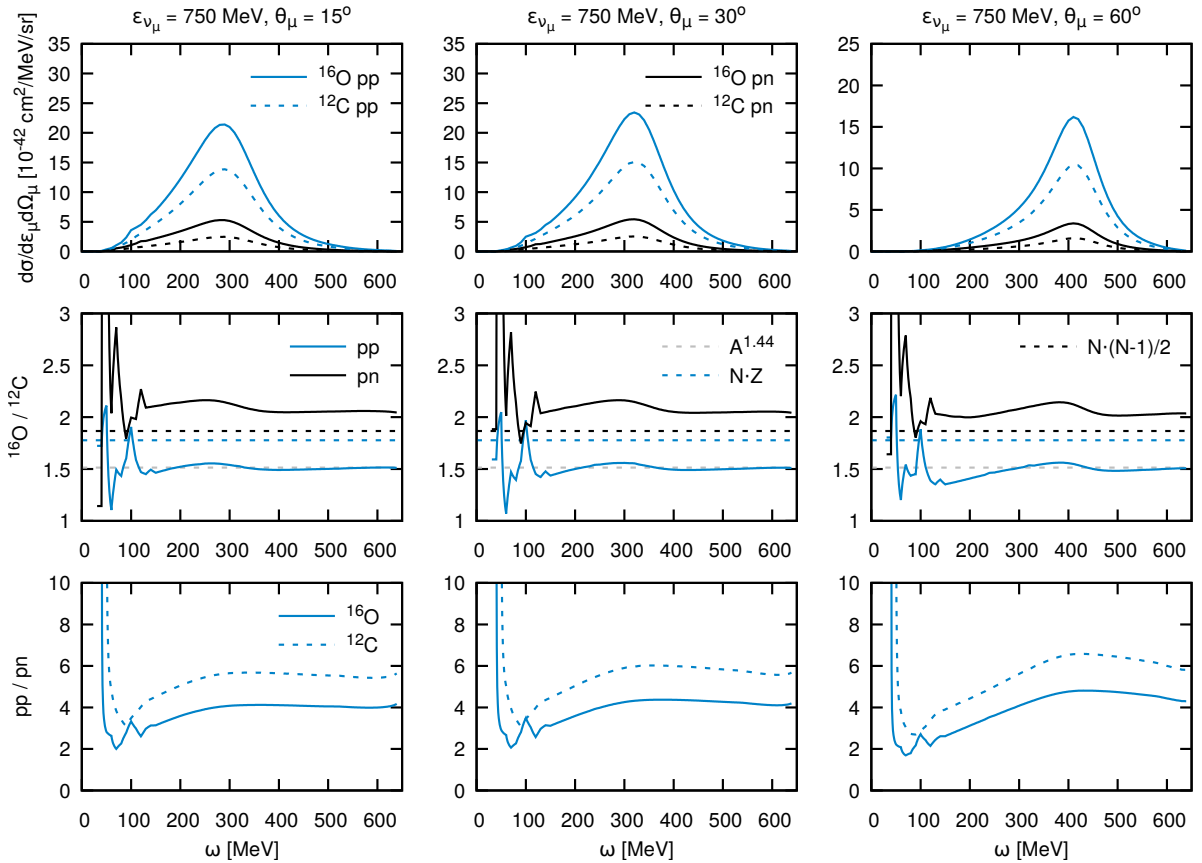


Figure 3.15: Contribution of the different outgoing nucleon pairs to the inclusive neutrino scattering cross sections induced by Δ -currents. (Top) the separation between proton-proton and proton-neutron final pairs presented with the blue and black lines, respectively. Here, the solid lines show the scattering off ¹⁶O, while the dashed lines show the scattering off the ¹²C nucleus. (Middle) ¹⁶O/¹²C ratio of the inclusive cross sections for proton-proton (green) and proton-neutron (black) pairs. The dashed lines present different ratios of nuclear constituents. (Bottom) ratio of different outgoing nucleon pair contributions to the investigated cross sections, where the solid and dashed lines correspond to the ¹⁶O and ¹²C target nuclei, respectively.

3.2 Consistent modeling of two-body currents

The picture of a nucleus as a collection of nucleons submerged in a mean-field nuclear potential accurately describes nuclear ground state and simple transition reactions. Such a model predicts discrete energy levels and many quantum-mechanical effects, e.g., Pauli blocking. However, as proved in exclusive electron scattering experiments, it is not sensitive enough to the local character of the short-, intermediate- and long-range nucleon-nucleon correlations, mediated by the heavier (ω , σ), medium (ρ) and lighter (π) mesons, respectively. In order to enhance its precision, it is important to take into consideration the variations in the properties of the IPM, including the presence of high-energy and high-momentum components in the nuclear wave function, as well as the reduced occupancy of the shells. To effectively represent these factors, one must consider the influence of two-body currents with diverse characteristics, which account for a wide range of nuclear correlations, in the subsequent level of accuracy. When it comes to lepton-induced reactions, this entails distributing the four-momentum transferred to the hadronic system among pairs of nucleons, usually leading in their subsequent knock-out in coincidence.

So far, we have discussed the independent modeling of different two-body currents in electron- and neutrino-nucleus scattering. To combine these contributions, we need to establish a framework that avoids any double-counting of the modeled physical effects. We construct SRC as operators that correct the initial nuclear state, mimicking the behavior of the nucleon-nucleon potential. The coupling strength between the bosons and SRC pairs is the same as the coupling to a single nucleon. Then, the MECs are explicit two-body currents of π -range that act dynamically when the hadronic system interacts with an external boson. We conclude that, provided we do not consider the correlation currents (Fig. 2.26), there is a clear separation of scales and effects between the modeled SRC and MEC contributions, which makes our approach consistent.

To combine the SRC and MEC models, we refer to the discussion of Ref. [42]. Extending the derivation of Section 2.3, we write the nuclear current involving IA and MECs as

$$\hat{j}_v^{\text{had}} \simeq \sum_{i=1}^A \hat{j}_v^{[1]}(i) + \sum_{i<j}^A \hat{j}_v^{[2],\text{MEC}}(i,j). \quad (3.2.1)$$

Then, we build an effective current by including the SRC effect as

$$\begin{aligned} \hat{j}_v^{\text{eff}} \simeq & \sum_{i=1}^A \hat{j}_v^{[1]}(i) + \sum_{i<j}^A \hat{j}_v^{[1],\text{SRC}}(i,j) + \left[\sum_{i<j}^A \hat{j}_v^{[1],\text{SRC}}(i,j) \right]^\dagger \\ & + \sum_{i<j}^A \hat{j}_v^{[2],\text{MEC}}(i,j) + \sum_{i<j}^A \hat{j}_v^{[2],\text{int}}(i,j) + \left[\sum_{i<j}^A \hat{j}_v^{[2],\text{int}}(i,j) \right]^\dagger, \end{aligned} \quad (3.2.2)$$

where the MEC-SRC interference term is

$$\hat{j}_v^{[2],\text{int}}(i,j) = \hat{j}_v^{[2],\text{MEC}}(i,j) \hat{l}(i,j), \quad (3.2.3)$$

where \hat{l} represents short-range correlations described in Section 2.3. From this formula, it is clear that our framework distinguishes the following interaction contributions: the one-body

current on an independent nucleon, the two-body behavior from the one-body current acting on a short-range correlated pair, the two-body meson-exchange current on independent nucleons, and the two-body meson-exchange current acting on a short-range correlated pair of nucleons. We combine these elements coherently, accounting for their interference. In the following, it will become clear that this interference is essential for the resulting cross sections. To study the contribution of SRCs and MECs to the lepton-induced one- and two-nucleon knock-out reactions, we will use the default choices for model ingredients, as described in the previous sections. In Appendix A and Appendix B, we summarize the matrix elements and cross section formulas for the 1p1h and 2p2h cases. Then, we describe the reduced matrix elements for vector and axial operators in Appendix C.

Full model: inclusive electron scattering

Previously, in Section 2.3, Section 2.4, and Section 3.1, we performed analyses of components of our model by comparing them to inclusive electron scattering data. Here, we combine our results and confront the complete model again with the data of Ref. [40]. In Fig. 3.16, we present the final inclusive electron scattering results, separated into the longitudinal and transverse responses, for fixed $|\vec{q}|$. The net effect on the 1p1h responses is a $|\vec{q}|$ -dependent reduction and a $|\vec{q}|$ -independent

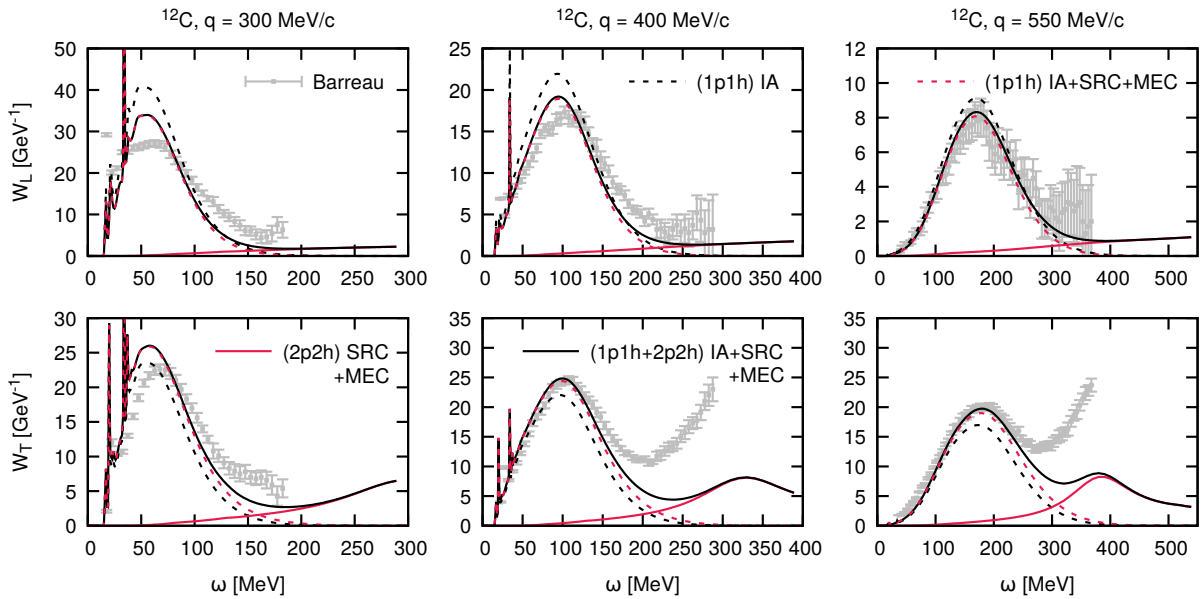


Figure 3.16: Inclusive hadronic responses for fixed momentum transfer values in electron scattering off the ^{12}C nucleus confronted with the experimental results of Ref. [40]. The black and red dashed lines present the 1p1h results with and without the two-body currents corrections, respectively. The solid blue line shows the 2p2h calculation, while the solid black line is the full calculation.

enhancement in the longitudinal and transverse ones, respectively. The 2p2h responses reflect the shape of the experimental data, leaving space for other essential processes in the transverse channel, such as single-pion production. In Fig. 3.17, we present the corrections to the 1p1h responses, comparing the effects of SRC, MEC, and only the Δ -currents. Generally, the longitudinal behavior is dominated by SRCs, while the transverse by MECs. We complete this part of the

analysis by presenting $2p2h$ responses in Fig. 3.18. Here, we observe how Δ -currents dominate the MEC contribution and how it interferes negatively with SRCs.

In Fig. 3.19, we present the complete model predictions for inclusive electron scattering cross sections for fixed values of the outgoing electron angle $\theta_{e'}$. Remembering that the SRC contribution is predominantly longitudinal and the MEC one purely transverse, we see a clear separation of physical scales of these mechanisms, especially in the two distinct peaks in the bottom left panel. We support the abovementioned observations with the general inclusive electron-nucleus cross section properties presented in Fig. 3.20. While the A -dependence of the emission of proton-proton pairs depends on kinematics and particular mechanisms involved, the emission of proton-neutron pairs follow the universal scaling of $A^{1.44}$. On top of that the ratio (pn/pp) of pair contributions is very irregular with respect to the kinematical conditions and varies from 5 to 20. Nevertheless, the final result is more consistent with the findings of Ref. [41] than the ratios presented in Fig. 3.10.

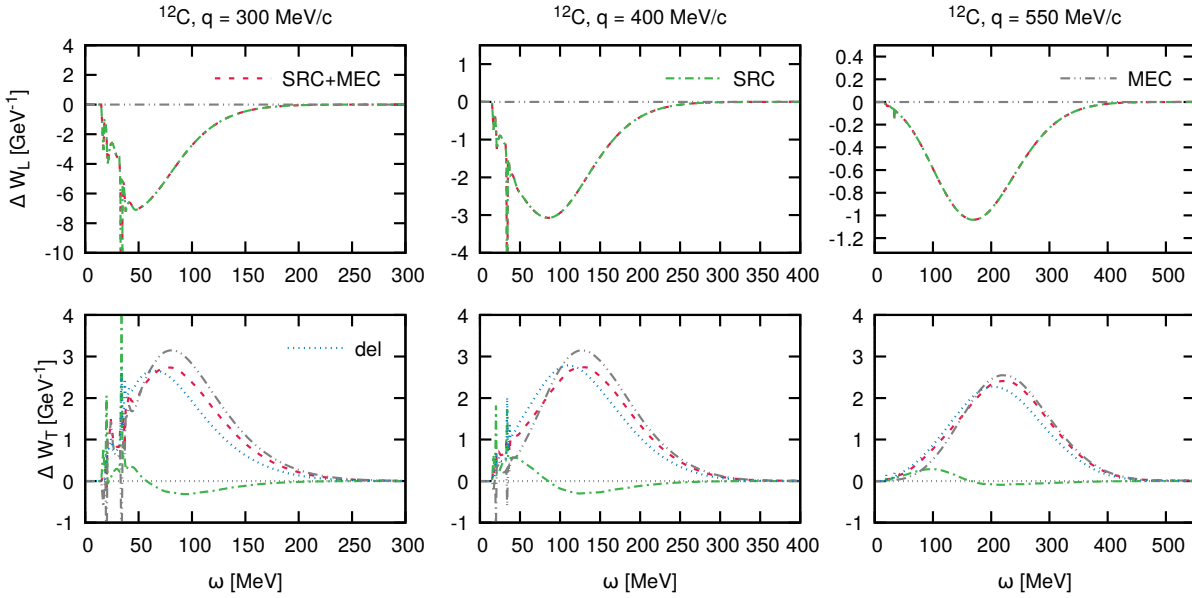


Figure 3.17: Corrections to the $1p1h$ hadronic responses for fixed momentum transfer values in electron scattering off the ^{12}C nucleus. Different curves correspond to the inclusion of the SRC or MEC dynamics, or both. The dotted line emphasizes the result of calculating Δ -current contributions only.

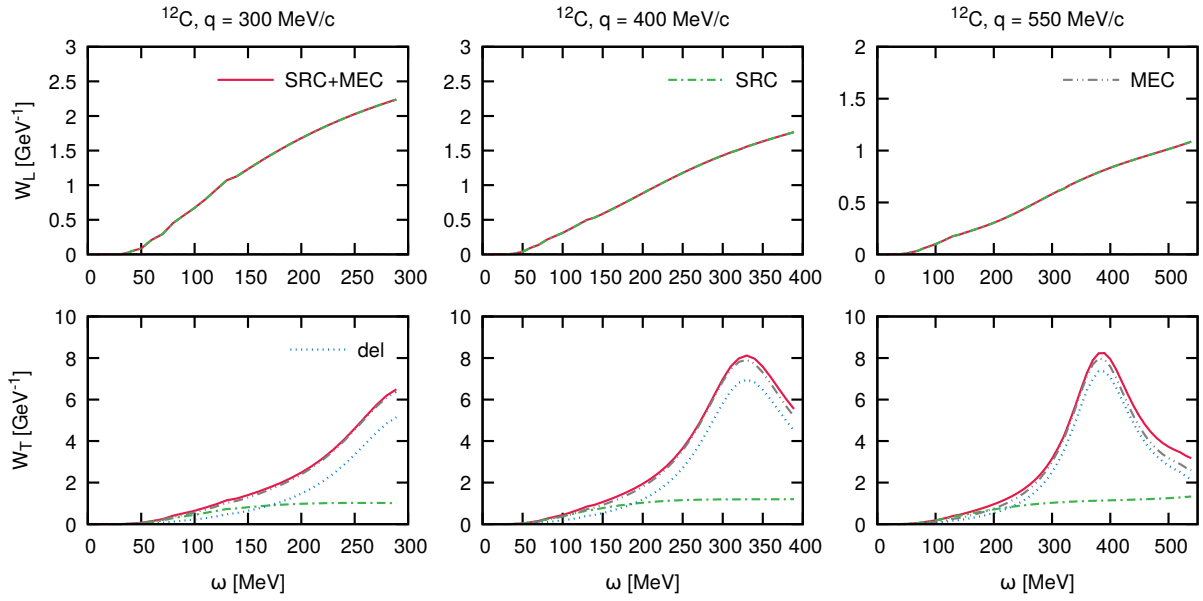


Figure 3.18: 2p2h hadronic responses for fixed momentum transfer values in electron scattering off the ^{12}C nucleus. Different curves correspond to the inclusion of the SRC or MEC dynamics, or both. The dotted line emphasizes the result of calculating Δ -current contributions only.

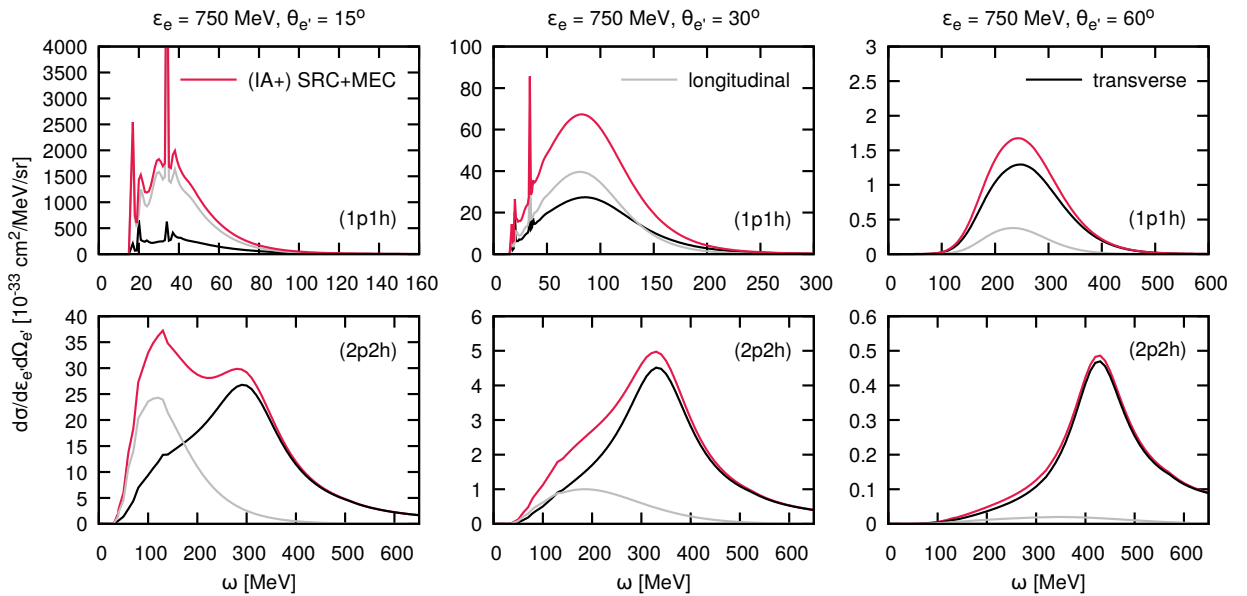


Figure 3.19: Inclusive cross sections for electron scattering off the ^{12}C nucleus for fixed outgoing electron angle $\theta_{e'}$ = 15° , 30° , 60° . The gray and black lines correspond to the longitudinal and transverse contributions, respectively. The red line shows the final calculation involving short-range correlations and meson-exchange currents.

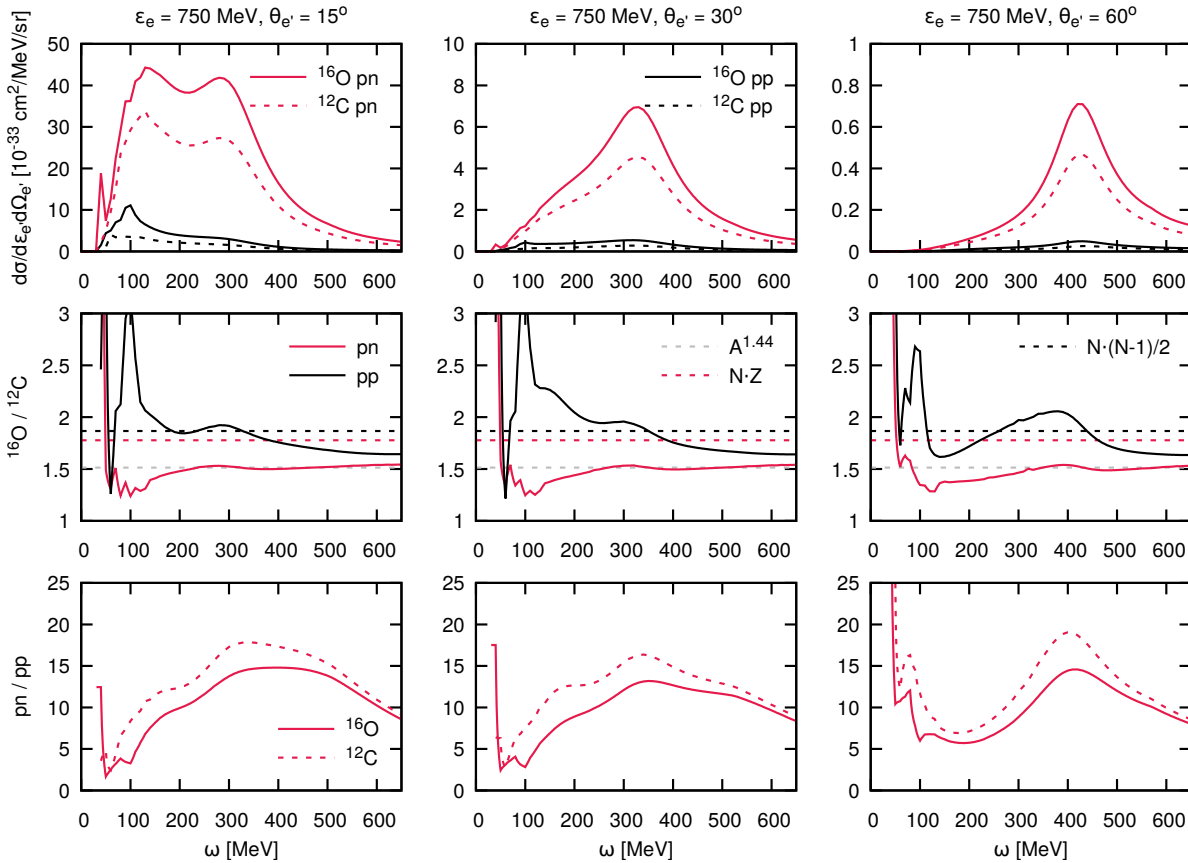


Figure 3.20: Contribution of the different outgoing nucleon pairs to the inclusive electron scattering cross sections induced by short-range correlations and meson-exchange currents. (Top) the separation between proton-neutron and proton-proton final pairs presented with the red and black lines, respectively. Here, the solid lines show the scattering off ^{16}O , while the dashed lines show the scattering off the ^{12}C nucleus. (Middle) $^{16}\text{O}/^{12}\text{C}$ ratio of the inclusive cross sections for proton-neutron (green) and proton-proton (black) pairs. The dashed lines present different ratios of nuclear constituents. (Bottom) ratio of different outgoing nucleon pair contributions to the investigated cross sections, where the solid and dashed lines correspond to the ^{16}O and ^{12}C target nuclei, respectively.

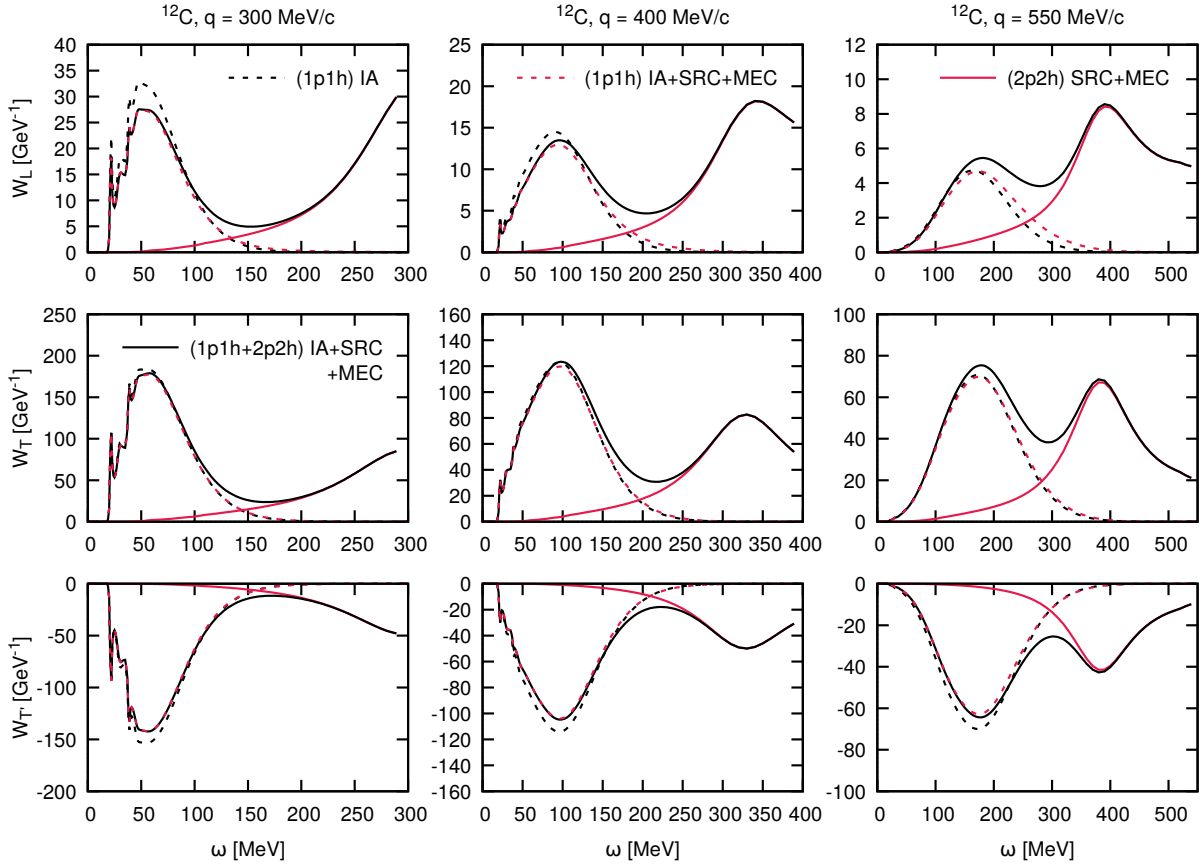


Figure 3.21: Inclusive hadronic responses for fixed momentum transfer values in neutrino scattering off the ^{12}C nucleus. The black and red dashed lines present the 1p1h results with and without the two-body currents corrections, respectively. The solid blue line shows the 2p2h calculation, while the solid black line is the full calculation.

Full model: inclusive neutrino scattering

In this subsection, we present the results of the complete model of inclusive neutrino-nucleus scattering mediated by one- and two-body currents. Fig. 3.21 illustrates the three kinds of responses for fixed values of the momentum transfer $|\vec{q}|$. We observe significant differences in the longitudinal channel relative to the electron case. Due to the longitudinal axial Δ -current and its combination with the seagull axial density, the MEC properties dominate the response for the higher ω and $|\vec{q}|$. The 1p1h response suppression is noticeable only for the lowest momentum transfer. The transverse responses have no MEC enhancement, and the 1p1h results remain unchanged. All calculations present a visible structure of two peaks: 1p1h and 2p2h. In Fig. 3.23, we show the corrections to 1p1h responses, comparing the contributions from SRC and MEC components. One can observe a nontrivial interplay between the two effects, which mainly results in a reduction at lower and an enhancement at higher regions of ω . The corresponding analysis of the 2p2h responses is presented in Fig. 3.24. Here, we observe a behavior that is very similar to one of the electron case, with the Δ -currents dominating the two-nucleon knock-out process.

Finally, we present neutrino-nucleus inclusive cross section calculations, including SRC and

MEC dynamics. Fig. 3.25 shows the results for an incoming muon neutrino energy of $\epsilon_{\nu_\mu} = 750$ MeV and fixed values of the outgoing muon angle $\theta_\mu = 15^\circ, 30^\circ, 60^\circ$. Compared to the electron results of Fig. 3.19, we find a significant reduction of the SRC contribution, as the conditions are more transverse in the neutrino case. We summarize the $2p2h$ cross section properties in Fig. 3.26. Once again, we see that the A -dependence of the complete model calculations on proton-neutron initial pairs scales as $A^{1.44}$. The (pp/pn) pairs emission ratio, which in the neutrino-induced reactions translates to the interactions on proton-neutron and neutron-neutron initial pairs, varies from 4 to 6. This result is consistent with the results of Ref. [21].

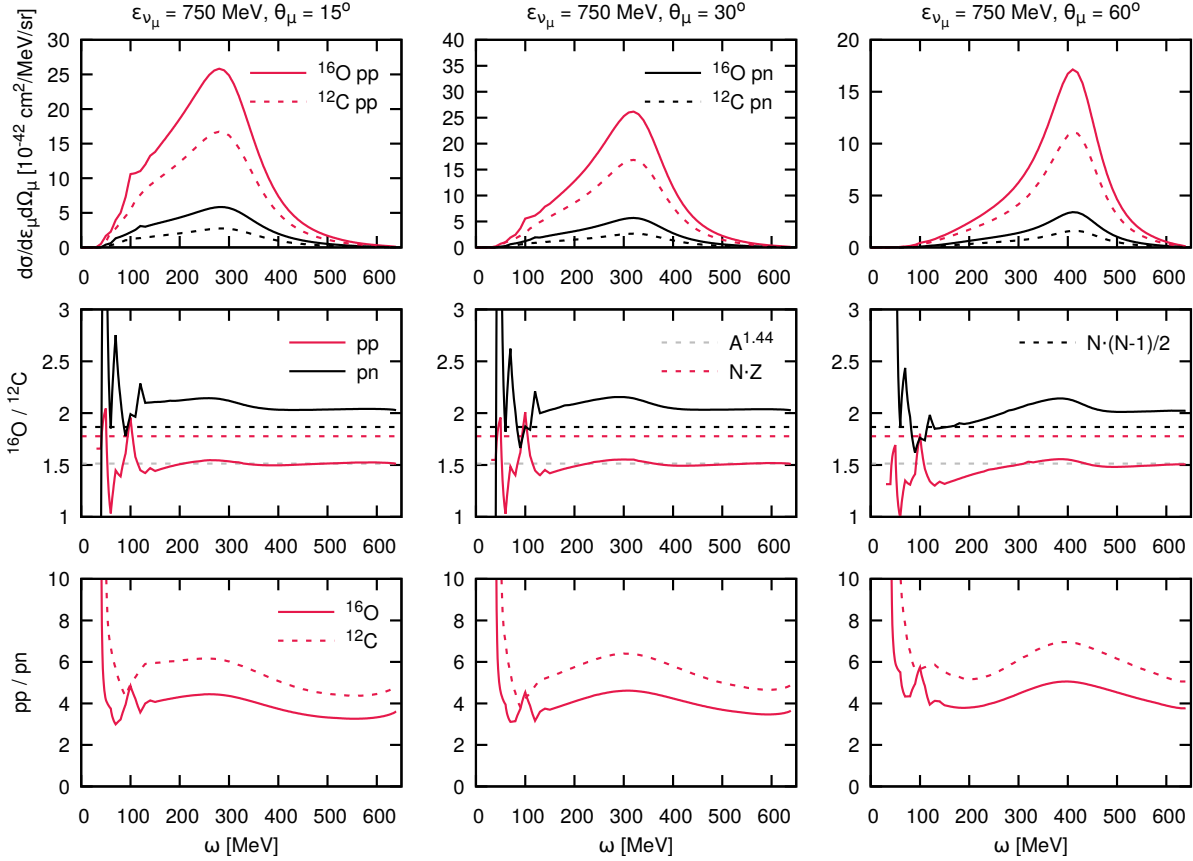


Figure 3.22: Contribution of the different outgoing nucleon pairs to the inclusive neutrino scattering cross sections induced by short-range correlations and meson-exchange currents. (Top) the separation between proton-proton and proton-neutron final pairs presented with the red and black lines, respectively. Here, the solid lines show the scattering off ^{16}O , while the dashed lines show the scattering off the ^{12}C nucleus. (Middle) $^{16}\text{O}/^{12}\text{C}$ ratio of the inclusive cross sections for proton-proton (green) and proton-neutron (black) pairs. The dashed lines present different ratios of nuclear constituents. (Bottom) ratio of different outgoing nucleon pair contributions to the investigated cross sections, where the solid and dashed lines correspond to the ^{16}O and ^{12}C target nuclei, respectively.

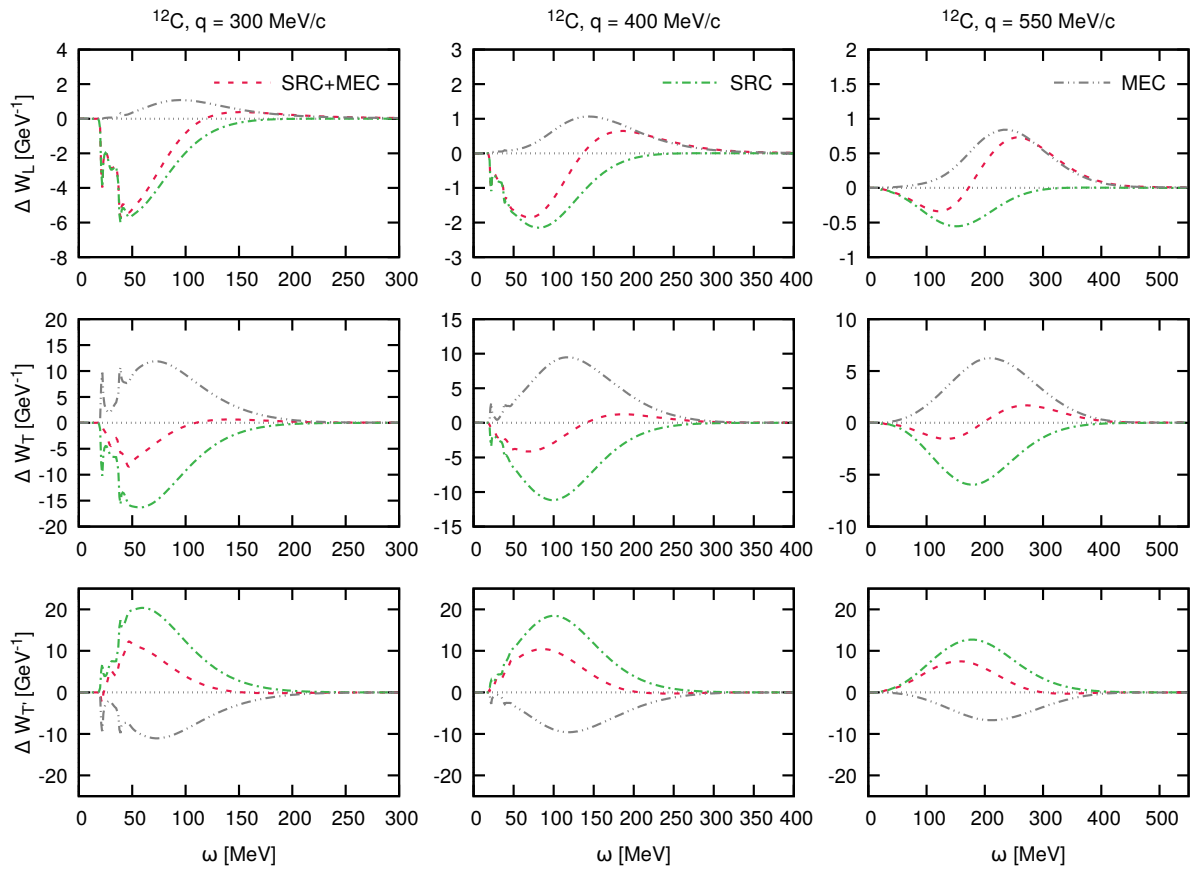


Figure 3.23: Corrections to the 1p1h hadronic responses for fixed momentum transfer values in neutrino scattering off the ^{12}C nucleus. Different curves correspond to the inclusion of the SRC or MEC dynamics, or both. The dotted result emphasizes the sole result of calculating Δ -currents contributions.

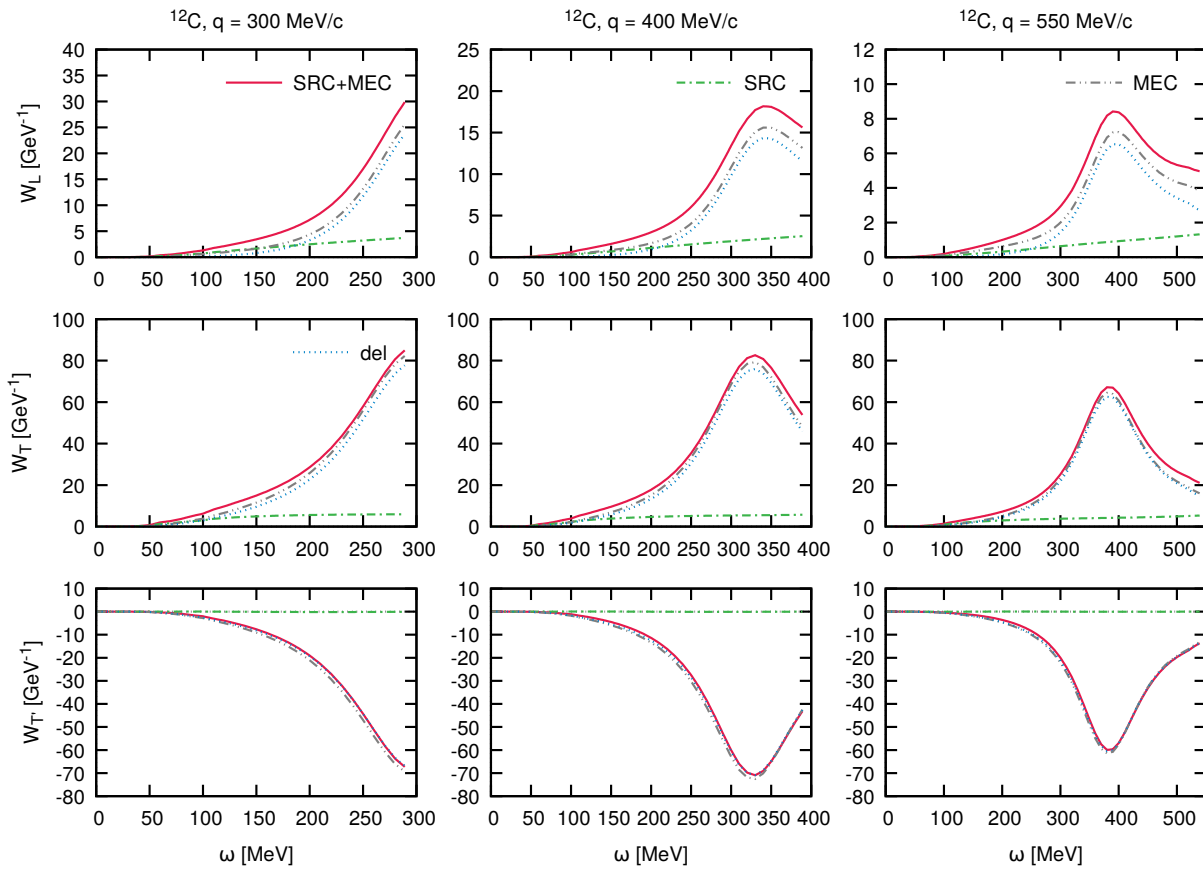


Figure 3.24: 2p2h hadronic responses for fixed momentum transfer values in neutrino scattering off the ^{12}C nucleus. Different curves correspond to the inclusion of the SRC or MEC dynamics, or both. The dotted result emphasizes the sole result of calculating Δ -currents contributions.

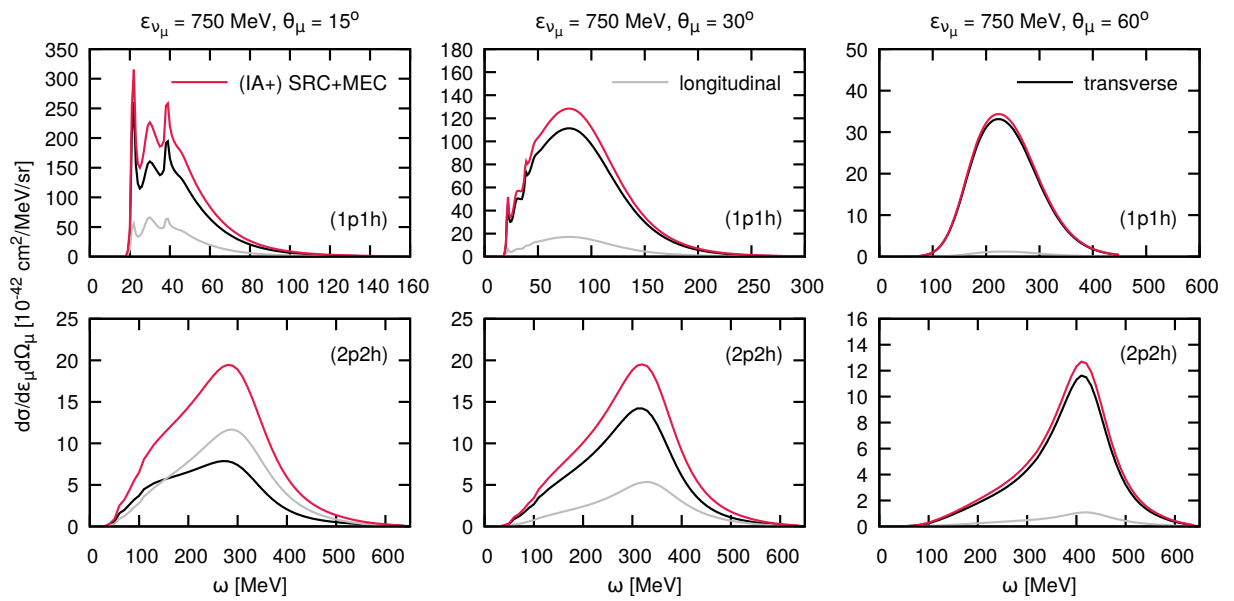


Figure 3.25: Inclusive cross sections for neutrino scattering off the ^{12}C nucleus for fixed outgoing muon angle $\theta_\mu = 15^\circ, 30^\circ, 60^\circ$. The gray and black lines correspond to the longitudinal and transverse contributions, respectively. The red line shows the final calculation involving short-range correlations and meson-exchange currents.

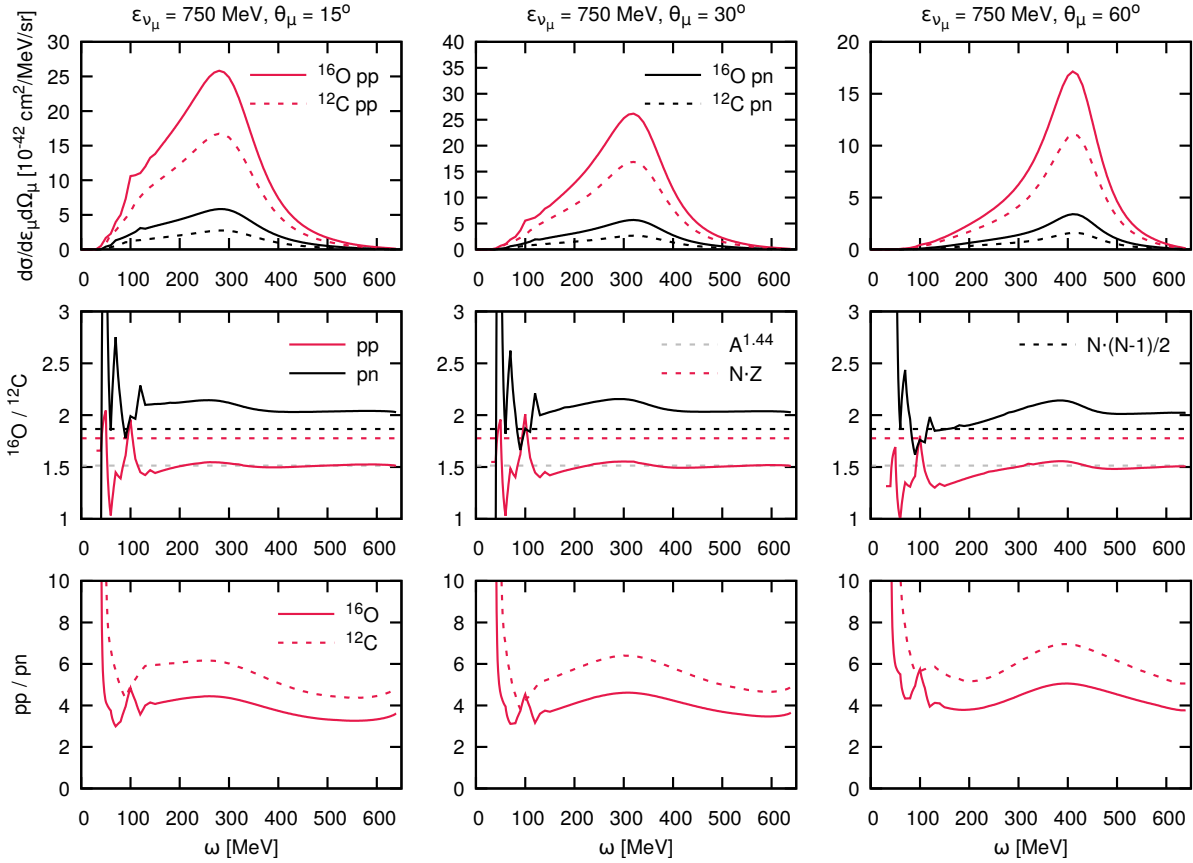


Figure 3.26: Contribution of the different outgoing nucleon pairs to the inclusive neutrino scattering cross sections induced by short-range correlations and meson-exchange currents. (Top) the separation between proton-proton and proton-neutron final pairs presented with the red and black lines, respectively. Here, the solid lines show the scattering off ^{16}O , while the dashed lines show the scattering off the ^{12}C nucleus. (Middle) $^{16}\text{O}/^{12}\text{C}$ ratio of the inclusive cross sections for proton-proton (green) and proton-neutron (black) pairs. The dashed lines present different ratios of nuclear constituents. (Bottom) ratio of different outgoing nucleon pair contributions to the investigated cross sections, where the solid and dashed lines correspond to the ^{16}O and ^{12}C target nuclei, respectively.

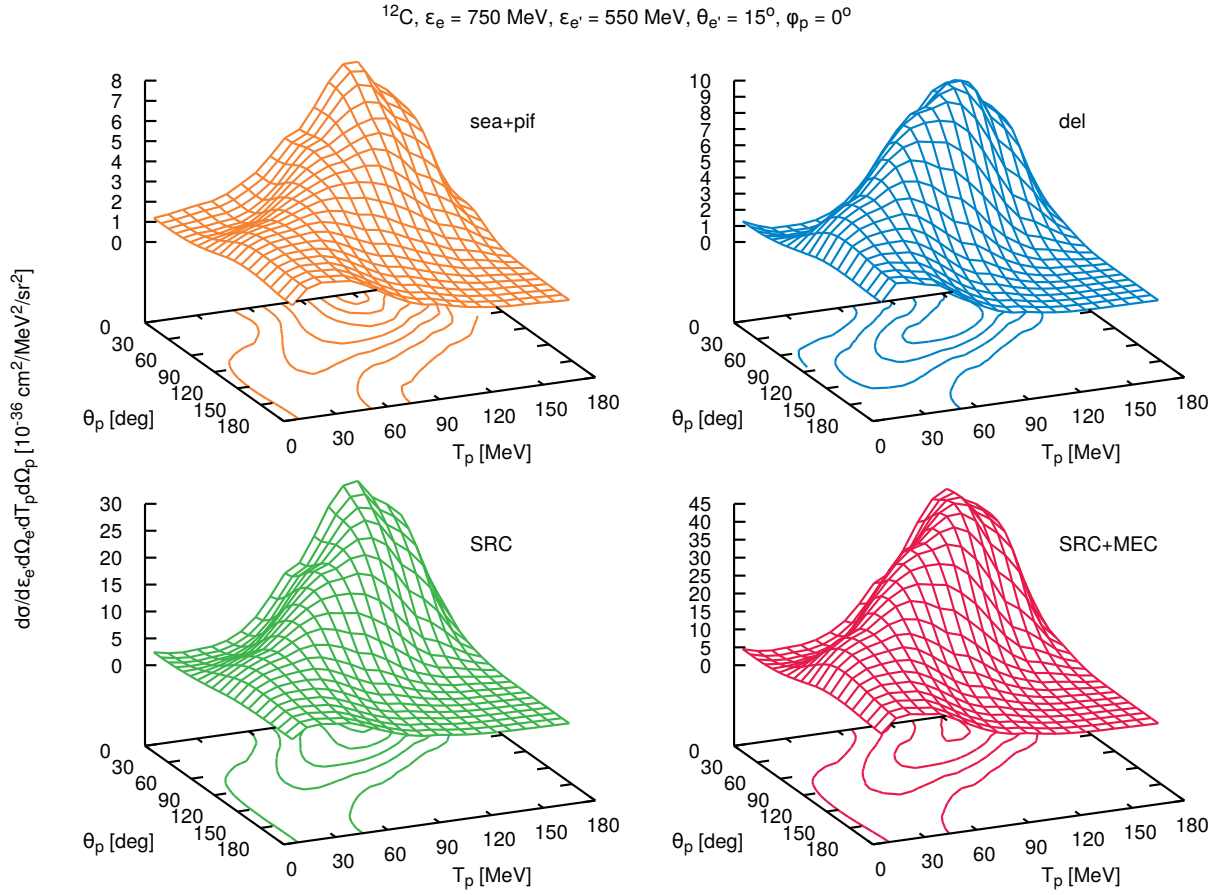


Figure 3.27: Semi-inclusive $^{12}\text{C}(e, e'p)$ cross section for the incoming energy $\epsilon_i = 750$ MeV at the deflection angle $\theta = 15^\circ$. The distributions correspond to the energy transfer $\omega = 200$ MeV and in-plane nucleon kinematics ($\phi = 0^\circ$). The calculations involve: (top left) seagull and pion-in-flight currents, (top right) Δ -currents, (bottom left) short-range correlations, and (bottom right) all the contributions added coherently.

Full model: semi-inclusive two-nucleon knock-out

The true strength of our model lies in its ability to produce exclusive cross section predictions that account for the kinematics of the outgoing nucleons in electron- and neutrino-induced two-nucleon knock-out reactions. We exemplify this power in a series of semi-inclusive cross section results with the kinematics corresponding to the previous inclusive cross sections and $\omega = 200$ MeV, targeting the dip region between the SRC and MEC contributions. Fig. 3.27 presents semi-inclusive electron-induced two-nucleon knock-out cross sections on the Carbon target, comparing particular dynamical models. We see that seagull+pion-in-flight, Δ -currents, and SRC calculations provide a similar shape as a function of the kinetic energy and angle of the detected nucleon. For such forward kinematics ($\theta_{e'} = 15^\circ$), the proton also peaks in the forward direction. In Fig. 3.28, we show the contributions from proton-proton and proton-neutron emission to the SRC+MEC calculation. Although the results differ in magnitude, their shape reflects the general features of this kinematical regime.

Fig. 3.29 presents semi-inclusive neutrino-induced two-nucleon knock-out cross sections on the Carbon target. The distributions are similar to the electron case, yet slightly less peaked, especially

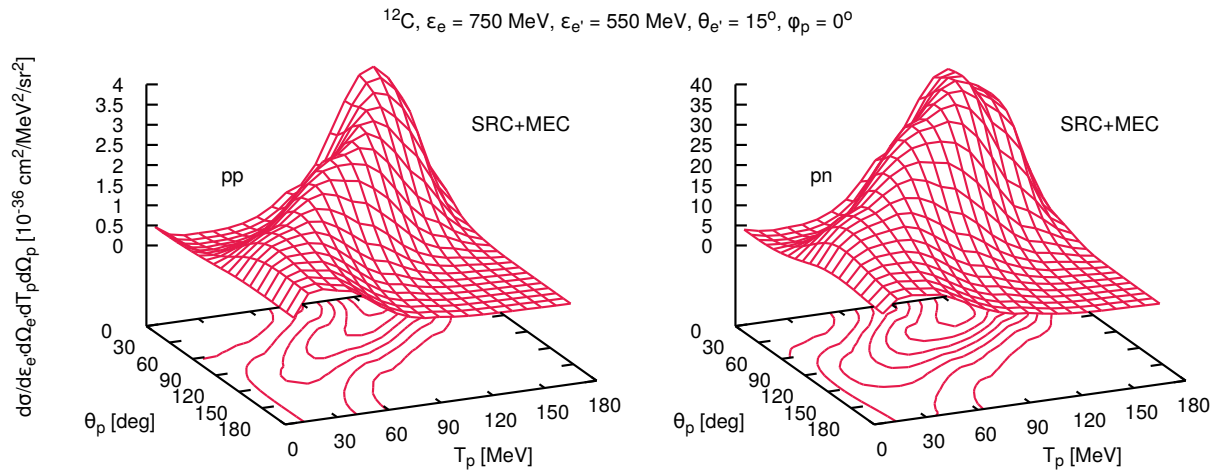


Figure 3.28: Semi-inclusive $^{12}\text{C}(e, e'p)$ cross section calculated with the full model, for the incoming energy $\epsilon_i = 750$ MeV at the deflection angle $\theta = 15^\circ$. The distributions correspond to the energy transfer $\omega = 200$ MeV and in-plane nucleon kinematics ($\phi = 0^\circ$). The calculations are separated into (left) the proton-proton and (right) proton-neutron outgoing pair contributions.

the seagull+pion-in-flight contribution. In Fig. 3.30, we show the results of proton-neutron and proton-proton emission to the SRC+MEC calculation. Here, the former is more peaked but retains properties similar to all distributions presented in this subsection.

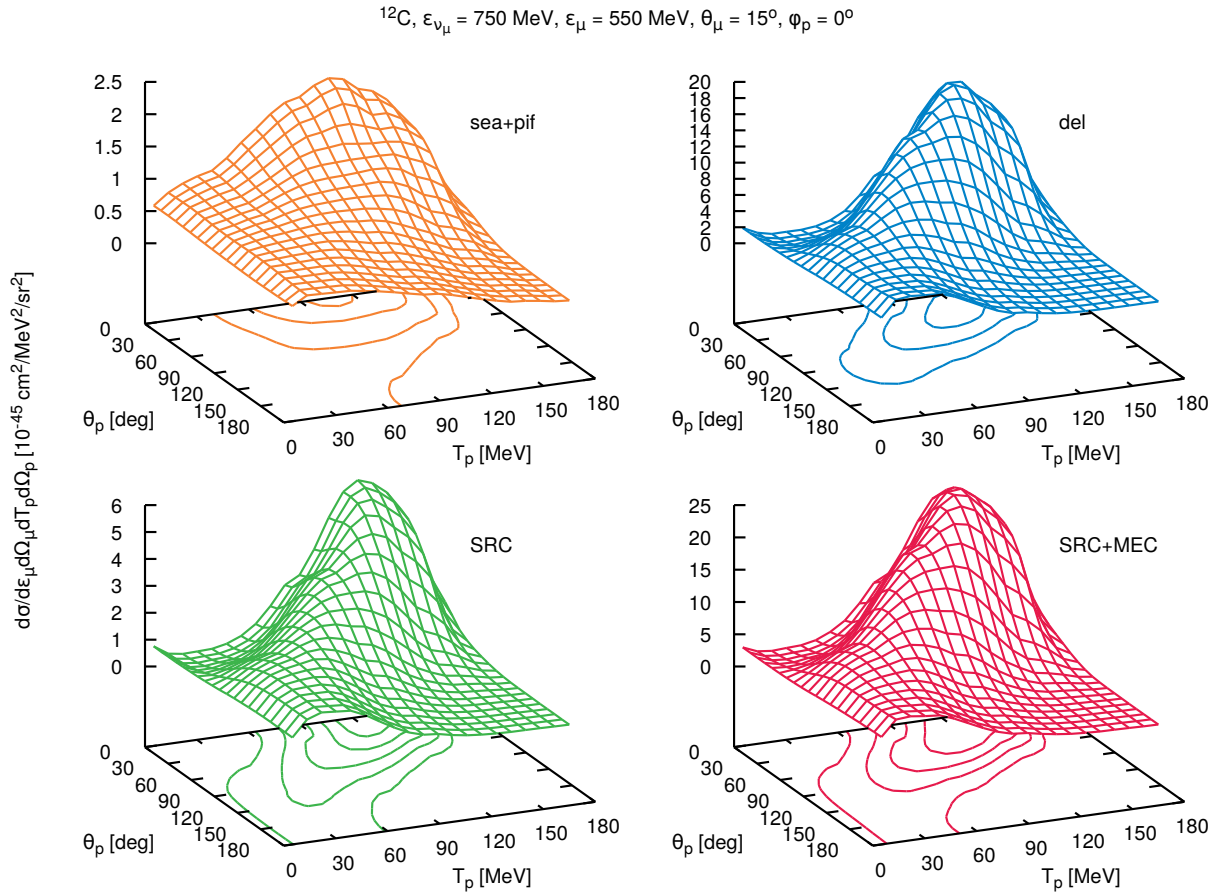


Figure 3.29: Semi-inclusive $^{12}\text{C}(\nu_\mu, \mu p)$ cross section for the incoming energy $\epsilon_i = 750$ MeV at the deflection angle $\theta = 15^\circ$. The distributions correspond to the energy transfer $\omega = 200$ MeV and in-plane nucleon kinematics ($\phi = 0^\circ$). The calculations involve: (top left) seagull and pion-in-flight currents, (top right) Δ -currents, (bottom left) short-range correlations, and (bottom right) all the contributions added coherently.

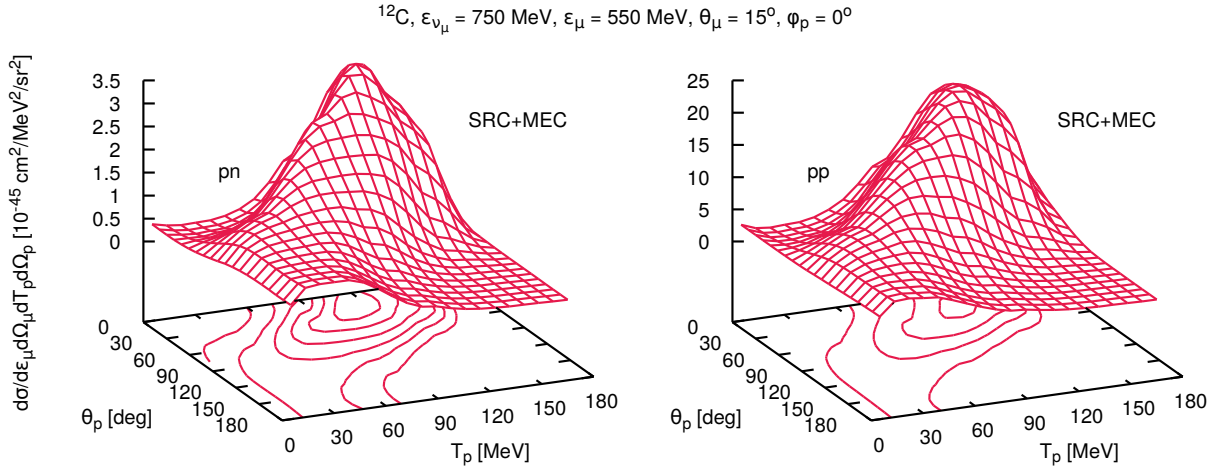


Figure 3.30: Semi-inclusive $^{12}\text{C}(\nu_\mu, \mu p)$ cross section calculated with the full model, for the incoming energy $\epsilon_i = 750$ MeV at the deflection angle $\theta = 15^\circ$. The distributions correspond to the energy transfer $\omega = 200$ MeV and in-plane nucleon kinematics ($\phi = 0^\circ$). The calculations are separated into (left) the proton-neutron and (right) proton-proton outgoing pair contributions.

Full model: exclusive two-nucleon knock-out

Exclusive cross sections in $2p2h$ reactions provide interaction probabilities on the whole 8-dimensional phase space. These calculations are the closest to the experimental picture, as modeled by Monte Carlo neutrino event generators. However cumbersome, such calculations, with the complete kinematics constrained, are numerically less demanding than the inclusive computations. Fig. 3.31 presents the electron-induced interaction cross sections for the kinematical conditions described in the previous subsection. The outgoing nucleons are in-plane, which means their relative ϕ angle is zero. Here, we see the characteristic back-to-back nucleon configurations for all models involved: seagull+pion-in-flight, Δ -currents, and SRC. In Fig. 3.32, we distinguish the emission of proton-proton and proton-neutron pairs. We observe that the angular distributions for the former are symmetric, while the difference in nucleon isospin introduces a small asymmetry.

Fig. 3.33 presents exclusive neutrino-induced two-nucleon knock-out cross sections on the Carbon target. One can see that the top left distribution (seagull+pion-in-flight) is the only one that provides back-to-back configurations for higher angles of the nucleons. However, the other, forward peaked, contributions provide significantly more strength and dominate the final result in angular distribution presented at the bottom right panel. We conclude this analysis by presenting the proton-neutron and proton-proton emission contributions to the exclusive neutrino-induced two-nucleon knock-out processes in Fig. 3.34. Here, the asymmetry that was anticipated from electron results does not appear. However, the left distribution has an irregular peak structure. Understanding the origin of this effect will require a dedicated investigation.

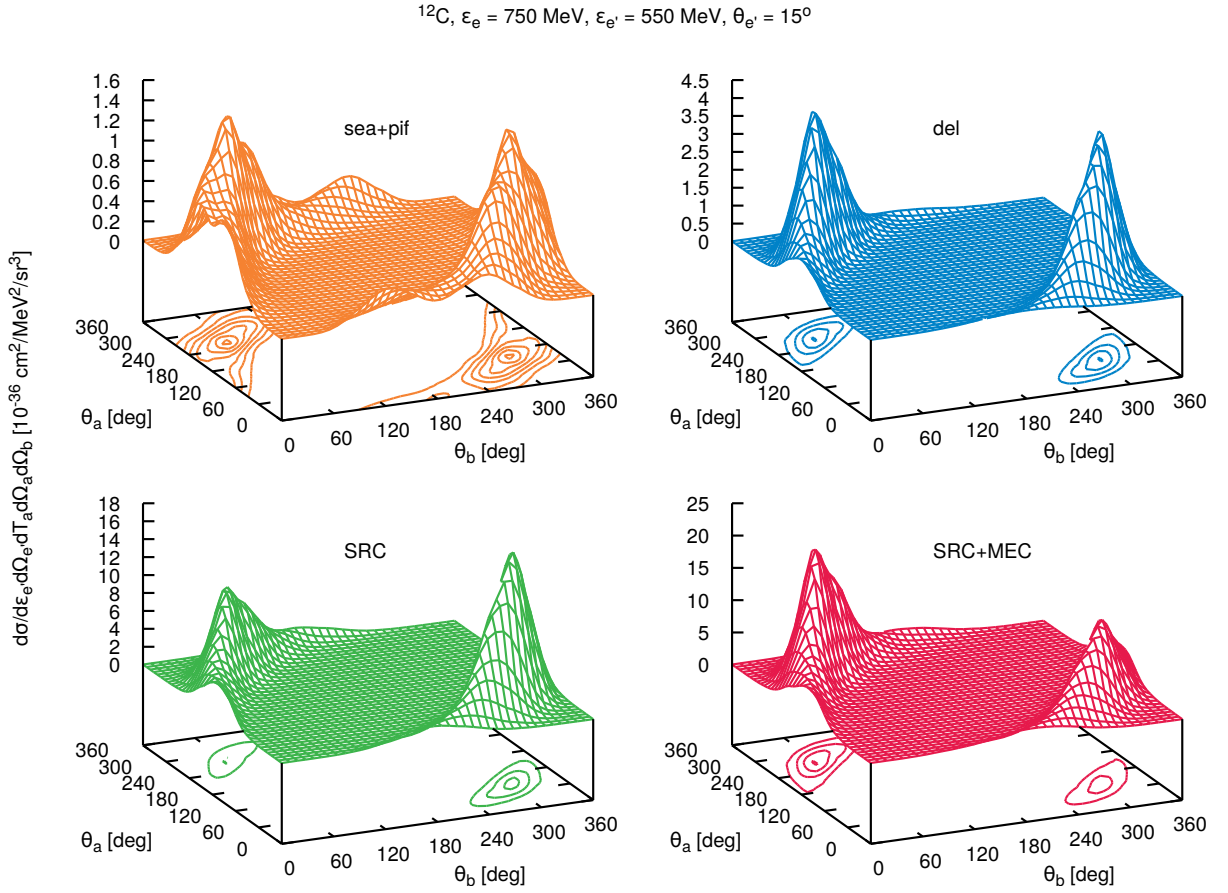


Figure 3.31: Exclusive $^{12}\text{C}(e, e'N_a N_b)$ cross section for the incoming energy $\epsilon_i = 750$ MeV at the deflection angle $\theta = 15^\circ$. The distributions correspond to the energy transfer $\omega = 200$ MeV and in-plane nucleon kinematics ($\phi = 0^\circ$). The calculations involve: (top left) seagull and pion-in-flight currents, (top right) Δ -currents, (bottom left) short-range correlations, and (bottom right) all the contributions added coherently.

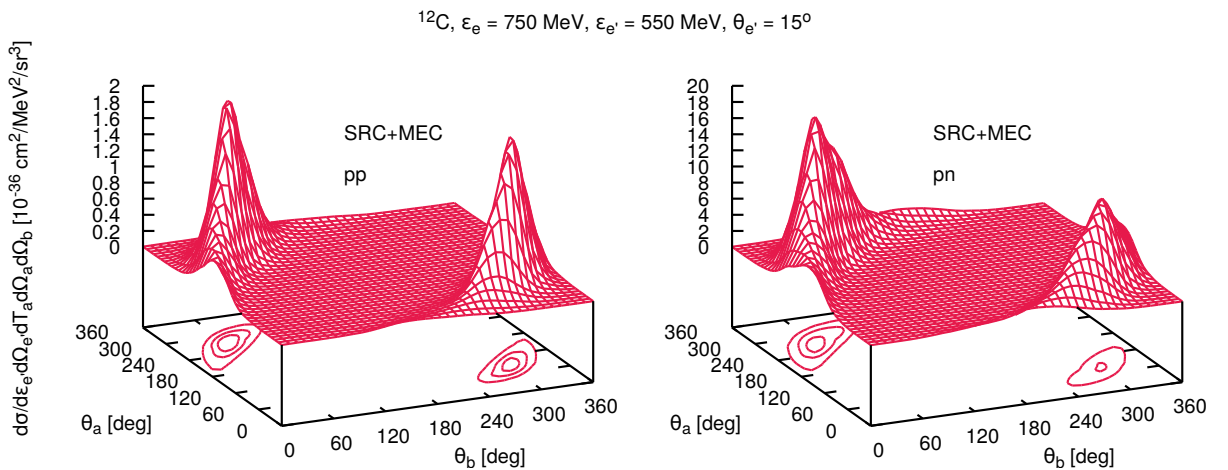


Figure 3.32: Exclusive $^{12}\text{C}(e, e'N_a N_b)$ cross section calculated with the full model, for the incoming energy $\epsilon_i = 750$ MeV at the deflection angle $\theta = 15^\circ$. The distributions correspond to the energy transfer $\omega = 200$ MeV and in-plane nucleon kinematics ($\phi = 0^\circ$). The calculations are separated into (left) the proton-proton and (right) proton-neutron outgoing pair contributions.

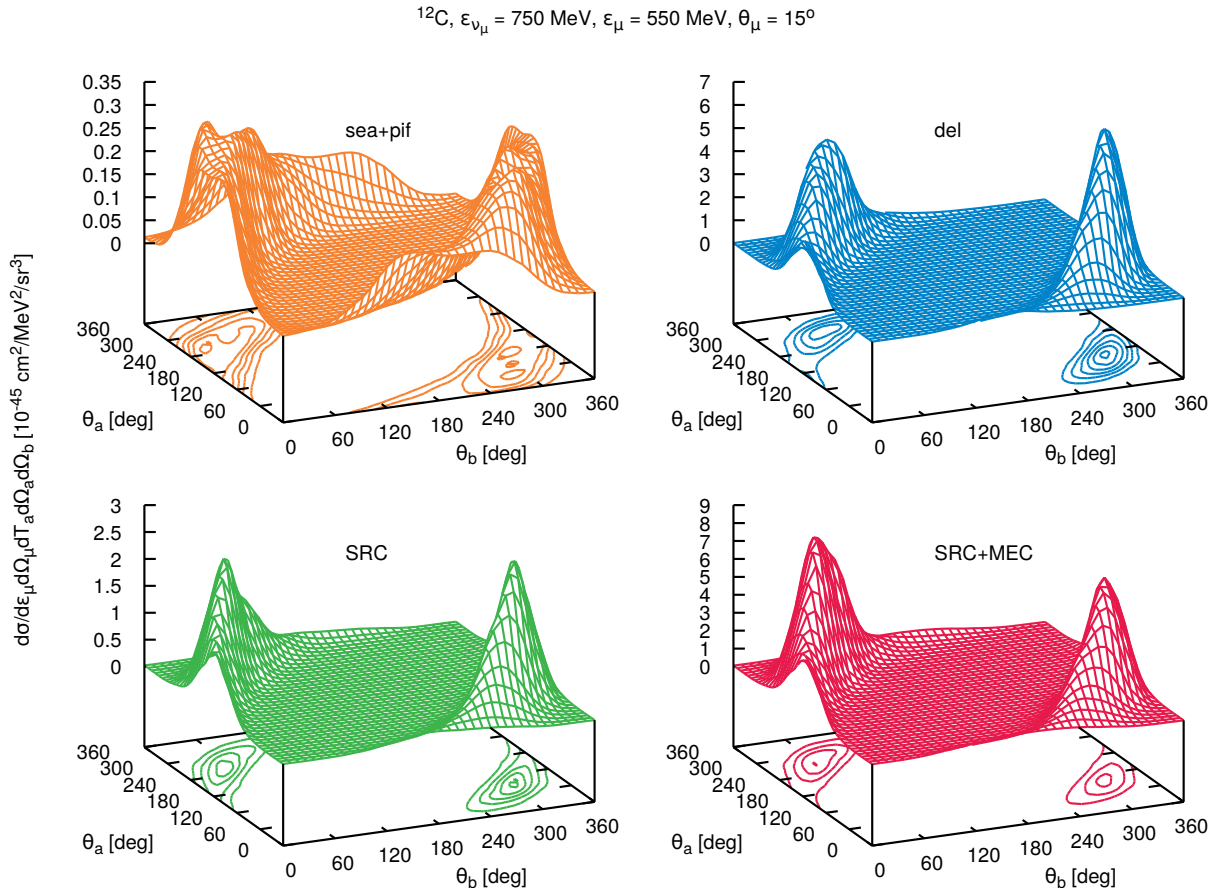


Figure 3.33: Exclusive $^{12}\text{C}(\nu_{\mu}, \mu N_a N_b)$ cross section for the incoming energy $\epsilon_i = 750 \text{ MeV}$ at the deflection angle $\theta = 15^{\circ}$. The distributions correspond to the energy transfer $\omega = 200 \text{ MeV}$ and in-plane nucleon kinematics ($\phi = 0^{\circ}$). The calculations involve: (top left) seagull and pion-in-flight currents, (top right) Δ -currents, (bottom left) short-range correlations, and (bottom right) all the contributions added coherently.

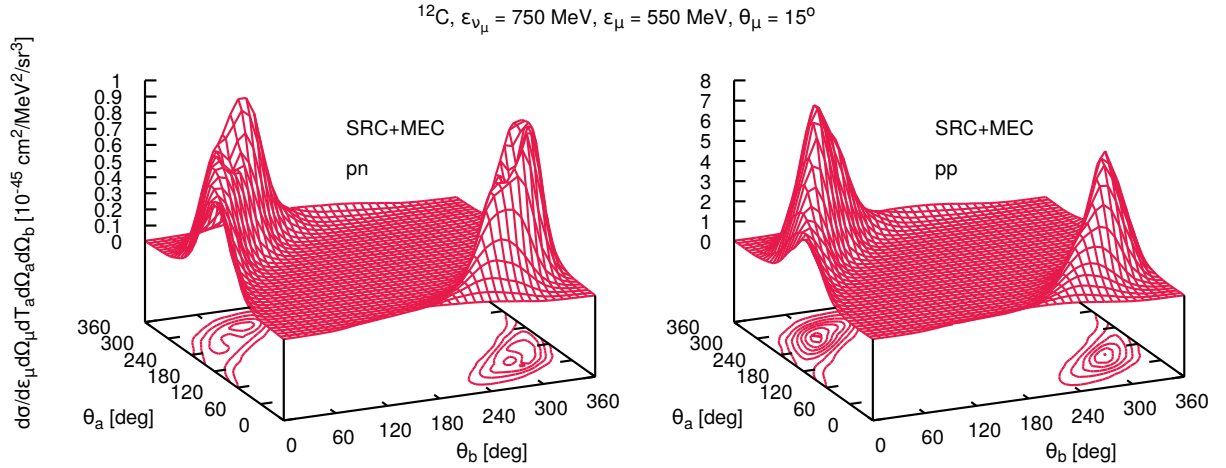


Figure 3.34: Exclusive $^{12}\text{C}(\nu_\mu, \mu N_a N_b)$ cross section calculated with the full model, for the incoming energy $\epsilon_i = 750 \text{ MeV}$ at the deflection angle $\theta = 15^\circ$. The distributions correspond to the energy transfer $\omega = 200 \text{ MeV}$ and in-plane nucleon kinematics ($\phi = 0^\circ$). The calculations are separated into (left) the proton-neutron and (right) proton-proton outgoing pair contributions.

3.3 Constraining the vector interaction

As encountered several times previously in this work, neutrino and electron interactions share many similarities. The models used to describe the dynamics of target nucleons in lepton-nucleus processes are almost equivalent. Moreover, weak interactions are composed of vector and axial parts, while only the former is found in electron interactions. However, this allows us to constrain at least the vector part of the model through comparisons with the extensive datasets of accurate electron scattering results. Thus, a prerequisite for a reliable neutrino-nucleus interaction model is the ability to reproduce its electron equivalent.

In our analyses performed in Section 2.3, Section 2.4, Section 3.1, and Section 3.2, we found differences in the behavior of our model while adjusting the theoretical assumptions and model components. Focusing on the vector interaction, we were able to eliminate the uncertainties connected to choosing non-relativistic formulations of the axial meson-exchange currents. We identify the most biased aspect of the SRC calculation to be the numerical input to the central correlation function. After the discussion of Fig. 2.16 and Fig. 2.17, we concluded that the Gearhart (GD) and VMC calculations provide a reasonable understanding of the potential model uncertainty. We consider the OMY solutions unrealistic[25]. Then, in the MEC contributions, we focus on the Δ -currents, which are the least constrained theoretically due to the involvement of spin $3/2$ -particles. As presented in Fig. 3.7 and Fig. 3.8, our calculations are very sensitive to the choice of the Δ -isobar propagator prescription. In what follows, we utilize the full model formulation. However, as presented by other theoretical groups [39], the overlap between the Δ -resonance modeled in MECs (virtual pion) and SPP (real pion) is not trivial, and double-counting of the excitation strength is inevitable. As argued by A. De Pace *et al.*, subtracting the imaginary part of the Δ propagator removes the components linked to the real pion production. As this approach

is relatively crude, we consider this as an uncertainty of our model. The answer to this problem depends on the particular single-pion production model used and requires a dedicated study. It is possible that a consistent formulation combining MECs and SPP does not exist and should be dealt with using phenomenological approaches.

Comparison to the JLab Hall A data

Before we compare to inclusive electron scattering data, we need a model for single-pion production to extend the reliability of our results to the first resonance peak. For this purpose, we use the Hybrid model of Ghent [3] in its latest parametrization [43]. This model has proved to provide accurate results for electron- [44] and neutrino-nucleus scattering processes [33,45].

In Fig. 3.35, we present our comparison to the inclusive electron scattering data of Ref. [46]. The 1p1h and 2p2h calculations involve the uncertainties originating in the degrees of freedom

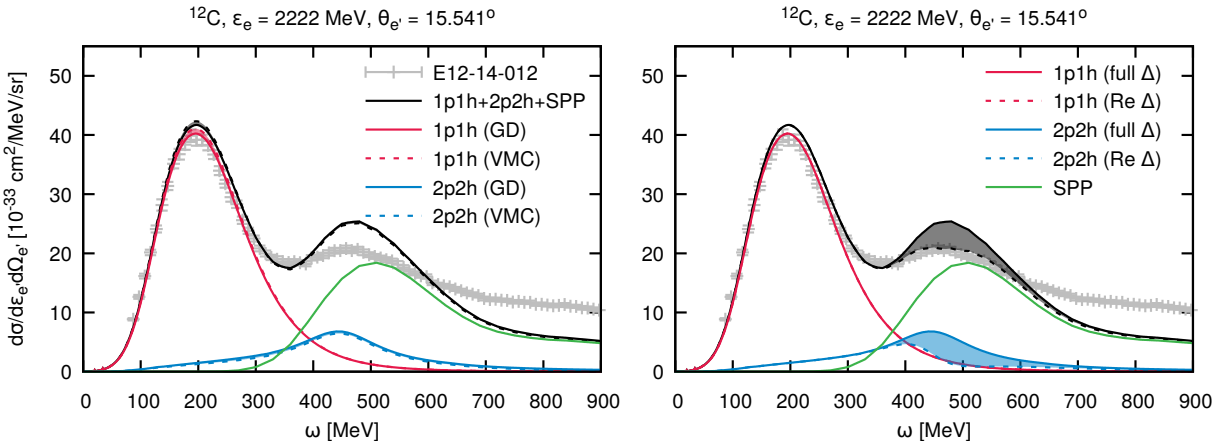


Figure 3.35: Inclusive $^{12}\text{C}(e, e')$ electron scattering cross section as a function of the energy transfer ω , for incoming projectile energy $\epsilon_e = 2222$ MeV and the deflection angle $\theta_{e'} = 15.541^\circ$ as measured by Ref. [46]. The red, blue, green, and black curves correspond to the calculated results from one-, two-nucleon knock-out, single-pion production, and combined channels, respectively. The 1p1h and 2p2h calculations include a selection of model uncertainties due to (left) the choice of the central correlation function, and (right) the descriptions of the Δ -isobar propagator, denoted by solid and dashed lines.

discussed above: the choice of the central correlation function and the treatment of the Δ propagator, respectively. As expected, the former modifies mostly the 1p1h part, while the latter only the 2p2h strength. We can see that all of the solutions slightly overestimate the height of the quasielastic peak, and an additional reduction is needed. This issue can be solved by introducing more nuclear effects accounting for nuclear correlations, but it goes beyond the scope of this study. The description of the Δ peak with the described models is challenging and requires using the complete removal of the imaginary part of the Δ propagator. This is consistent with the results of Ref. [47], even considering the lower inelastic interaction strength presented therein. We summarize our results, including both modeling degrees of freedom in Fig. 3.36.

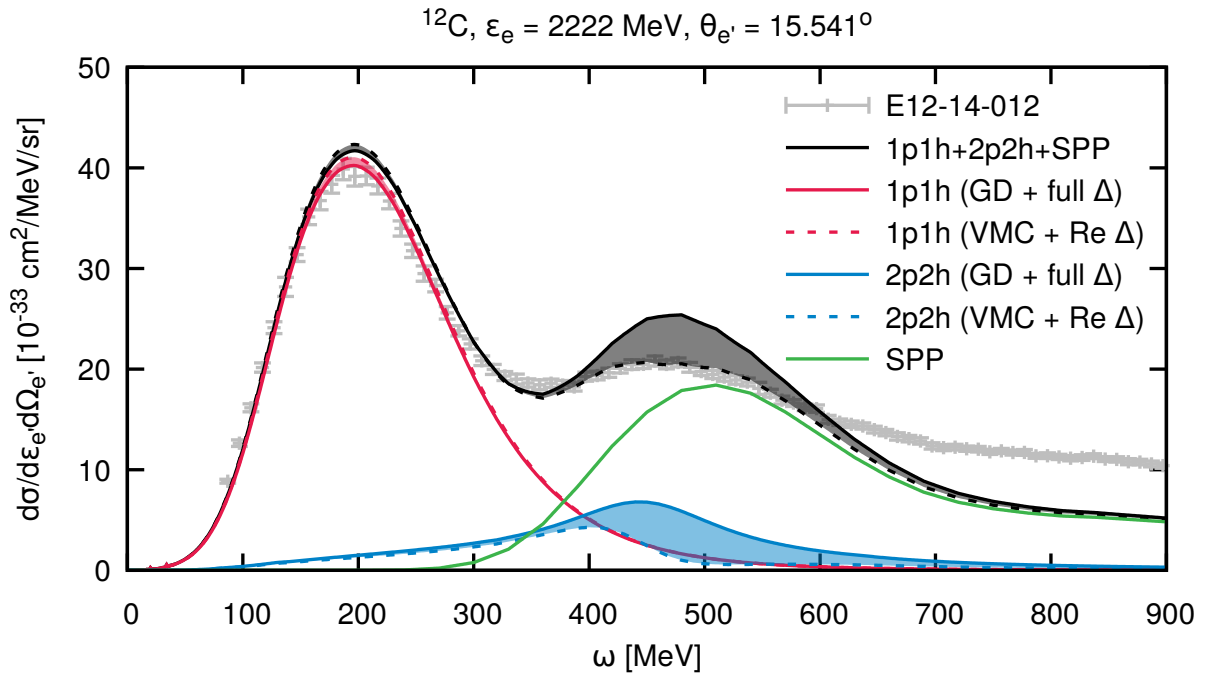


Figure 3.36: Inclusive $^{12}\text{C}(e, e')$ electron scattering cross section as a function of the energy transfer ω , for in coming projectile energy $\epsilon_e = 2222$ MeV and the deflection angle $\theta_{e'} = 15.541^\circ$ as measured by Ref. [46]. The red, blue, green, and black curves correspond to the calculated results from one-, two-nucleon knock-out, single-pion production, and combined channels, respectively. The 1p1h and 2p2h calculations include a selection of model uncertainties due to the choice of the central correlation function and the descriptions of the Δ -isobar propagator, denoted by solid and dashed lines.

Systematic study of model uncertainties

In this subsection, we wish to extend our comparisons to inclusive electron scattering datasets covering various kinematical regimes on the ^{12}C and ^{16}O nuclear targets. Following the approach of Ref. [39], we arrange our comparisons in an increasing order of the momentum transfer at the quasielastic peak ($|\vec{q}_{\text{QE}}|$). Fig. 3.37 presents the 1p1h and 2p2h electron scattering results of our model compared to the experimental dataset in 4 kinematical setups on the Carbon target. In the top left panel ($|\vec{q}_{\text{QE}}| \simeq 286$ MeV/c), we see a significant need to reduce the 1p1h peak and extend its tail in ω . This lack of additional spectroscopic-factors-like reduction is a general feature of our model for lower energies and requires an introduction of more long-range correlation effects. In this panel, the 2p2h contribution misses strength around $\omega \simeq 200$ MeV. Then, in the top right ($|\vec{q}_{\text{QE}}| \simeq 508$ MeV/c) and bottom left ($|\vec{q}_{\text{QE}}| \simeq 443$ MeV/c) panels, we see the typical intermediate-energy behavior with the slight overestimation of the quasielastic peak and the 2p2h contribution not filling the dip-region completely. The fact that the former kinematics is more transverse (higher $|\vec{q}_{\text{QE}}|$) and the 2p2h contribution is more pronounced does not alter our conclusions on the modeling. Finally, in the bottom right panel ($|\vec{q}_{\text{QE}}| \simeq 791$ MeV/c), we observe the most energetic kinematics, where the combination of the 2p2h and SPP results overestimate the Δ -peak. The origin of this effect is unresolved and requires further studies.

Fig. 3.38 presents the inclusive electron scattering results off the Oxygen target. Similarly

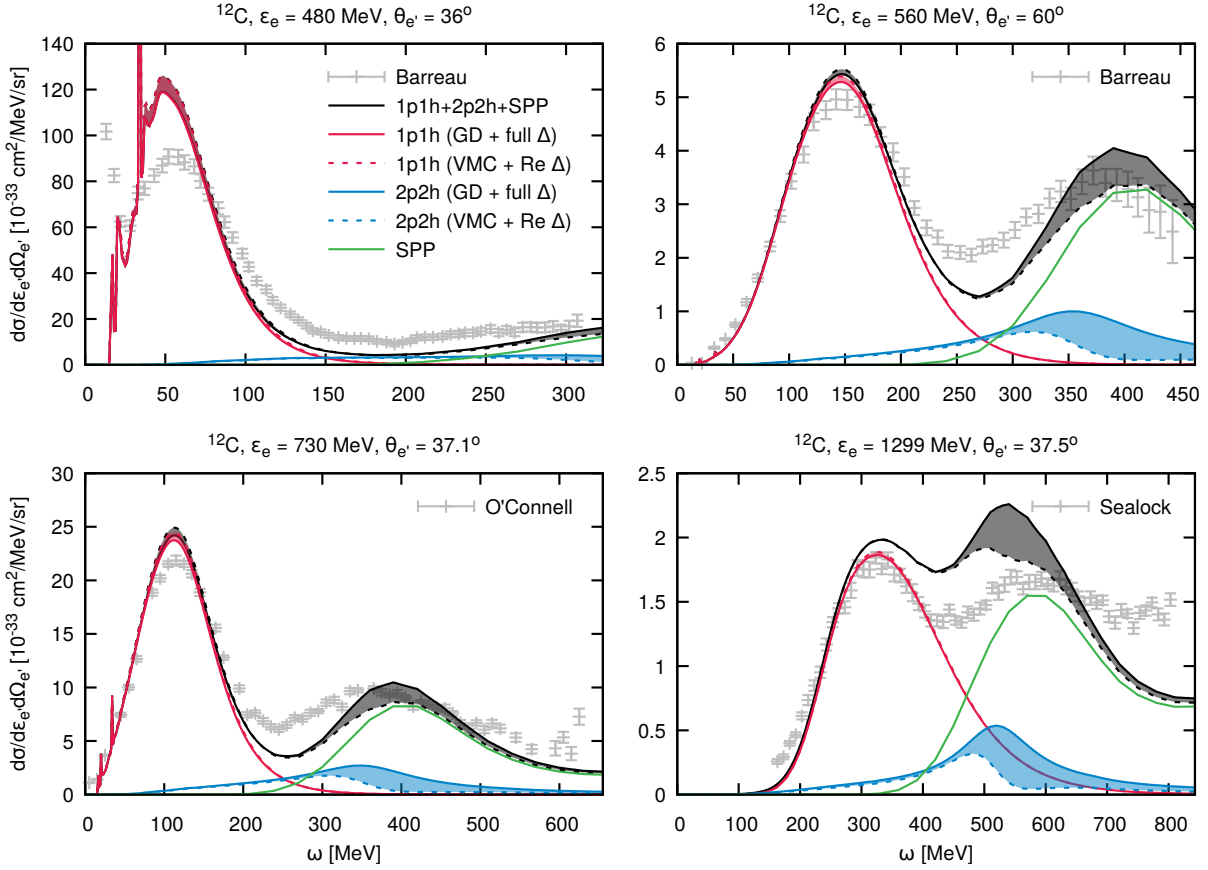


Figure 3.37: Inclusive $^{12}\text{C}(e, e')$ electron scattering cross section as a function of the energy transfer ω , for different sets of experimental kinematics: (top left, top right) [40], (bottom left) [48], (bottom right) [49]. The red, blue, green, and black curves correspond to the calculated results from one-, two-nucleon knock-out, single-pion production, and combined channels, respectively. The 1p1h and 2p2h calculations include a selection of model uncertainties due to the choice of the central correlation function and the descriptions of the Δ -isobar propagator, denoted by solid and dashed lines.

to the calculations on Carbon, we compare four different datasets in their specific kinematical conditions to the results of our model. We present the uncertainties around the degrees of freedom described above. In the top left panel ($|\vec{q}_{QE}| \simeq 373 \text{ MeV}/c$), we see that the data in the quasielastic peak are inconclusive, but the model predictions are relatively accurate. In the top right panel ($|\vec{q}_{QE}| \simeq 447 \text{ MeV}/c$), we match the strength of the nucleon- and Δ peaks, slightly underestimating the dip region between them. The latter region is correctly reproduced in the bottom left panel ($|\vec{q}_{QE}| \simeq 636 \text{ MeV}/c$). However, the other two regions are overestimated. Finally, in the bottom right panel ($|\vec{q}_{QE}| \simeq 798 \text{ MeV}/c$), we again observe that the 2p2h+SPP predictions significantly overshoot the data in the Δ -peak. We conclude the general properties of our predictions as follows. The 1p1h results tend to slightly overestimate the quasielastic peak for the lowest energies, while giving proper predictions for higher ones. The dip region is reproduced accurately for the intermediate energies. It tends to be underestimated and overestimated for the less and more energetical kinematics, respectively. Our model compares favorably to data around the Δ -peak but provides significantly too much strength for higher projectile energies.

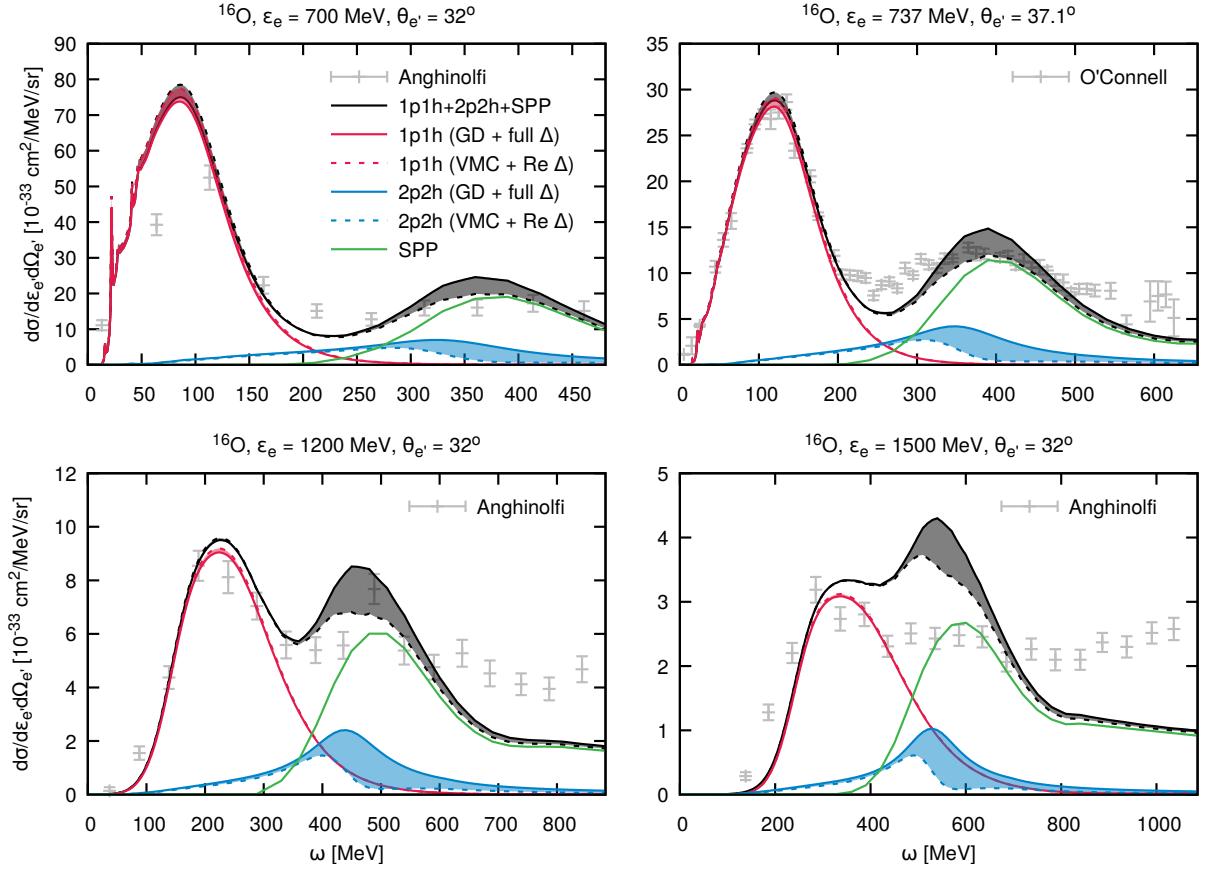


Figure 3.38: Inclusive $^{16}\text{O}(e, e')$ electron scattering cross section as a function of the energy transfer ω , for different sets of experimental kinematics: (top left, bottom left, bottom right) [50], (top right) [48]. The red, blue, green, and black curves correspond to the calculated results from one-, two-nucleon knock-out, single-pion production, and combined channels, respectively. The 1p1h and 2p2h calculations include a selection of model uncertainties due to the choice of the central correlation function and the descriptions of the Δ -isobar propagator, denoted by solid and dashed lines.

3.4 Numerical convergence

Understanding a given model's numerical accuracy and limitations is vital to consider its results trustworthy. In any circumstance, the more analytical calculations constitute a theoretical framework, the easier to handle the model becomes. However, they are also time-consuming and stall the research progress. The analytical computations are a substantial strength of our model and allow to enhance its performance and limit numerical precision issues to a small number of numerical efforts. Working in the angular momentum basis and applying multipole decomposition allows us to, after tedious calculations, reduce the numerical problem down to single-dimensional position or momentum integrals. Then, parameters, such as the number of multipoles in the expansion, the maximum number of partial waves of the continuum nucleon wave functions, or the regions and precision of position integrals, can control the numerical accuracy. For most effects, we rely on the experiences of the Ghent group and previous works therein [42]. In this section, we discuss the model behavior under the change of the total number of multipoles involved in

our calculations.

One-nucleon knock-out calculations

To investigate the numerical convergence of the $1p1h$ calculations, we present the IA inclusive electron scattering results for different values of the outgoing electron theta. In Fig. 3.39 and Fig. 3.40, we show the results on the Carbon and Oxygen targets, respectively. We observe that the required number of multipoles varies mainly with kinematics. For the most forward case, 6 – 8 multipoles are enough; for the intermediate conditions—8 – 10, while for the highest presented angle—12. Thus, the most transverse the kinematics is, the more difficult it is to converge. These conclusions do not change substantially for the different nuclei investigated here.

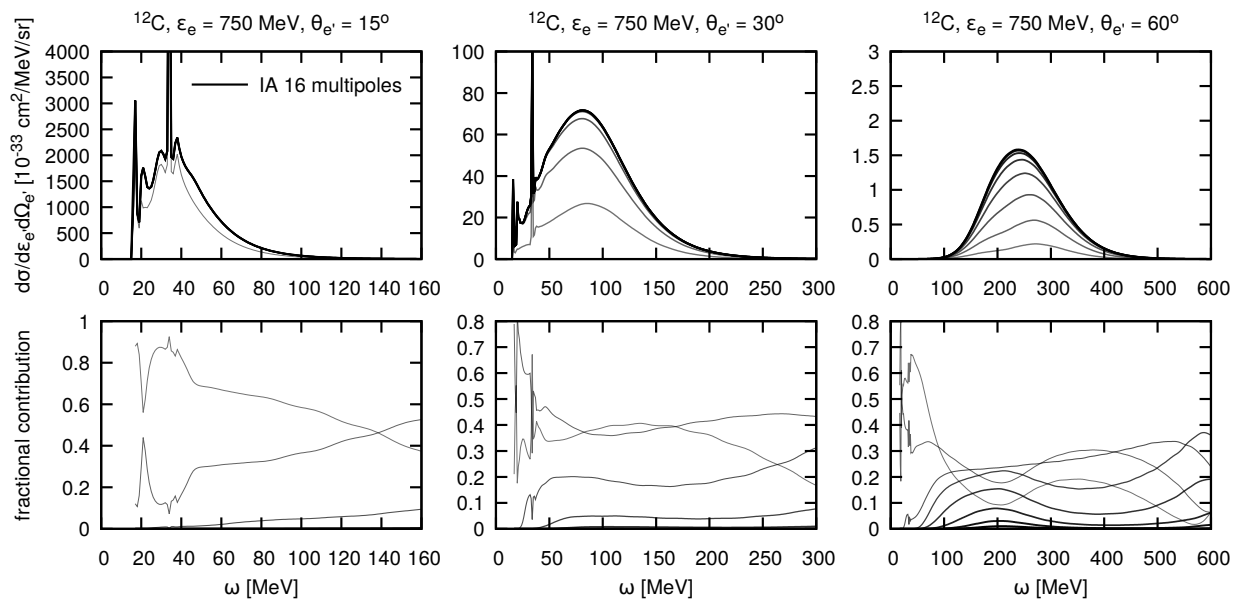


Figure 3.39: (top) numerical convergence of the IA inclusive electron scattering calculations on Carbon for the projectile energy $\epsilon_e = 750$ MeV and fixed outgoing electron angles $\theta_{e'} = 15^\circ, 30^\circ, 60^\circ$. Each consecutive darker and thicker line corresponds to adding 2 multipoles to the calculations. (bottom) fractional contributions of particular lines to the total cross section result.

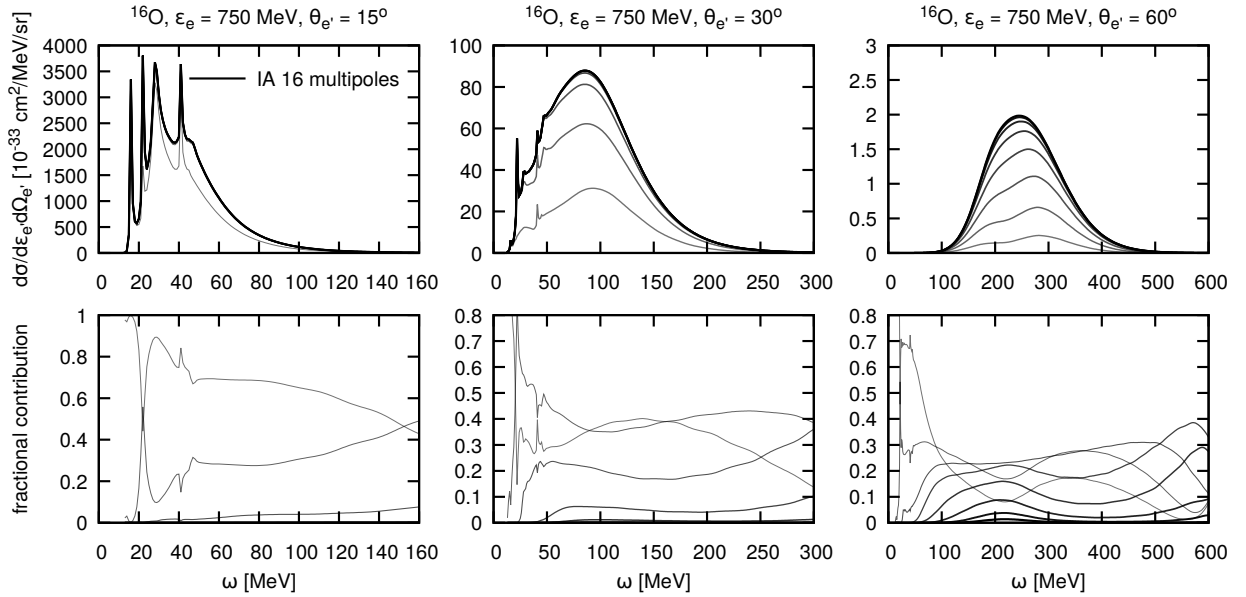


Figure 3.40: (top) numerical convergence of the IA inclusive electron scattering calculations on Oxygen for the projectile energy $\epsilon_e = 750$ MeV and fixed outgoing electron angles $\theta_{e'}$ = 15° , 30° , 60° . Each consecutive darker and thicker line corresponds to adding 2 multipoles to the calculations. (bottom) fractional contributions of particular lines to the total cross section result.

Two-nucleon knock-out calculations

While investigating the required multipole number for our two-body current calculations to converge, we distinguish the effect on the SRCs, seagull+pion-in-flight currents, and Delta-currents. In Fig. 3.41 and Fig. 3.42, we show the results on the Carbon and Oxygen targets, respectively. First, we observe that the particle multipole number contributions do not differ significantly between the investigated interaction dynamics. For the most forward scattering ($\theta_{e'}$), we need to use ~ 6 multipoles in the peak, but as many as $8 - 10$ multipoles to describe the higher- ω tail. At intermediate kinematics, we need ~ 8 multipoles to represent the peak behavior correctly and ~ 10 in the tail. For the most transverse conditions, the contributions of each multipole pair do not vary with ω . Here, we need at least 10 multipoles to provide reliable cross section predictions. In general, our observations reasonably agree with the summary presented in Ref. [11]. Here, we conclude the current status of our model that provides predictions for one- and two-nucleon knock-out reactions and was benchmarked against the electron-scattering data. We presented illustrations of the strength of this formalism in predicting neutrino-nucleus cross sections including these reaction mechanisms. Next step in this research program is the implementation in NuWro. In the following chapters, we will outline a scheme of how this can be accomplished.

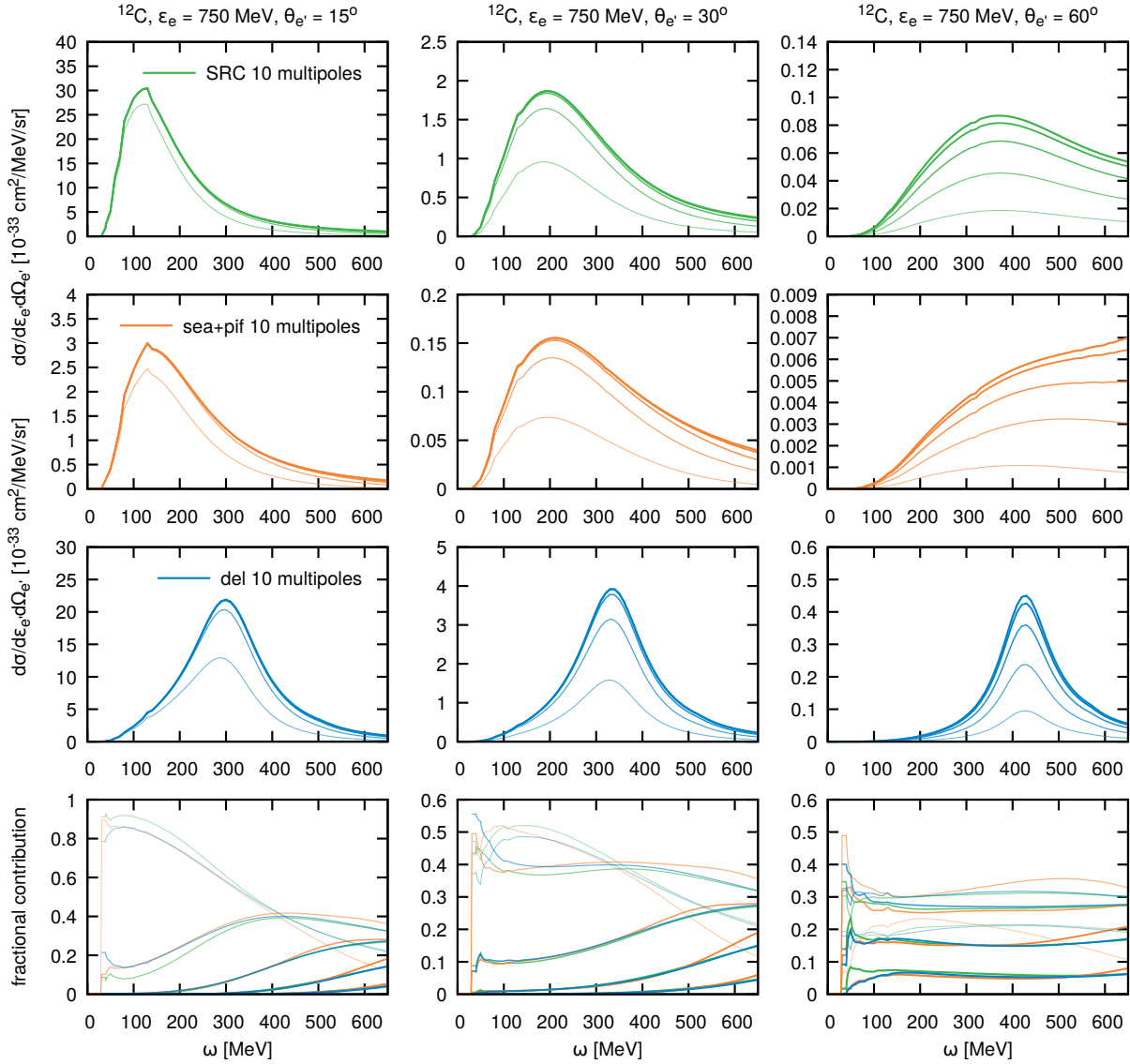


Figure 3.41: Multipole decomposition of the 2p2h inclusive electron scattering calculations on Carbon for the projectile energy $\epsilon_e = 750$ MeV and fixed outgoing electron angles $\theta_{e'} = 15^\circ, 30^\circ, 60^\circ$. The results are obtained with the short-range correlations, seagull+pion-in-flight currents, and the Δ -currents, for the first three rows, respectively. Each consecutive darker and thicker line corresponds to adding 2 multipoles to the calculations. (bottom) fractional contributions of particular lines to the total cross section result.

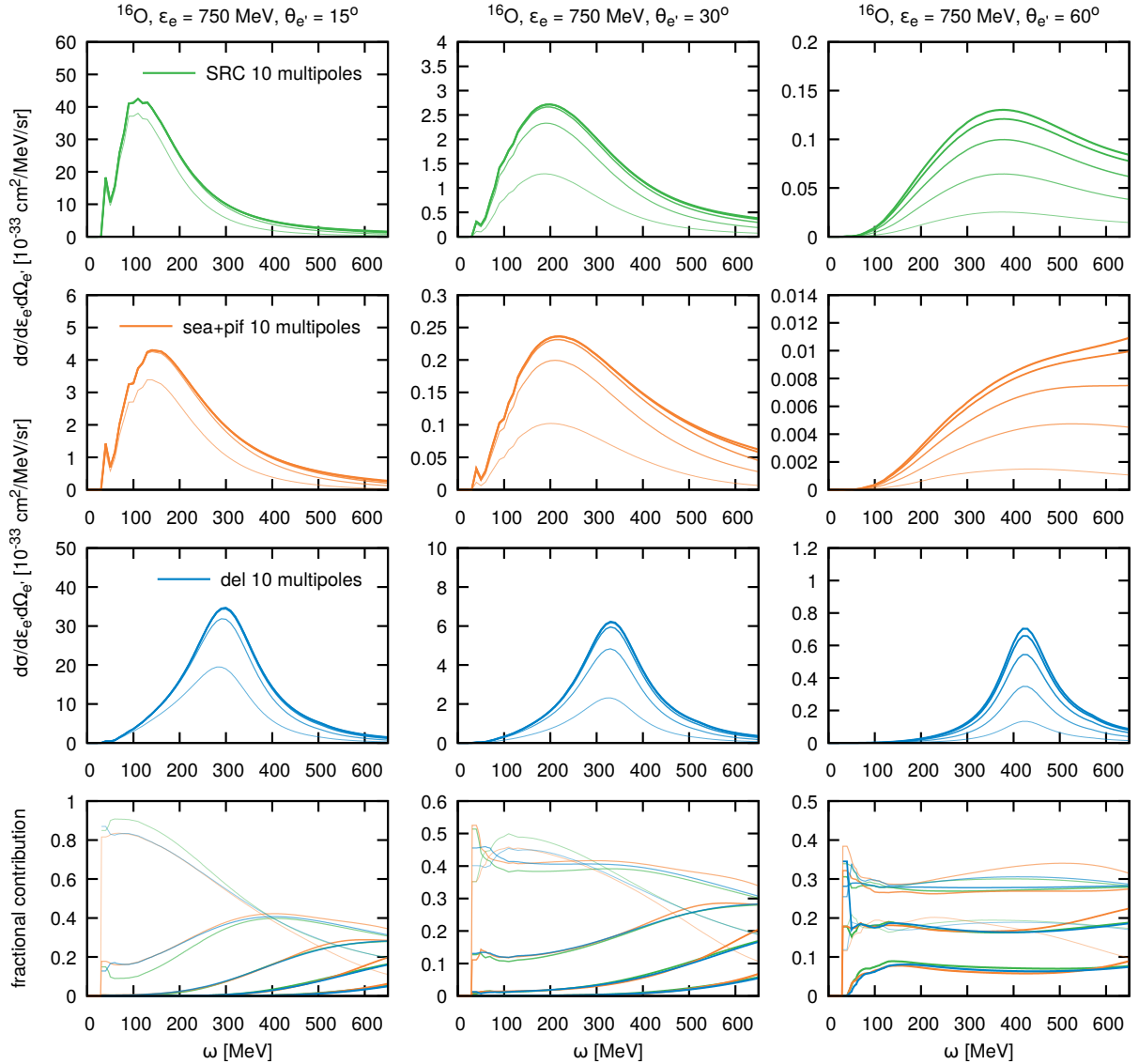


Figure 3.42: Multipole decomposition of the 2p2h inclusive electron scattering calculations on Oxygen for the projectile energy $\epsilon_e = 750$ MeV and fixed outgoing electron angles $\theta_{e'} = 15^\circ, 30^\circ, 60^\circ$. The results are obtained with the short-range correlations, seagull+pion-in-flight currents, and the Δ -currents, for the first three rows, respectively. Each consecutive darker and thicker line corresponds to adding 2 multipoles to the calculations. (bottom) fractional contributions of particular lines to the total cross section result.

References

- [1] K. Niewczas *et al.* in preperation.
- [2] T. E. O. Ericson and W. Weise, *Pions and Nuclei* (Clarendon Press, Oxford, UK, 1988).
- [3] R. González-Jiménez, N. Jachowicz, K. Niewczas, *et al.* *Phys. Rev. D* **95**, 113007 (2017).
- [4] D. O. Riska and G. E. Brown, *Phys. Lett. B* **38**, 193 (1972).
- [5] E. Ivanov and E. Truhlik, *Nucl. Phys. A* **316**, 437 (1979).
- [6] J. W. Van Orden and T. W. Donnelly, *Annals Phys.* **131**, 451 (1981).
- [7] W. M. Alberico, M. Ericson, and A. Molinari, *Annals Phys.* **154**, 356 (1984).
- [8] M. J. Dekker, P. J. Brussaard, and J. A. Tjon, *Phys. Lett. B* **266**, 249 (1991).
- [9] M. J. Dekker, P. J. Brussaard, and J. A. Tjon, *Phys. Rev. C* **49**, 2650 (1994).
- [10] J. E. Amaro, A. M. Lallena, G. Co, *et al.* *Phys. Lett. B* **277**, 249 (1992).
- [11] J. E. Amaro, A. M. Lallena, and G. Co, *Nucl. Phys. A* **578**, 365 (1994).
- [12] A. De Pace, M. Nardi, W. M. Alberico, *et al.* *Nucl. Phys. A* **726**, 303 (2003).
- [13] I. S. Towner, *Phys. Rept.* **155**, 263 (1987).
- [14] S. Boffi, C. Giusti, F. d. Pacati, *et al.* *Electromagnetic Response of Atomic Nuclei*, Vol. 20, *Oxford Studies in Nuclear Physics* (Clarendon Press, Oxford UK, 1996).
- [15] M. Martini, M. Ericson, G. Chanfray, *et al.* *Phys. Rev. C* **80**, 065501 (2009).
- [16] J. Nieves, I. Ruiz Simo, and M. J. Vicente Vacas, *Phys. Rev. C* **83**, 045501 (2011).
- [17] G. D. Megias, J. E. Amaro, M. B. Barbaro, *et al.* *Phys. Rev. D* **94**, 093004 (2016).
- [18] S. Dolan, G. D. Megias, and S. Bolognesi, *Phys. Rev. D* **101**, 033003 (2020).
- [19] N. Rocco, C. Barbieri, O. Benhar, *et al.* *Phys. Rev. C* **99**, 025502 (2019).
- [20] I. Ruiz Simo, J. E. Amaro, M. B. Barbaro, *et al.* *J. Phys. G* **44**, 065105 (2017).
- [21] I. Ruiz Simo, J. E. Amaro, M. B. Barbaro, *et al.* *Phys. Lett. B* **762**, 124 (2016).
- [22] V. L. Martinez-Consentino, J. E. Amaro, and I. Ruiz Simo, *Phys. Rev. D* **104**, 113006 (2021).
- [23] J. Ryckebusch, M. Vanderhaeghen, L. Machenil, *et al.* *Nucl. Phys. A* **568**, 828 (1994).
- [24] V. Van der Sluys, J. Ryckebusch, and M. Waroquier, *Phys. Rev. C* **51**, 2664 (1995).
- [25] J. Ryckebusch, V. Van der Sluys, K. Heyde, *et al.* *Nucl. Phys. A* **624**, 581 (1997).
- [26] J. Ryckebusch, D. Debruyne, W. Van Nespén, *et al.* *Phys. Rev. C* **60**, 034604 (1999).
- [27] L. E. Marcucci, D. O. Riska, and R. Schiavilla, *Phys. Rev. C* **58**, 3069 (1998).
- [28] P. Stoler, *Phys. Rept.* **226**, 103 (1993).
- [29] V. V. Frolov *et al.* *Phys. Rev. Lett.* **82**, 45 (1999).
- [30] G. Shen, L. E. Marcucci, J. Carlson, *et al.* *Phys. Rev. C* **86**, 035503 (2012).
- [31] W. Rarita and J. Schwinger, *Phys. Rev.* **60**, 61 (1941).
- [32] M. Vanderhaeghen, K. Heyde, J. Ryckebusch, *et al.* *Nucl. Phys. A* **595**, 219 (1995).
- [33] R. González-Jiménez, K. Niewczas, and N. Jachowicz, *Phys. Rev. D* **97**, 013004 (2018).

- [34] E. Oset and L. L. Salcedo, Nucl. Phys. A **468**, 631 (1987).
- [35] J. Nieves, E. Oset, and C. Garcia-Recio, Nucl. Phys. A **554**, 509 (1993).
- [36] M. Hjorth-Jensen, H. Muther, and A. Polls, Phys. Rev. C **50**, 501 (1994).
- [37] T. Wilbois, P. Wilhelm, and H. Arenhovel, Phys. Rev. C **54**, 3311 (1996).
- [38] K. Gottfried, Nucl. Phys. **5**, 5557 (1958).
- [39] G. D. Megias, J. E. Amaro, M. B. Barbaro, *et al.* Phys. Rev. D **94**, 013012 (2016).
- [40] P. Barreau, M. Bernheim, J. Duclos, *et al.* Nuclear Physics A **402**, 515 (1983).
- [41] I. Ruiz Simo, J. E. Amaro, M. B. Barbaro, *et al.* Phys. Rev. C **94**, 054610 (2016).
- [42] T. Van Cuyck, Short-range correlations and meson-exchange currents in neutrino-nucleus scattering, PhD thesis (Ghent University, 2017).
- [43] A. Nikolakopoulos, R. González-Jiménez, N. Jachowicz, *et al.* Phys. Rev. D **107**, 053007 (2023).
- [44] R. González-Jiménez, M. B. Barbaro, J. A. Caballero, *et al.* Phys. Rev. C **101**, 015503 (2020).
- [45] A. Nikolakopoulos, R. González-Jiménez, K. Niewczas, *et al.* Phys. Rev. D **97**, 093008 (2018).
- [46] M. Murphy *et al.* Phys. Rev. C **100**, 054606 (2019).
- [47] M. B. Barbaro, J. A. Caballero, A. De Pace, *et al.* Phys. Rev. C **99**, 042501 (2019).
- [48] J. S. O'Connell, W. R. Dodge, J. W. Lightbody, *et al.* Phys. Rev. C **35**, 1063 (1987).
- [49] R. M. Sealock, K. L. Giovanetti, S. T. Thornton, *et al.* Phys. Rev. Lett. **62**, 1350 (1989).
- [50] M. Anghinolfi, M. Battaglieri, N. Bianchi, *et al.* Nuclear Physics A **602**, 405 (1996).

4

Cascade model of final-state interactions

The hadron cascade model is an essential part of Monte Carlo neutrino event generators that governs final state interactions of knocked-out nucleons and produced pions. This mechanism of simulating inelastic nucleon-nucleus scattering is essential to provide the multiplicities of particles observed in an actual detector set-up. We show that such a model enriched with physically motivated modifications of nucleon-nucleon cross sections and incorporation of nuclear correlation effects can reproduce experimental nuclear transparency data. Using this framework, we estimate the uncertainty of nucleon final state interaction effects and apply it to recent neutrino-nucleus cross section measurements that include an outgoing proton in the experimental signal. The material in this chapter is based on work that was published previously as Physical Review C 100 (2019) 015505.

4.1 In-medium propagation of nucleons

The description of the transport of hadrons in nuclear matter is a challenge encountered in many areas of fundamental research, such as astrophysics, the phenomenology of heavy-ion collisions, and a broad spectrum of nuclear physics applications. The first notable attempt at modeling this process was a Monte Carlo approach based on the ideas of R. Serber [1] and implemented by Metropolis *et al.* [2,3]. Many others later followed this concept of cascading hadrons and significantly developed the model [4–7]. However, as discussed in Refs. [1,8], cascade models have their applicability constrained by their fundamental theoretical assumptions. These doubts motivated the development of two alternative solutions that went beyond this simplified picture and were successfully used in, e.g., heavy-ion physics. The first one is based on Boltzmann-Uehling-Uhlenbeck (BUU) equations [9], formulated to evolve the one-body phase-space density under the influence of a mean field. The second one, Quantum Molecular Dynamics (QMD) [10], is formu-

lated in terms of nucleon coordinates and momenta under the action of a many-body Hamiltonian. Both approaches implicitly contain a two-body collision term. A detailed comparison of 15 independent implementations of BUU and QMD models shows surprisingly considerable differences in their predictions [11].

The transport problem is also essential for investigating elementary projectiles scattering off atomic nuclei that involve final-state interactions of knocked-out nucleons and produced mesons. It is particularly relevant in neutrino physics, where further progress in reducing systematic errors in long- and short-baseline oscillation experiments [12] requires more extensive measurements of final-state protons. On the one hand, it is needed in calorimetric techniques to reconstruct neutrino energies. As discussed, e.g., in Refs. [13,14], more exclusive final state measurements better estimate the neutrino energy. Also, the investigation of final-state protons allows us to learn about the size of multinucleon ejection contribution to the inclusive cross section, which is relevant even if neutrino energy is reconstructed based on the observation of the final-state muon only.

Analyses of oscillation experiments require reliable theoretical predictions for the complexity of nuclear response to neutrino probes with broad, energetic spectra. For this purpose, we use event generators, such as NEUT, GENIE, NuWro, and GiBUU [15]. The first three of them model FSI using the intranuclear cascade model. A critical test that the FSI model should pass is the ability to reproduce nuclear transparency data from electron scattering studies [16]. *Nuclear transparency* is the probability that a knocked-out nucleon is not subject to re-interactions inside the residual nucleus. In the case of the Carbon target, used in MINERvA [17] and T2K [18] experiments, typical transparency values are $\sim 65\%$. Therefore, in most events, knocked-out nucleons interact at most once.

Nuclear transparency

Modeling scattering processes on nuclear targets relies on describing nucleon propagation within a nuclear medium. To estimate the magnitude of nucleon distortion, one can introduce a measure called nuclear transparency, defined as the probability of a struck nucleon escaping the nucleus without significant re-interactions. Much attention has been brought to this subject following the hypothesis of color transparency (CT) [16]. Such a phenomenon should suppress the probability of in-medium nucleon-nucleon interaction at very high energies. CT has been extensively studied in many experiments, using quasi-free $A(e, e'p)$ scattering off various nuclei without definite conclusions [16].

The general idea behind the measurement of the nuclear transparency in quasielastic $A(e, e'p)$ reactions is to confront an experimental yield of knocked-out protons with a theoretical prediction that does not include the distortion due to FSI. In these experiments, where an electron ejects a proton p out of a nucleus A , using measured values of energy $\omega = E - E'$ and momentum $\vec{q} = \vec{k} - \vec{k}'$ transfers (E and \vec{k} are the initial electron energy and momentum, primed values refer to the final electron), one defines the missing momentum and the missing energy as

$$\vec{p}_m \equiv \vec{p}_p - \vec{q}, \quad (4.1.1)$$

$$E_m \equiv \omega - T_p - T_{A-1}. \quad (4.1.2)$$

Here T_p and $T_{A-1} = |\vec{p}_m|^2/2M_{A-1}$ are the kinetic energies of the knocked-out proton and the residual nucleus, respectively. Then, one defines nuclear transparency, measured for a fixed four-momentum transfer $Q^2 \equiv |\vec{q}|^2 - \omega^2$, as

$$T(Q^2) = \frac{\int_V d^3p_m dE_m Y_{\text{exp}}(E_m, \vec{p}_m)}{\int_V d^3p_m dE_m Y_{\text{PWIA}}(E_m, \vec{p}_m)}, \quad (4.1.3)$$

where Y_{exp} and Y_{PWIA} are proton yields of the measurement and theoretical calculation, respectively. The phase space V is restricted to the quasielastic region by the conditions $E_m \lesssim 80$ MeV and $|\vec{p}_m| \lesssim 300$ MeV, which ensure the suppression of inelastic processes. The theoretical prediction Y_{PWIA} is calculated under the plane wave impulse approximation hypothesis, i.e., that the knocked-out nucleon undergoes no re-interactions. One should be aware that the definition mentioned above suffers from a model dependency as it relies on the accuracy of theoretical PWIA computations.

Over the years, the following experiments have reported nuclear transparency measurements:

- D.F. Geesaman, G. Garino *et al.* at Bates Linear Accelerator Center [19,20],
- NE-18 at Stanford Linear Accelerator Center [21,22],
- E91-013 in Hall C at Thomas Jefferson National Accelerator Facility [23,24],
- E94-139 in Hall C at Thomas Jefferson National Accelerator Facility [25],
- E97-006 in Hall C at Thomas Jefferson National Accelerator Facility [26].

The measurements were done in different kinematical setups, with outgoing protons momenta in the range from ~ 0.5 to ~ 5.5 GeV/c, and for various nuclear targets, with the most widely used ^{12}C and ^{56}Fe . We summarize the information about the kinematics of transparency measurements in Table 4.1.

The PWIA models used by experimental groups describe the proton target in the independent particle shell models (IPSM). The IPSM-based calculations are known to overestimate single-particle strength in exclusive reactions [29]. We attribute this discrepancy to the shell depletion due to nucleon-nucleon correlations that cannot be fully accounted for in mean-field approaches. NE-18 at SLAC was the first experiment that introduced correlation factors c_A in the definition of transparency to correct for drawing single-particle strength outside the phase space V . This involves a correction of

$$Y_{\text{PWIA}}(E_m, \vec{p}_m) = c_A Y_{\text{IPSM}}(E_m, \vec{p}_m) \quad (4.1.4)$$

with values $c_A = 0.90, 0.82$ for ^{12}C and ^{56}Fe , respectively. These numbers are higher than typically used spectroscopic factors, as they result from the integration over a specific phase space V [26]. In this study, we compare our results to transparency results as experimental groups published them. Our treatment of correlation factors agrees with that from Ref. [30].

It is important to emphasize that the methods of introducing correlation factors are a subject of ongoing debate. Some authors argue that because the experiments were conducted in the transverse kinematics, which is less sensitive to the high-value tail of the nucleon momentum distribution, the use of correlation factors is not justified [31]. Theoretical arguments suggest that

Ref.	Beam energy (MeV)	Central electron energy (MeV)	Central electron angle (deg)	Central proton momentum (MeV/c)	Central proton angle (deg)
[19,20]	780	565	50.3	572.5	50.1, 58.2, 67.9, 72.9
[21,22]	2015	1390	35.5	1200	43.4, 46.2, 49.0, 51.8, 54.6
	3188	1470	47.7	2450	27.7, 30.5, 33.3
	4212	1470	53.4	3540	20.9, 22.6
	5120	1470	56.6	4490	15.9, 16.7, 17.3
[23,24,27]	2445	2075	20.5	882.8	35.4, 39.4, 43.4, 47.4, 51.4, 55.4, 59.4, 63.4, 67.4, 71.4, 75.4
	3245	2255	28.6	1661.7	32.6, 36.6, 40.6, 44.6, 48.6, 52.6
	2445	1755	32.0	1343	31.5, 35.5, 39.5, 43.5, 47.5, 51.5, 55.5
	3245	1400	50.0	2572.5	25.5, 28.0, 30.5
	845	475	78.5	882.8	27.8, 31.8, 35.8, 39.8, 43.8, 47.8
	1645	675	80.0	1661.7	22.8, 26.8, 30.8, 34.8
	[25,28]	3059	1300	54.0	2520
4463		1200	64.6	4090	15.3
5560		1270	64.6	5150	12.8
[26]	3298	2950	14.4	850	60.3
	3298	2750	17.0	1000	56.2
	3123	2500	22.2	1250	49.7
	3298	2400	25.4	1500	44.6
	3298	2280	29.0	1700	40.7

Table 4.1: Kinematical setups of $A(e, e'p)$ experiments that reported nuclear transparency measurements.

soft Q^2 -dependent correlation factors would be more appropriate [32], but many recent papers on nuclear transparency ignore them altogether [16]. CLAS Collaboration measured the nuclear transparency of protons from short-range correlated pairs [33] and concluded that transparency ratios Al/C , Fe/C , and Pb/C are consistent with the absence of the correlation factors in the definition Eq. (4.1.3). Moreover, theoretical computations based on the Glauber theory [34–36] and the relativistic optical potential [34,35,37] provide similar conclusions.

4.2 Exclusive electron scattering simulations

Analyses of neutrino oscillation and cross section experiments require Monte Carlo simulations to accurately reconstruct neutrino energy and estimate the systematic uncertainties. NuWro [38] is a versatile neutrino Monte Carlo generator developed at the University of Wrocław that can accurately model various neutrino-nucleus interaction channels in a PWIA-motivated framework. This makes it a reliable tool for providing simulations needed in accelerator-based neutrino experiments. In Section 1.4, we describe NuWro solutions for describing the quasielastic and inelastic scattering off bound nucleons together with many nuclear effects, including two-nucleon knock-out reactions. In this study [39], we attempt to constrain the NuWro model of final-state interactions using exclusive electron scattering input. Thus, the most critical generator ingredient is the intranuclear cascade model.

The cascade model describes the in-medium propagation of pions and nucleons. Its scheme is inspired by the seminal papers by N. Metropolis et al. [2,3], but relevant physics ingredients are new. We base the Monte Carlo sampling on the classical formula that expresses the probability for a particle to propagate over a distance Δx with no re-interaction

$$P(\Delta x) = \exp(-\Delta x/\lambda), \quad (4.2.1)$$

where $\lambda = (\rho\sigma)^{-1}$ is the mean free path calculated locally, expressed in terms of nuclear density ρ and an effective interaction cross section σ . In actual computations, we distinguish proton or neutron densities and proton-proton or proton-neutron cross sections. Here, a step of $\Delta x = 0.2$ fm is sufficient to grasp the structure of a nuclear density profile. The performance of the pion part of this cascade model was benchmarked on numerous neutrino-nucleus pion production cross section measurements showing, in general, a good agreement with the data, see, e.g., Ref. [40]. In this study, we focus on the nucleon cascade model.

To perform computations, we use NuWro version 19.02 [41]. This version uses a custom fit to the experimental free nucleon-nucleon cross sections, both elastic and inelastic, which improves the agreement with the 2016 PDG dataset [15]. The fraction of single-pion production within inelastic interactions was adjusted to follow the fits of Ref. [42]. Moreover, we have updated the center-of-momentum (COM) frame angular distributions for the elastic scattering using the parametrization of Ref. [43].

For the in-medium modification of the elastic cross sections, we use the results of Pandharipande and Pieper's study [44], where the two main effects come from Pauli blocking and in-medium nucleon effective mass. The Pauli blocking is included in NuWro on an event-by-event basis, a straightforward way in Monte Carlo simulations. We checked that NuWro cascade performance reproduces the results from Ref. [44] with sufficient accuracy. For the inelastic nucleon-nucleon scattering, we adopt a phenomenological in-medium cross section (σ_{NN}^*) parametrization [45]

$$\sigma_{NN}^* = (1 - \eta \frac{\rho}{\rho_0}) \sigma_{NN}^{\text{free}}, \quad (4.2.2)$$

where $\eta = 0.2$, and ρ, ρ_0 are the local and saturation nuclear densities, respectively.

Following the experiences of Refs. [30,36,44], we have included effects coming from nucleon-nucleon short-range correlations. In general, one assumes the density that enters the mean free

path in Eq. (4.2.1) to be the one of nuclear matter at point \vec{r}_2 , as experienced by a propagating nucleon known to be in a position \vec{r}_1 . It can be expressed in terms of one- ($\rho_A^{[1]}$) and two-body ($\rho_A^{[2]}$) densities as

$$\rho_{\text{eff}}^{[1]}(\vec{r}_2|\vec{r}_1) = \frac{\rho_A^{[2]}(\vec{r}_1, \vec{r}_2)}{\rho_A^{[1]}(\vec{r}_1)}, \quad (4.2.3)$$

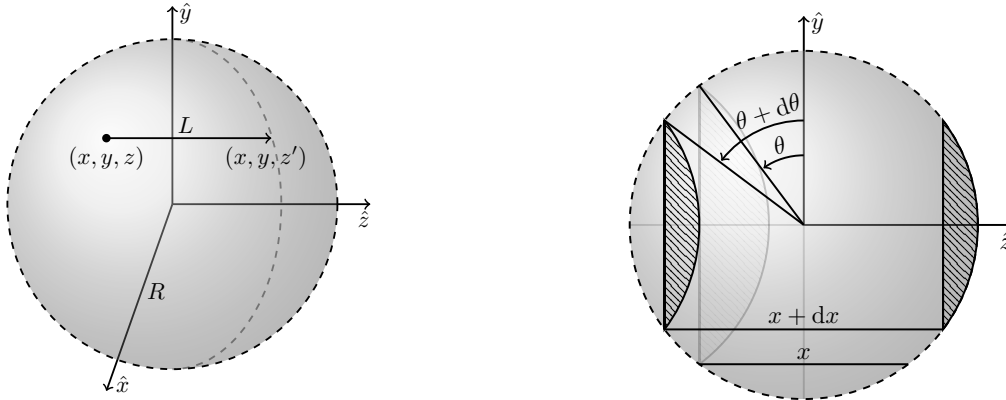
normalized to the number of remaining nucleons $\int d^3\vec{r}_2 \rho_{\text{eff}}^{[1]}(\vec{r}_2|\vec{r}_1) = A - 1$. We introduce correlation effects through the following substitution

$$\begin{aligned} \rho_{\text{eff,IPSM}}^{[1]}(\vec{r}_2|\vec{r}_1) &= \rho_{A-1}^{[1]}(\vec{r}_2) \\ &\rightarrow \rho_{A-1}^{[1]}(\vec{r}_2)g(|\vec{r}_{21}|)N(|\vec{r}_2|), \end{aligned} \quad (4.2.4)$$

where $g(|\vec{r}_{21}|)$ is the nucleus-dependent pair distribution function [44], and $N(|\vec{r}_2|)$ is introduced to keep the global normalization condition. For the choice of $g(|\vec{r}_{21}|)$, we rely on distributions of nucleon-nucleon distances obtained in *ab initio* computations for light nuclei, including Carbon [46,47]. For heavier nuclei, including Iron, we approximate $g(|\vec{r}_{21}|)$ by the *ab initio*-calculated infinite nuclear matter distributions $g_{\text{inf}}(\rho_{\text{avg}}, |\vec{r}_{21}|)$ of Ref. [44], evaluated at average nuclear density. In our computations, we include effects coming from different shapes of $g(|\vec{r}_{21}|)$ for nucleon pairs of the distinct isospin configurations, and following the scheme summarized in Eq. 4.2.4, we define effective densities.

Verifying the cascade algorithm

Access to analytical calculations is an essential tool in benchmarking numerical algorithms. Here, we will investigate methods of calculating nuclear transparency for a ball of radius R and constant density, as depicted in Fig. 4.1.



(a) Average length of propagation in nucleon knock-out reactions. (b) Spherical caps of an equal propagation length in the \hat{z} -direction.

Figure 4.1: Graphical representation of the spatial in-medium nucleon propagation properties in knock-out reactions.

We commence with calculating the average distance $\langle L \rangle$ traveled by a nucleon from a random interaction point, in one direction, to the edge of the nucleus, see Fig. 4.1a. We obtain this

quantity as follows

$$\begin{aligned} \langle L \rangle &= \frac{1}{V} \int_V dx dy dz (z' - z) = \frac{1}{V} \int_V dx dy dz (\sqrt{R^2 - x^2 - y^2} - z) \\ &= \frac{2\pi R^4}{V} \int_{-1}^1 dr \int_0^1 d \cos \theta \cos \theta^2 \sqrt{1 - \cos^2 \theta + r^2 \cos^2 \theta} = \frac{3}{4} R. \end{aligned} \quad (4.2.5)$$

Another useful quantity is the probability distribution of random points in a ball of radius R in terms of their distance to the surface in one direction, denoted as $f_R(x)$. In order to find the function, one needs to make the following observation: the points that are in the same distance x form a spherical cap of a radius R , cut by the angle θ ; see the two-dimensional projection in Fig. 4.1b. In order to find the function, one needs to make the following observation: the points in the same distance x form a spherical cap of a radius R , cut by the angle θ ; see the two-dimensional projection in Fig. 14. We obtain the distribution $f_R(x)$ by integrating the spherical caps. However, as it is a function of x , we consider the Jacobian ($dx = 2R \cos \theta d\theta$) and obtain

$$f_R(x) = \int_0^{2\pi} d\phi \int_{\frac{\pi}{2}}^{\theta'} d\theta R^2 \sin \theta 2R \cos \theta = 4\pi R^3 \left(1 - \frac{x^2}{4R^2}\right). \quad (4.2.6)$$

Imposing the normalization over the whole nucleus to unity, the probability reads

$$f_R(x) = \frac{3}{4R} \left(1 - \frac{x^2}{4R^2}\right) \quad (4.2.7)$$

and reconstructs the average propagation length of Eq. (4.2.5). Finally, we use it to calculate the analytical transparency

$$T = \int_0^{2R} f_R(x) e^{-x\rho\sigma} dx = 3e^{-A} \left(\frac{1}{A^2} + \frac{1}{A^3}\right) + 3\left(\frac{1}{2A} - \frac{1}{A^3}\right), \quad (4.2.8)$$

where $A = 2\rho\sigma R = 2R\lambda^{-1}$ and λ is the mean free path. We obtain a percent-level precision by comparing this formula to the equivalent Monte Carlo results of NuWro.

NuWro as a tool in transparency studies

While using Monte Carlo event generators, one can define the "MC transparency" as a fraction of events with no nucleon re-interactions. This is the method we used in the previous subsection. However, experimentally, one cannot distinguish these events from those with "soft" FSI. Because of that, to make a comparison reliable, we go through all the steps of the experimental procedures to extract the theoretical counterpart of the measured transparency. NuWro keeps the information about particles before and after FSI. We can use this property in the computation of nuclear transparency. Particles after FSI correspond to those detected in experiments, while particles before FSI correspond to the theoretical computations in PWIA. At the moment of this study, NuWro (in version 19.02) did not yet have a complete electron scattering module; hence, we use neutral current (NC) interactions on bound proton targets. In doing so, we collect samples of NC events with the same (electron mass is negligible) kinematics as in the transparency electron scattering experiments. In both electron and neutrino cases, a radial distribution of interaction points inside the nucleus is the same and given by the nucleus density profile.

The main challenge is to reproduce experimental situations with complete information on the kinematics and applied cuts. For every kinematical setup, we ran a simulation with the neutrino beam energy equal to E_e . Then, we fixed the energy $E_{e'}$ and the in-plane angle $\theta_{e'}$ for the outgoing electron or neutrino around the central value of the spectrometer. Analogously fixed were the momentum p_p and the in-plane angle θ_p for the knocked-out proton. As in all the experiments, the electron and proton spectrometers were set in-plane, the out-of-plane angles were fixed to the same value $\phi_{e'} = \phi_p$. The exclusive cross section formula is symmetric with respect to the rotation of the system. Thus, only the relative out-of-plane angle between the electron and proton plays a role, here set to $\phi_{e'p} = 0$. We fixed all of the variables $E_{e'}$, $\theta_{e'}$, p_p , θ_p , $\phi_{e'p}$ with the accuracy provided by the spectrometers' energy or angular acceptance, namely $\Delta E_{e'}$, $\Delta \theta_{e'}$, Δp_p , $\Delta \theta_p$, $\Delta \phi_{e'p} = \Delta \phi_{e'} + \Delta \phi_p$. On top of those cuts, additional conditions were imposed using the information about the E_m , $|\vec{p}_m|$. Finally, we summarize the beam energies and central spectrometers values for every setup in Tab. 4.1, while the acceptances and the cuts on missing variables in Tab. 4.2.

To establish a proper framework for comparing nuclear transparency results with experiments, we tested different ways of modeling the initial nuclear state in NuWro. We compared the SF- and LFG-based simulations with exclusive properties of the knocked-out protons reported by the E91-013 experiment at JLAB. As shown in Fig. 4.2, SF in NuWro can accurately reproduce a measured shape of the angular distributions of knocked-out protons. The angular dependence of

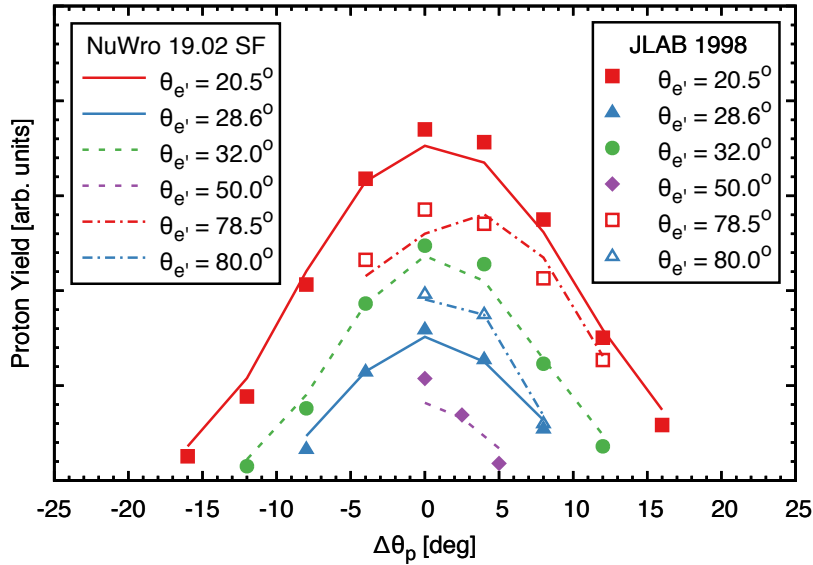


Figure 4.2: Angular distributions of the proton yield, as measured in the E91-013 experiment at JLAB. Points represent data from Ref. [24] with the convention proposed in Ref. [27]. Lines are results computed with SF in NuWro. $\Delta\theta_p = 0$ corresponds to the free proton target case. Both distributions are normalized to the same area.

transparency reproduces a generally flat shape that can be seen in Fig. 2. of Ref. [23] with sufficient precision. However, the angular distributions of the measured yield of protons for the LFG-based simulations peak too strongly around the central value, which leads to the overestimation of the proton transparency. Due to its simplicity, the LFG model fails to correctly predict the exclusive kinematics, a prerequisite in reliable nuclear transparency studies.

Ref.	Targets used	Electron energy acceptance (%)	Electron angle acceptance (deg)	Proton momentum acceptance (%)	Proton angle acceptance (deg)	Common plane acceptance (deg)	Missing energy cut (MeV)	Missing momentum cut (MeV/c)
[19,20]	C, Fe	3.5	1.4	25	1.1	10.8	80	-
[21,22]	C, Fe	5	0.9	5	0.9	4.6	100	250
[23,24,27]	C, Fe	10	2.4	20	3.4	4.6	80	300
[25,28]	C, Fe	15	3.4	8	2.4	9.4	80	300
[26]	C	9.6	2.4	15	3.4	7	80	300

Table 4.2: Table of cuts used by experimental groups and introduced in our simulations.

We conclude that only NuWro simulations that use the spectral function framework as a model for the initial nuclear state can give reliable results compared to exclusive electron scattering experiments. Unfortunately, such a conclusion imposes a limitation on nuclear targets that can be simulated, as the hole spectral functions are available only for a limited number of nuclei making an estimation of the A -dependence of nuclear transparency impossible in NuWro. The

only targets we can reliably compare with the transparency measurements are ^{12}C and ^{56}Fe .

A similar study was done using the Giessen BUU transport model [48,49]. The experimental data from three JLab and SLAC experiments [22,23,25] were analyzed using detailed information about the angular acceptance of spectrometers. Interesting ingredients of the BUU discussion are: an investigation of the impact of restricted angular acceptance on final results, a study of transparency dependence on atomic mass $T(A) \sim A^\alpha$, an estimation of theoretical uncertainty due to not precisely known correlation factors c_A Ref. [31]. The final BUU results are similar to those presented in this study regarding the large proton momentum transparency saturation values. However, there is a visible difference at the lowest momentum (Q^2) experimental point: NuWro transparency continues to rise while the BUU transparency drops.

4.3 Constraining the FSI model

Using the tools and following the procedure described in the previous section, we attempt to estimate the accuracy with which the NuWro cascade model reproduces exclusive electron scattering data. In Fig. 4.3, we present the transparency simulation results for Carbon and Iron together with data points collected from several experiments. In experimental papers, transparency is dis-

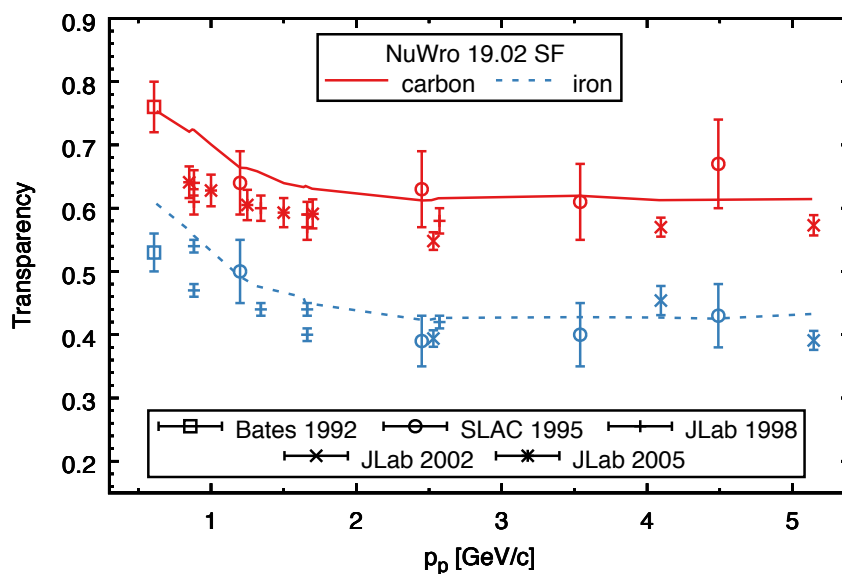


Figure 4.3: Nuclear transparency as a function of proton momentum. Lines represent results obtained with NuWro 19.02 using SF for the Carbon and Iron targets. Experimental points come from experimental papers mentioned in the text.

cussed as a function of Q^2 , but this variable can be translated into an average proton momentum. The transparency curve has a characteristic shape reproduced in all theoretical computations: a saturation at larger values of proton momentum and a decline in the region of ~ 1 GeV/c. One can explain the saturation by a roughly constant value of the total free nucleon-nucleon cross sections for larger values of the incident nucleon momentum. A region of transparency decline comes from a complicated interplay of various nuclear effects and is the most difficult to model.

NuWro simulations for Carbon reproduce the transparency data quite well. For application

in neutrino physics, the most critical region is that of low nucleon momentum, starting from ~ 500 MeV/c, a detection threshold in experiments like T2K and MINERvA. We can see that the value of the first available experimental point, from Ref. [20], is reproduced well, but then, the decline of NuWro transparency is not steep enough. Predictions from our model are slightly above the data in the saturation region. The same shape of the transparency curve results from the calculations for the Iron target. We can attribute minor differences, including data overshooting at low momenta, to nucleon-nucleon correlation effects being introduced more approximately with respect to Carbon, as discussed in Section 4.2. In general, the agreement with the data points is satisfactory.

Model uncertainties

As already discussed, nucleon FSI effects contribute to the background in all attempts to measure multinucleon ejection contribution to the inclusive cross section. Thus, more is needed to have a good qualitative agreement with the transparency data, but also it is vital to estimate the uncertainty inherent in the nucleon FSI model. Our approach is to assess the uncertainty of the nucleon mean free path as calculated by NuWro. We tried to define a 1σ error bound by demanding that $2/3$ of experimental points together with experimental errors are entirely inside the bound. To achieve that, we multiply the mean free paths calculated within NuWro by a constant overall scaling factor. We show this result in Fig. 4.4. The upper and lower dashed curves

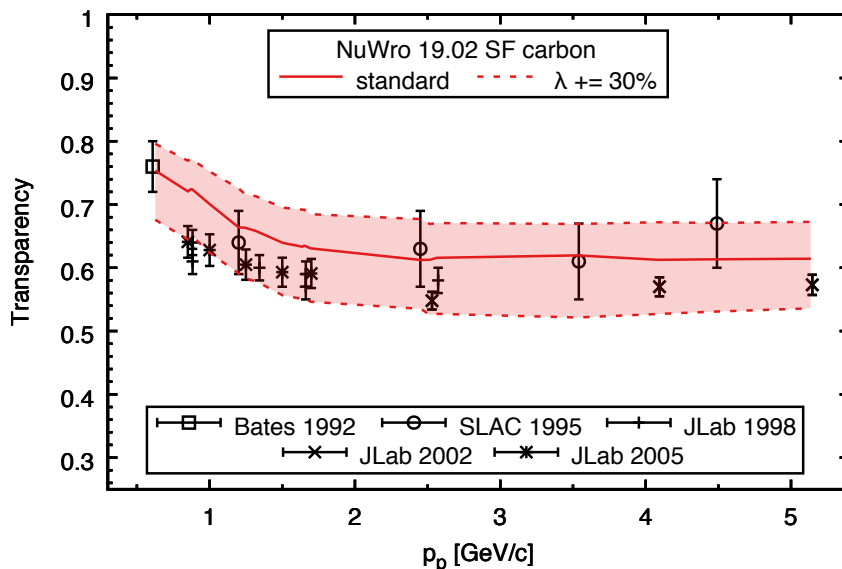


Figure 4.4: Nuclear transparency as a function of proton momentum. Lines represent results obtained with NuWro 19.02 using SF for the Carbon target. Dashed lines are results computed after scaling mean free paths by $\pm 30\%$. Experimental points come from the papers mentioned in the text.

were obtained by scaling up and down central mean free paths by 30%.

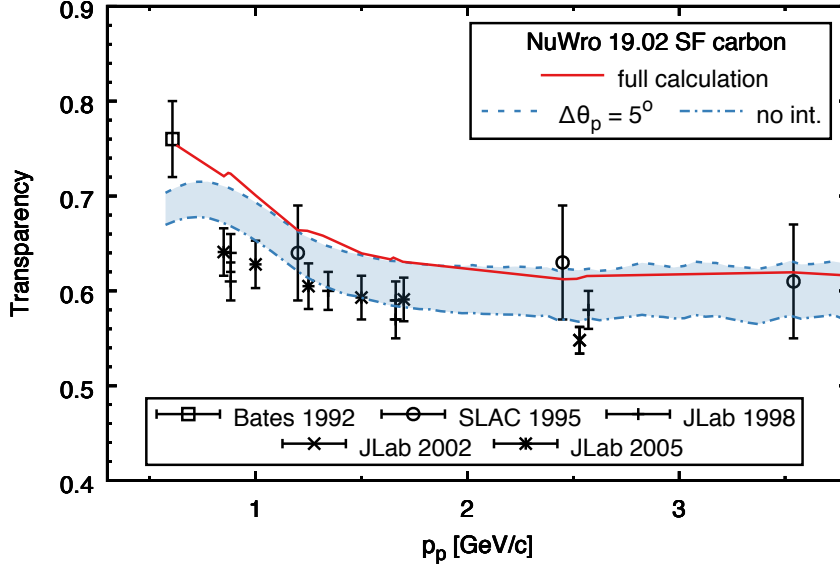


Figure 4.5: Nuclear transparency, calculated with the full model and with the approximation discussed in the text, as a function of proton momentum.

Monte Carlo transparency

In the Monte Carlo approach, a natural way to study nuclear transparency is to follow individual cascaded protons and check whether they interact. However, as discussed earlier, such a definition might not catch particular aspects of the situation that are important from the experimental perspective and is expected to underestimate the final result. A refinement of the naive MC transparency definition is to consider a finite angular acceptance of spectrometers, allowing protons to interact softly without a significant direction change, e.g., $\Delta\theta_p = 5^\circ$. The value of 5° approximately coincides with an angle that expands a solid angle in experimental acceptances; see Table 4.2.

In Fig. 4.5, we show the results for Carbon using different transparency definitions. One can see that while the "no interactions" definition is too strict, the softer definition " $\Delta\theta_p = 5^\circ$ " works quite well, especially in the saturation region. However, it cannot reproduce the first experimental point at $p_p \simeq 625$ GeV/c. Knowing this behavior, the definition " $\Delta\theta_p = 5^\circ$ " can be used for less exhausting cascade checks. Note that in these results, we have not considered the fate of short-range correlated nucleons existing in our SF implementation above the 2-nucleon missing energy emission threshold. This means that the interactions of the second knocked-out nucleon contributed to the "no int." definition of transparency. After accounting for this phenomenon, we find the results consistent with the " $\Delta\theta_p = 5^\circ$ " definition up to $p_p \simeq 700$ GeV/c. Then, the more strict definition provides lower values of transparency by about 2 points in the saturation region. These "no int." corrected results are consistently below the full calculation curve.

Cascade model ingredients

To understand the sources of uncertainties in our model, we present the impact of its various ingredients on predicted transparency. In Fig. 4.6, we show results obtained with:

- a bare cascade model with free nucleon-nucleon cross sections, projectile binding energy, and target nucleon Fermi motion effects,
- a model that, on top of the bare model, includes Pauli blocking (labeled "+ Pauli blocking"),
- a model that additionally includes in-medium nucleon-nucleon cross section effects (labeled "+ in-medium effects"),
- the full model that includes nucleon-nucleon correlation effects (labeled "+ correlations").

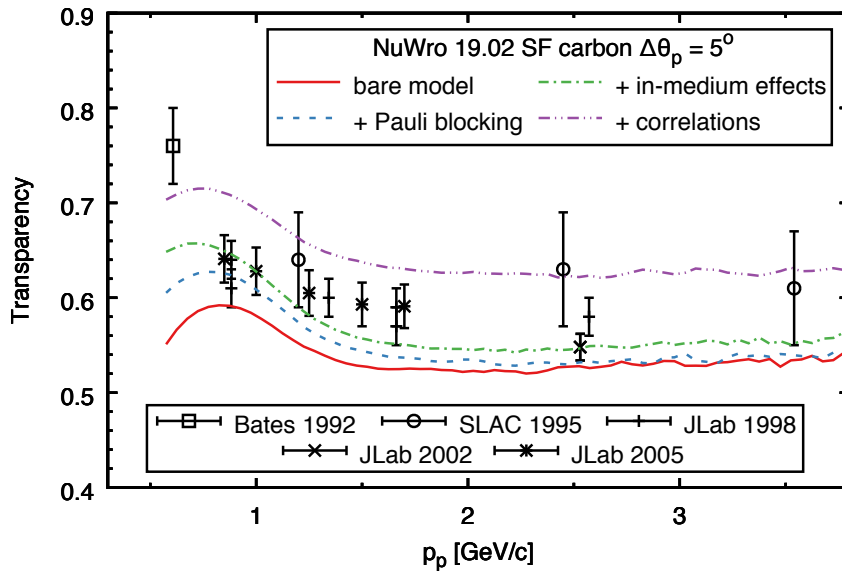


Figure 4.6: Nuclear transparency as a function of proton momentum obtained with different ingredients of the theoretical model, see explanations in the text.

We can see that in the region of proton momenta below 1 GeV/c, all the theoretical ingredients of the model are relevant, while for larger values of the momenta, correlation effects play the most critical role.

The basic observation about the bare model is that it underpredicts the experimentally measured transparency by a significant amount. The proton momentum dependence of the corresponding curve reflects the momentum dependence of free proton-proton or proton-neutron cross sections. The effect of Pauli blocking is significant for lower momenta and slowly disappears with increasing proton momentum. Although it may not be intuitive that the impact of Pauli blocking extends up to $p_p \simeq 2.5$ GeV/c, for larger elastic scattering energies, the COM angular distributions get more forward or backward peaked, leading to kinematics that are prone to be Pauli blocked. As emphasized in Section 4.2, the in-medium nucleon-nucleon cross section modifications are modeled differently for elastic and inelastic interactions. This is reflected in nuclear transparency, where the modification of elastic cross sections has a stronger impact with lowering proton momentum, while the inelastic part has a constant behavior. The effect of the nuclear correlations strongly depends on the average mean free paths in a given energy region. The free nucleon-nucleon cross section is higher in the saturation region, and therefore, the mean free paths are

lower, and the effect of correlations is more pronounced. In general, all sophisticated physical ingredients always move the predicted transparency in one direction, making it larger.

There is a significant difference in transparency behavior at the lowest values of proton momentum or Q^2 between the results presented here and the ones of Ref. [48], Fig. 3. A maximum at $Q^2 \simeq 1$ (GeV/c)², which one can see there, comes from the bare model maximum at $p_p \simeq 0.8$ GeV/c, see Fig. 4.6. In our model, this structure mostly disappears when we introduce the in-medium modifications of the nucleon-nucleon cross sections.

4.4 Consequences for neutrino analyses

The description of nuclear effects, particularly the multinucleon ejection mechanism, is one of the important uncertainties in neutrino oscillation analyses. Despite numerous theoretical [50–58], experimental [59–63], and phenomenological [64–66] investigations to refine the accuracy of this depiction, crude implementations in Monte Carlo event generators hamper efforts to draw conclusions based on more detailed final states, such as those with only one muon and proton in the final state. In the context of NuWro, as the remaining models have either satisfactory physical content (an exact SF implementation for the CCQE channel) or were successfully compared with data (for single pion production, see Refs. [67,68]), one can attempt to investigate the separation of multinucleon ejection events, assuming a proper control of the FSI modeling. In the following subsections, we present two applications of the cascade model uncertainties mentioned above on the MC predictions in the $CC0\pi$ experimental channel.

Application I: Single transverse variables

As the first application, we discuss T2K measurements of single transverse variables [69]. These variables are defined in the following way

$$\delta p_T = |\delta \vec{p}_T| = |(\vec{p}_p)_T + \vec{k}'_T|, \quad (4.4.1)$$

$$\delta \alpha_T = \arccos \left(\frac{-\vec{k}'_T \cdot \delta \vec{p}_T}{k'_T \delta p_T} \right), \quad (4.4.2)$$

$$\delta \phi_T = \arccos \left(\frac{-\vec{k}'_T \cdot (\vec{p}_p)_T}{k'_T (p_p)_T} \right), \quad (4.4.3)$$

where k' , p_p correspond to the outgoing lepton and proton, and index T denotes the transverse projection w.r.t. the beam direction. NuWro results obtained with the SF model are known to produce better results than the LFG ones [69]. Due to many adjustments in the FSI model, the results obtained with NuWro 19.02 differ notably from the ones of older versions of NuWro. The most significant effect is an increase in normalization. This only changes the values of χ^2 for the SF-based results only a little but makes the χ^2 values larger for the LFG-based ones.

Fig. 4.7 shows how much uncertainty comes from possible NuWro FSI mismodeling. We see that applying a global decrease of the cascade mean free paths by 30% decreases the normalization of the results. We checked that this does not significantly change the calculated values of χ^2 .

Making mean free paths 30% larger causes a slight increase in the value of χ^2 . A general conclusion is that the error coming from FSI strength is well under control for single transverse variables.

Application II: Proton multiplicities

An observable that is potentially very sensitive to nucleon FSI effects is a distribution of the number of reconstructed protons. The dominant contribution to the experimental signal comes from CCQE events. Thanks to FSI, there is a fraction of CCQE events with more than one proton; otherwise, such events would be impossible. Another impact of FSI is that due to rescattering, some protons lose kinetic energy dropping below the detection threshold, resulting in events with no detected protons. Generally, the FSI net effect is primarily a migration of events from $N = 1$ to $N = 0$.

In Fig. 4.8, we compare NuWro predictions with the T2K data from Ref. [69]. We see that the uncertainty coming from the unknown strength of FSI is not large. Here, larger nucleon mean free paths result in increasing proton multiplicities. The data shape suggests that FSI strength should be set at the highest value acceptable by the nuclear transparency data. The impact of FSI on the distribution is smaller than expected. It is because the experimental proton acceptance cuts eliminate most of the events with FSI.

We conclude that the FSI uncertainty applied to recent T2K data, which are potentially sensitive to nucleon FSI, gives an uncertainty that suggests that FSI modeling is under control and that there should be other sources of data and MC disagreement that is still seen in NuWro results. There is a solid foundation for using these datasets in future research of multinucleon ejection contributions and especially a very uncertain hadronic part of its modeling [70].

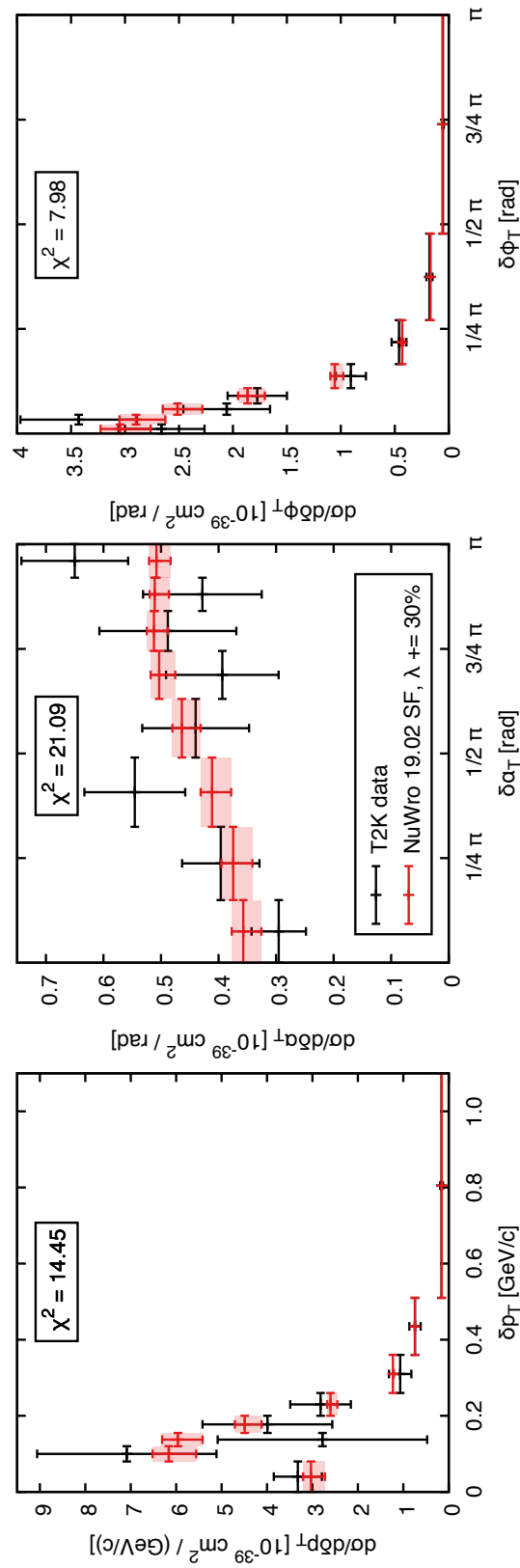


Figure 4.7: Impact of FSI uncertainty in NuWro predictions for single transverse variables. Experimental points are taken from Ref. [69].

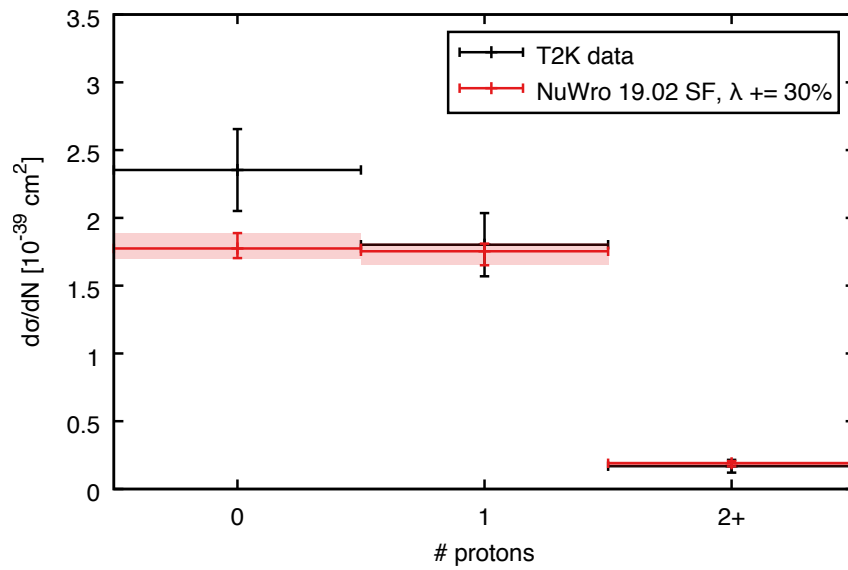


Figure 4.8: Impact of FSI uncertainty in NuWro predictions for proton multiplicities. Experimental points are taken from Ref. [69].

References

- [1] R. Serber, *Phys. Rev.* **72**, 1114 (1947).
- [2] N. Metropolis, R. Bivins, M. Storm, *et al.* *Phys. Rev.* **110**, 185 (1958).
- [3] N. Metropolis, R. Bivins, M. Storm, *et al.* *Phys. Rev.* **110**, 204 (1958).
- [4] H. W. Bertini, *Phys. Rev.* **188**, 1711 (1969).
- [5] J. Cugnon, *Phys. Rev. C* **22**, 1885 (1980).
- [6] K. K. Gudima, S. G. Mashnik, and V. D. Toneev, *Nucl. Phys. A* **401**, 329 (1983).
- [7] T. T. Böhlen, F. Cerutti, M. P. W. Chin, *et al.* *Nucl. Data Sheets* **120**, 211 (2014).
- [8] Y. Yariv *et al.* In ND 2007 (June 2008), p. 296.
- [9] O. Buss, T. Gaitanos, K. Gallmeister, *et al.* *Phys. Rept.* **512**, 1 (2012).
- [10] J. Aichelin, *Phys. Rept.* **202**, 233 (1991).
- [11] Y.-X. Zhang *et al.* *Phys. Rev. C* **97**, 034625 (2018).
- [12] L. Alvarez-Ruso *et al.* *Prog. Part. Nucl. Phys.* **100**, 1 (2018).
- [13] U. Mosel, O. Lalakulich, and K. Gallmeister, *Phys. Rev. Lett.* **112**, 151802 (2014).
- [14] A. P. Furmanski and J. T. Sobczyk, *Phys. Rev. C* **95**, 065501 (2017).
- [15] C. Patrignani *et al.* *Chin. Phys. C* **40**, 100001 (2016).
- [16] D. Dutta, K. Hafidi, and M. Strikman, *Prog. Part. Nucl. Phys.* **69**, 1 (2013).
- [17] L. Aliaga *et al.* *Nucl. Instrum. Meth. A* **743**, 130 (2014).
- [18] K. Abe *et al.* *Nucl. Instrum. Meth. A* **659**, 106 (2011).
- [19] D. F. Geesaman *et al.* *Phys. Rev. Lett.* **63**, 734 (1989).
- [20] G. Garino *et al.* *Phys. Rev. C* **45**, 780 (1992).
- [21] N. Makins *et al.* *Phys. Rev. Lett.* **72**, 1986 (1994).
- [22] T. G. O'Neill *et al.* *Phys. Lett. B* **351**, 87 (1995).
- [23] D. Abbott *et al.* *Phys. Rev. Lett.* **80**, 5072 (1998).
- [24] D. Dutta *et al.* *Phys. Rev. C* **68**, 064603 (2003).
- [25] K. Garrow *et al.* *Phys. Rev. C* **66**, 044613 (2002).
- [26] D. Rohe *et al.* *Phys. Rev. C* **72**, 054602 (2005).
- [27] D. Dutta, The $(e, e'p)$ reaction mechanism in the quasielastic region, PhD thesis (Northwestern University, 1999).
- [28] D. W. McKee, Nuclear Transparency and Single Particle Spectral Functions from Quasielastic $A(e, e'p)$ reactions up to $Q^2 = 8.1 \text{ GeV}^2$, PhD thesis (New Mexico State University, 2003).
- [29] J. M. Udias, P. Sarriguren, E. Moya de Guerra, *et al.* *Phys. Rev. C* **48**, 2731 (1993).
- [30] O. Benhar, *Nucl. Phys. B Proc. Suppl.* **159**, edited by F. Cavanna, J. G. Morfin, and T. Nakaya, 168 (2006).
- [31] L. Frankfurt, M. Strikman, and M. Zhalov, *Phys. Lett. B* **503**, 73 (2001).

- [32] L. Lapikas, G. van der Steenhoven, L. Frankfurt, *et al.* Phys. Rev. C **61**, 064325 (2000).
- [33] O. Hen *et al.* Phys. Lett. B **722**, 63 (2013).
- [34] P. Lava, M. C. Martinez, J. Ryckebusch, *et al.* Phys. Lett. B **595**, 177 (2004).
- [35] M. C. Martinez, P. Lava, N. Jachowicz, *et al.* Phys. Rev. C **73**, 024607 (2006).
- [36] W. Cosyn and J. Ryckebusch, Phys. Rev. C **87**, 064608 (2013).
- [37] J. J. Kelly, Phys. Rev. C **71**, 064610 (2005).
- [38] T. Golan, C. Juszczak, and J. T. Sobczyk, Phys. Rev. C **86**, 015505 (2012).
- [39] K. Niewczas and J. T. Sobczyk, Phys. Rev. C **100**, 015505 (2019).
- [40] C. L. McGivern *et al.* Phys. Rev. D **94**, 052005 (2016).
- [41] Nuwro official repository, <https://github.com/NuWro/nuwro>.
- [42] J. Bystricky, P. La France, F. Lehar, *et al.* J. Phys. (France) **48**, 1901 (1987).
- [43] J. Cugnon, J. Vandermeulen, and D. L'Hote, Nucl. Instrum. Meth. B **111**, 215 (1996).
- [44] V. R. Pandharipande and S. C. Pieper, Phys. Rev. C **45**, 791 (1992).
- [45] D. Klakow, G. Welke, and W. Bauer, Phys. Rev. C **48**, 1982 (1993).
- [46] Variational monte carlo calculations of two-nucleon densities, <https://www.phy.anl.gov/theory/research/density2>.
- [47] J. Carlson, S. Gandolfi, F. Pederiva, *et al.* Rev. Mod. Phys. **87**, 1067 (2015).
- [48] T. Leitner, O. Buss, and U. Mosel, Acta Phys. Polon. B **40**, edited by A. Ankowski and J. Sobczyk, 2585 (2009).
- [49] J. Lehr, In-medium-eigenschaftenvon nukleonen und nukleonresonanzen in einem semiklassischen transportmodell, PhD thesis (Giessen University, 2003).
- [50] M. Martini, M. Ericson, G. Chanfray, *et al.* Phys. Rev. C **81**, 045502 (2010).
- [51] M. Martini, M. Ericson, and G. Chanfray, Phys. Rev. C **84**, 055502 (2011).
- [52] J. Nieves, I. Ruiz Simo, and M. J. Vicente Vacas, Phys. Rev. C **83**, 045501 (2011).
- [53] G. D. Megias, J. E. Amaro, M. B. Barbaro, *et al.* Phys. Rev. D **94**, 093004 (2016).
- [54] T. Van Cuyck, N. Jachowicz, R. González-Jiménez, *et al.* Phys. Rev. C **94**, 024611 (2016).
- [55] T. Van Cuyck, N. Jachowicz, R. González-Jiménez, *et al.* Phys. Rev. C **95**, 054611 (2017).
- [56] A. Lovato, S. Gandolfi, J. Carlson, *et al.* Phys. Rev. C **97**, 022502 (2018).
- [57] N. Rocco, C. Barbieri, O. Benhar, *et al.* Phys. Rev. C **99**, 025502 (2019).
- [58] U. Mosel and K. Gallmeister, Phys. Rev. C **96**, [Addendum: Phys.Rev.C 99, 035502 (2019)], 015503 (2017).
- [59] K. Abe *et al.* Phys. Rev. D **93**, 112012 (2016).
- [60] K. Abe *et al.* Phys. Rev. D **97**, 012001 (2018).
- [61] C. E. Patrick *et al.* Phys. Rev. D **97**, 052002 (2018).
- [62] R. Gran *et al.* Phys. Rev. Lett. **120**, 221805 (2018).
- [63] X. G. Lu *et al.* Phys. Rev. Lett. **121**, 022504 (2018).

- [64] R. Gran, J. Nieves, F. Sanchez, *et al.* Phys. Rev. D **88**, 113007 (2013).
- [65] K. Niewczas and J. T. Sobczyk, Phys. Rev. C **93**, 035502 (2016).
- [66] X. -G. Lu, L. Pickering, S. Dolan, *et al.* Phys. Rev. C **94**, 015503 (2016).
- [67] R. González-Jiménez, K. Niewczas, and N. Jachowicz, Phys. Rev. D **97**, 013004 (2018).
- [68] A. Nikolakopoulos, R. González-Jiménez, K. Niewczas, *et al.* Phys. Rev. D **97**, 093008 (2018).
- [69] K. Abe *et al.* Phys. Rev. D **98**, 032003 (2018).
- [70] J. T. Sobczyk, Phys. Rev. C **86**, 015504 (2012).

5

Generator implementation philosophy

Oscillation analyses rely on Monte Carlo event generators, providing theoretical predictions of neutrino interactions on nuclear targets. Pions produced in these processes provide a significant fraction of oscillation signal and background on both elementary scattering and detector simulation levels. Thus, it is critical to develop techniques that will allow us to accommodate state-of-the-art theoretical models describing single-pion production (SPP) into MCs. Based on comparison studies, we propose a novel implementation strategy that combines satisfactory efficiency with high precision in reproducing details of theoretical model predictions, including pion angular distributions. The proposed implementation is model-independent, providing a framework that can include any model for SPP and be extended to other reactions, including one- and two-nucleon knock-out. The following discussion was published previously in a slightly different format as Physical Review D 103 (2021) 053003.

5.1 Single-pion production

Single-pion production is one of the main reaction channels relevant for accelerator-based neutrino experiments, where neutrino energies range from a couple of hundred MeVs up to several GeVs [1]. Indeed, it is challenging to distinguish neutral pions from electrons in experiments with detectors using Cherenkov radiation, such as T2K [2] and MiniBooNE [3]. This makes their production the main background for the detection of low-energy electrons. A good understanding of this background is essential for future CP violation measurements in the Hyper-Kamiokande experiment [4] and in attempts to understand the excess of ν_e -like events reported by the MiniBooNE collaboration [5]. Moreover, produced pions issue a significant background for other neutrino experiments, such as MicroBooNE [6], as it is challenging to distinguish charged pions from muons in Liquid Argon Time Projection Chambers. Regarding oscillation analyses, SPP also

contributes to the commonly used $CC0\pi$ experimental topology [7], provided that the pions are reabsorbed in the nuclear medium or remain undetected. Furthermore, this interaction channel is a part of the signal for oscillation experiments, especially with higher-energy neutrino beams such as NOvA [8] and DUNE [9], but also for T2K [10].

Over the past few years, the MINERvA, T2K, ArgoNeuT, and MiniBooNE experiments [11–16] have collected an increasingly large dataset for (anti)neutrino-induced single-pion production on nuclear targets. Subsequently, it has been compared to predictions from several models, revealing significant differences in their data description. Moreover, there are apparent tensions between the MiniBooNE, T2K, and MINERvA SPP measurements [17–20] themselves. Ref. [21] showed that a simultaneous agreement between the results of the ANL and BNL bubble chamber data and the MINERvA experiment could not be reached. Furthermore, it was not possible to provide a consistent description using a single parameter tune for the different SPP channels measured by the latter.

The use of nuclear targets in neutrino oscillation experiments considerably complicates the description of single-pion production because the presence of such a medium affects all of the hadrons in the process. On top of that, final-state interactions, such as pion absorption or charge exchange pion-nucleon scattering, alter the experimental signal entirely. It is seemingly an intractable problem to provide a detailed microscopic description of FSI over the sizable phase space of these experiments. For this reason, the FSI are usually treated in an approximate way using intranuclear cascade models [22–24] implemented in various Monte Carlo neutrino event generators.

An accurate model for such scattering off the nucleon is a prerequisite for a good description of neutrino-induced single-pion production on nuclei in the factorized approach used in MCs. Several studies have been conducted on neutrino-induced SPP off the nucleon [25–40]. However, the available models have not readily found their way into Monte Carlo event generators, and if so, without accounting for their full kinematic complexity.

In this work, we perform a detailed study of possible strategies to implement single-pion production models in neutrino event generators. Based on the results of this study, we propose a novel algorithm for the case of SPP on the nucleon target to allow for further progress in the accommodation of information from recent experimental measurements. The algorithm is model-independent, as it only relies on the kinematics of the process and ensures no relevant information is lost on a neutrino-nucleon interaction level. Such a solution allows for any theoretical model to be implemented in MCs, facilitating a comparison of different approaches. Additionally, owing to the separation of the leptonic and hadronic currents, it provides flexibility to modify the former, e.g., with BSM physics. Furthermore, with appropriately implemented hadronic currents, one can calculate cross sections for charged current, neutral current, and electron-induced SPP with a consistent treatment of both the vector and axial components. We claim that the proposed algorithm will be of great importance for future implementations of neutrino-nucleus single-pion production, dealing with a considerable number of degrees of freedom and hence a critical demand to maintain both numerical efficiency and precision. This general philosophy can be extended in the future to implement state-of-the-art models for other interaction channels, such as one- and two-nucleon knock-out discussed in Chapter 2 and Chapter 3.

Kinematics and cross section

We commence by describing the kinematics of lepton-induced single-pion production, where an incoming lepton with four-momentum $k = (E, \vec{k})$ scatters off a nucleon p_i by exchange of a single gauge boson with four-momentum $q = (\omega, \vec{q})$, thereby producing a pion. We denote the four-momenta of the final-state lepton, pion, and recoiling nucleon by k' , k_π , and p_N , and their rest masses by m , M_π , and M_N , respectively. It is convenient to describe such a process in the hadronic center-of-momentum system (CMS), with the lepton plane defining the x - z plane and the direction of the momentum transfer \vec{q} defining the z -axis, as depicted in Fig. 5.1. In the hadronic CMS,

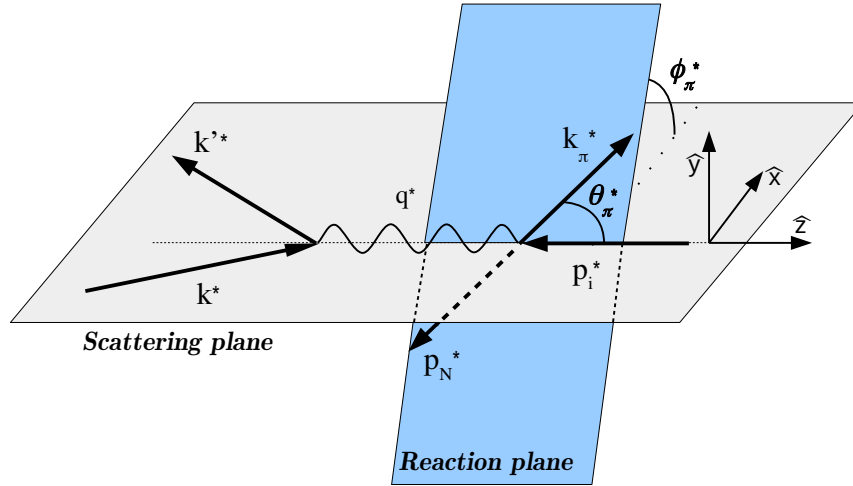


Figure 5.1: Kinematics of lepton-induced single-pion production on the nucleon in the hadronic center-of-momentum frame of reference.

for which we denote quantities with a superscript $*$, the final hadronic system is at rest, meaning $\vec{k}_\pi^* = -\vec{p}_N^*$. We characterize the kinematics by the Lorentz invariants: the invariant hadronic mass $W^2 = (q + p_i)^2 = (k_\pi + p_N)^2$ and the exchanged four-momentum squared $Q^2 = -q^2 = -(k - k')^2$, along with the produced pion solid angle Ω_π^* .

Within the Born approximation, we can describe the cross section as a contraction of the leptonic and hadronic tensors. The standard calculation of the leptonic tensor for massless incoming leptons yields

$$L_{\mu\nu} = k_\mu k'_\nu + k'_\mu k_\nu - \eta_{\mu\nu} k \cdot k' - ih \epsilon_{\mu\nu\alpha\beta} k^\alpha k'^\beta, \quad (5.1.1)$$

where η is the metric tensor with signature $(+, -, -, -)$, $\epsilon_{\mu\nu\alpha\beta}$ is the antisymmetric Levi-Civita tensor ($\epsilon_{0123} = +1$), and h is the helicity of the incoming lepton. We define the hadronic tensor as

$$H^{\mu\nu} = \overline{\sum} J^{\mu\dagger} J^\nu, \quad (5.1.2)$$

with the hadronic current J^μ , and averaging and summation over the spin of the initial and final nucleon are assumed. Representing the hadronic current in terms of initial and final state nucleon spinors and the transition operator \mathcal{O}^μ as

$$J^\mu = \bar{u}(p_N, s_N) \mathcal{O}^\mu u(p_i, s_i), \quad (5.1.3)$$

one obtains for the hadronic tensor

$$H^{\mu\nu} = \frac{1}{8M_N^2} \text{Tr} \left((\not{p}_i + M_N) \tilde{\mathcal{O}}^\mu (\not{p}_N + M_N) \mathcal{O}^\nu \right), \quad (5.1.4)$$

where $\tilde{\mathcal{O}}^\mu = \gamma_0 (\mathcal{O}^\mu)^\dagger \gamma_0$. With these definitions, the cross section is

$$\frac{d^4\sigma}{dWdQ^2d\Omega_\pi^*} = \frac{1}{2} \frac{\mathcal{F}_{CC}^2}{(2\pi)^4} \frac{|\vec{k}_\pi^*|}{|\vec{k}'^2|} L_{\mu\nu} H^{\mu\nu}, \quad (5.1.5)$$

where the coupling constant for the charged current case that we consider in this chapter is

$$\mathcal{F}_{CC} = \frac{G_F \cos \theta_c}{\sqrt{2}}. \quad (5.1.6)$$

Using the invariance of the leptonic tensor under rotations of the hadronic plane around \vec{q} , one can factorize the dependence of the cross section on the azimuthal angle in terms of trigonometric functions, as shown explicitly in Refs. [26,41–43]. Specifically, in the given CMS, we express the cross section as

$$\begin{aligned} \frac{d^4\sigma}{dWdQ^2d\Omega_\pi^*} &= \frac{1}{2} \frac{\mathcal{F}_{CC}^2}{(2\pi)^4} \frac{|\vec{k}_\pi^*|}{|\vec{k}'^2|} \times [A + B \cos(\phi_\pi^*) \\ &+ C \cos(2\phi_\pi^*) + D \sin(\phi_\pi^*) + E \sin(2\phi_\pi^*)], \end{aligned} \quad (5.1.7)$$

where the functions A, \dots, E do not depend on the azimuthal pion angle ϕ_π^* . Below, we write them explicitly, in terms of the elements of the leptonic and hadronic tensors, computed for the kinematics of Fig. 5.1 (with $\phi_\pi^* = 0$), and making use of the symmetry properties of $L_{\mu\nu}$, as

$$\begin{aligned} A &= L_{00} H^{00} + 2L_{30} H_s^{30} + L_{33} H^{33} \\ &+ \frac{L_{11} + L_{22}}{2} (H^{11} + H^{22}) + 2iL_{12} H_a^{12}, \end{aligned} \quad (5.1.8)$$

$$B = 2L_{01} H_s^{01} + L_{13} H_s^{13} + iL_{02} H_a^{02} + iL_{23} H_a^{23}, \quad (5.1.9)$$

$$C = \frac{L_{11} - L_{22}}{2} (H^{11} - H^{22}), \quad (5.1.10)$$

$$D = 2 [-L_{01} H_s^{02} - L_{13} H_s^{23} + iL_{02} H_a^{01} + iL_{23} H_a^{13}], \quad (5.1.11)$$

$$E = (L_{22} - L_{11}) H_s^{12}, \quad (5.1.12)$$

where H_s and H_a correspond to the symmetric (real) and antisymmetric (imaginary) parts of the hadronic tensor:

$$H^{\mu\nu} = H_s^{\mu\nu} + iH_a^{\mu\nu}, \quad H_{s,a}^{\mu\nu} \in \mathbb{R}. \quad (5.1.13)$$

For antineutrino interactions, the terms including the imaginary part of the hadronic tensor change sign as all of the off-diagonal terms of the leptonic tensor involving a Lorentz index 2 are purely antisymmetric and proportional to the helicity, while the others are symmetric.

In the context of this study, it is essential to notice that the double-differential cross section $d^2\sigma/dWdQ^2$ and the triple-differential $d^3\sigma/dWdQ^2d\cos\theta_\pi^*$ are entirely determined by the function A as the other contributions disappear after integration over the azimuthal pion angle ϕ_π^* .

We remark that the presented expressions apply to all electroweak SPP processes, thereby facilitating a consistent treatment of the vector current across electron- and neutrino-induced cases implemented in event generators. Furthermore, a similar separation of the angular dependence is valid for one-nucleon knock-out on a nuclear target or for any semi-leptonic process in which a single on-shell particle defines the hadronic plane for that matter. Thus, similar methods as the ones outlined in the next section should apply to the implementation of microscopic models for exclusive one-nucleon knock-out.

5.2 Monte Carlo algorithms

The kinematics for weak single-pion production off the nucleon given an incoming neutrino energy, the target nucleon momentum, and an arbitrarily chosen lepton scattering plane, is fully described by four independent variables. In what follows, these quantities are considered to be random variables with a probability distribution defined by Eq. 5.1.7. While constructing Monte Carlo event generators, one of the major tasks is to generate these variables efficiently. Here, we discuss several of our approaches, each of them presenting a different trade-off between efficiency, precision, and reliance on precomputed assets.

4D algorithm

The most straightforward approach is to use directly the full cross section formula (5.1.7). The available phase space of the independent variables W , Q^2 , $\cos \theta_\pi^*$, ϕ_π^* is

$$\begin{aligned} W &\in [M, \sqrt{s} - m], \\ Q^2 &\in [2\underline{E}E' - m^2 - 2\underline{E}|\underline{k}'|, 2\underline{E}E' - m^2 + 2\underline{E}|\underline{k}'|], \\ \cos \theta_\pi^* &\in [-1, 1], \\ \phi_\pi^* &\in [0, 2\pi], \end{aligned} \tag{5.2.1}$$

where $s = (k + p_i)^2$, and the underline marks the quantities calculated in the lepton+hadron center-of-momentum frame:

$$\begin{aligned} \underline{E} &= \frac{s - M_N^2}{2\sqrt{s}}, \quad \underline{E}' = \frac{s + m^2 - W^2}{2\sqrt{s}}, \\ |\underline{k}'| &= \frac{\sqrt{(s - m^2 - W^2)^2 - 4m^2W^2}}{2\sqrt{s}}. \end{aligned} \tag{5.2.2}$$

In this approach, for each event, we sample four independent variables, adding a randomly selected lepton scattering plane. We perform the sampling following the order presented in Eq. 5.2.1, starting from W , because the range in Q^2 is W -dependent and because one needs both W and Q^2 to specify the hadronic CMS needed to select $\cos \theta_\pi^*$ and ϕ_π^* . Such information is enough to generate the full kinematics of an event trial. Each of them has an assigned *event weight*, given by Eq. 5.1.7 multiplied by the Monte Carlo phase space factor

$$V_{4D} = (\sqrt{s} - m - M_N) \cdot 4\underline{E}|\underline{k}'| \cdot 2 \cdot 2\pi. \tag{5.2.3}$$

The average value of this weight is equal to the total cross section. We obtain the final set of events by applying the accept-reject algorithm on the collection of trials. We will refer to this strategy of generating events as the "4D algorithm".

Although asymptotically correct, we expect this approach to be inefficient, especially with increasing neutrino energies. The efficiency of an accept-reject algorithm depends on the interplay between the distribution's shape and the sampling envelope. Since the former is initially unknown, we choose the latter to be the maximal value of the cross section (Eq. 5.1.7), calculated in real-time. As we increase the phase space, we access new regions of low, relative to the envelope, cross section values, leading to event trials with a minimal chance of acceptance. The interplay between the acceptance efficiency and the computation time needed to calculate an event weight are the main features contrasting the proposed algorithms. In the 4D algorithm, for every event trial, we evaluate the value of the cross section given by Eq. 5.1.7 once.

3D algorithm

In the second approach, we isolate the dependence of the cross section on the azimuthal pion angle. After performing an integration over ϕ_π^* , the differential cross section depends only on the function A , and its explicit dependence on $H_{\mu\nu}$ reads

$$\begin{aligned} \frac{d^3\sigma}{dWdQ^2d\cos\theta_\pi^*} &= \frac{1}{2} \frac{\mathcal{F}_{CC}^2}{(2\pi)^3} \frac{|\vec{k}_\pi^*|}{|\vec{k}'^2|} [L_{00}H^{00}(W, Q^2, \cos\theta_\pi^*) \\ &+ 2L_{30}H_s^{30}(W, Q^2, \cos\theta_\pi^*) + L_{33}H^{33}(W, Q^2, \cos\theta_\pi^*) \\ &+ \frac{L_{11} + L_{22}}{2}(H^{11} + H^{22})(W, Q^2, \cos\theta_\pi^*) \\ &+ 2iL_{12}H_a^{12}(W, Q^2, \cos\theta_\pi^*)], \end{aligned} \quad (5.2.4)$$

where the hadronic tensor elements are functions of three variables: $W, Q^2, \cos\theta_\pi^*$. In this case, only three variables are sampled and we attribute event trials with weights obtained from multiplying the results of Eq. 5.2.4 by the new Monte Carlo phase space volume

$$V_{3D} = (\sqrt{s} - m - M) \cdot 4E|\vec{k}'| \cdot 2. \quad (5.2.5)$$

As before, the average of the event weights yields the total cross section. We obtain the final set of, yet incomplete, events using the same accept-reject method, with the sampling envelope given by the maximum of Eq. 5.2.4. Due to the reduced phase space dimensionality, the accept-reject algorithm for incomplete events, without an assigned value of the pion azimuthal angle, is more efficient.

For already selected events, we sample the variable ϕ_π^* using the known probability distribution given, for fixed values of $W, Q^2, \cos\theta_\pi^*$, by

$$\begin{aligned} f(\phi_\pi^*) &= A + B \cos(\phi_\pi^*) + C \cos(2\phi_\pi^*) \\ &+ D \sin(\phi_\pi^*) + E \sin(2\phi_\pi^*), \end{aligned} \quad (5.2.6)$$

and its cumulative distribution function:

$$\begin{aligned} F(\phi_\pi^*) &= \frac{\phi_\pi^*}{2\pi} + \frac{B}{2\pi A} \sin\phi_\pi^* + \frac{C}{4\pi A} \sin 2\phi_\pi^* \\ &+ \frac{D}{2\pi A} (1 - \cos\phi_\pi^*) + \frac{E}{4\pi A} (1 - \cos 2\phi_\pi^*). \end{aligned} \quad (5.2.7)$$

As the derivative of the $F(\phi_\pi^*)$ function is known algebraically, its inversion with the Newton method is efficient and converges rapidly. In what follows, we will call this procedure the "3D algorithm".

2D algorithm

The starting point for this approach is the formula

$$\begin{aligned} \frac{d^2\sigma}{dWdQ^2} = & \frac{1}{2} \frac{\mathcal{F}_{CC}^2}{(2\pi)^3} \frac{|\vec{k}_\pi^*|}{|\vec{k}'^2|} \left[L_{00}\tilde{H}^{00}(W, Q^2) \right. \\ & + 2L_{30}\tilde{H}_s^{30}(W, Q^2) + L_{33}\tilde{H}^{33}(W, Q^2) \\ & + \frac{L_{11} + L_{22}}{2}(\tilde{H}^{11} + \tilde{H}^{22})(W, Q^2) \\ & \left. + 2iL_{12}\tilde{H}_a^{12}(W, Q^2) \right], \end{aligned} \quad (5.2.8)$$

obtained from Eq. 5.2.4 by integrating out the $\cos\theta_\pi^*$ variable and adopting the notation:

$$\tilde{H}^{\mu\nu}(W, Q^2) = \int_{-1}^1 H^{\mu\nu}(W, Q^2, \cos\theta_\pi^*) d\cos\theta_\pi^*. \quad (5.2.9)$$

As a result, we express the double-differential cross section in terms of 5 combinations of hadronic tensor elements, which depend solely on W and Q^2 . We store their values in the form of lightweight tables.

The first step of the "2D algorithm" is to sample a pair of variables (W, Q^2) with the probability density defined by Eq. 5.2.8. We perform it efficiently, using the precalculated tables with a suitable bilinear interpolation. At this point, we build an incomplete event trial and compute its weight, analogously to the previous approaches, by multiplying the values obtained from Eq. 5.2.8 by the Monte Carlo phase space factor

$$V_{2D} = (\sqrt{s} - m - M) \cdot 4E|\vec{k}'|. \quad (5.2.10)$$

We accept the set of incomplete events according to their weights, relative to the maximum of Eq. 5.2.8, and only then we assign the values of $\cos\theta_\pi^*$ and ϕ_π^* . Such an approach saves a considerable amount of time, avoiding the computation of a full event before applying the accept-reject algorithm.

We select the value of $\cos\theta_\pi^*$ using a probability distribution governed by the function A . To optimize this task, we exploit the smooth character of this function in the region of interest. Having W and Q^2 fixed, we calculate the values of $A(\cos\theta_\pi^*)$ at k points and approximate as a polynomial of degree $k - 1$. Then, we obtain the cumulative distribution function as a polynomial of degree k and sample the $\cos\theta_\pi^*$ variable using the inverse sampling method. For $(k \leq 3)$, we perform the inversion algebraically, while for larger k , numerically, with the bisection method. We have checked that, for most kinematics, the degree of $k = 3$ provides sufficient precision, while the distributions are almost exact on the whole phase space for degrees $k \geq 7$. We will discuss the choice of the optimal value of k in the second next section.

Depending on the implementation effort and allowed memory, it is also possible to store in tables hadronic tensor elements $H_{\mu\nu}(W, Q^2, \cos\theta_\pi^*)$ that allow obtaining the full $A(W, Q^2, \cos\theta_\pi^*)$

function. Then, in each event, the maximum of the $\cos \theta_\pi^*$ distribution is given explicitly, and one can sample its value using the accept-reject method. Such an approach enables us to reduce the time-consumption of each trial event further. In what follows, we will denote this approach as the "2D algorithm (table)".

Finally, to finish building the kinematics for the accepted events, we need to sample the variable ϕ_π^* . We proceed by repeating the method used for the "3D algorithm".

5.3 Numerical tools

To reliably test the performance of the abovementioned sampling algorithms, we performed simulations using the Ghent Low Energy Model (LEM) of single-pion production implemented in the NuWro Monte Carlo event generator. The particular implementation works on a restricted phase space defined by the condition $W < 1.5$ GeV.

Ghent Low Energy Model of SPP

This single-pion production model is based on the work of Hernández, Nieves, and Valverde (HNV), first presented in Ref. [29] with later improvements of Refs. [44,45]. It contains a microscopic description of the SPP at the amplitude level and includes, in addition to the contributions from the $\Delta(1232)$ and $D_{13}(1520)$ resonances (both direct and crossed channel Feynman diagrams), the lowest-order background diagrams derived from chiral perturbation theory (ChPT). Additionally, it includes a relative phase between the ChPT terms and the dominant partial wave of the Δ -pole, which partially restores unitarity [45].

The Ghent LEM [38] is a custom variant of the model with an independently written code. On top of the standard version, it includes additional s- and u-channel contributions from the spin-1/2 resonances $P_{11}(1440)$ and $S_{11}(1535)$ [46]. However, this model does not include the phenomenological contact term introduced in Ref. [47]. Additionally, the same model, working in the relativistic plane wave impulse approximation, was extended to describe neutrino scattering on nuclei [18,19].

NuWro Monte Carlo event generator

NuWro is a versatile Monte Carlo neutrino event generator, which has been developed by the theoretical group of the University of Wrocław since 2005. It is applicable for simulations in the range of neutrino energies covered by the accelerator-based neutrino oscillation experiments, with an upper bound of ~ 100 GeV. We have extensively described its philosophy and physical components in Chapter 1. Here, similarly to the study of Chapter 4, we rely on NuWro version 19.02.2 [48].

The NuWro single-pion production model combines the contribution from the $\Delta(1232)$ resonance excitation [49] with a non-resonant background obtained by extrapolating the DIS contribution to lower values of W , blended incoherently in the region $W \in (1.3, 1.6)$ GeV [50]. The generated events follow the double-differential cross sections $d^2\sigma/dWdQ^2$ for both the resonant and non-resonant parts. On top of that, the model obtains the Ω_π^* distributions using the

parametrized ones measured by the BNL bubble chamber experiment [51] for the former, while for the latter, obtains the kinematics using the PYTHIA6 hadronization routines [52]. Alternatively, one can use the parametrization obtained by the ANL experiment [53]. In this study, we refer to this model as "isobar NuWro".

In NuWro, for all of the described single-pion production model implementations, we apply additional optimizations of sampling in the (W, Q^2) plane. As it is common for all models and methods presented in this work, this has no impact on our findings nor conclusions.

5.4 Implementation performance

We have implemented the Ghent LEM in NuWro, applying the five versions of the strategies presented in Sec. 5.2, labeled: "4D alg.", "3D alg.", "2D alg. ($k = 3$)", "2D alg. ($k = 7$)", "2D alg. (table)". We summarize their performance in Table 5.1, with four numerical computations: for two neutrino energies $E = 1.0, 2.5$ GeV, and off both proton and neutron nucleon targets. In the respective columns of these tables, one can find: an average weight σ and its standard deviation s_{1M} calculated from 1 million trial events, computer time τ needed to calculate a trial event (before the accept-reject algorithm is applied) in arbitrary units, efficiency ϵ of the accept-reject algorithm, and the relative increase of computer time α needed to generate an event with complete kinematics. In the last columns, we present values of S_{1M} that is a measure of the performance of a given algorithm: an estimate of the time needed to produce a sample of $N = 1 \times 10^6$ events. In a given simulation of efficiency ϵ , one has to generate N/ϵ trial events, out of which N events are accepted and require the complete kinematics, while $N/\epsilon - N$ are the rejected trial events that require only the weight calculation. Since the computation of a trial event takes time τ and of a complete event $\tau(1 + \alpha)$, the overall computer time needed to generate a set of N events becomes

$$S_N = N \cdot \tau \cdot (1 + \alpha) + \left(\frac{N}{\epsilon} - N\right) \cdot \tau = N \cdot \tau \cdot \left(\frac{1}{\epsilon} + \alpha\right). \quad (5.4.1)$$

Thus, the value of S_N depends on three variables: τ , ϵ , α , that fully characterize each algorithm.

The first, most significant difference between various approaches appears in the values of τ and show that, in the models used, the time needed for generating a trial event is ~ 20 times smaller for the 2D algorithm off protons, relative to the 3D and 4D algorithms, while off neutrons the difference rises about twice as much. The former stems solely from the computational cost needed to evaluate the hadronic tensor, which is the bottleneck of the Ghent LEM, while the latter comes from the fact that neutrino-induced SPP off the neutron involves two possible final states and both cross sections need to be evaluated to obtain the weight of any of those events.

The differences in ϵ for simulations with the same conditions come from the differential cross section shapes as well as the size of the sampled phase space that grows with increasing energy. Due to the dominance of the Δ^{++} resonance, the SPP cross sections for neutrino scattering off the proton target are much more peaked, leading to lower event acceptance efficiency. On the other hand, the differences in efficiencies between particular algorithms within the same simulations come from different dimensionalities of the sampled phase spaces and the fact that the cross sections are not uniform in the additional variables $(\cos \theta_{\pi^*}, \phi_{\pi^*})$.

	model	$\sigma[\text{cm}^2]$	$s_{1\text{M}}[\text{cm}^2]$	τ	ϵ	α	$S_{1\text{M}}$
	4D alg.	5.1724e-39	7.8e-42	8.01e-07	0.12	-	6.9
	3D alg.	5.1661e-39	7.7e-42	8.02e-07	0.13	1.0	6.9
2D alg.	(k = 7)	5.1586e-39	7.5e-42	4.04e-08	0.16	143.9	6.1
	(k = 3)	5.1623e-39	7.5e-42	4.04e-08	0.16	72.0	3.2
	(table)	5.1613e-39	7.5e-42	4.03e-08	0.16	18.6	1.0

(a) E = 1.0 GeV neutrinos off proton target.

	model	$\sigma[\text{cm}^2]$	$s_{1\text{M}}[\text{cm}^2]$	τ	ϵ	α	$S_{1\text{M}}$
	4D alg.	2.5105e-39	2.7e-42	1.83e-06	0.15	-	12.1
	3D alg.	2.5095e-39	2.7e-42	1.83e-06	0.18	0.5	11.2
2D alg.	(k = 7)	2.5126e-39	2.6e-42	4.11e-08	0.21	169.4	7.2
	(k = 3)	2.5124e-39	2.6e-42	4.10e-08	0.21	85.1	3.7
	(table)	2.5116e-39	2.6e-42	4.08e-08	0.21	22.0	1.1

(b) E = 1.0 GeV neutrinos off neutron target.

	model	$\sigma[\text{cm}^2]$	$s_{1\text{M}}[\text{cm}^2]$	τ	ϵ	α	$S_{1\text{M}}$
	4D alg.	6.8637e-39	11.2e-42	8.04e-07	0.08	-	9.9
	3D alg.	6.8634e-39	10.8e-42	8.01e-07	0.10	1.0	8.8
2D alg.	(k = 7)	6.8327e-39	10.5e-42	3.98e-08	0.12	149.1	6.3
	(k = 3)	6.8510e-39	10.5e-42	4.08e-08	0.12	72.6	3.3
	(table)	6.8450e-39	10.5e-42	4.04e-08	0.12	19.0	1.1

(c) E = 2.5 GeV neutrinos off proton target.

	model	$\sigma[\text{cm}^2]$	$s_{1\text{M}}[\text{cm}^2]$	τ	ϵ	α	$S_{1\text{M}}$
	4D alg.	4.5860e-39	4.7e-42	1.84e-06	0.14	-	13.5
	3D alg.	4.5851e-39	4.4e-42	1.83e-06	0.18	0.5	11.4
2D alg.	(k = 7)	4.5762e-39	4.2e-42	4.19e-08	0.20	169.6	7.3
	(k = 3)	4.5805e-39	4.2e-42	4.13e-08	0.20	86.0	3.8
	(table)	4.5809e-39	4.2e-42	4.12e-08	0.20	22.3	1.1

(d) E = 2.5 GeV neutrinos off neutron target.

Table 5.1: Tables of the performance of the algorithms, based on 1M event simulations. The values of τ are normalized to obtain $S_{1\text{M}} = 1.0$ for the "2D alg. (table)" model.

Values of the third characteristic variable α represent all of the secondary effort, relative to the event trial computation time, needed to generate the full kinematics of an accepted event. One can see that for the 3D algorithm, in which sampling of the ϕ_π^* variable requires to compute the hadronic tensor one additional time, relative to the 4D method, α equals 1.0 and 0.5 for the proton and neutron targets, respectively. The 2D algorithm methods, on top of the ϕ_π^* sampling, require additional effort to assign the $\cos\theta_\pi^*$ variable. The increase in α while going from the 2D (table) method to the ones that use polynomial interpolation is almost proportional to the number of times ($k = 3, 7, \dots$) we calculate the hadronic tensor. We expect that one can avoid such behavior using a model implementation that separates the angular dependence algebraically, e.g., in a partial wave expansion, where one can compute the hadronic tensor for different values of $\cos\theta_\pi^*$ at fixed values of Q^2 and W in a much shorter time. However, in general, the $\cos\theta_\pi^*$ dependence is not a priori known. Thus, in this study, we opted to present the most model-independent case.

The resultant performance of all the optimization methods in reducing the total simulation time S_N is notable. Considering its execution time and susceptibility to the investigated factors, we conclude that the "2D alg. (table)" method performs best, and in what follows, we use it to generate all of the Monte Carlo simulation results. To strengthen this reasoning, we emphasize that in actual simulations, there is an additional, global computational effort needed to specify the weight of particular interaction channels and initialize the event sampling envelope. In NuWro, we know it as generating *test events* that require solely an event weight calculation, which is less demanding using the 2D algorithms.

Inclusive cross sections

To illustrate the accuracy of the implementation of the single-pion production model in NuWro within the "2D alg. (table)" framework, we show several comparisons with the exact results obtained with the original Ghent LEM code. For every presented plot, we compute the Monte Carlo results by averaging over six simulations with 10M events across the whole phase space. The additional band represents a 1σ error on the average.

In Fig. 5.2, we compare the results for the inclusive cross sections as a function of W at fixed Q^2 for electron neutrinos and antineutrinos with an energy of $E = 1$ GeV, including all possible single-pion production channels. For each value of $Q^2 = 0.1, 0.5$ GeV², we gathered Monte Carlo events in bins with a width of $\Delta Q^2 = 0.01$ GeV² and $\Delta W = 5$ MeV. One can see that the "2D alg. (table)" method provides excellent accuracy. The statistical uncertainty on its results is the smallest for (anti)neutrino reactions on the (neutron)proton, as these are cases with only a single SPP channel accessible. For the other target/helicity combinations, the simulations split the events over two final states, with the one of the higher cross section receiving a larger share, which is reflected in the uncertainty.

Angular distributions of the pion

The main strength of the presented approach is the exact implementation of the outgoing pion angular distributions. To illustrate this, in Fig. 5.3, we plot the cross sections as a function of $\cos\theta_\pi^*$ for values of $W = 1230, 1270, 1310$ MeV and fixed $Q^2 = 0.1$ GeV² with incoming

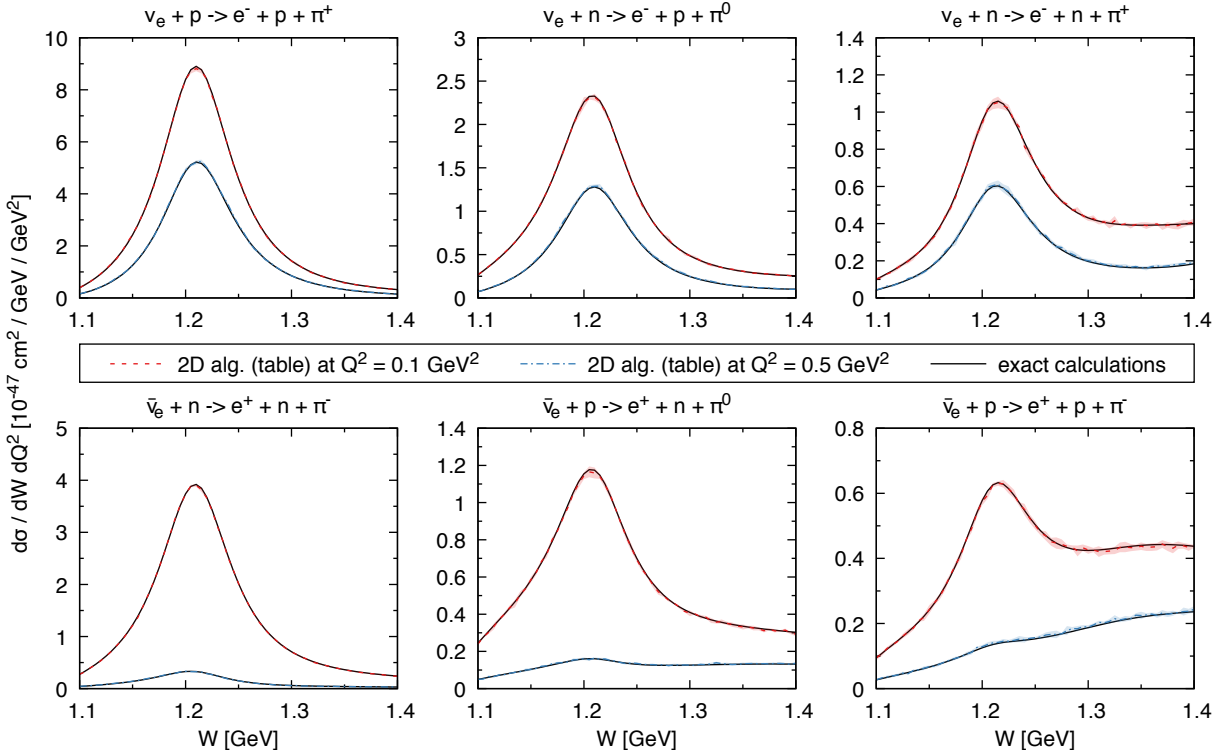


Figure 5.2: Double-differential cross sections for the ν_e - and $\bar{\nu}_e$ -induced single-pion production processes as a function of W for different values of Q^2 with incoming energy $E = 1$ GeV. Solid lines are showing the Ghent LEM results, while the (dot)-dashed ones are results of the "2D algorithm (tables)" method implemented in NuWro.

(anti)neutrino energy $E = 1$ GeV. We obtained NuWro results in the same way as described the previous subsection. Here, we gathered events in bins of $\Delta Q^2 = 0.01$ GeV², $\Delta W = 5$ MeV, and $\Delta \cos \theta_\pi^* = 0.04$. The obtained Monte Carlo results precisely reproduce the exact model calculations. The shape of the $\cos \theta_\pi^*$ distribution varies with both the interaction channel and kinematics. This behavior is in contrast to the commonly used approach in which the angular dependence of the outgoing pion-nucleon pair is described isotropically or by a distribution independent of the kinematics.

The next comparison, in Fig. 5.4, concerns the single-differential cross sections as a function of ϕ_π^* for electron neutrinos and antineutrinos with an energy of $E = 1$ GeV, averaged over $\Delta \phi_\pi^* = \pi/25$ rad bins. Since the procedure for sampling ϕ_π^* is practically exact, shapes of these distributions exemplify the total numerical error propagating from the bilinear and trilinear interpolation of the tabularized information used to sample the values of (W, Q^2) and $\cos \theta_{\pi'}$, respectively. Hence, one can interpret this comparison as a good measure of the full accuracy of the proposed algorithm. Regarding the physical results themselves, one immediately notices the asymmetry of $d\sigma/d\phi_\pi^*$ around $\phi_\pi^* = \pi$, corresponding to pions produced above or below the lepton scattering plane. As seen in Eq. 5.1.7, the D and E functions, which give contributions proportional to $\sin(\phi_\pi^*)$ and $\sin(2\phi_\pi^*)$, respectively, are responsible for such behavior. As explained thoroughly in Ref. [43], these asymmetries emerge from relative phase differences between the distinct contributions to the amplitude. Hence, they are not present in models that are described

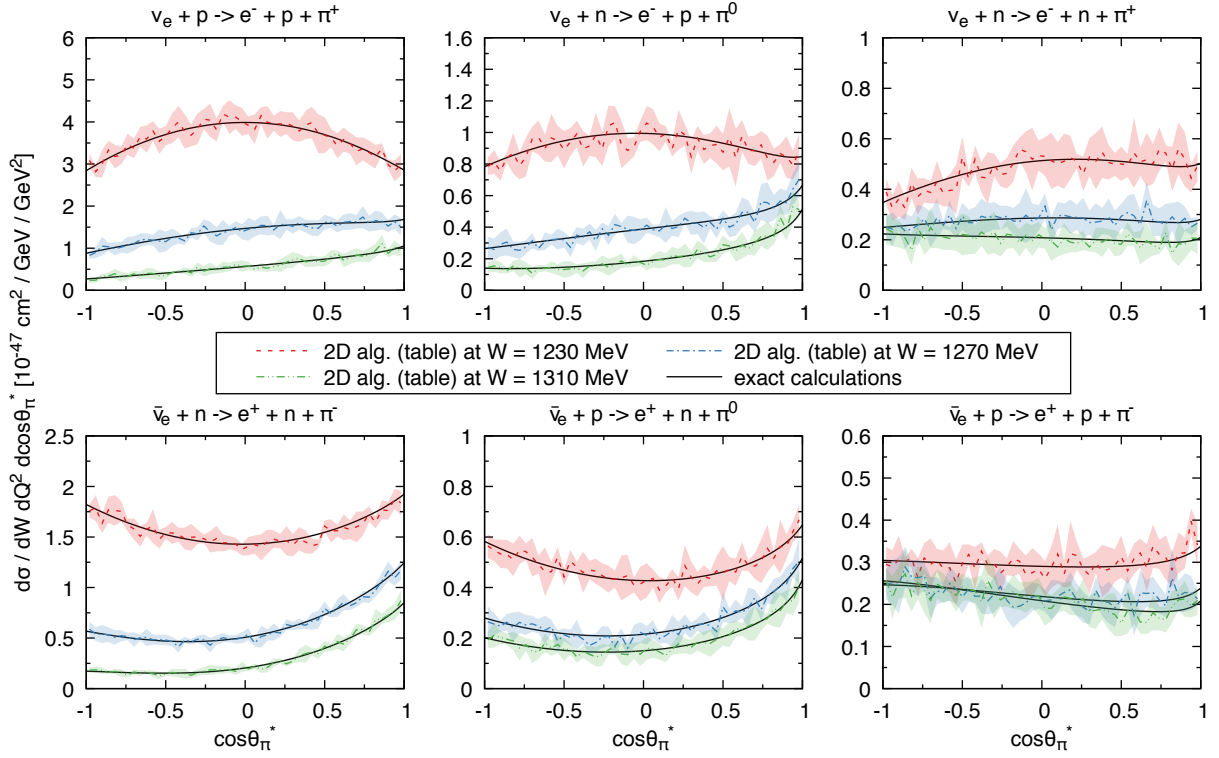


Figure 5.3: Triple-differential cross sections for the ν_{e^-} and $\bar{\nu}_{e^-}$ -induced single-pion production processes as a function of $\cos \theta_{\pi^*}$ for different values of W and fixed $Q^2 = 0.1 \text{ GeV}^2$ with incoming energy $E = 1 \text{ GeV}$. Solid lines show the Ghent LEM results, while the (dot-)dashed ones are results of the "2D algorithm (tables)" method implemented in NuWro.

by incoherent sums of resonances, or resonance and background contributions. In the Ghent Low Energy Model, the asymmetry can only arise from the interference between the imaginary part of the resonance propagator (plus the Olsson phases in the case of Δ) and the non-resonant background. Such an asymmetry is also not present in unpolarized electron scattering because both the D function, with the vector-vector contribution proportional to the polarization, and the E function, being a purely vector-axial interference term, disappear in that case.

In Figs. 5.5 and 5.6, we show the full two-dimensional Ω_{π^*} dependence in the different electron (anti)neutrino-induced SPP channels with $E = 1 \text{ GeV}$ for fixed $Q^2 = 0.1 \text{ GeV}^2$ and $W = 1230 \text{ MeV}$, i.e., at the $\Delta(1232)$ peak. Here, we average the Monte Carlo results over $\Delta Q^2 = 0.01 \text{ GeV}^2$, $\Delta W = 5 \text{ MeV}$, $\Delta \cos \theta_{\pi^*} = 0.04$, and $\Delta \phi_{\pi^*} = \pi/25 \text{ rad}$ bins. Although we performed these NuWro simulations again in the same way again, it is challenging to produce a sufficiently large sample of events to reduce statistical fluctuations. Still, the agreement we find is remarkably good. Analyzing the presented distributions, one can see that the $\nu(p, p\pi^+)$ and $\bar{\nu}(n, n\pi^-)$ cross sections are roughly symmetric with respect to ϕ_{π^*} . These interaction channels only allow isospin 3/2 contributions in the s-channel and are thus dominated by the $\Delta(1232)$ resonance, with minimal impact from the background and thereby minimal interference to generate the asymmetry. The other channels, however, do show a more asymmetric shape as the background contribution grows in relative importance.

In Fig. 5.7, we also present the Ω_{π^*} dependence of the "isobar NuWro" model for the same kine-

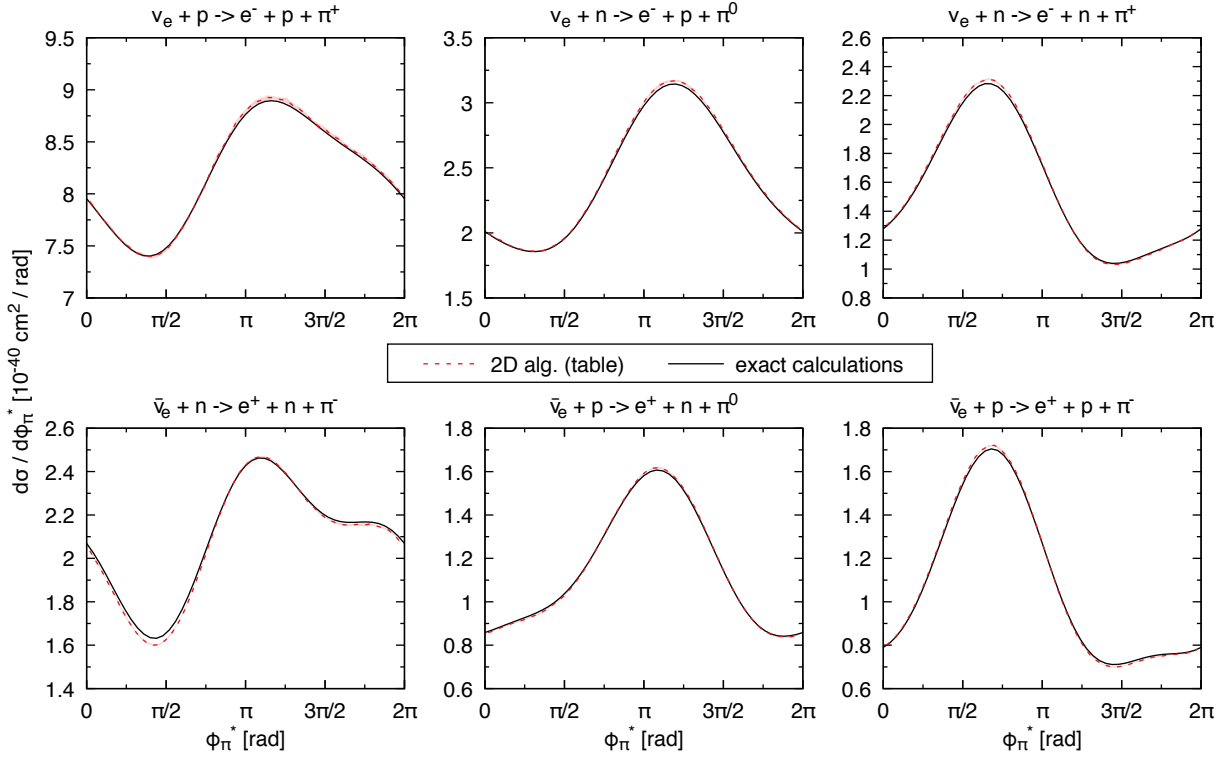


Figure 5.4: Single-differential cross sections for the ν_e - and $\bar{\nu}_e$ -induced single-pion production processes as a function of ϕ_π^* with incoming energy $E = 1$ GeV. Solid lines show the Ghent LEM results, while the dashed ones are results of the "2D algorithm (tables)" method implemented in NuWro.

mathematical setup. This model uses angular distributions from the BNL parametrization of Ref. [51], as implemented in NuWro 19.02.2. In the case of neutrino-induced charged pion production off the proton these results are similar to the Ghent LEM, while for the other reaction channels they are quite different. Such behavior originates from the fact that the BNL (ANL) parametrization is obtained from data for the former reaction in the $\Delta(1232)$ region. This comparison illustrates that a straightforward application of the same angular distribution to other reaction channels and other phase space regions should be avoided.

Finally, in Fig. 5.8, we show a shape-only comparison with the single-differential cross sections $d\sigma/d\cos\theta_\pi^*$ and $d\sigma/d\phi_\pi^*$ measured by the ANL [53] and BNL [51] experiments. To obtain this, we performed simulations with the $E_{\text{ANL}} \in (0.2, 6.1)$ GeV and $E_{\text{BNL}} \in (0.1, 7.5)$ GeV muon neutrino fluxes off the proton target, and applied a cut on the invariant hadronic mass $W < 1.4$ GeV. The theoretical results provide a good agreement for the $d\sigma/d\cos\theta_\pi^*$ differential cross section, especially in the BNL case, while due to the lack of statistics, the $d\sigma/d\phi_\pi^*$ results are not conclusive.

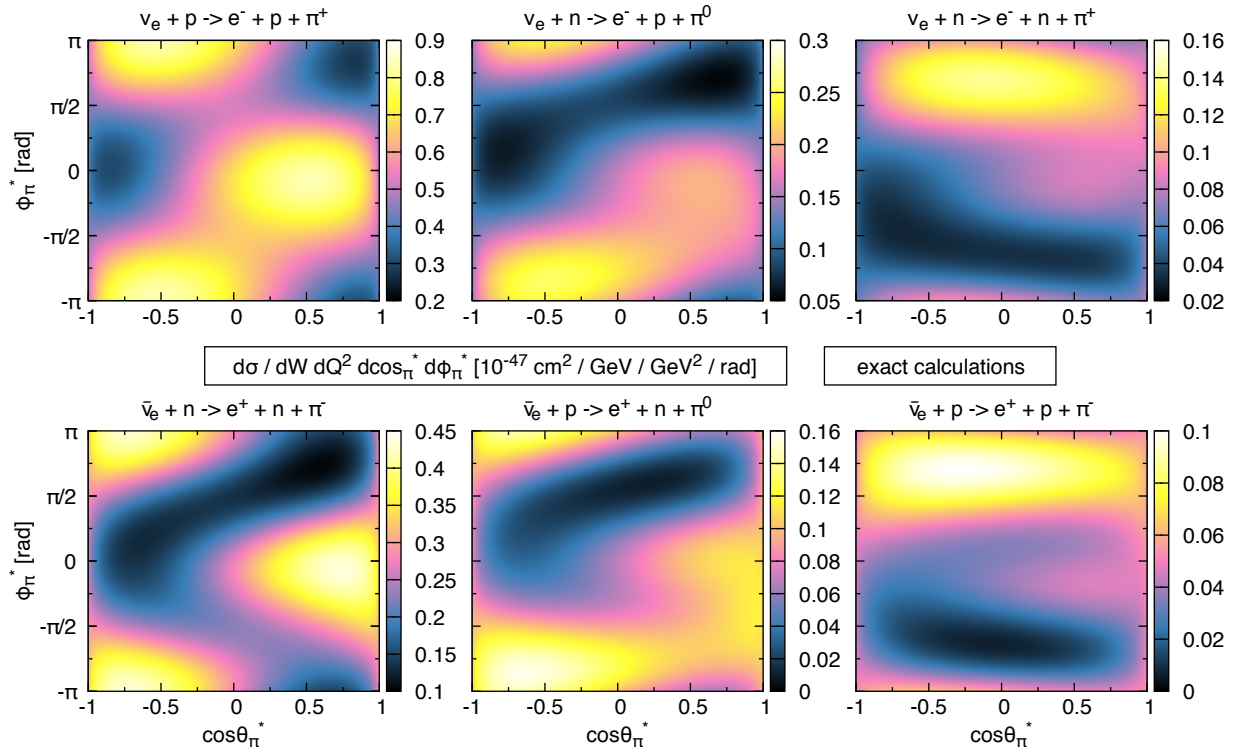


Figure 5.5: Quadruple-differential cross sections for the ν_e - and $\bar{\nu}_e$ -induced single-pion production processes as a function of $\cos\theta_\pi^*$ and ϕ_π^* for fixed $W = 1230 \text{ MeV}$ and $Q^2 = 0.1 \text{ GeV}^2$ with incoming energy $E = 1 \text{ GeV}$. The presented heatmaps are the Ghent LEM results.

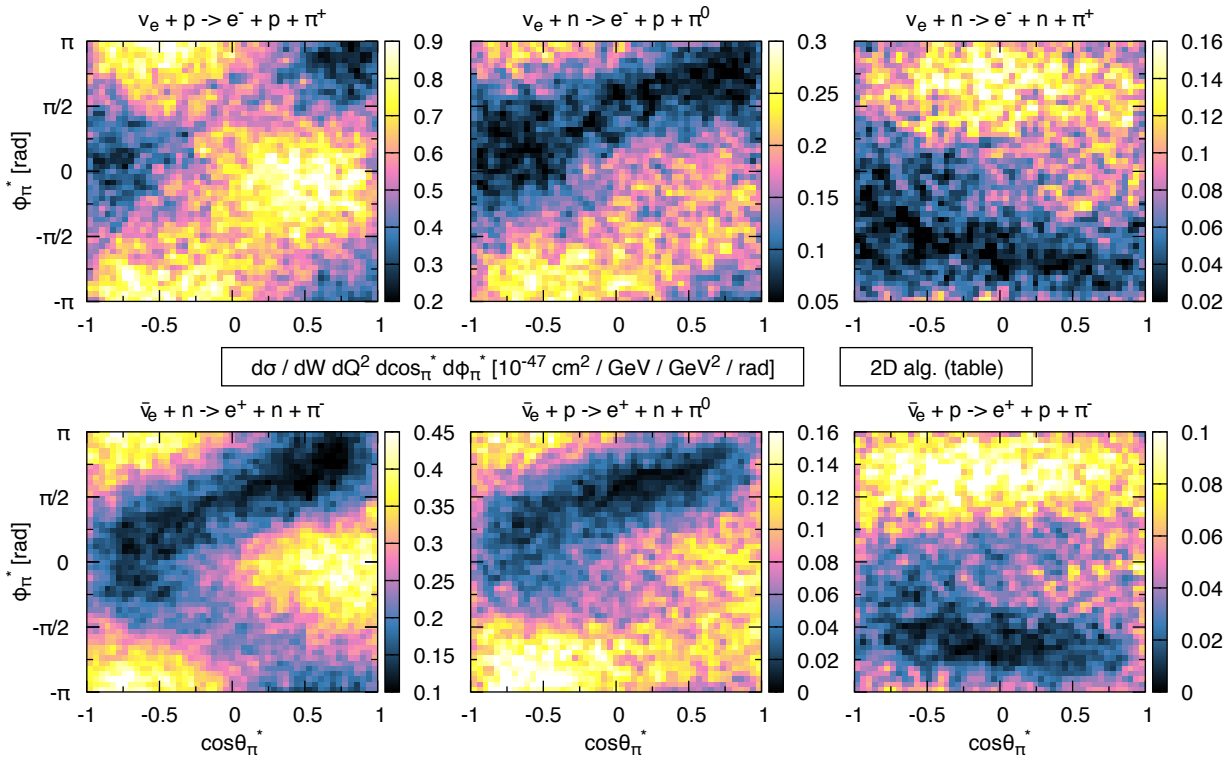


Figure 5.6: Quadruple-differential cross sections for the ν_e - and $\bar{\nu}_e$ -induced single-pion production processes as a function of $\cos\theta_{\pi^*}$ and ϕ_{π^*} for fixed $W = 1230 \text{ MeV}$ and $Q^2 = 0.1 \text{ GeV}^2$ with incoming energy $E = 1 \text{ GeV}$. The presented heatmaps are the results of the "2D algorithm (tables)" method implemented in NuWro.

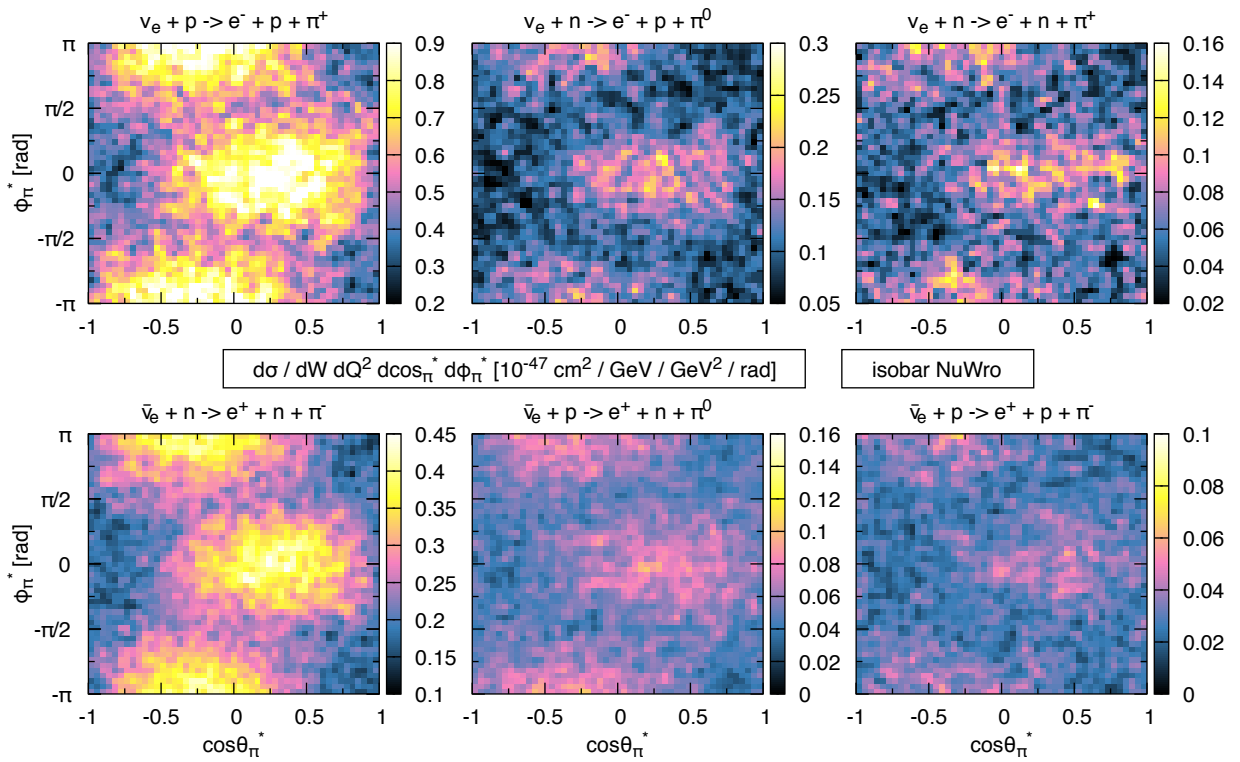


Figure 5.7: Quadruple-differential cross sections for the ν_e - and $\bar{\nu}_e$ -induced single-pion production processes as a function of $\cos\theta_\pi^*$ and ϕ_π^* for fixed $W = 1230 \text{ MeV}$ and $Q^2 = 0.1 \text{ GeV}^2$ with incoming energy $E = 1 \text{ GeV}$. The presented heatmaps are the results of the "isobar NuWro" model, the nominal single-pion production choice.

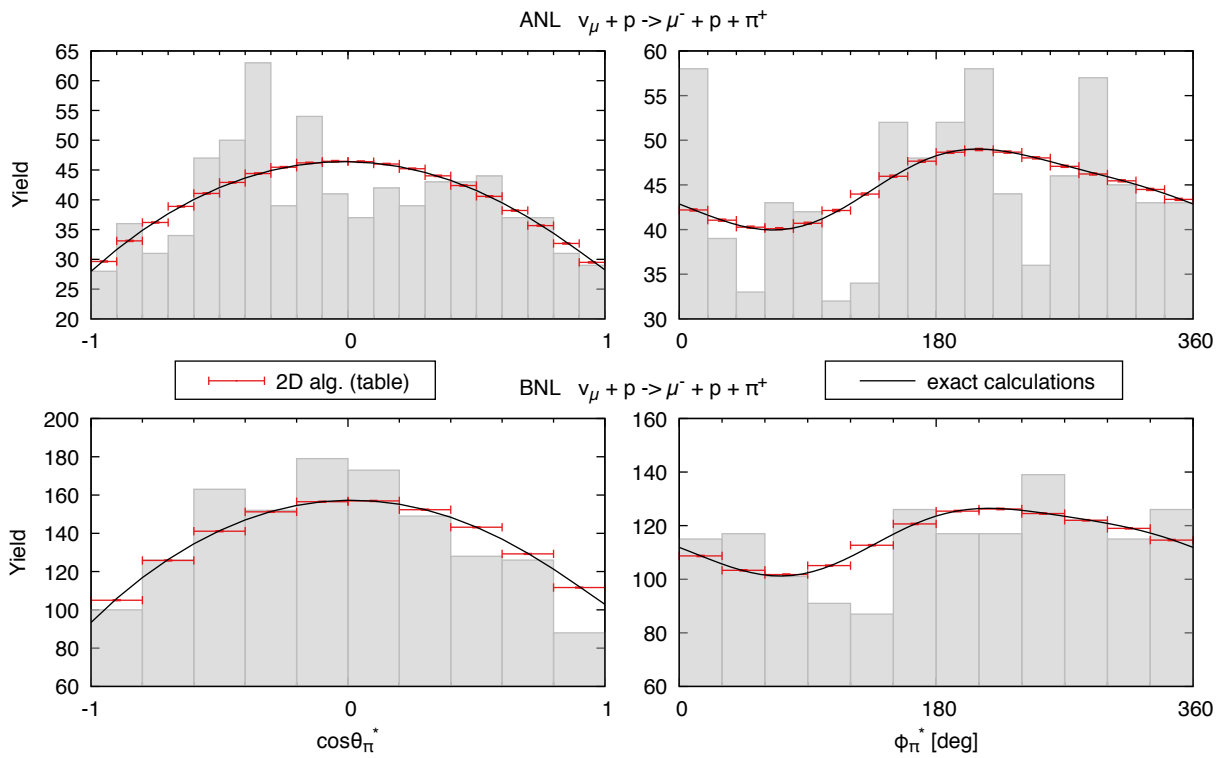


Figure 5.8: Pion angular distributions for the neutrino-induced single-pion production on the proton as a function of $\cos\theta_\pi^*$ or ϕ_π^* and data from the ANL [53] and BNL [51] bubble chamber experiments. Solid lines show the Ghent LEM results, while the bins are the results of the "2D algorithm (tables)" method implemented in NuWro. We normalize our cross section predictions to the total experimental yield.

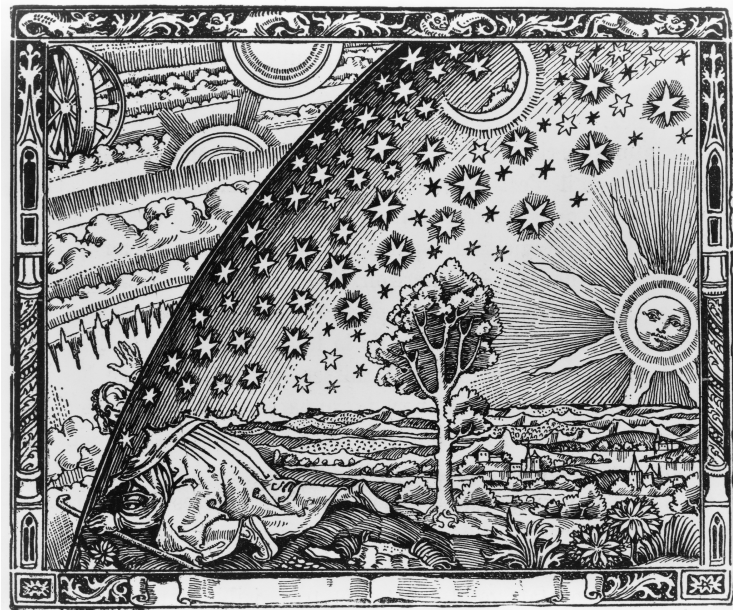
References

- [1] L. Alvarez-Ruso *et al.* Prog. Part. Nucl. Phys. **100**, 1 (2018).
- [2] K. Abe *et al.* Nucl. Instrum. Meth. A **659**, 106 (2011).
- [3] A. A. Aguilar-Arevalo *et al.* Phys. Rev. Lett. **110**, 161801 (2013).
- [4] K. Abe *et al.* PTEP **2015**, 053C02 (2015).
- [5] A. A. Aguilar-Arevalo *et al.* Phys. Rev. Lett. **121**, 221801 (2018).
- [6] Microboone experiment, <https://microboone.fnal.gov>.
- [7] O. Lalakulich, U. Mosel, and K. Gallmeister, Phys. Rev. C **86**, 054606 (2012).
- [8] M. A. Acero *et al.* Phys. Rev. D **98**, 032012 (2018).
- [9] B. Abi *et al.* arXiv:2002.03005 (2020).
- [10] K. Abe *et al.* Nature **580**, [Erratum: Nature 583, E16 (2020)], 339 (2020).
- [11] O. Altinok *et al.* Phys. Rev. D **96**, 072003 (2017).
- [12] B. Eberly *et al.* Phys. Rev. D **92**, 092008 (2015).
- [13] K. Abe *et al.* Phys. Rev. D **95**, 012010 (2017).
- [14] R. Acciarri *et al.* Phys. Rev. D **98**, 052002 (2018).
- [15] A. A. Aguilar-Arevalo *et al.* Phys. Rev. D **83**, 052007 (2011).
- [16] A. A. Aguilar-Arevalo *et al.* Phys. Rev. D **83**, 052009 (2011).
- [17] J. T. Sobczyk. and J. Zmuda, Phys. Rev. C **87**, 065503 (2013).
- [18] R. González-Jiménez, K. Niewczas, and N. Jachowicz, Phys. Rev. D **97**, 013004 (2018).
- [19] A. Nikolakopoulos, R. González-Jiménez, K. Niewczas, *et al.* Phys. Rev. D **97**, 093008 (2018).
- [20] U. Mosel and K. Gallmeister, Phys. Rev. C **96**, [Addendum: Phys.Rev.C 99, 035502 (2019)], 015503 (2017).
- [21] P. Stowell *et al.* Phys. Rev. D **100**, 072005 (2019).
- [22] T. Golan, C. Juszczak, and J. T. Sobczyk, Phys. Rev. C **86**, 015505 (2012).
- [23] K. Niewczas and J. T. Sobczyk, Phys. Rev. C **100**, 015505 (2019).
- [24] L. L. Salcedo, E. Oset, M. J. Vicente-Vacas, *et al.* Nucl. Phys. A **484**, 557 (1988).
- [25] D. Rein and L. M. Sehgal, Annals Phys. **133**, 79 (1981).
- [26] T. Sato, D. Uno, and T. S. H. Lee, Phys. Rev. C **67**, 065201 (2003).
- [27] J. E. Amaro, M. B. Barbaro, J. A. Caballero, *et al.* Phys. Rev. C **71**, 015501 (2005).
- [28] S. Ahmad, M. Sajjad Athar, and S. K. Singh, Phys. Rev. D **74**, 073008 (2006).
- [29] E. Hernandez, J. Nieves, and M. Valverde, Phys. Rev. D **76**, 033005 (2007).
- [30] O. Buss, T. Leitner, U. Mosel, *et al.* Phys. Rev. C **76**, 035502 (2007).
- [31] C. Praet, O. Lalakulich, N. Jachowicz, *et al.* Phys. Rev. C **79**, 044603 (2009).
- [32] M. Martini, M. Ericson, G. Chanfray, *et al.* Phys. Rev. C **80**, 065501 (2009).
- [33] X. Zhang and B. D. Serot, Phys. Rev. C **86**, 035504 (2012).

- [34] H. Kamano, S. X. Nakamura, T. S. H. Lee, *et al.* Phys. Rev. C **88**, 035209 (2013).
- [35] S. X. Nakamura, H. Kamano, and T. Sato, Phys. Rev. D **92**, 074024 (2015).
- [36] M. Rafi Alam, M. Sajjad Athar, S. Chauhan, *et al.* Int. J. Mod. Phys. E **25**, 1650010 (2016).
- [37] M. V. Ivanov, G. D. Megias, R. González-Jiménez, *et al.* J. Phys. G **43**, 045101 (2016).
- [38] R. González-Jiménez, N. Jachowicz, K. Niewczas, *et al.* Phys. Rev. D **95**, 113007 (2017).
- [39] C. Barbero, G. López Castro, and A. Mariano, Phys. Lett. B **728**, 282 (2014).
- [40] D. Badagnani, A. Mariano, and C. Barbero, J. Phys. G **44**, 025001 (2017).
- [41] T. Donnelly, Progress in Particle and Nuclear Physics **13**, 183 (1985).
- [42] D. Drechsel and L. Tiator, J. Phys. G **18**, 449 (1992).
- [43] J. E. Sobczyk, E. Hernández, S. X. Nakamura, *et al.* Phys. Rev. D **98**, 073001 (2018).
- [44] E. Hernández, J. Nieves, and M. J. Vicente Vacas, Phys. Rev. D **87**, 113009 (2013).
- [45] L. Alvarez-Ruso, E. Hernández, J. Nieves, *et al.* Phys. Rev. D **93**, 014016 (2016).
- [46] O. Lalakulich, E. A. Paschos, and G. Piranishvili, Phys. Rev. D **74**, 014009 (2006).
- [47] E. Hernández and J. Nieves, Phys. Rev. D **95**, 053007 (2017).
- [48] Nuwro official repository, <https://github.com/NuWro/nuwro>.
- [49] K. M. Graczyk, D. Kielczewska, P. Przewlocki, *et al.* Phys. Rev. D **80**, 093001 (2009).
- [50] C. Juszczak, J. A. Nowak, and J. T. Sobczyk, Nucl. Phys. B Proc. Suppl. **159**, edited by F. Cavanna, J. G. Morfin, and T. Nakaya, 211 (2006).
- [51] T. Kitagaki *et al.* Phys. Rev. D **34**, 2554 (1986).
- [52] T. Sjostrand, S. Mrenna, and P. Z. Skands, JHEP **05**, 026 (2006).
- [53] G. M. Radecky *et al.* Phys. Rev. D **25**, [Erratum: Phys.Rev.D 26, 3297 (1982)], 1161 (1982).

6

Summary and outlook



L'atmosphère : météorologie populaire (Paris, 1888)

6.1 Research synopsis

The precise measurement of neutrino properties is among the highest priorities in fundamental particle physics, involving extensive experimental efforts worldwide. Accelerator-based neutrino experiments offer a unique framework for such studies, providing oscillation measurements and hints of CP violation in the leptonic sector. However, since these experiments rely on the interaction

of neutrinos with bound nucleons inside atomic nuclei, understanding the hadronic and nuclear physics of these interactions constitutes a challenging source of uncertainty. Modeling neutrino-nucleus scattering processes is a complex many-body problem, traditionally performed in an independent-particle model picture, focusing on quasielastic neutrino-nucleon interactions or the excitation of nucleon resonances. Improving our knowledge of such cross sections to the required percent level precision involves investigating beyond the first approximation, incorporating the effects of nucleon correlations and multinucleon knock-out processes.

The presented research involves a novel, multidirectional approach to tackling modern neutrino physics problems by combining the theoretical expertise of the Ghent group and the Monte Carlo neutrino event generator NuWro, explicitly used in experimental analyses. The nuclear physics of Ghent involves a non-relativistic, mean-field-based model for both the initial and final hadronic states. On top of that, we add dynamically generated short-range nucleon correlations and explicit two-body dynamics with meson-exchange currents involving isobar degrees of freedom. This framework, exhaustively compared against electron scattering, provides predictions for inclusive, semi-inclusive, and exclusive cross sections for neutrino-nucleus interactions leading to 1-particle-1-hole and 2-particle-2-hole final states.

NuWro is a Monte Carlo neutrino event generator widely used in the accelerator-based neutrino experiments community. This software, initiated in 2005 by the theoretical group from Wrocław, provides reliable predictions for the vital neutrino-nucleus scattering channels and involves a homegrown cascade model that simulates the final-state interactions of outgoing hadrons. Such a factorized approach allows for combining accurate inclusive cross section calculations while predicting the necessary multiplicity of particles, which we observe as experimental topologies in the detectors. Investigating the possibility of a consistent framework combining the interaction models of Ghent and NuWro is the ultimate goal of this research. Therefore, we focused on the following aspects of Monte Carlo simulations: the inelastic final-state interactions missing in quantum-mechanical lepton-nucleus scattering models and the methodology of optimizing generator implementations. In the former, we introduced the effects of short-range correlations into the cascade model of NuWro and constrained its behavior with exclusive electron scattering data. In the latter, we developed an algorithm that makes the implementation of multi-dimensional cross section models in their full exclusive complexity possible and provide proof of principle of the feasibility of such a scheme.

Theoretical modeling of two-nucleon knock-out processes

The Ghent framework for the description of nuclear dynamics assumes that protons and neutrons move according to the Schrödinger equation in a mean-field potential determined through a Hartree-Fock calculation based on an effective Skyrme-type nucleon-nucleon force. This independent-particle picture is remarkably accurate in describing the ground-state characteristics of spherical nuclei. In electron- and neutrino-nucleus scattering processes, it provides reliable predictions for inclusive reactions in a *distorted-wave impulse approximation*. However, to increase its accuracy and introduce multinucleon knock-out dynamics, the model features two methods of incorporating nuclear correlations: attributed to nuclear states and the dynamics of the hadronic current. The

former introduces short-range nucleon-nucleon correlations using one-body currents modified with the central, spin-isospin, and tensor correlation functions. For inclusive electron scattering calculations, we find that this reduces the 1p1h strength, especially in the longitudinal responses, and introduces a small 2p2h contribution. These effects reflect our intuition for the influence of SRCs as corresponding to spectroscopic factors and the high-momentum component of the nuclear wave function, respectively. For neutrino scattering, we find similar effects, with a higher 2p2h contribution in the longitudinal channel and a stronger 1p1h reduction in the transverse one. In our analysis, we emphasize the role of uncertainties originating from the choice of the central correlation numerical input. We conclude that the VMC and the solution by C. Gearhart *et al.* are well-constrained and provide similar results, with the latter bringing a slightly higher effect, as expected.

We include two-body meson-exchange currents of pionic range to model the explicitly dynamical two-nucleon knock-out. As one can argue that a mean-field-based model like ours implicitly involves nucleon-pole diagrams, we limit ourselves to calculating the seagull, pion-in-flight, and Δ -isobar current diagrams. In this investigation, we have performed three analyses to study the effect of the first two mechanisms combined, the third one separately, and all of them together, with coherently added short-range correlations. We found similar effects for inclusive electron- and neutrino-nucleus scattering in the former, with little influence on the 1p1h responses and a small 2p2h contribution. The seagull and pion-in-flight currents modify the IA responses in the opposite direction and experience a substantial negative interference in two-nucleon knock-out reactions. The Δ -currents depend strongly on the description of the isobar propagators and the approximations involved therein. Similarly to the previous analysis, we found the effect to be similar for both the electron and neutrino cases: an enhancement of 1p1h and a dominant contribution to the 2p2h responses. Combining the effects of MECs and SRCs coherently brings many subtle effects in all investigated processes as they act in different energy scales and experience negative interference. The complete model for inclusive electron scattering provides a reduction and enhancement of IA 1p1h results for the longitudinal and transverse responses, respectively. In two-nucleon knock-out, we observe the characteristic Δ -resonance peak and the SRC strength around the quasielastic peak, especially for very forward scattering. The kinematics is more transverse for neutrino interactions, and the double-peaked structure vanishes. Contrary to the electron 1p1h case, the SRC effect reduces the transverse responses. At the same time, MECs also increase the longitudinal ones, so the net effect is less apparent and strongly depends on the kinematics. Finally, to constrain the vector part of the modeled neutrino-nucleus interaction, we systematically compared our predictions to inclusive electron scattering data, including the 1p1h, 2p2h, and single-pion production dynamics. We concluded that the combined model accurately reproduces the selected datasets. However, the comparison to the data would benefit from a stronger reduction of the 1p1h channel for lower energies and a better constraining of the 2p2h cross sections for the more energetic kinematics.

Methodology of Monte Carlo simulations

Monte Carlo event generators model neutrino-nucleus scattering by factorizing the process into the primary neutrino interaction vertex and a model that independently simulates the final-state interactions of knocked-out nucleons and produced pions. As a second research line devoted to the multinucleon knock-out reactions, we studied the role of short-range nucleon-nucleon correlations in the FSI model of NuWro. Such effects can be added by employing the local-density approximation and evaluating correlations-modified single-nucleon densities, which enter the calculations of mean free paths in the cascade model. We found this approach to provide a significantly reduced probability of interactions near the propagation starting point as the nucleons locally experience a hole in nuclear density. This effect vanishes over longer distances as the nucleus normalization conditions force the density to be compensated elsewhere. To constrain such a model, one can investigate nuclear transparency in exclusive electron scattering. This measure provides experimental hints about the general magnitude of FSI effects in nuclear matter. The improved nucleon cascade model of NuWro is reasonably successful in reproducing nuclear transparency data in the energy region critical to neutrino-nucleus scattering physics. In terms of the nucleon mean free paths, we estimated the 1σ error of our model to be around 30%. This was applied to recent T2K data to suggest that FSI modeling is under control and that the disagreement between NuWro results and data finds its origin in other sources.

The true strength of the microscopic model we developed in this work lies in its ability to produce exclusive cross section predictions that account for the kinematics of the outgoing nucleons in electron- and neutrino-induced two-nucleon knock-out reactions. These predictions are crucial from the experimental point of view and should be implemented in Monte Carlo generators in their full complexity. However, two significant obstacles limit our progress: exclusive model predictions span a multidimensional phase space, and evaluating the cross section for each set of kinematical variables is a challenging numerical problem. Depending on particular model characteristics, the former tends to decrease the efficiency of Monte Carlo event sampling with every next dimension in the computation. Based on comparison studies, we propose a novel implementation strategy that combines a satisfactory efficiency with high precision in reproducing the theoretical model prediction details. By introducing a sequential importance sampling of events, we allow for the flexibility of choosing a different trade-off between efficiency, precision, and reliance on precomputed assets. This leads to an algorithm that minimizes the number of evaluations of theoretical model computations needed to generate every event in a simulation. We have tested the new algorithm with the Ghent Low Energy Model for single-pion production implemented in the NuWro Monte Carlo event generator and concluded that this approach makes the implementation of exclusive neutrino-nucleus interaction models feasible.

6.2 Future prospects

The model of lepton-induced one- and two-nucleon knock-out developed here is a sophisticated framework allowing for accurate theoretical predictions and control over the internal degrees of freedom. This model can be used to compute inclusive, semi-inclusive, and exclusive cross

sections for electron- and neutrino-nucleus interactions. However, the model requires further development, and, as we demonstrated in this study, there are clear paths for future work. In the one-nucleon knock-out reaction channel, the model tends to overestimate the inclusive electron scattering strength for low-energy kinematics. This effect points to the need for stronger long-range correlations, which can be included using the CRPA model, also developed in Ghent. This model could be used for calculating $1p1h$ nuclear responses instead of the IA ones. The potential double-counting of the SRC dynamics could be controlled by refitting the phenomenological cut-off parameter Λ , which allows for constraining the strength the residual interaction in CRPA [1]. In the two-nucleon knock-out reaction channel, much stress should be put on the treatment of relativistic effects and adjusting the $2p2h$ contribution to fill the dip region between the quasielastic and Δ -resonance peak more. These adjustments could resolve the model pathologies found in the inclusive electron-scattering scattering comparisons.

The model we develop in this work should be implemented in Monte Carlo generators, such as NuWro, in its full exclusive complexity to become fully useful in experimental analyses. So far, this cumbersome numerical challenge has yet to be accomplished in any software development. As we presented in Chapter 5, it is possible to build an optimized framework based on importance sampling in Monte Carlo methods, that minimizes the number of evaluations of the theoretical model and increase the sampling efficiency. The first steps to achieving this are inclusive model implementations through precomputed assets, such as tables of integrated nuclear responses. This approach would provide progress in Monte Carlo prediction accuracy while facilitating future implementation refinements.

Bridging the gap between the theory and experiment

Attempting to bring our model to the experimental community, we present the preliminary results of implementing the microscopic two-nucleon knock-out model in the NuWro Monte Carlo neutrino event generator. To achieve this, we used a similar methodology to other $2p2h$ models, such as SuSAv2 [2] or the model developed by the Valencia group [3]. These theoretical calculations enter NuWro as tabularized inclusive nuclear responses that allow for an efficient evaluation of neutrino-nucleus cross sections. The kinematics of the outgoing nucleons is considered using the phase-space model of Ref. [4]. In our implementation, the responses are computed on a 10 MeV grid in ω and $|\vec{q}|$ variables up to the value of $|\vec{q}| = 1.3$ MeV/c. In Fig. 6.1, we show the total cross section for the models mentioned above and the $1p1h$ calculation with the model of O. Benhar *et al.* [5]. The predictions of our model include the distinction between the distorted- and plane-wave calculations. In Fig. 6.2, we present the double-differential neutrino scattering cross sections on hydrocarbon and compare them to the experimental results of T2K [6]. Finally, in Fig. 6.3 and Fig. 6.4, we confront the preliminary NuWro implementation with the single-transverse variables measured by T2K [7]. We conclude that, similarly to the electron scattering comparisons of Chapter 3, the preferred choice of our $2p2h$ model includes the VMC central correlation function and retaining only the real part of the Δ -propagator. However, the description of the implementation and its refinement will require a more detailed and dedicated study.

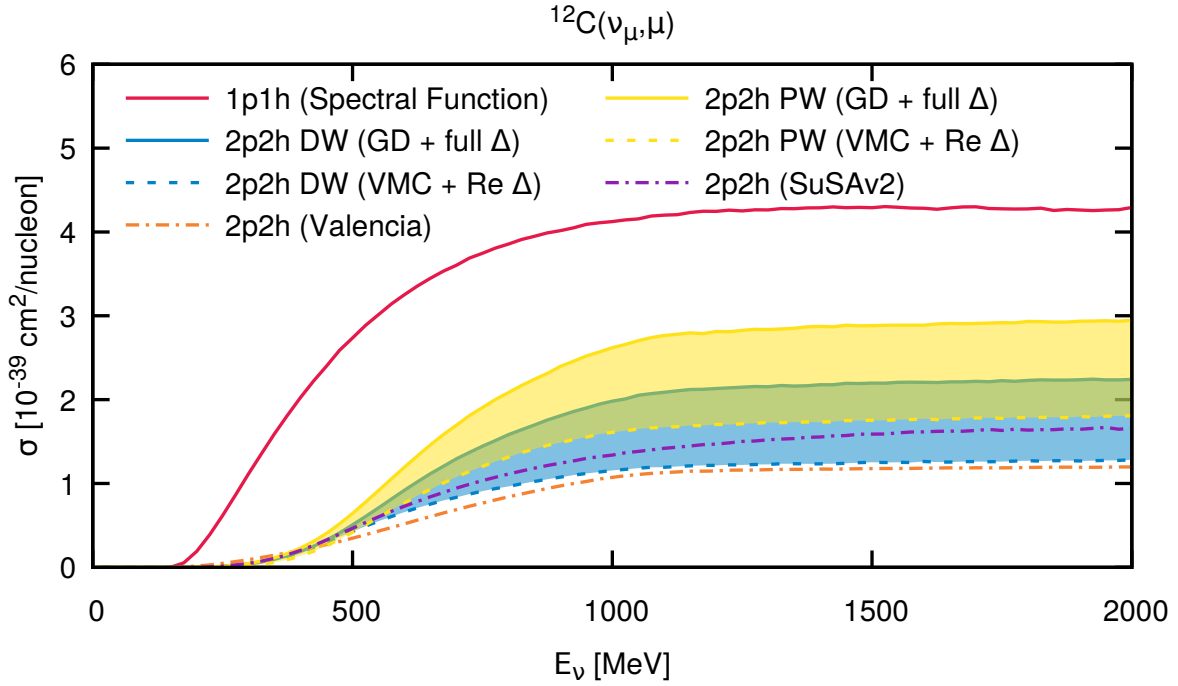


Figure 6.1: Total neutrino-nucleus scattering cross section on the Carbon target, obtained with NuWro. The red solid line presents the one-nucleon knock-out contribution evaluated using the Spectral Function. The blue and yellow lines were obtained using our model of two-nucleon knock-out, described in this study. The dot-dashed curves are other 2p2h solutions available in NuWro.

Final remarks

As neutrino oscillation physics enters the precision era, modeling neutrino-nucleus interactions constitutes an increasingly challenging source of systematic uncertainties for new measurements. While the experimental collaborations focus on building modern, giant detectors, such as DUNE or HyperKamiokande, it is essential to acknowledge the theoretical progress that needs to meet the requirements of experimental analyses. Neutrino-nucleus cross sections are considered to be known with a precision not exceeding 20% [8]. At the time of this research, the statistical uncertainties still dominate the experimental picture. However, future advancement will increase the stress on the tensions in modeling neutrino interactions and their implementations in Monte Carlo neutrino events generators. Only a combined effort of experimental and theoretical communities will ensure continuous progress in investigating the fascinating physics of neutrinos and fully unveil how the theoretical modeling can impact the oscillation program.

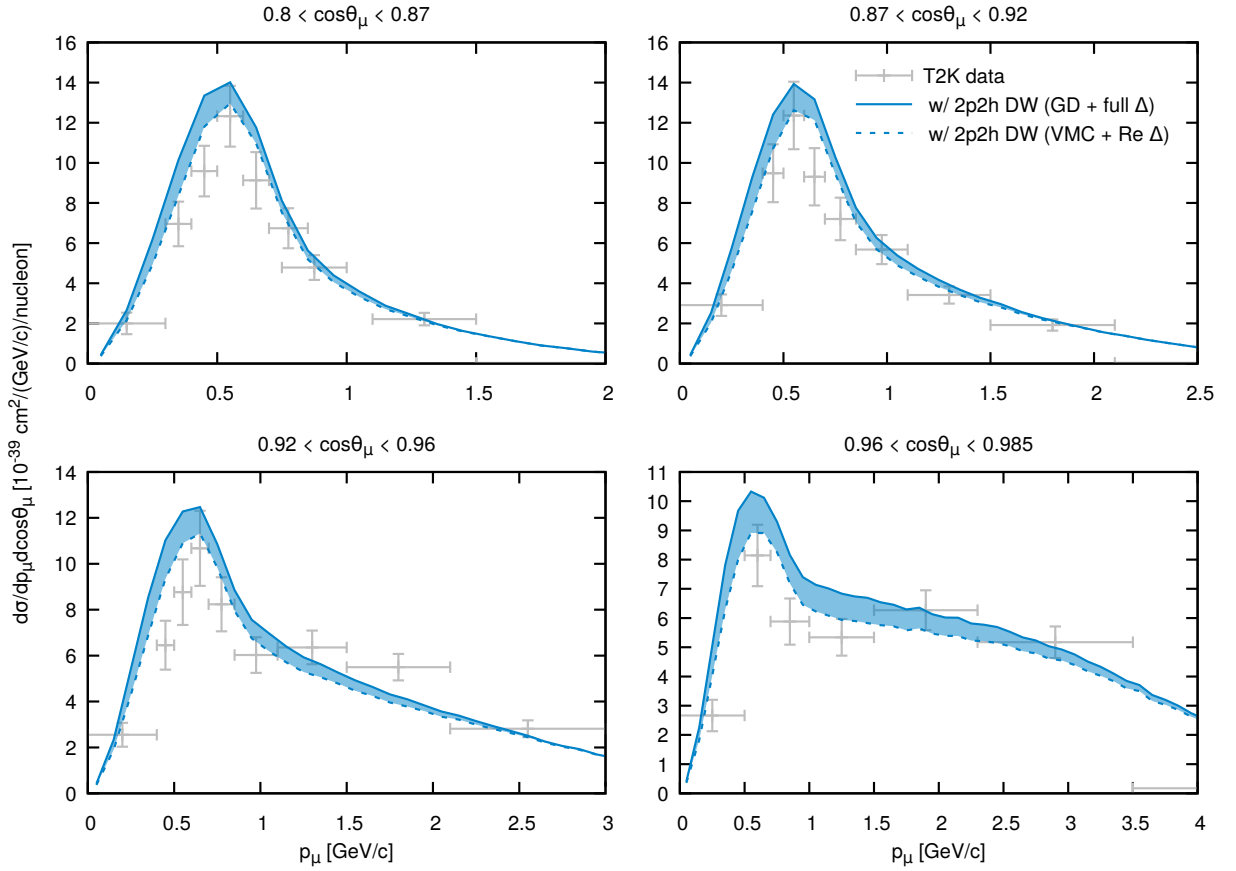


Figure 6.2: Double-differential inclusive neutrino-nucleus scattering cross section on the hydrocarbon target (C_xH_x), as measured by T2K [6]. The theoretical predictions were obtained using the default parametrization of NuWro and the Spectral Function. The 2p2h contribution comes from our model, as described in the text.

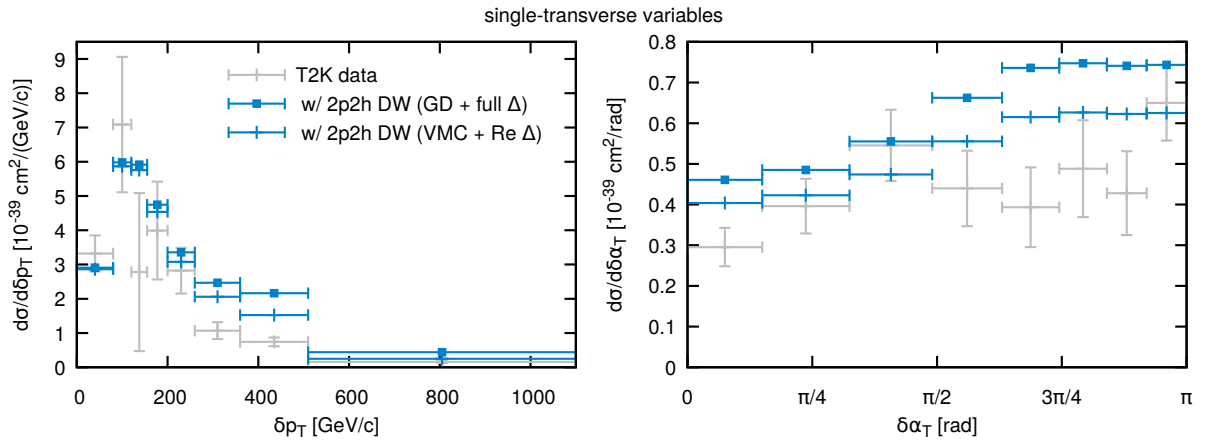


Figure 6.3: Single-transverse variables δp_T and $\delta \alpha_T$ of Ref. [7]. The theoretical predictions were obtained using the default parametrization of NuWro and the Spectral Function. The 2p2h contribution comes from our model, as described in the text.

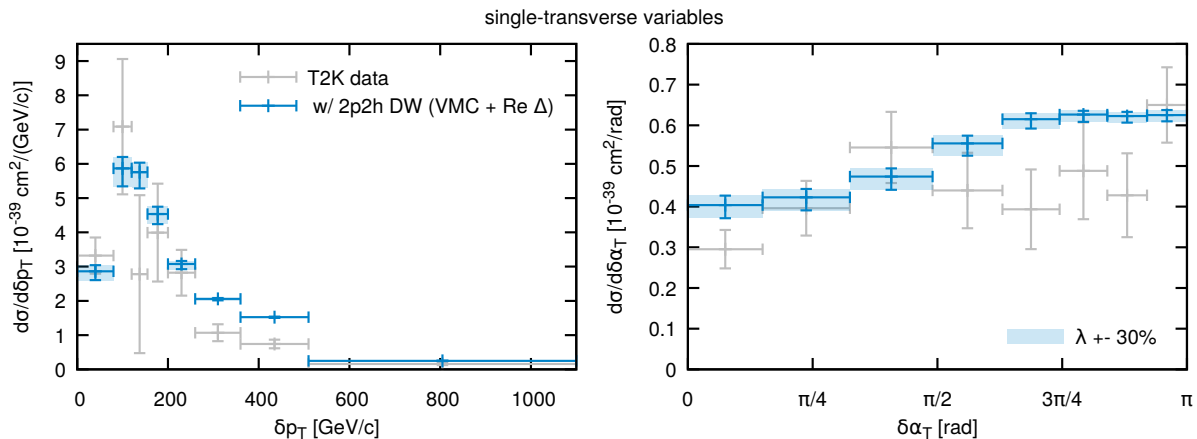


Figure 6.4: Single-transverse variables δp_T and $\delta\alpha_T$ of Ref. [7]. The theoretical predictions were obtained using the default parametrization of NuWro and the Spectral Function. The 2p2h contribution comes from our model, with the VMC central correlation function and only the real part of the Δ -resonance propagator. The blue boxes represent the uncertainty from varying the FSI mean free path by $\pm 30\%$.

References

- [1] V. Pandey, N. Jachowicz, T. Van Cuyck, *et al.* Phys. Rev. C **92**, 024606 (2015).
- [2] S. Dolan, G. D. Megias, and S. Bolognesi, Phys. Rev. D **101**, 033003 (2020).
- [3] J. Nieves, I. Ruiz Simo, and M. J. Vicente Vacas, Phys. Rev. C **83**, 045501 (2011).
- [4] J. T. Sobczyk, Phys. Rev. C **86**, 015504 (2012).
- [5] O. Benhar, A. Fabrocini, S. Fantoni, *et al.* Nucl. Phys. A **579**, 493 (1994).
- [6] K. Abe *et al.* Phys. Rev. D **98**, 012004 (2018).
- [7] K. Abe *et al.* Phys. Rev. D **98**, 032003 (2018).
- [8] L. Alvarez-Ruso *et al.* Prog. Part. Nucl. Phys. **100**, 1 (2018).

Appendices

A One-nucleon knock-out matrix elements

For the starting point of our calculations of one-nucleon knock-out matrix elements and cross sections [1], we take the formula derived in Eq. (2.1.27) as

$$\begin{aligned} \frac{d\sigma^X}{d\epsilon_f d\Omega_f d\Omega_N} &= \frac{|\vec{p}_N| E_N}{(2\pi)^3} f_{1p1h}^{-1} \zeta \sigma^X \\ &\times [\mathcal{V}_{CC} \mathcal{W}_{CC} + \mathcal{V}_{CL} \mathcal{W}_{CL} + \mathcal{V}_{LL} \mathcal{W}_{LL} + \mathcal{V}_T \mathcal{W}_T + \mathcal{V}_{TT} \mathcal{W}_{TT} \\ &+ \mathcal{V}_{TC} \mathcal{W}_{TC} + \mathcal{V}_{TL} \mathcal{W}_{TL} + \mathfrak{h} (\mathcal{V}_{T'} \mathcal{W}_{T'} + \mathcal{V}_{TC'} \mathcal{W}_{TC'} + \mathcal{V}_{TL'} \mathcal{W}_{TL'})]. \end{aligned} \quad (\text{A.1})$$

In this equation, the nuclear responses \mathcal{W}_x encapsulate the hadronic information about these processes. They are bilinear products of currents given by

$$\mathcal{J}_V^{\text{had}} = \langle \Psi_{1p1h} | \hat{\mathcal{J}}_V^{\text{had}}(\vec{q}) | \Psi_i \rangle \simeq \langle \Phi_{1p1h} | \hat{\mathcal{J}}_V^{\text{had}}(\vec{q}) | \Phi_{\text{g.s.}} \rangle, \quad (\text{A.2})$$

where we distinguish the true, fully correlated states $|\Psi\rangle$ and the uncorrelated, Slater determinants $|\Phi\rangle$. The investigated $1p1h$ hadronic final states contain one nucleon in the continuum, which can be explicitly distinguished by writing

$$\mathcal{J}_V^{\text{had}} = \langle \Phi_{A-1}(E_{\text{exc}}, J_R M_R); \vec{p}_N m_{s_N} | \hat{\mathcal{J}}_V^{\text{had}}(\vec{q}) | \Phi_{\text{g.s.}} \rangle. \quad (\text{A.3})$$

Here, we will show how we can describe these states relative to the wave function of the nuclear ground state. We commence by obtaining a one-hole residual state Φ_{A-1} as

$$|\Phi_{A-1}(E_{\text{exc}}, J_R M_R)\rangle = |h^{-1}(E_{\text{exc}}, j_h m_h)\rangle = (-1)^{j_h+m_h} \hat{c}_{j_h, -m_h}^\dagger | \Phi_{\text{g.s.}} \rangle. \quad (\text{A.4})$$

Then, for the continuum states, we use the explicit wave function normalization and the phase shifts discussed in Section 2.2 and build the following one-nucleon state

$$\begin{aligned} |\vec{p}_N m_{s_N}\rangle &= \sum_{l, m_l} \sum_{j, m_j} (4\pi) \frac{\sqrt{\pi}}{\sqrt{2M_N |\vec{p}_N|}} i^l e^{i(\delta_l + \sigma_l)} Y_{lm_l}^*(\Omega_N) \\ &\times \langle l, m_l; 1/2, m_{s_N} | j, m_j \rangle \hat{c}_{ljm_j}^\dagger | \Phi_{\text{g.s.}} \rangle. \end{aligned} \quad (\text{A.5})$$

Finally, we combine the two formulas to obtain the uncorrelated $1p1h$ state as

$$\begin{aligned} |\Phi_{1p1h}\rangle &= |\Phi_{A-1}(E_{\text{exc}}, J_R M_R); \vec{p}_N m_{s_N}\rangle_{\text{as}} \\ &= \sum_{l, m_l} \sum_{j, m_j} (4\pi) \frac{\sqrt{\pi}}{\sqrt{2M_N |\vec{p}_N|}} i^l e^{i(\delta_l + \sigma_l)} Y_{lm_l}^*(\Omega_N) (-1)^{j_h+m_h} \\ &\times \langle l, m_l; 1/2, m_{s_N} | j, m_j \rangle \hat{c}_{ljm_j}^\dagger \hat{c}_{j_h, -m_h} | \Phi_{\text{g.s.}} \rangle. \end{aligned} \quad (\text{A.6})$$

Note that within our framework, both one- and two-body nuclear currents lead to one-nucleon knock-out processes. Thus, we write the nuclear current in the following form

$$\mathcal{J}_V^{\text{had}} = \mathcal{J}_V^{[1]} + \mathcal{J}_V^{[2]} \quad (\text{A.7})$$

and the hadronic tensor, distinguishing the one-body, interference, and two-body terms, as

$$\begin{aligned} W_{\mu\nu} &= W_{\mu\nu}^{[1]} + W_{\mu\nu}^{[1,2]} + W_{\mu\nu}^{[2]} \\ &= \sum_{J_R, M_R} \sum_{m_{s_N}} \left(\mathcal{J}_\mu^{[1]\dagger} \mathcal{J}_\nu^{[1]} + 2\Re \left(\mathcal{J}_\mu^{[1]\dagger} \mathcal{J}_\nu^{[2]} \right) + \mathcal{J}_\mu^{[2]\dagger} \mathcal{J}_\nu^{[2]} \right). \end{aligned} \quad (\text{A.8})$$

Exclusive one-body matrix elements

We employ the second quantization picture to properly evaluate the nuclear operators and their symmetries. The one-body operator is of the form

$$\hat{O}_{JM}^{[1]}(|\vec{q}|) = \sum_{\alpha, \beta} \langle \alpha | \hat{O}_{JM}^{[1]}(|\vec{q}|) | \beta \rangle \hat{c}_{\alpha}^{\dagger} \hat{c}_{\beta}. \quad (\text{A.9})$$

Then, we incorporate it into our nuclear matrix element, using the result of Eq. (A.6), and write

$$\begin{aligned} \langle \Phi_{1p1h} | \hat{O}_{JM}^{[1]}(|\vec{q}|) | \Phi_{g.s.} \rangle &= \sum_{l, m_l} \sum_{j, m_j} (4\pi) \frac{\sqrt{\pi}}{\sqrt{2M_N |\vec{p}_N|}} (-i)^l e^{-i(\delta_l + \sigma_l)} Y_{lm_l}(\Omega_N) \\ &\times (-1)^{j_h + m_h} \langle l, m_l; 1/2, m_{s_N} | j, m_j \rangle \\ &\times \sum_{\alpha, \beta} \langle \alpha | \hat{O}_{JM}^{[1]}(|\vec{q}|) | \beta \rangle \langle \Phi_{g.s.} | \hat{c}_h^{\dagger} \hat{c}_p \hat{c}_{\alpha}^{\dagger} \hat{c}_{\beta} | \Phi_{g.s.} \rangle. \end{aligned} \quad (\text{A.10})$$

Following Ref. [2], we can further simplify the summation over states α and β as

$$\sum_{\alpha, \beta} \langle \alpha | \hat{O}_{JM}^{[1]}(|\vec{q}|) | \beta \rangle \langle \Phi_{g.s.} | \hat{c}_h^{\dagger} \hat{c}_p \hat{c}_{\alpha}^{\dagger} \hat{c}_{\beta} | \Phi_{g.s.} \rangle = -\langle p | \hat{O}_{JM}^{[1]}(|\vec{q}|) | h \rangle. \quad (\text{A.11})$$

Then, we use the Wigner-Eckart theorem to obtain

$$\langle p | \hat{O}_{JM}^{[1]}(|\vec{q}|) | h \rangle = (-1)^{j-m_j} \begin{pmatrix} j & J & j_h \\ -m_j & M & m_h \end{pmatrix} \langle p || \hat{O}_J^{[1]}(|\vec{q}|) || h \rangle \quad (\text{A.12})$$

and write the final result as

$$\begin{aligned} \langle \Phi_{1p1h} | \hat{O}_{JM}^{[1]}(|\vec{q}|) | \Phi_{g.s.} \rangle &= \sum_{l, m_l} \sum_{j, m_j} (4\pi) \frac{\sqrt{\pi}}{\sqrt{2M_N |\vec{p}_N|}} (-i)^l e^{-i(\delta_l + \sigma_l)} Y_{lm_l}(\Omega_N) \\ &\times (-1)^{j_h + m_h + 1} \langle l, m_l; 1/2, m_{s_N} | j, m_j \rangle \\ &\times (-1)^{j-m_j} \begin{pmatrix} j & J & j_h \\ -m_j & M & m_h \end{pmatrix} \langle p || \hat{O}_J^{[1]}(|\vec{q}|) || h \rangle. \end{aligned} \quad (\text{A.13})$$

Using the partial wave expansion and the formulas of Eq. (2.1.41), we write the one-body nuclear currents as follows

$$\begin{aligned} \mathcal{J}_0^{[1]} &= +\sqrt{4\pi} \sum_{J \geq 0} i^J \hat{J} \sum_{l, m_l} \sum_{j, m_j} (4\pi) \frac{\sqrt{\pi}}{\sqrt{2M_N |\vec{p}_N|}} (-i)^l e^{-i(\delta_l + \sigma_l)} Y_{lm_l}(\Omega_N) \\ &\times (-1)^{j_h + m_h + 1} \langle l, m_l; 1/2, m_{s_N} | j, m_j \rangle (-1)^{j-m_j} \\ &\times \begin{pmatrix} j & J & j_h \\ -m_j & 0 & m_h \end{pmatrix} \langle p || \hat{\mathcal{C}}_J^{\text{Coul}, [1]}(|\vec{q}|) || h \rangle, \end{aligned} \quad (\text{A.14})$$

$$\begin{aligned} \mathcal{J}_3^{[1]} &= -\sqrt{4\pi} \sum_{J \geq 0} i^J \hat{J} \sum_{l, m_l} \sum_{j, m_j} (4\pi) \frac{\sqrt{\pi}}{\sqrt{2M_N |\vec{p}_N|}} (-i)^l e^{-i(\delta_l + \sigma_l)} Y_{lm_l}(\Omega_N) \\ &\times (-1)^{j_h + m_h + 1} \langle l, m_l; 1/2, m_{s_N} | j, m_j \rangle (-1)^{j-m_j} \\ &\times \begin{pmatrix} j & J & j_h \\ -m_j & 0 & m_h \end{pmatrix} \langle p || \hat{\mathcal{L}}_J^{\text{long}, [1]}(|\vec{q}|) || h \rangle, \end{aligned} \quad (\text{A.15})$$

$$\begin{aligned}
\mathcal{J}_{\pm 1}^{[1]} &= -\sqrt{2\pi} \sum_{J \geq 1} i^J \hat{J} \sum_{l, m_l} \sum_{j, m_j} (4\pi) \frac{\sqrt{\pi}}{\sqrt{2M_N |\vec{p}_N|}} (-i)^l e^{-i(\delta_l + \sigma_l)} Y_{lm_l}(\Omega_N) \\
&\times (-1)^{j_h + m_h + 1} \langle l, m_l; 1/2, m_{s_N} | j, m_j \rangle (-1)^{j - m_j} \\
&\times \begin{pmatrix} j & J & j_h \\ -m_j & \pm 1 & m_h \end{pmatrix} \left[\langle \mathbf{p} \parallel \hat{J}_J^{\text{elec}, [1]}(|\vec{q}|) \parallel \mathbf{h} \rangle \pm \langle \mathbf{p} \parallel \hat{J}_J^{\text{magn}, [1]}(|\vec{q}|) \parallel \mathbf{h} \rangle \right].
\end{aligned} \tag{A.16}$$

Finally, we use the obtained formulas to construct hadronic response functions \mathcal{W}_x . For example, we present the Coulomb response

$$\begin{aligned}
\mathcal{W}_{CC}^{[1]} &= \sum_{j_h, m_h} 4\pi \sum_{J, J' \geq 0} i^{J-J'} \hat{J} \hat{J}' \sum_{l, m_l} \sum_{l', m_{l'}} \sum_{j, m_j} \sum_{j', m_{j'}} \frac{(2\pi)^3}{M_N |\vec{p}_N|} (-i)^{l-l'} \\
&\times e^{-i(\delta_l + \sigma_l - \delta_{l'} - \sigma_{l'})} Y_{lm_l}(\Omega_N) Y_{l'm_{l'}}^*(\Omega_N) (-1)^{j - m_j + j' - m_{j'}} \\
&\times \langle l, m_l; 1/2, m_{s_N} | j, m_j \rangle \langle l', m_{l'}; 1/2, m_{s_N} | j', m_{j'} \rangle \\
&\times \begin{pmatrix} j & J & j_h \\ -m_j & 0 & m_h \end{pmatrix} \begin{pmatrix} j' & J' & j_h \\ -m_{j'} & 0 & m_h \end{pmatrix} \\
&\times \langle \mathbf{p} \parallel \hat{C}_J^{\text{Coul}, [1]}(|\vec{q}|) \parallel \mathbf{h} \rangle \left(\langle \mathbf{p}' \parallel \hat{C}_{J'}^{\text{Coul}, [1]}(|\vec{q}|) \parallel \mathbf{h} \rangle \right)^*
\end{aligned} \tag{A.17}$$

obtained from the $\mathcal{J}_0^{[1]}$ current and its complex conjugate. We calculate all the other one-body functions in an analogical way.

Exclusive two-body and interference matrix elements

The main difference between the treatment of one- and two-body operators appear in the second quantization, using which we write the latter as

$$\hat{O}_{JM}^{[2]}(|\vec{q}|) = \frac{1}{4} \sum_{\alpha, \beta, \gamma, \delta} \langle \alpha \beta | \hat{O}_{JM}^{[2]}(|\vec{q}|) | \gamma \delta \rangle \hat{c}_\alpha^\dagger \hat{c}_\beta^\dagger \hat{c}_\delta \hat{c}_\gamma. \tag{A.18}$$

Then, analogically to the one-body case, we obtain the following matrix element

$$\begin{aligned}
\langle \Phi_{1p1h} | \hat{O}_{JM}^{[2]}(|\vec{q}|) | \Phi_{g.s.} \rangle &= \sum_{l, m_l} \sum_{j, m_j} (4\pi) \frac{\sqrt{\pi}}{\sqrt{2M_N |\vec{p}_N|}} (-i)^l e^{-i(\delta_l + \sigma_l)} Y_{lm_l}(\Omega_N) \\
&\times (-1)^{j_h + m_h} \langle l, m_l; 1/2, m_{s_N} | j, m_j \rangle \\
&\times \frac{1}{4} \sum_{\alpha, \beta, \gamma, \delta} \langle \alpha \beta | \hat{O}_{JM}^{[2]}(|\vec{q}|) | \gamma \delta \rangle \langle \Phi_{g.s.} | \hat{c}_h^\dagger \hat{c}_p \hat{c}_\alpha^\dagger \hat{c}_\beta^\dagger \hat{c}_\delta \hat{c}_\gamma | \Phi_{g.s.} \rangle.
\end{aligned} \tag{A.19}$$

We simplify the summation from the last line as

$$\frac{1}{4} \sum_{\alpha, \beta, \gamma, \delta} \langle \alpha \beta | \hat{O}_{JM}^{[2]}(|\vec{q}|) | \gamma \delta \rangle \langle \Phi_{g.s.} | \hat{c}_h^\dagger \hat{c}_p \hat{c}_\alpha^\dagger \hat{c}_\beta^\dagger \hat{c}_\delta \hat{c}_\gamma | \Phi_{g.s.} \rangle = \sum_{h'} \langle \mathbf{p} h' | \hat{O}_{JM}^{[2]}(|\vec{q}|) | \mathbf{h} h' \rangle_{as}. \tag{A.20}$$

Note that this result yields an opposite sign to Eq. (A.11). We use this result to write

$$\begin{aligned}
& \sum_{h'} \langle ph' | \hat{O}_{JM}^{[2]}(|\vec{q}|) | hh' \rangle_{as} \\
&= \sum_{l_{h'}} \sum_{j_{h'}, m_{j_{h'}}} \langle jm_j; j_{h'} m_{j_{h'}} | \hat{O}_{JM}^{[2]}(|\vec{q}|) | j_h m_{j_h}; j_{h'} m_{j_{h'}} \rangle_{as} \\
&= \sum_{l_{h'}} \sum_{j_{h'}, m_{j_{h'}}} \sum_{J_1, M_1} \sum_{J_2, M_2} \langle j, m_j; j_{h'}, m_{j_{h'}} | J_1, M_1 \rangle \langle j, m_j; j_{h'}, m_{j_{h'}} | J_2, M_2 \rangle \\
&\times (-1)^{J_1 - M_1} \begin{pmatrix} J_1 & J & J_2 \\ -M_1 & M & M_2 \end{pmatrix} \langle ph'; J_1 || \hat{O}_J^{[2]}(|\vec{q}|) || hh'; J_2 \rangle_{as},
\end{aligned} \tag{A.21}$$

where we employ the Wigner-Eckart theorem again. Finally, we obtain the matrix element as

$$\begin{aligned}
& \langle \Phi_{1p1h} | \hat{O}_{JM}^{[2]}(|\vec{q}|) | \Phi_{g.s.} \rangle \\
&= \sum_{l, m_l} \sum_{j, m_j} \sum_{l_{h'}, j_{h'}} \sum_{J_1, J_2} \frac{1}{\sqrt{1 + \delta_{hh'}}} (4\pi) \frac{\sqrt{\pi}}{\sqrt{2M_N |\vec{p}_N|}} (-i)^l e^{-i(\delta_l + \sigma_l)} Y_{lm_l}(\Omega_N) \\
&\times \langle l, m_l; 1/2, m_{s_N} | j, m_j \rangle \begin{pmatrix} j & J & j_h \\ m_j & -M & -m_h \end{pmatrix} \begin{Bmatrix} j & J & j_h \\ J_2 & j_{h'} & J_1 \end{Bmatrix} \\
&\times \hat{J}_1 \hat{J}_2 (-1)^{-j+j_{h'}-J_2-M} \langle ph'; J_1 || \hat{O}_J^{[2]}(|\vec{q}|) || hh'; J_2 \rangle_{as},
\end{aligned} \tag{A.22}$$

where we included an additional normalization of the two-particle state $(1 + \delta_{hh'})^{-1/2}$ [2]. Here, we restrict ourselves to the time-like component of the hadronic current for clarity of notation. Using the partial wave expansion and the formulas of Eq. (2.1.41), we write the two-body current as follows

$$\begin{aligned}
\mathcal{J}_0^{[2]} &= \sqrt{4\pi} \sum_{J \geq 0} i^J \hat{J} \sum_{l, m_l} \sum_{j, m_j} \sum_{l_{h'}, j_{h'}} \sum_{J_1, J_2} \frac{1}{\sqrt{1 + \delta_{hh'}}} (4\pi) \frac{\sqrt{\pi}}{\sqrt{2M_N |\vec{p}_N|}} (-i)^l e^{-i(\delta_l + \sigma_l)} \\
&\times Y_{lm_l}(\Omega_N) \langle l, m_l; 1/2, m_{s_N} | j, m_j \rangle \begin{pmatrix} j & J & j_h \\ m_j & 0 & -m_h \end{pmatrix} \begin{Bmatrix} j & J & j_h \\ J_2 & j_{h'} & J_1 \end{Bmatrix} \\
&\times \hat{J}_1 \hat{J}_2 (-1)^{-j+j_{h'}-J_2} e_{ph';hh'}^{\text{Coul},[2]}(J_1, J, J_2),
\end{aligned} \tag{A.23}$$

where we define

$$\begin{aligned}
e_{ph';hh'}^{\text{Coul},[2]}(J_1, J, J_2) &= \langle ph'; J_1 || \hat{C}_J^{\text{Coul},[2]}(|\vec{q}|) || hh'; J_2 \rangle_{as} \\
&- (-1)^{j_h+j_{h'}+J_2} \langle ph'; J_1 || \hat{C}_J^{\text{Coul},[2]}(|\vec{q}|) || h'h; J_2 \rangle_{as}.
\end{aligned} \tag{A.24}$$

We combine the obtained results to write the two-body Coulomb response as

$$\begin{aligned}
\mathcal{W}_{\text{CC}}^{[2]} = & \sum_{j_h, m_h} 4\pi \sum_{J, J' \geq 0} i^{J-J'} \widehat{J} \widehat{J}' \sum_{l, m_l} \sum_{j, m_j} \sum_{l', m_{l'}} \sum_{j', m_{j'}} \sum_{l_{h_1}, j_{h_1}} \sum_{l_{h_2}, j_{h_2}} \sum_{J_1, J'_1} \sum_{J_2, J'_2} \\
& \times \frac{1}{\sqrt{1 + \delta_{h h_1}} \sqrt{1 + \delta_{h h_2}}} \frac{(2\pi)^3}{2M_N |\vec{p}_N|} (-i)^{l-l'} e^{-i(\delta_l + \sigma_l - \delta_{l'} - \sigma_{l'})} \\
& \times Y_{l m_l}(\Omega_N) Y_{l' m_{l'}}^*(\Omega_N) \widehat{J}_1 \widehat{J}_2 \widehat{J}'_1 \widehat{J}'_2 (-1)^{-j-j'+j_{h_1}+j_{h_2}-J_2-J'_2} \\
& \times \langle l, m_l; 1/2, m_{s_N} | j, m_j \rangle \begin{pmatrix} j & J & j_h \\ m_j & 0 & -m_h \end{pmatrix} \begin{Bmatrix} j & J & j_h \\ J_2 & j_{h_1} & J_1 \end{Bmatrix} \\
& \times \langle l', m_{l'}; 1/2, m_{s_N} | j', m_{j'} \rangle \begin{pmatrix} j' & J' & j_h \\ m_{j'} & 0 & -m_h \end{pmatrix} \begin{Bmatrix} j' & J' & j_h \\ J'_2 & j_{h_2} & J'_1 \end{Bmatrix} \\
& \times \mathcal{C}_{p h_1; h h_1}^{\text{Coul}, [2]}(J_1, J, J_2) \left(\mathcal{C}_{p' h_2; h h_2}^{\text{Coul}, [2]}(J'_1, J', J'_2) \right)^*
\end{aligned} \tag{A.25}$$

and the interference one as

$$\begin{aligned}
\mathcal{W}_{\text{CC}}^{[1,2]} = & \sum_{j_h, m_h} 2\Re \left[4\pi \sum_{J, J' \geq 0} i^{J-J'} \widehat{J} \widehat{J}' \sum_{l, m_l} \sum_{l', m_{l'}} \sum_{j, m_j} \sum_{j', m_{j'}} \sum_{l_{h'}, j_{h'}} \sum_{J_1, J_2} \frac{(2\pi)^3}{M_N |\vec{p}_N|} (-i)^{l-l'} \right. \\
& \times e^{-i(\delta_l + \sigma_l - \delta_{l'} - \sigma_{l'})} Y_{l m_l}(\Omega_N) Y_{l' m_{l'}}^*(\Omega_N) (-1)^{j_h + m_h + 1 + j - m_j - j' + j_{h'} - J_2} \widehat{J}_1 \widehat{J}_2 \\
& \times \langle l, m_l; 1/2, m_{s_N} | j, m_j \rangle \begin{pmatrix} j & J & j_h \\ -m_j & 0 & m_h \end{pmatrix} \\
& \times \langle l', m_{l'}; 1/2, m_{s_N} | j', m_{j'} \rangle \begin{pmatrix} j' & J' & j_h \\ m_{j'} & 0 & -m_h \end{pmatrix} \begin{Bmatrix} j' & J' & j_h \\ J_2 & j_{h'} & J_1 \end{Bmatrix} \\
& \left. \times \langle p \parallel \widehat{\mathcal{C}}_J^{\text{Coul}, [1]}(|\vec{q}|) \parallel h \rangle \left(\mathcal{C}_{p' h'; h h'}^{\text{Coul}, [2]}(J_1, J', J_2) \right)^* \right].
\end{aligned} \tag{A.26}$$

Within this picture, each of the one- and two-body current-mediated $1p1h$ hadronic response is a sum of all three parts

$$\mathcal{W}_{\text{CC}} = \mathcal{W}_{\text{CC}}^{[1]} + \mathcal{W}_{\text{CC}}^{[2]} + \mathcal{W}_{\text{CC}}^{[1,2]}. \tag{A.27}$$

Inclusive one-body matrix elements

We can interpret the inclusive one-nucleon knock-out through the exclusive cross section formula integrated over the outgoing nucleon ($d\Omega_N$). Thus, we obtain

$$\frac{d\sigma^X}{d\epsilon_f d\Omega_f} = \int d\Omega_N \frac{d\sigma^X}{d\epsilon_f d\Omega_f d\Omega_N}. \tag{A.28}$$

Here, for simplicity, we assume that the residual nucleus has no recoil ($f_{1p1h} = 1$). Furthermore, as neither the leptonic kinematical factors nor the Mott-like prefactor depend on Ω_N , we write the general inclusive cross section formulas

$$\frac{d\sigma^W}{d\epsilon_f d\Omega_f} = 4\pi\sigma^W \zeta [\mathcal{V}_{\text{CC}} \mathcal{W}_{\text{CC}} + \mathcal{V}_{\text{CL}} \mathcal{W}_{\text{CL}} + \mathcal{V}_{\text{LL}} \mathcal{W}_{\text{LL}} + \mathcal{V}_{\text{T}} \mathcal{W}_{\text{T}} + h \mathcal{V}_{\text{T}'} \mathcal{W}_{\text{T}'}], \tag{A.29}$$

$$\frac{d\sigma^\gamma}{d\epsilon_f d\Omega_f} = 4\pi\sigma^{\text{Mott}} [\mathcal{V}_{\text{L}}^e \mathcal{W}_{\text{CC}} + \mathcal{V}_{\text{T}}^e \mathcal{W}_{\text{T}}], \tag{A.30}$$

where we multiply the hadronic responses with a common factor $(4\pi(2\pi)^3/|\vec{p}_N|M_N)^{-1}$. As the five hadronic responses $\{\text{TC}, \text{TL}, \text{TT}, \text{TC}', \text{TL}'\}$ are odd functions of Ω_N , they cancel out, and we are left with five or (CVC-constrained) two responses in the neutrino and electron case, respectively.

In the next step, we perform integrals of the following type

$$\begin{aligned}
\int d\Omega_N \mathcal{W}_{CC}^{[1]} &= \int d\Omega_N \sum_{j_h, m_h} 4\pi \sum_{J, J' \geq 0} i^{J-J'} \hat{J} \hat{J}' \sum_{l, m_l} \sum_{l', m_{l'}} \sum_{j, m_j} \sum_{j', m_{j'}} \frac{(2\pi)^3}{M_N |\vec{p}_N|} (-i)^{l-l'} \\
&\times e^{-i(\delta_l + \sigma_l - \delta_{l'} - \sigma_{l'})} Y_{lm_l}(\Omega_N) Y_{l'm_{l'}}^*(\Omega_N) (-1)^{j-m_j+j'-m_{j'}} \\
&\times \langle l, m_l; 1/2, m_{s_N} | j, m_j \rangle \langle l', m_{l'}; 1/2, m_{s_N} | j', m_{j'} \rangle \\
&\times \begin{pmatrix} j & J & j_h \\ -m_j & 0 & m_h \end{pmatrix} \begin{pmatrix} j' & J' & j_h \\ -m_{j'} & 0 & m_h \end{pmatrix} \\
&\times \langle \mathbf{p} \parallel \hat{\mathcal{C}}_J^{\text{Coul}, [1]}(|\vec{q}|) \parallel \mathbf{h} \rangle \left(\langle \mathbf{p}' \parallel \hat{\mathcal{C}}_{J'}^{\text{Coul}, [1]}(|\vec{q}|) \parallel \mathbf{h} \rangle \right)^*.
\end{aligned} \tag{A.31}$$

We can simplify this equation using the orthogonality of spherical harmonics, three-j symbols, and Clebsch-Gordan coefficients. This yields the following responses

$$\frac{1}{4\pi} \frac{|\vec{p}_N|M_N}{(2\pi)^3} \int d\Omega_N \mathcal{W}_{CC}^{[1]} = \sum_{j_h} \sum_{J \geq 0} \sum_{l, j} \left| \langle \mathbf{p} \parallel \hat{\mathcal{C}}_J^{\text{Coul}, [1]}(|\vec{q}|) \parallel \mathbf{h} \rangle \right|^2, \tag{A.32}$$

$$\begin{aligned}
&\frac{1}{4\pi} \frac{|\vec{p}_N|M_N}{(2\pi)^3} \int d\Omega_N \mathcal{W}_{CL}^{[1]} \\
&= - \sum_{j_h} \sum_{J \geq 0} \sum_{l, j} 2\Re \left[\langle \mathbf{p} \parallel \hat{\mathcal{C}}_J^{\text{Coul}, [1]}(|\vec{q}|) \parallel \mathbf{h} \rangle \left(\langle \mathbf{p} \parallel \hat{\mathcal{L}}_J^{\text{long}, [1]}(|\vec{q}|) \parallel \mathbf{h} \rangle \right)^* \right],
\end{aligned} \tag{A.33}$$

$$\frac{1}{4\pi} \frac{|\vec{p}_N|M_N}{(2\pi)^3} \int d\Omega_N \mathcal{W}_{LL}^{[1]} = \sum_{j_h} \sum_{J \geq 0} \sum_{l, j} \left| \langle \mathbf{p} \parallel \hat{\mathcal{L}}_J^{\text{long}, [1]}(|\vec{q}|) \parallel \mathbf{h} \rangle \right|^2, \tag{A.34}$$

$$\begin{aligned}
&\frac{1}{4\pi} \frac{|\vec{p}_N|M_N}{(2\pi)^3} \int d\Omega_N \mathcal{W}_T^{[1]} \\
&= \sum_{j_h} \sum_{J \geq 1} \sum_{l, j} 2\Re \left(\left| \langle \mathbf{p} \parallel \hat{\mathcal{J}}_J^{\text{elec}, [1]}(|\vec{q}|) \parallel \mathbf{h} \rangle \right|^2 + \left| \langle \mathbf{p} \parallel \hat{\mathcal{J}}_J^{\text{magn}, [1]}(|\vec{q}|) \parallel \mathbf{h} \rangle \right|^2 \right),
\end{aligned} \tag{A.35}$$

and

$$\begin{aligned}
&\frac{1}{4\pi} \frac{|\vec{p}_N|M_N}{(2\pi)^3} \int d\Omega_N \mathcal{W}_{T'}^{[1]} \\
&= \sum_{j_h} \sum_{J \geq 1} \sum_{l, j} 2\Re \left[\langle \mathbf{p} \parallel \hat{\mathcal{J}}_J^{\text{elec}, [1]}(|\vec{q}|) \parallel \mathbf{h} \rangle \left(\langle \mathbf{p} \parallel \hat{\mathcal{J}}_J^{\text{magn}, [1]}(|\vec{q}|) \parallel \mathbf{h} \rangle \right)^* \right].
\end{aligned} \tag{A.36}$$

Inclusive two-body and interference matrix elements

Integrating the terms involving two-body currents is analogical to the previous case. Here, we encounter integrals of form

$$\begin{aligned} \int d\Omega_N \mathcal{W}_{CC}^{[2]} &= 4\pi \frac{(2\pi)^3}{2M_N |\vec{p}_N|} \sum_{j_h} \sum_{J \geq 0} \sum_{l,j} \sum_{l_{h_1}, j_{h_1}} \sum_{l_{h_2}, j_{h_2}} \sum_{J_1, J'_1} \sum_{J_2, J'_2} \hat{J}_1 \hat{J}_2 \hat{J}'_1 \hat{J}'_2 \\ &\times \frac{1}{\sqrt{1 + \delta_{hh_1}} \sqrt{1 + \delta_{hh_2}}} (-1)^{j_{h_1} + j_{h_2} - J_2 - J'_2} \left\{ \begin{matrix} j & J & j_h \\ J_2 & j_{h_1} & J_1 \end{matrix} \right\} \\ &\times \left\{ \begin{matrix} j' & J & j_h \\ J'_2 & j_{h_2} & J'_1 \end{matrix} \right\} e_{ph_1;hh_1}^{\text{Coul},[2]}(J_1, J, J_2) \left(e_{ph_2;hh_2}^{\text{Coul},[2]}(J'_1, J, J'_2) \right)^*, \end{aligned} \quad (\text{A.37})$$

exemplified by the Coulomb one. Then, for greater numerical simplicity, we compress the notation and obtain the two-body matrix elements like

$$\begin{aligned} \frac{1}{4\pi} \frac{|\vec{p}_N| M_N}{(2\pi)^3} \int d\Omega_N \mathcal{W}_{CC}^{[2]} &= \sum_{j_h} \sum_{J \geq 0} \sum_{l,j} \\ &\times \left| \sum_{l_{h_1}, j_{h_1}} \sum_{J_1, J_2} \hat{J}_1 \hat{J}_2 \frac{1}{\sqrt{1 + \delta_{hh_1}}} (-1)^{j_{h_1} - J_2} \left\{ \begin{matrix} j & J & j_h \\ J_2 & j_{h_1} & J_1 \end{matrix} \right\} e_{ph_1;hh_1}^{\text{Coul},[2]}(J_1, J, J_2) \right|^2 \end{aligned} \quad (\text{A.38})$$

and the interference terms

$$\begin{aligned} \frac{1}{4\pi} \frac{|\vec{p}_N| M_N}{(2\pi)^3} \int d\Omega_N \mathcal{W}_{CC}^{[1,2]} &= - \sum_{j_h} \sum_{J \geq 0} \sum_{l,j} 2\Re \left[\langle p \parallel \hat{C}_J^{\text{Coul},[1]}(|\vec{q}|) \parallel h \rangle \right. \\ &\times \left. \left(\sum_{l_{h'}, j_{h'}} \sum_{J_1, J_2} \hat{J}_1 \hat{J}_2 \frac{1}{\sqrt{1 + \delta_{hh'}}} (-1)^{j_h + j_{h'} - J_2} \left\{ \begin{matrix} j & J & j_h \\ J_2 & j_{h'} & J_1 \end{matrix} \right\} e_{ph_1;hh'}^{\text{Coul},[2]}(J_1, J, J_2) \right)^* \right] \end{aligned} \quad (\text{A.39})$$

similarly. Finally, we obtain the other responses following the same steps.

B Two-nucleon knock-out matrix elements

For the starting point of our calculations of two-nucleon knock-out matrix elements and cross sections [1], we take the formula derived in Eq. (2.1.28) as

$$\begin{aligned} \frac{d\sigma^X}{d\epsilon_f d\Omega_f dT_{N_a} d\Omega_{N_a} d\Omega_{N_b}} &= \frac{|\vec{p}_{N_a}| E_{N_a} |\vec{p}_{N_b}| E_{N_b}}{(2\pi)^6} f_{2p2h}^{-1} \zeta \sigma^X \\ &\times [\mathcal{V}_{CC} \mathcal{W}_{CC} + \mathcal{V}_{CL} \mathcal{W}_{CL} + \mathcal{V}_{LL} \mathcal{W}_{LL} + \mathcal{V}_T \mathcal{W}_T + \mathcal{V}_{TT} \mathcal{W}_{TT} \\ &+ \mathcal{V}_{TC} \mathcal{W}_{TC} + \mathcal{V}_{TL} \mathcal{W}_{TL} + h(\mathcal{V}_{T'} \mathcal{W}_{T'} + \mathcal{V}_{TC'} \mathcal{W}_{TC'} + \mathcal{V}_{TL'} \mathcal{W}_{TL'})], \end{aligned} \quad (\text{B.1})$$

In this equation, the nuclear responses \mathcal{W}_x encapsulate the hadronic information about these processes. They are bilinear products of currents given by

$$\mathcal{J}_v^{\text{had}} = \langle \Psi_{2p2h} | \hat{\mathcal{J}}_v^{\text{had}}(\vec{q}) | \Psi_i \rangle \simeq \langle \Phi_{2p2h} | \hat{\mathcal{J}}_v^{\text{had}}(\vec{q}) | \Phi_{g.s.} \rangle, \quad (\text{B.2})$$

where we distinguish the true, fully correlated states $|\Psi\rangle$ and the uncorrelated, Slater determinants $|\Phi\rangle$. The investigated 2p2h hadronic final states contain two nucleons in the continuum, which can be explicitly distinguished by writing

$$\mathcal{J}_v^{\text{had}} = \langle \Phi_{A-2}(E_{\text{exc}}, J_R M_R); \vec{p}_{N_a} m_{s_{N_a}}; \vec{p}_{N_b} m_{s_{N_b}} | \hat{\mathcal{J}}_v^{[2]}(\vec{q}) | \Phi_{g.s.} \rangle. \quad (\text{B.3})$$

Here, we will show how we can describe these states relative to the wave function of the nuclear ground state. We commence by obtaining a two-hole residual state Ψ_{A-2} as

$$\begin{aligned} |\Phi_{A-2}(E_{\text{exc}}, J_R M_R)\rangle &= |(hh')^{-1}(E_{\text{exc}}, J_R M_R)\rangle = \sum_{m_h m_{h'}} \frac{1}{\sqrt{1 + \delta_{hh'}}} \\ &\times \langle j_h m_h; j_{h'} m_{h'} | J_R M_R \rangle (-1)^{j_h + m_h + j_{h'} + m_{h'}} \hat{c}_{j_h, -m_h} \hat{c}_{j_{h'}, -m_{h'}} | \Phi_{g.s.} \rangle. \end{aligned} \quad (\text{B.4})$$

Then, for the continuum states, we use the states derived in Eq. (A.5) to build the uncorrelated 2p2h state

$$\begin{aligned} |\Phi_{2p2h}\rangle &= |\Phi_{A-2}(E_{\text{exc}}, J_R M_R); \vec{p}_{N_a} m_{s_{N_a}}; \vec{p}_{N_b} m_{s_{N_b}}\rangle_{\text{as}} \\ &= \sum_{l_a m_{l_a}} \sum_{j_a m_{j_a}} \sum_{l_b m_{l_b}} \sum_{j_b m_{j_b}} \sum_{m_h m_{h'}} \frac{1}{\sqrt{1 + \delta_{hh'}}} (4\pi)^2 \frac{\pi}{2M_N \sqrt{|\vec{p}_{N_a}| |\vec{p}_{N_b}|}} \\ &\times i^{l_a + l_b} e^{i(\delta_{l_a} + \sigma_{l_a} + \delta_{l_b} + \sigma_{l_b})} Y_{l_a m_{l_a}}^*(\Omega_{N_a}) Y_{l_b m_{l_b}}^*(\Omega_{N_b}) \\ &\times \langle l_a, m_{l_a}; 1/2, m_{s_{N_a}} | j_a, m_{j_a} \rangle \langle l_b, m_{l_b}; 1/2, m_{s_{N_b}} | j_b, m_{j_b} \rangle \\ &\times \langle j_h, m_h; j_{h'}, m_{h'} | J_R, M_R \rangle (-1)^{j_h + m_h + j_{h'} + m_{h'}} \\ &\times \hat{c}_{l_a j_a m_{j_a}}^\dagger \hat{c}_{l_b j_b m_{j_b}}^\dagger \hat{c}_{j_h, -m_h} \hat{c}_{j_{h'}, -m_{h'}} | \Phi_{g.s.} \rangle \end{aligned} \quad (\text{B.5})$$

Note that within our framework, only two-body nuclear currents lead to two-nucleon knock-out processes

$$W_{\mu\nu} = W_{\mu\nu}^{[2]}. \quad (\text{B.6})$$

Exclusive matrix elements

Analogically to the one-nucleon knock-out case, we commence by writing our two-body operator in the second quantization picture as

$$\hat{O}_{JM}^{[2]}(|\vec{q}|) = \frac{1}{4} \sum_{\alpha, \beta, \gamma, \delta} \langle \alpha\beta | \hat{O}_{JM}^{[2]}(|\vec{q}|) | \gamma\delta \rangle \hat{c}_\alpha^\dagger \hat{c}_\beta^\dagger \hat{c}_\delta \hat{c}_\gamma. \quad (\text{B.7})$$

Then, we write the transition element as follows

$$\begin{aligned} \langle \Phi_{2p2h} | \hat{O}_{JM}^{[2]}(|\vec{q}|) | \Phi_{g.s.} \rangle &= \sum_{l_a, m_{l_a}} \sum_{j_a, m_{j_a}} \sum_{l_b, m_{l_b}} \sum_{j_b, m_{j_b}} \sum_{m_h, m_{h'}} (4\pi)^2 (-i)^{l_a+l_b} \\ &\times \frac{1}{\sqrt{1+\delta_{hh'}}} \frac{\pi}{2M_N \sqrt{|\vec{p}_{N_a}| |\vec{p}_{N_b}|}} e^{-i(\delta_{l_a} + \sigma_{l_a} + \delta_{l_b} + \sigma_{l_b})} Y_{l_a m_{l_a}}(\Omega_{N_a}) Y_{l_b m_{l_b}}(\Omega_{N_b}) \\ &\times \langle l_a, m_{l_a}; 1/2, m_{s_{N_a}} | j_a, m_{j_a} \rangle \langle l_b, m_{l_b}; 1/2, m_{s_{N_b}} | j_b, m_{j_b} \rangle \\ &\times \langle j_h, m_h; j_{h'}, m_{h'} | J_R, M_R \rangle (-1)^{j_h+m_h+j_{h'}+m_{h'}} \\ &\times \frac{1}{4} \sum_{\alpha, \beta, \gamma, \delta} \langle \alpha\beta | \hat{O}_{JM}^{[2]}(|\vec{q}|) | \gamma\delta \rangle \langle \Phi_{g.s.} | \hat{c}_{h'}^\dagger \hat{c}_h^\dagger \hat{c}_{p_b} \hat{c}_{p_a} \hat{c}_\alpha^\dagger \hat{c}_\beta^\dagger \hat{c}_\delta \hat{c}_\gamma | \Phi_{g.s.} \rangle. \end{aligned} \quad (\text{B.8})$$

Using the commutative rules of creation and annihilation operators [2], we obtain

$$\begin{aligned} \frac{1}{4} \sum_{\alpha, \beta, \gamma, \delta} \langle \alpha\beta | \hat{O}_{JM}^{[2]}(|\vec{q}|) | \gamma\delta \rangle \langle \Phi_{g.s.} | \hat{c}_{h'}^\dagger \hat{c}_h^\dagger \hat{c}_{p_b} \hat{c}_{p_a} \hat{c}_\alpha^\dagger \hat{c}_\beta^\dagger \hat{c}_\delta \hat{c}_\gamma | \Phi_{g.s.} \rangle \\ = -\frac{1}{2} \langle p_a p_b | \hat{O}_{JM}^{[2]}(|\vec{q}|) | hh' \rangle_{as}. \end{aligned} \quad (\text{B.9})$$

Then, we couple the particle and hole states into combined quantum states and use the Wigner-Eckart theorem to obtain

$$\begin{aligned} -\frac{1}{2} \langle p_a p_b | \hat{O}_{JM}^{[2]}(|\vec{q}|) | hh' \rangle_{as} &= -\frac{1}{2} \langle j_a m_{j_a}; j_b m_{j_b} | \hat{O}_{JM}^{[2]}(|\vec{q}|) | j_h m_{j_h}; j_{h'} m_{j_{h'}} \rangle_{as} \\ &= \frac{1}{2} \sum_{J_1, M_1} \sum_{J_3, M_3} \hat{J}_1^{-1} (-1)^{j_h+j_{h'}+J_3+1} \langle j_h, m_h; j_{h'}, m_{h'} | J_3, -M_3 \rangle \\ &\times \langle j_a, m_{j_b}; m_{j_a}, J_1 | j_b, M_1 \rangle \langle J_3, M; M_3, J_1 | J, M_1 \rangle \\ &\times \langle p_a p_b; J_1 | \hat{O}_J^{[2]}(|\vec{q}|) | hh'; J_R \rangle_{as}. \end{aligned} \quad (\text{B.10})$$

We combine the obtained results into the following matrix element

$$\begin{aligned} \langle \Phi_{2p2h} | \hat{O}_{JM}^{[2]}(|\vec{q}|) | \Phi_{g.s.} \rangle &= \frac{1}{2} \sum_{l_a, m_{l_a}} \sum_{j_a, m_{j_a}} \sum_{l_b, m_{l_b}} \sum_{j_b, m_{j_b}} \sum_{J_1, M_1} (4\pi)^2 (-i)^{l_a+l_b} \\ &\times \frac{1}{\sqrt{1+\delta_{hh'}}} \frac{\pi}{2M_N \sqrt{|\vec{p}_{N_a}| |\vec{p}_{N_b}|}} e^{-i(\delta_{l_a} + \sigma_{l_a} + \delta_{l_b} + \sigma_{l_b})} Y_{l_a m_{l_a}}(\Omega_{N_a}) Y_{l_b m_{l_b}}(\Omega_{N_b}) \\ &\times \langle l_a, m_{l_a}; 1/2, m_{s_{N_a}} | j_a, m_{j_a} \rangle \langle l_b, m_{l_b}; 1/2, m_{s_{N_b}} | j_b, m_{j_b} \rangle \\ &\times \langle j_a, m_{j_a}; j_b, m_{j_b} | J_1, M_1 \rangle \langle J_R, -M_R; J, M | J_1, M_1 \rangle \hat{J}_1^{-1} (-1)^{J_R+M_R+1} \\ &\times \langle p_a p_b; J_1 | \hat{O}_J^{[2]}(|\vec{q}|) | hh'; J_R \rangle_{as}. \end{aligned} \quad (\text{B.11})$$

Finally, we write the explicit formulas for the nuclear two-body current elements as

$$\begin{aligned}
j_0^{[2]} = & +\sqrt{4\pi} \sum_{J \geq 0} i^J \hat{J} \frac{1}{2} \sum_{l_a, m_{l_a}} \sum_{j_a, m_{j_a}} \sum_{l_b, m_{l_b}} \sum_{j_b, m_{j_b}} \sum_{J_1, M_1} \frac{1}{\sqrt{1 + \delta_{hh'}}} (4\pi)^2 (-i)^{l_a + l_b} \\
& \times \frac{\pi}{2M_N \sqrt{|\vec{p}_{N_a}| |\vec{p}_{N_b}|}} e^{-i(\delta_{l_a} + \sigma_{l_a} + \delta_{l_b} + \sigma_{l_b})} Y_{l_a m_{l_a}}(\Omega_{N_a}) Y_{l_b m_{l_b}}(\Omega_{N_b}) \\
& \times \langle l_a, m_{l_a}; 1/2, m_{s_{N_a}} | j_a, m_{j_a} \rangle \langle l_b, m_{l_b}; 1/2, m_{s_{N_b}} | j_b, m_{j_b} \rangle \\
& \times \langle j_a, m_{j_a}; j_b, m_{j_b} | J_1, M_1 \rangle \langle J_R, -M_R; J, 0 | J_1, M_1 \rangle \hat{J}_1^{-1} (-1)^{J_R + M_R + 1} \\
& \times \mathcal{C}_{p_a p_b; hh'}^{\text{Coul}, [2]}(J_1, J, J_R),
\end{aligned} \tag{B.12}$$

$$\begin{aligned}
j_3^{[2]} = & -\sqrt{4\pi} \sum_{J \geq 0} i^J \hat{J} \frac{1}{2} \sum_{l_a, m_{l_a}} \sum_{j_a, m_{j_a}} \sum_{l_b, m_{l_b}} \sum_{j_b, m_{j_b}} \sum_{J_1, M_1} \frac{1}{\sqrt{1 + \delta_{hh'}}} (4\pi)^2 (-i)^{l_a + l_b} \\
& \times \frac{\pi}{2M_N \sqrt{|\vec{p}_{N_a}| |\vec{p}_{N_b}|}} e^{-i(\delta_{l_a} + \sigma_{l_a} + \delta_{l_b} + \sigma_{l_b})} Y_{l_a m_{l_a}}(\Omega_{N_a}) Y_{l_b m_{l_b}}(\Omega_{N_b}) \\
& \times \langle l_a, m_{l_a}; 1/2, m_{s_{N_a}} | j_a, m_{j_a} \rangle \langle l_b, m_{l_b}; 1/2, m_{s_{N_b}} | j_b, m_{j_b} \rangle \\
& \times \langle j_a, m_{j_a}; j_b, m_{j_b} | J_1, M_1 \rangle \langle J_R, -M_R; J, 0 | J_1, M_1 \rangle \hat{J}_1^{-1} (-1)^{J_R + M_R + 1} \\
& \times \mathcal{L}_{p_a p_b; hh'}^{\text{long}, [2]}(J_1, J, J_R),
\end{aligned} \tag{B.13}$$

and

$$\begin{aligned}
j_{\pm 1}^{[2]} = & -\sqrt{2\pi} \sum_{J \geq 1} i^J \hat{J} \frac{1}{2} \sum_{l_a, m_{l_a}} \sum_{j_a, m_{j_a}} \sum_{l_b, m_{l_b}} \sum_{j_b, m_{j_b}} \sum_{J_1, M_1} \frac{1}{\sqrt{1 + \delta_{hh'}}} (4\pi)^2 (-i)^{l_a + l_b} \\
& \times \frac{\pi}{2M_N \sqrt{|\vec{p}_{N_a}| |\vec{p}_{N_b}|}} e^{-i(\delta_{l_a} + \sigma_{l_a} + \delta_{l_b} + \sigma_{l_b})} Y_{l_a m_{l_a}}(\Omega_{N_a}) Y_{l_b m_{l_b}}(\Omega_{N_b}) \\
& \times \langle l_a, m_{l_a}; 1/2, m_{s_{N_a}} | j_a, m_{j_a} \rangle \langle l_b, m_{l_b}; 1/2, m_{s_{N_b}} | j_b, m_{j_b} \rangle \\
& \times \langle j_a, m_{j_a}; j_b, m_{j_b} | J_1, M_1 \rangle \langle J_R, -M_R; J, \pm 1 | J_1, M_1 \rangle \hat{J}_1^{-1} (-1)^{J_R + M_R + 1} \\
& \times \left[\mathcal{J}_{p_a p_b; hh'}^{\text{elec}, [2]}(J_1, J, J_R) \pm \mathcal{J}_{p_a p_b; hh'}^{\text{magn}, [2]}(J_1, J, J_R) \right],
\end{aligned} \tag{B.14}$$

where we define

$$\begin{aligned}
\mathcal{O}_{p_a p_b; hh'}^{[2]}(J_1, J, J_R) = & \langle p_a p_b; J_1 \| \hat{\mathcal{O}}_J^{[2]}(|\vec{q}|) \| hh'; J_R \rangle_{\text{as}} \\
& - (-1)^{j_n + j_{h'} + J_R} \langle p_a p_b; J_1 \| \hat{\mathcal{O}}_J^{[2]}(|\vec{q}|) \| h'h; J_R \rangle_{\text{as}}.
\end{aligned} \tag{B.15}$$

With these prescriptions, we can calculate the ten nuclear responses \mathcal{W}_x by taking bilinear combinations of the currents and summing over the final nuclear states, e.g.,

$$\mathcal{W}_{CC} = \sum_{J_R, M_R} \sum_{m_{s_a}, m_{s_b}} |\mathcal{J}_0|^2. \tag{B.16}$$

Semi-inclusive matrix elements

The calculation of the semi-inclusive cross section requires integrating over one of the knocked-out nucleons. Experimentally, it means that the information about it is absorbed, and we do not know the isospin or other properties. Therefore, we model this process as an incoherent sum over

proton and neutron knock-outs in the following way

$$\begin{aligned} \frac{d\sigma^X}{d\epsilon_f d\Omega_f dT_N d\Omega_N} &= \int d\Omega_{p'} \frac{d\sigma^X}{d\epsilon_f d\Omega_f dT_N d\Omega_N d\Omega_{p'}} \\ &+ \int d\Omega_{n'} \frac{d\sigma^X}{d\epsilon_f d\Omega_f dT_N d\Omega_N d\Omega_{n'}}. \end{aligned} \quad (\text{B.17})$$

Such analytical integration of the 2p2h nuclear responses requires a deeper understanding of the two-nucleon kinematics. In our formalism, only the angular information on one of the nucleons is constrained, making the value of its momentum a subject of modeling. Here, we follow the approach presented in Ref. [3], which is inspired by the original work of K. Gottfried [4] and works in the *quasi-deuteron kinematics*. Here, we neglect the nuclear recoil and evaluate an average momentum

$$\vec{p}_{N_b}^{\text{avg}} = \vec{q} - \vec{p}_{N_a}, \quad (\text{B.18})$$

where \vec{p}_{N_a} is the momentum of the detected nucleon. This approximation allows us to calculate the essential momentum-dependent properties of both outgoing nucleons. We exemplify the calculations with the Coulomb hadronic response

$$\begin{aligned} \int d\Omega_b \mathcal{W}_{CC} &= \frac{1}{4} \sum_{J_R} \sum_{J, J' \geq 0} \sum_{l_a, j_a} \sum_{l_{a'}, j_{a'}} \sum_{l_b, j_b} \sum_{J_1, J'_1} \sum_{J_3} \\ &\times (-1)^{1+j_{a'}+J_1+J_R-1/2} P_{J_3}(\cos \theta_a) \langle J', 0; J, 0 | J_3, 0 \rangle \\ &\times \mathcal{B}(p_a p_{a'}, p_b, h, h', J_1, J, J'_1, J', J_R, J_3) \\ &\times \mathcal{C}_{p_a p_b; h h'}^{\text{Coul}, [2]}(J_1, J, J_R) \left(\mathcal{C}_{p_{a'} p_b; h h'}^{\text{Coul}, [2]}(J'_1, J', J_R) \right)^*, \end{aligned} \quad (\text{B.19})$$

where

$$\begin{aligned} &\mathcal{B}(p_a p_{a'}, p_b, h, h', J_1, J, J'_1, J', J_R, J_3) \\ &= i^{J-J'-l_a-l_{a'}} e^{-i(\delta_{l_a} + \sigma_{l_a} - \delta_{l_{a'}} - \sigma_{l_{a'}})} \widehat{j}_a \widehat{j}_{a'} \widehat{j}_1 \widehat{j}_2 \frac{1}{2} (1 + (-1)^{l_a+l_{a'}+J_3}) \\ &\times \langle j_a, 1/2; j_{a'}, -1/2 | J_3, 0 \rangle \begin{Bmatrix} J'_1 & J' & J_R \\ J & J_1 & J_3 \end{Bmatrix} \begin{Bmatrix} j_a & J_1 & j_b \\ J'_1 & j'_b & J_3 \end{Bmatrix}. \end{aligned} \quad (\text{B.20})$$

Inclusive matrix elements

The ultimate step of this derivation aims to obtain the cross section prescription for the inclusive two-nucleon knock-out process. We need to integrate the semi-inclusive formula as

$$\frac{d\sigma^X}{d\epsilon_f d\Omega_f} = \int dT_p d\Omega_p \frac{d\sigma^X}{d\epsilon_f d\Omega_f dT_p d\Omega_p}. \quad (\text{B.21})$$

As shown explicitly in Ref. [1], the angular integration involves only Legendre polynomials $P(\cos \theta_a)$ or odd functions of ϕ_a . Hence, it is a straightforward calculation, but not for the energy integral. Unfortunately, in our model, the time-like dependence of most ingredients is not analytical, and we perform the final integral numerically.

C Reduced matrix elements

The reduced matrix elements are the expectation values of different combinations of operators we encounter in our theoretical calculations. In this appendix, we summarize the equations, which appear while evaluating the hadronic currents of our interest. We commence by presenting the basic reduced matrix elements that are the most elementary combinations of spherical harmonics Y , derivatives ∇ and the spin operator σ . We express them through the radial transition densities defined as

$$\langle \mathbf{a} \parallel \hat{O} \parallel \mathbf{b} \rangle \equiv \int d\mathbf{r} \langle \mathbf{a} \parallel \hat{O} \parallel \mathbf{b} \rangle_r, \quad (\text{C.1})$$

where we denote $r = |\vec{r}|$. Then, they will serve as a base for more complex matrix elements of the IA and MEC currents. We present these formulations for the neutrino scattering case. The exhaustive description of the SRC matrix elements, which, in this work, were not updated, can be found in Ref. [1].

$$\langle \alpha \| Y_J(\Omega_r) \| \mathbf{b} \rangle_r = \frac{\hat{j}_\alpha \hat{j}_b}{\sqrt{4\pi}} (-1)^{-1/2+j_b+J} \begin{pmatrix} l_\alpha & l_b & J \\ 1/2 & -1/2 & 0 \end{pmatrix} \frac{1}{2} (1 + (-1)^{l_\alpha+J+l_b}) |\bar{r}|^2 \phi_\alpha^*(|\bar{r}|) \phi_b(|\bar{r}|) \quad (\text{C.2})$$

$$\langle \alpha \| [Y_L(\Omega_r) \otimes \sigma]_J \| \mathbf{b} \rangle_r = \sqrt{\frac{3}{2\pi}} \hat{j}_\alpha \hat{j}_b \hat{L} \hat{\Gamma}_\alpha \hat{L}_\alpha \hat{L}_b (-1)^{l_\alpha} \begin{pmatrix} l_\alpha & L & l_b \\ 0 & 0 & 0 \end{pmatrix} \begin{Bmatrix} l_\alpha & 1/2 & j_\alpha \\ l_b & 1/2 & j_b \\ L & 1 & J \end{Bmatrix} |\bar{r}|^2 \phi_\alpha^*(|\bar{r}|) \phi_b(|\bar{r}|) \quad (\text{C.3})$$

$$\begin{aligned} \langle \alpha \| [Y_{J+\kappa}(\Omega_r) \otimes (\hat{\nabla} - \hat{\nabla}^*)]_J \| \mathbf{b} \rangle_r &= \frac{\hat{J} + \kappa}{\sqrt{4\pi}} (-1)^{l_b+J} \\ &\times \left(\begin{Bmatrix} J+\kappa & 1 & J \\ l_b & l_\alpha & l_b+1 \end{Bmatrix} \hat{L}_\alpha \sqrt{2l_b+3} \begin{pmatrix} l_\alpha & J+\kappa & l_b+1 \\ 0 & 0 & 0 \end{pmatrix} r^2 \phi_\alpha^*(r) \sqrt{l_b+1} \left(\frac{\partial}{\partial r} - \frac{l_b}{r} \right) \phi_b(r) \right) \\ &- \left(\begin{Bmatrix} J+\kappa & 1 & J \\ l_b & l_\alpha & l_b-1 \end{Bmatrix} \hat{L}_\alpha \sqrt{2l_b-1} \begin{pmatrix} l_\alpha & J+\kappa & l_b-1 \\ 0 & 0 & 0 \end{pmatrix} r^2 \phi_\alpha^*(r) \sqrt{l_b} \left(\frac{l_b+1}{r} + \frac{\partial}{\partial r} \right) \phi_b(r) \right) \\ &+ \left(\begin{Bmatrix} 1 & J+\kappa & J \\ l_b & l_\alpha & l_\alpha+1 \end{Bmatrix} \sqrt{l_\alpha+1} \hat{L}_b \begin{pmatrix} l_\alpha+1 & J+\kappa & l_b \\ 0 & 0 & 0 \end{pmatrix} r^2 \phi_b^*(r) \sqrt{l_\alpha+1} \left(\frac{\partial}{\partial r} - \frac{l_\alpha}{r} \right) \phi_\alpha(r) \right) \\ &- \left(\begin{Bmatrix} 1 & J+\kappa & J \\ l_b & l_\alpha & l_\alpha-1 \end{Bmatrix} \sqrt{l_\alpha-1} \hat{L}_b \begin{pmatrix} l_\alpha-1 & J+\kappa & l_b \\ 0 & 0 & 0 \end{pmatrix} r^2 \phi_b^*(r) \sqrt{l_\alpha} \left(\frac{l_\alpha+1}{r} + \frac{\partial}{\partial r} \right) \phi_\alpha(r) \right) \end{aligned} \quad (\text{C.4})$$

$$\begin{aligned}
& \langle l_a \parallel [Y_L(\Omega) \otimes (\vec{\nabla} - \hat{\nabla})]_J \parallel l_b \rangle_r = \frac{\hat{J}L}{\sqrt{4\pi}} \\
& = \left(\begin{array}{ccc} L & 1 & J \\ l_b & l_a & l_b+1 \end{array} \right) \hat{l}_a \sqrt{2l_b+3} (-1)^{l_b+J} \begin{pmatrix} l_a & L & l_b+1 \\ 0 & 0 & 0 \end{pmatrix} r^2 \phi_a^*(r) \sqrt{l_b+1} \left(\frac{\partial}{\partial r} - \frac{l_b}{r} \right) \phi_b(r) \\
& - \left(\begin{array}{ccc} L & 1 & J \\ l_b & l_a & l_b-1 \end{array} \right) \hat{l}_a \sqrt{2l_b-1} (-1)^{l_b+J} \begin{pmatrix} l_a & L & l_b-1 \\ 0 & 0 & 0 \end{pmatrix} r^2 \phi_a^*(r) \sqrt{l_b} \left(\frac{l_b+1}{r} + \frac{\partial}{\partial r} \right) \phi_b(r) \\
& + \left(\begin{array}{ccc} 1 & L & J \\ l_b & l_a & l_a+1 \end{array} \right) \sqrt{l_a+1} \hat{l}_b (-1)^{l_b+1+L} \begin{pmatrix} l_a+1 & L & l_b \\ 0 & 0 & 0 \end{pmatrix} r^2 \phi_b^*(r) \sqrt{l_a+1} \left(\frac{\partial}{\partial r} - \frac{l_a}{r} \right) \phi_a(r) \\
& - \left(\begin{array}{ccc} 1 & L & J \\ l_b & l_a & l_a-1 \end{array} \right) \sqrt{l_a-1} \hat{l}_b (-1)^{l_b+1+L} \begin{pmatrix} l_a-1 & L & l_b \\ 0 & 0 & 0 \end{pmatrix} r^2 \phi_b^*(r) \sqrt{l_a} \left(\frac{l_a+1}{r} + \frac{\partial}{\partial r} \right) \phi_a(r)
\end{aligned} \tag{C.5}$$

$$\langle a \parallel Y_L(\Omega) \sigma \cdot (\vec{\nabla} - \hat{\nabla}) \parallel b \rangle_r = \sum_J \hat{J} (-1)^{-L-J} \sqrt{\hat{\sigma}_{aJb}} \hat{\sigma} \left\{ \begin{array}{ccc} l_a & 1/2 & j_a \\ l_b & 1/2 & j_b \\ J & 1 & L \end{array} \right\} \langle l_a \parallel [Y_L(\Omega) \otimes (\vec{\nabla} - \hat{\nabla})]_J \parallel l_b \rangle \tag{C.6}$$

Impulse approximation

$$\langle \mathbf{a} \parallel \hat{\mathcal{C}}_f^{\text{Coul}} [\hat{\rho}_V^{[1]}(\vec{\mathbf{r}})] \parallel \mathbf{b} \rangle = G_E(Q^2) \int d\mathbf{r} \langle \mathbf{a} | \tau_+ | \mathbf{b} \rangle \langle \mathbf{a} \parallel j_{\mathbf{r}}(q\mathbf{r}) Y_{\mathbf{r}}(\Omega_{\mathbf{r}}) \parallel \mathbf{b} \rangle_{\mathbf{r}} \quad (\text{C.7})$$

$$\langle \mathbf{a} \parallel \hat{\mathcal{C}}_f^{\text{Coul}} [\hat{\rho}_A^{[1]}(\vec{\mathbf{r}})] \parallel \mathbf{b} \rangle = \frac{G_A(Q^2)}{2M_N i} \int d\mathbf{r} \langle \mathbf{a} | \tau_+ | \mathbf{b} \rangle \langle \mathbf{a} \parallel j_{\mathbf{r}}(q\mathbf{r}) Y_{\mathbf{r}}(\Omega_{\mathbf{r}}) \sigma \cdot (\vec{\nabla} - \hat{\nabla}) \parallel \mathbf{b} \rangle_{\mathbf{r}} \quad (\text{C.8})$$

$$\langle \mathbf{a} \parallel \hat{\mathcal{O}}_f^{\kappa} [\hat{j}_{\text{con}}^{[1]}(\vec{\mathbf{r}})] \parallel \mathbf{b} \rangle = \frac{G_E(Q^2)}{2M_N i} \int d\mathbf{r} \langle \mathbf{a} | \tau_+ | \mathbf{b} \rangle \langle \mathbf{a} \parallel j_{\mathbf{r}+\kappa}(q\mathbf{r}) [Y_{\mathbf{r}+\kappa}(\Omega_{\mathbf{r}}) \otimes (\vec{\nabla} - \hat{\nabla})]_{\mathbf{r}} \parallel \mathbf{b} \rangle_{\mathbf{r}} \quad (\text{C.9})$$

$$\langle \mathbf{a} \parallel \hat{\mathcal{O}}_f^{\kappa} [\hat{j}_{\text{mag}}^{[1]}(\vec{\mathbf{r}})] \parallel \mathbf{b} \rangle = i\sqrt{6}q \frac{G_M(Q^2)}{2M_N} \int d\mathbf{r} \langle \mathbf{a} | \tau_+ | \mathbf{b} \rangle \sum_{\eta=\pm 1} \sqrt{J+\kappa+\delta_{\eta,+1}} \\ \times \left\{ \begin{array}{cc} J+\kappa & 1 \\ 1 & J+\kappa+\eta \end{array} \right\} \langle \mathbf{a} \parallel j_{\mathbf{r}+\kappa+\eta}(q\mathbf{r}) [Y_{\mathbf{r}+\kappa+\eta}(\Omega_{\mathbf{r}}) \otimes \sigma]_{\mathbf{r}} \parallel \mathbf{b} \rangle_{\mathbf{r}} \quad (\text{C.10})$$

$$\langle \mathbf{a} \parallel \hat{\mathcal{O}}_f^{\kappa} [\hat{j}_A^{[1]}(\vec{\mathbf{r}})] \parallel \mathbf{b} \rangle = G_A(Q^2) \int d\mathbf{r} \langle \mathbf{a} | \tau_+ | \mathbf{b} \rangle \langle \mathbf{a} \parallel j_{\mathbf{r}+\kappa}(q\mathbf{r}) [Y_{\mathbf{r}+\kappa}(\Omega_{\mathbf{r}}) \otimes \sigma]_{\mathbf{r}} \parallel \mathbf{b} \rangle_{\mathbf{r}} \quad (\text{C.11})$$

$$\langle \mathbf{a} \parallel \hat{\mathcal{O}}_f^{\kappa} [\hat{j}_{A,\text{ps}}^{[1]}(\vec{\mathbf{r}})] \parallel \mathbf{b} \rangle = \frac{2}{\pi} G_A(Q^2) \int d\mathbf{r} \int d\mathbf{r}' r'^2 \int dp \frac{p^4}{p^2 + m_{\pi}^2} \Gamma_{\pi}(p^2) \sum_{\eta=\pm 1} \sum_{e=\pm 1} (-1)^1 \sqrt{J+\kappa+\delta_{\eta,+1}} \sqrt{J+\kappa+\eta+\delta_{e,+1}} \langle \mathbf{a} | \tau_+ | \mathbf{b} \rangle \\ \times \left\{ \begin{array}{cc} J & 1 \\ J+\kappa+\eta & 1 \end{array} \right\} \left\{ \begin{array}{cc} 1 & J+\kappa \\ 1 & J+\kappa+\eta+e \end{array} \right\} \langle \mathbf{a} \parallel j_{\mathbf{r}+\kappa+\eta+e}(q\mathbf{r}) [Y_{\mathbf{r}+\kappa+\eta+e}(\Omega_{\mathbf{r}}) \otimes \sigma]_{\mathbf{r}} \parallel \mathbf{b} \rangle_{\mathbf{r}} \quad (\text{C.12})$$

Meson-exchange currents

$$\begin{aligned}
\langle ab; J_1 \parallel \hat{O}_J^{\text{Coul}} [\hat{\rho}_A^{[2], \text{axi}}(\vec{r}_1, \vec{r}_2)] \parallel cd; J_2 \rangle &= \frac{1}{g_A} \left(\frac{f_{\pi NN}}{m_\pi} \right)^2 \frac{1}{\sqrt{4\pi}} \sum_{\mathbf{l}} \sum_{J_3, \eta=\pm 1} \frac{2}{\pi} \sum_{\mathbf{l}} \widehat{J}_1 \widehat{J}_2 \widehat{J}_3 (-1)^{J_3+1} \\
&\times \langle ab \parallel (\mathcal{J}_V)_+ \parallel cd \rangle \sqrt{\mathbf{l} + \delta_{\eta, +1}} \begin{pmatrix} J & \mathbf{l} & J_3 \\ 0 & 0 & 0 \end{pmatrix} \int dp \frac{p^3}{p^2 + m_\pi^2} F_\pi(p^2) \Gamma_\pi^2(p^2) \int d\mathbf{r}_1 \int d\mathbf{r}_2 \\
&\times (\langle j_a \parallel j_J(q\mathbf{r}_1) j_l(\mathbf{p}\mathbf{r}_1) Y_{J_3}(\Omega_1) \parallel j_c \rangle_{\mathbf{r}_1} \langle j_b \parallel j_{l+\eta}(\mathbf{p}\mathbf{r}_2) [Y_{l+\eta}(\Omega_2) \otimes \sigma_2]_{\mathbf{l}} \parallel j_d \rangle_{\mathbf{r}_2} \\
&\times \left\{ \begin{matrix} j_a & j_b & J_1 \\ j_c & j_d & J_2 \\ J_3 & \mathbf{l} & J \end{matrix} \right\} - (-1)^{l+J_3+J} \left\{ \begin{matrix} j_a & j_b & J_1 \\ j_c & j_d & J_2 \\ \mathbf{l} & J_3 & J \end{matrix} \right\} \\
&\times \langle j_a \parallel j_{l+\eta}(\mathbf{p}\mathbf{r}_1) [Y_{l+\eta}(\Omega_1) \otimes \sigma_1]_{\mathbf{l}} \parallel j_c \rangle_{\mathbf{r}_1} \langle j_b \parallel j_J(q\mathbf{r}_2) j_l(\mathbf{p}\mathbf{r}_2) Y_{J_3}(\Omega_2) \parallel j_d \rangle_{\mathbf{r}_2} \end{pmatrix} \quad (\text{C.13})
\end{aligned}$$

$$\begin{aligned}
\langle ab; J_1 \parallel \hat{O}_J^{\text{K}} [\hat{\rho}_V^{[2], \text{sea}}(\vec{r}_1, \vec{r}_2)] \parallel cd; J_2 \rangle &= \left(\frac{f_{\pi NN}}{m_\pi} \right)^2 \frac{1}{\sqrt{4\pi}} \sum_{\mathbf{l}} \sum_{J_3, J_4, \eta=\pm 1} \frac{2}{\pi} \sum_{\mathbf{l}} \widehat{J}_1 \widehat{J}_2 \widehat{J}_3 \widehat{J}_4 \widehat{J} + \kappa (-1)^{J_3+l+1+\kappa} \\
&\times \langle ab \parallel (\mathcal{J}_V)_+ \parallel cd \rangle \sqrt{\mathbf{l} + \delta_{\eta, +1}} \begin{pmatrix} \mathbf{l} & J_3 & J + \kappa \\ 0 & 0 & 0 \end{pmatrix} \left\{ \begin{matrix} \mathbf{l} & J_3 & J + \kappa \\ \mathbf{l} & J & J_4 \end{matrix} \right\} \int dp \frac{p^3}{p^2 + m_\pi^2} \Gamma_\pi^2(p^2) \int d\mathbf{r}_1 \int d\mathbf{r}_2 \\
&\times (\langle j_a \parallel j_{l+\eta}(\mathbf{p}\mathbf{r}_1) [Y_{l+\eta}(\Omega_1) \otimes \sigma_1]_{\mathbf{l}} \parallel j_c \rangle_{\mathbf{r}_1} \langle j_b \parallel j_{J+\kappa}(q\mathbf{r}_2) j_l(\mathbf{p}\mathbf{r}_2) [Y_{J_3}(\Omega_2) \otimes \sigma_2]_{J_4} \parallel j_d \rangle_{\mathbf{r}_2} \\
&\times \left\{ \begin{matrix} j_a & j_b & J_1 \\ j_c & j_d & J_2 \\ \mathbf{l} & J_4 & J \end{matrix} \right\} - (-1)^{l+J_4+J} \left\{ \begin{matrix} j_a & j_b & J_1 \\ j_c & j_d & J_2 \\ J_4 & \mathbf{l} & J \end{matrix} \right\} \\
&\times \langle j_a \parallel j_{J+\kappa}(q\mathbf{r}_1) j_l(\mathbf{p}\mathbf{r}_1) [Y_{J_3}(\Omega_1) \otimes \sigma_1]_{J_4} \parallel j_c \rangle_{\mathbf{r}_1} \langle j_b \parallel j_{l+\eta}(\mathbf{p}\mathbf{r}_2) [Y_{l+\eta}(\Omega_2) \otimes \sigma_2]_{\mathbf{l}} \parallel j_d \rangle_{\mathbf{r}_2} \end{pmatrix} \quad (\text{C.14})
\end{aligned}$$

$$\begin{aligned}
\langle \mathbf{ab}; J_1 \parallel \hat{\mathcal{O}}_J^\kappa [\hat{\mathcal{J}}_V^{[2], \text{pif}}(\vec{\mathbf{r}}_1, \vec{\mathbf{r}}_2)] \parallel \mathbf{cd}; J_2 \rangle &= \left(\frac{f_{\pi \text{NN}}}{m_\pi} \right)^2 \frac{1}{\sqrt{4\pi}} \left(\frac{2}{\pi} \right)^2 \sum_{l, l'} \sum_{J_3} \sum_{\eta=\pm 1} \sum_{\eta'=\pm 1} \sum_{\epsilon=\pm 1} \widehat{Y}_{J_1}^{l, l'} \widehat{Y}_{J_2}^{l, l'} \widehat{Y}_{J_3}^{l, l'} \langle \mathbf{ab} \parallel (J_V)_+ \mid \mathbf{cd} \rangle \\
&\times \sqrt{l + \delta_{\eta, +1}} \sqrt{l' + \delta_{\eta', +1}} \sqrt{l + \eta' + \delta_{\epsilon, +1}} \begin{pmatrix} l & J + \kappa & l' \\ 0 & 0 & 0 \end{pmatrix} \begin{Bmatrix} J + \kappa & l & l' \\ J_3 & 1 & J \end{Bmatrix} \left\{ \begin{matrix} 1 & l' & l' + \eta' \\ 1 & l' + \eta' + \epsilon & J_3 \end{matrix} \right\} \\
&\times \int d\mathbf{p}_1 \frac{p_1^3}{p_1^2 + m_\pi^2} \Gamma_\pi(p_1^2) \int d\mathbf{p}_2 \frac{p_2^4}{p_2^2 + m_\pi^2} \Gamma_\pi(p_2^2) \int d\mathbf{r}_1 \int d\mathbf{r}_2 \int d\mathbf{r} \, m^2 j_l(\mathbf{p}_1 \mathbf{r}) j_{l'}(\mathbf{p}_2 \mathbf{r}) j_{J+\kappa}(\mathbf{q} \mathbf{r}) \\
&\times \left(\langle j_a \parallel j_{l+\eta}(\mathbf{p}_1 \mathbf{r}_1) [Y_{l+\eta}(\Omega_1) \otimes \sigma_1]_{l_1} \parallel j_c \rangle_{r_1} \langle j_b \parallel j_{l'+\eta'+\epsilon}(\mathbf{p}_2 \mathbf{r}_2) [Y_{l'+\eta'+\epsilon}(\Omega_2) \otimes \sigma_2]_{J_3} \parallel j_d \rangle_{r_2} \right. \\
&\times \left. \left\{ \begin{matrix} j_a & j_b & J_1 \\ j_c & j_d & J_2 \\ l & J_3 & J \end{matrix} \right\} - (-1)^{l+J_3+J} \left\{ \begin{matrix} j_a & j_b & J_1 \\ j_c & j_d & J_2 \\ J_4 & l & J \end{matrix} \right\} \right) \\
&\times \langle j_a \parallel j_{l'+\eta'+\epsilon}(\mathbf{p}_2 \mathbf{r}_1) [Y_{l'+\eta'+\epsilon}(\Omega_1) \otimes \sigma_1]_{J_3} \parallel j_c \rangle_{r_1} \langle j_b \parallel j_{l+\eta}(\mathbf{p}_1 \mathbf{r}_2) [Y_{l+\eta}(\Omega_2) \otimes \sigma_2]_{l_1} \parallel j_d \rangle_{r_2} \rangle
\end{aligned} \tag{C.15}$$

$$\begin{aligned}
\langle \mathbf{ab}; J_1 \parallel \hat{O}_J^\kappa [\hat{J}_V^{[2],\Delta}(\vec{r}_1, \vec{r}_2)] \parallel \mathbf{cd}; J_2 \rangle &= \frac{1}{9} \frac{q}{\pi^{3/2}} \frac{f_{\gamma N \Delta} f_{\pi N \Delta} f_{\pi N N}}{m_\pi^3} G_{\gamma N \Delta}(Q^2) \int \frac{p^4}{p^2 + m_\pi^2} \Gamma_\pi^2(p^2) \int d\mathbf{r}_1 \int d\mathbf{r}_2 \sum_{\mathbf{l}} \\
&\left\{ \sum_{\eta=\pm 1} \sum_{\epsilon=\pm 1} \sum_{\rho=\pm 1} \sum_{J_3, J_4, J_5, J_6} \sqrt{l+\delta_{\eta,+1}} \sqrt{J+\kappa+\delta_{\epsilon,+1}} \sqrt{l+\eta+\delta_{\rho,+1}} \widehat{l j + \kappa + \epsilon} \right. \\
&\times \left. \begin{Bmatrix} J_6 & 1 & J \\ 1 & J+\kappa+e & 1 \end{Bmatrix} \begin{Bmatrix} J & J_6 & 1 \\ J_4 & J_5 & J_3 \end{Bmatrix} \begin{Bmatrix} J_3 & 1 & l \\ J+\kappa+e & J_4 & J_6 \end{Bmatrix} \begin{Bmatrix} J_3 & 1 & l \\ l+\eta & 1 & l+\eta+\rho \end{Bmatrix} \right\} \\
&\times [6(G_\Delta^{\text{res}} + G_\Delta^{\text{nres}}) \langle \mathbf{ab} | (J_V)_+ | \mathbf{cd} \rangle - 24i(G_\Delta^{\text{res}} - G_\Delta^{\text{nres}}) \langle \mathbf{ab} | (2\tau_2)_+ | \mathbf{cd} \rangle] \\
&\times \langle j_a \parallel j_{J+\kappa+\rho}(\mathbf{qr}_1) j_l(\mathbf{pr}_1) [Y_{J_4}(\Omega_1) \otimes \sigma_1]_{J_5} \parallel j_c \rangle_{r_1} \langle j_b \parallel j_{l+\eta+\epsilon}(\mathbf{pr}_2) [Y_{l+\eta+\epsilon}(\Omega_2) \otimes \sigma_2]_{J_3} \parallel j_d \rangle_{r_2} \left. \begin{Bmatrix} j_a & j_b & J_1 \\ j_c & j_d & J_2 \\ J_3 & J_5 & J \end{Bmatrix} \right\} \\
&- (-1)^{J+J_3+J_5} \left\langle \begin{Bmatrix} j_a & j_b & J_1 \\ j_c & j_d & J_2 \\ J_3 & J_5 & J \end{Bmatrix} \right\rangle \langle j_a \parallel j_{l+\eta+\epsilon}(\mathbf{pr}_1) [Y_{l+\eta+\epsilon}(\Omega_1) \otimes \sigma_1]_{J_3} \parallel j_c \rangle_{r_1} \langle j_b \parallel j_{J+\kappa+\rho}(\mathbf{qr}_2) j_l(\mathbf{pr}_2) [Y_{J_4}(\Omega_2) \otimes \sigma_2]_{J_5} \parallel j_d \rangle_{r_2} \\
&\times [6(G_\Delta^{\text{res}} + G_\Delta^{\text{nres}}) \langle \mathbf{ab} | (J_V)_+ | \mathbf{cd} \rangle - 24i(G_\Delta^{\text{res}} - G_\Delta^{\text{nres}}) \langle \mathbf{ab} | (2\tau_1)_+ | \mathbf{cd} \rangle] \\
&+ i\sqrt{6} \sum_{\eta=\pm 1} \sum_{\epsilon=\pm 1} \sum_{\rho=\pm 1} \sum_{J_3, J_4} \sqrt{l+\delta_{\eta,+1}} \sqrt{J+\kappa+\delta_{\epsilon,+1}} \sqrt{l+\eta+\delta_{\rho,+1}} \widehat{l j + \kappa + \epsilon} \\
&\times (-1)^{J+\kappa} \begin{pmatrix} l & J_4 & J+\kappa+e \\ 0 & 0 & 0 \end{pmatrix} \begin{Bmatrix} J & J+\kappa & 1 \\ 1 & 1 & J+\kappa+e \end{Bmatrix} \begin{Bmatrix} J & 1 & J+\kappa+e \\ l & J_4 & J_3 \end{Bmatrix} \begin{Bmatrix} J_3 & 1 & l \\ l+\eta & 1 & l+\eta+\rho \end{Bmatrix} \\
&\times [4(G_\Delta^{\text{res}} + G_\Delta^{\text{nres}}) \langle \mathbf{ab} | (2\tau_2)_+ | \mathbf{cd} \rangle - 2i(G_\Delta^{\text{res}} - G_\Delta^{\text{nres}}) \langle \mathbf{ab} | (J_V)_+ | \mathbf{cd} \rangle] \\
&\times \langle j_a \parallel j_{J+\kappa+\rho}(\mathbf{qr}_1) j_l(\mathbf{pr}_1) Y_{J_4}(\Omega_1) \parallel j_c \rangle_{r_1} \langle j_b \parallel j_{l+\eta+\epsilon}(\mathbf{pr}_2) [Y_{l+\eta+\epsilon}(\Omega_2) \otimes \sigma_2]_{J_3} \parallel j_d \rangle_{r_2} \left. \begin{Bmatrix} j_a & j_b & J_1 \\ j_c & j_d & J_2 \\ J_3 & J_4 & J \end{Bmatrix} \right\} \\
&- (-1)^{J+J_3+J_4} \left\langle \begin{Bmatrix} j_a & j_b & J_1 \\ j_c & j_d & J_2 \\ J_3 & J_4 & J \end{Bmatrix} \right\rangle \langle j_a \parallel j_{l+\eta+\epsilon}(\mathbf{pr}_1) [Y_{l+\eta+\epsilon}(\Omega_1) \otimes \sigma_1]_{J_3} \parallel j_c \rangle_{r_1} \langle j_b \parallel j_{J+\kappa+\rho}(\mathbf{qr}_2) j_l(\mathbf{pr}_2) Y_{J_4}(\Omega_2) \parallel j_d \rangle_{r_2} \\
&\times [4(G_\Delta^{\text{res}} + G_\Delta^{\text{nres}}) \langle \mathbf{ab} | (2\tau_1)_+ | \mathbf{cd} \rangle - 2i(G_\Delta^{\text{res}} - G_\Delta^{\text{nres}}) \langle \mathbf{ab} | (J_V)_+ | \mathbf{cd} \rangle]
\end{aligned} \tag{C.16}$$

$$\langle \mathbf{ab}; J_1 \parallel \hat{\mathcal{O}}_f^\kappa [\hat{J}_A^{[2],\Delta}(\vec{r}_1, \vec{r}_2)] \parallel \mathbf{cd}; J_2 \rangle = \frac{1}{18} \frac{1}{\pi^{3/2}} \frac{f_{\text{YNA}}^2}{m_\pi^2} G_A(Q^2) \int \frac{p^4}{p^2 + m_\pi^2} \Gamma_\pi^2(p^2) \int d\mathbf{r}_1 \int d\mathbf{r}_2 \sum_{\mathbf{l}} \quad (\text{C.17})$$

$$\left\{ \sum_{\eta=\pm 1} \sum_{\epsilon=\pm 1} \sum_{J_3, J_4} \sum_{J_5, J_6} \sqrt{l+\delta_{\eta,+1}} \sqrt{l+\eta+\delta_{\epsilon,+1}} \widehat{\mathcal{J}}_1 \widehat{\mathcal{J}}_2 \widehat{\mathcal{J}}_3 \widehat{\mathcal{J}}_4 \widehat{\mathcal{J}}_5 \widehat{\mathcal{J}}_6^2 (-1)^{J+1+\kappa} \right. \\
\times \begin{pmatrix} J+\kappa & J_4 & l \\ 0 & 0 & 0 \end{pmatrix} \begin{pmatrix} J_3 & 1 & l \\ l+\eta & 1 & l+\eta+\epsilon \end{pmatrix} \begin{pmatrix} 1 & J & J_6 \\ 1 & J_5 & l & J_3 \end{pmatrix} \begin{pmatrix} 1 & J & J_6 \\ J+\kappa & 1 & 1 \end{pmatrix} \\
\times \left[i\sqrt{6}(G_\Delta^{\text{res}} + G_\Delta^{\text{nres}}) \langle \mathbf{ab} \mid (\mathcal{J}_V)_+ \mid \mathbf{cd} \rangle + 2\sqrt{6}(G_\Delta^{\text{res}} - G_\Delta^{\text{nres}}) \langle \mathbf{ab} \mid (2\tau_2)_+ \mid \mathbf{cd} \rangle \right] \\
\times \langle j_a \parallel j_{J+\kappa}(\mathbf{qr}_1) j_l(\mathbf{pr}_1) \rangle [Y_{J_4}(\Omega_1) \otimes \sigma_1]_{J_5} \parallel j_c \rangle_{r_1} \langle j_b \parallel j_{l+\eta+\epsilon}(\mathbf{pr}_2) [Y_{l+\eta+\epsilon}(\Omega_2) \otimes \sigma_2]_{J_3} \parallel j_d \rangle_{r_2} \left. \begin{pmatrix} j_a & j_b & J_1 \\ j_c & j_d & J_2 \\ J_5 & J_3 & J \end{pmatrix} \right\} \\
- (-1)^{J+J_3+J_5} \begin{pmatrix} j_a & j_b & J_1 \\ j_c & j_d & J_2 \\ J_3 & J_5 & J \end{pmatrix} \langle j_a \parallel j_{l+\eta+\epsilon}(\mathbf{pr}_1) [Y_{l+\eta+\epsilon}(\Omega_1) \otimes \sigma_1]_{J_3} \parallel j_c \rangle_{r_1} \langle j_b \parallel j_{J+\kappa}(\mathbf{qr}_2) j_l(\mathbf{pr}_2) [Y_{J_4}(\Omega_2) \otimes \sigma_2]_{J_5} \parallel j_d \rangle_{r_2} \\
\times \left[i\sqrt{6}(G_\Delta^{\text{res}} + G_\Delta^{\text{nres}}) \langle \mathbf{ab} \mid (\mathcal{J}_V)_+ \mid \mathbf{cd} \rangle + 2\sqrt{6}(G_\Delta^{\text{res}} - G_\Delta^{\text{nres}}) \langle \mathbf{ab} \mid (2\tau_1)_+ \mid \mathbf{cd} \rangle \right] \\
+ \sum_{\eta=\pm 1} \sum_{\epsilon=\pm 1} \sum_{J_3, J_4} \sqrt{l+\delta_{\eta,+1}} \sqrt{l+\eta+\delta_{\epsilon,+1}} \widehat{\mathcal{J}}_1 \widehat{\mathcal{J}}_2 \widehat{\mathcal{J}}_3 \widehat{\mathcal{J}}_4 (-1)^J \begin{pmatrix} J+\kappa & J_4 & l \\ 0 & 0 & 0 \end{pmatrix} \begin{pmatrix} J_3 & 1 & l \\ l+\eta & 1 & l+\eta+\epsilon \end{pmatrix} \begin{pmatrix} J & J+\kappa & 1 \\ l & J_3 & J_4 \end{pmatrix} \\
\times \left[2(G_\Delta^{\text{res}} + G_\Delta^{\text{nres}}) \langle \mathbf{ab} \mid (2\tau_2)_+ \mid \mathbf{cd} \rangle + i(G_\Delta^{\text{res}} - G_\Delta^{\text{nres}}) \langle \mathbf{ab} \mid (\mathcal{J}_V)_+ \mid \mathbf{cd} \rangle \right] \\
\times \langle j_a \parallel j_{J+\kappa}(\mathbf{qr}_1) j_l(\mathbf{pr}_1) Y_{J_4}(\Omega_1) \parallel j_c \rangle_{r_1} \langle j_b \parallel j_{l+\eta+\epsilon}(\mathbf{pr}_2) [Y_{l+\eta+\epsilon}(\Omega_2) \otimes \sigma_2]_{J_3} \parallel j_d \rangle_{r_2} \left. \begin{pmatrix} j_a & j_b & J_1 \\ j_c & j_d & J_2 \\ J_4 & J_3 & J \end{pmatrix} \right\} \\
- (-1)^{J+J_3+J_4} \begin{pmatrix} j_a & j_b & J_1 \\ j_c & j_d & J_2 \\ J_3 & J_4 & J \end{pmatrix} \langle j_a \parallel j_{l+\eta+\epsilon}(\mathbf{pr}_1) [Y_{l+\eta+\epsilon}(\Omega_1) \otimes \sigma_1]_{J_3} \parallel j_c \rangle_{r_1} \langle j_b \parallel j_{J+\kappa}(\mathbf{qr}_2) j_l(\mathbf{pr}_2) Y_{J_4}(\Omega_2) \parallel j_d \rangle_{r_2} \\
\times \left[2(G_\Delta^{\text{res}} + G_\Delta^{\text{nres}}) \langle \mathbf{ab} \mid (2\tau_1)_+ \mid \mathbf{cd} \rangle + i(G_\Delta^{\text{res}} - G_\Delta^{\text{nres}}) \langle \mathbf{ab} \mid (\mathcal{J}_V)_+ \mid \mathbf{cd} \rangle \right] \Big\}$$

References

- [1] T. Van Cuyck, Short-range correlations and meson-exchange currents in neutrino-nucleus scattering, PhD thesis (Ghent University, 2017).
- [2] K. L. G. Heyde, The nuclear shell model (Springer Berlin, Heidelberg, 1990).
- [3] J. Ryckebusch, V. Van der Sluys, K. Heyde, *et al.* Nucl. Phys. A **624**, 581 (1997).
- [4] K. Gottfried, Nucl. Phys. **5**, 5557 (1958).